

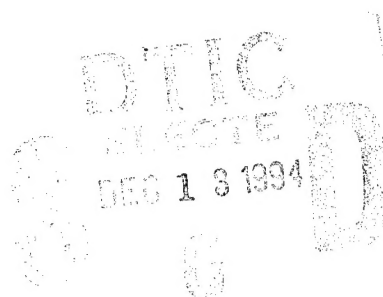


**US Army Corps
of Engineers**
Waterways Experiment
Station

Technical Report CERC-94-14
September 1994

Physical and Numerical Model Studies of Barbers Point Harbor, Oahu, Hawaii

by *Michael J. Briggs, Linda S. Lillycrop,
Gordon S. Harkins, Edward F. Thompson,
Debra R. Green*



DTIC
SELECTE
DEC 13 1994
D

Approved For Public Release; Distribution Is Unlimited

19941205 004

The contents of this report are not to be used for advertising, publication, or promotional purposes. Citation of trade names does not constitute an official endorsement or approval of the use of such commercial products.



PRINTED ON RECYCLED PAPER

Physical and Numerical Model Studies of Barbers Point Harbor, Oahu, Hawaii

by Michael J. Briggs, Linda S. Lillycrop,
Gordon S. Harkins, Edward F. Thompson,
Debra R. Green

U.S. Army Corps of Engineers
Waterways Experiment Station
3909 Halls Ferry Road
Vicksburg, MS 39180-6199

Accession For	
NTIS	CRA&I <input checked="" type="checkbox"/>
DTIC	TAB <input type="checkbox"/>
Unannounced <input type="checkbox"/>	
Justification	
By	
Distribution /	
Availability Codes	
Dist	Avail and/or Special
A-1	

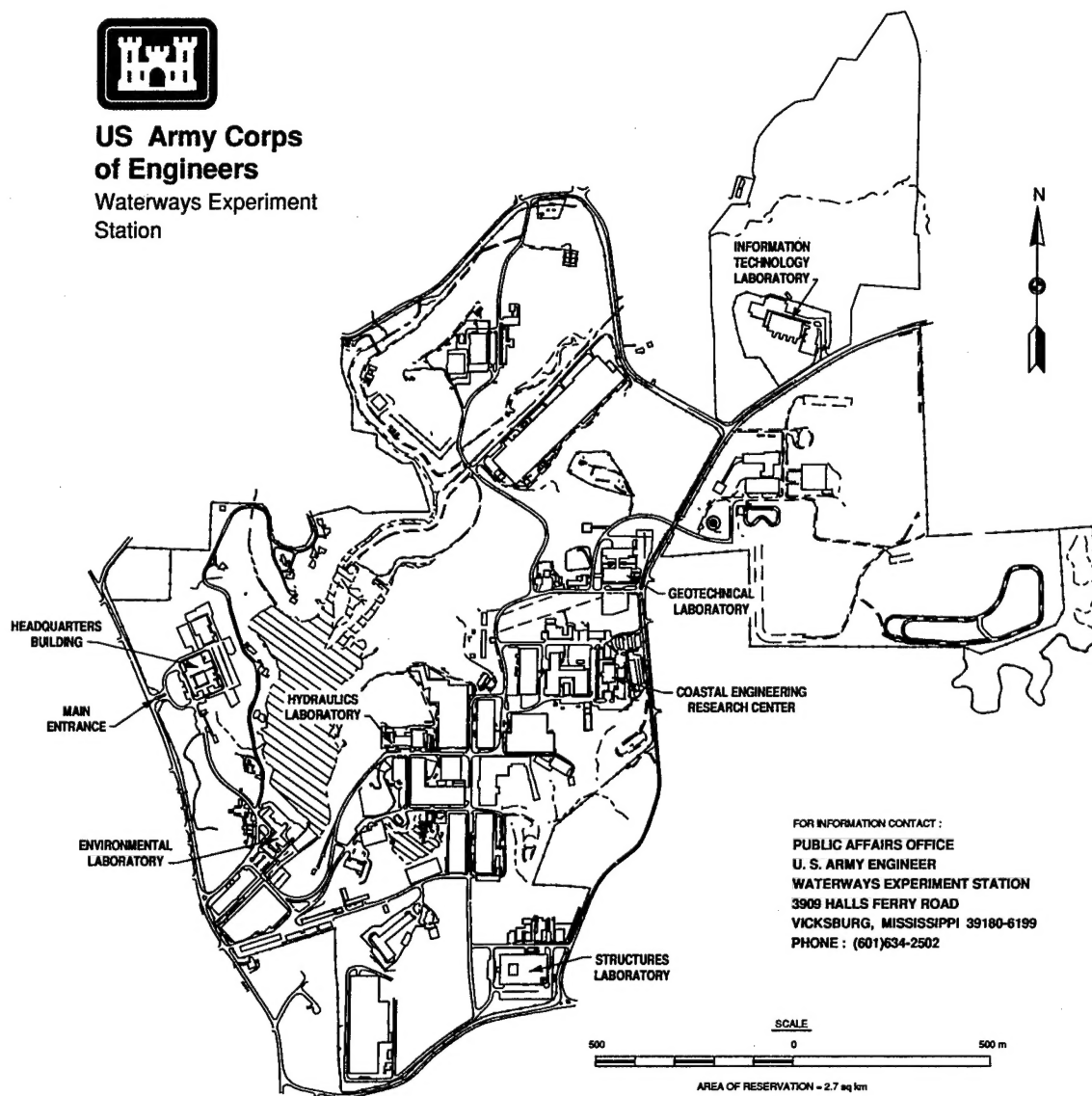
Final report

Approved for public release; distribution is unlimited

DTIC QUALITY INSPECTED 3



**US Army Corps
of Engineers**
Waterways Experiment
Station



Waterways Experiment Station Cataloging-in-Publication Data

Physical and numerical model studies of Barbers Point Harbor, Oahu, Hawaii / by Michael J. Briggs ... [et al.] ; prepared for U.S. Army Engineer Division, Pacific Ocean.

282 p. : ill. ; 28 cm. — (Technical report ; CERC-94-14)

Includes bibliographic references.

1. Barbers Point Harbor (Hawaii) — Design and construction — Simulation methods. 2. Harbors — Hawaii — Oahu — Models. 3. Channels (Hydraulic engineering) — Hawaii — Design and construction — Mathematical models. 4. Dredging — Hawaii — Oahu — Planning. I. Briggs, Michael Jeffrey. II. United States. Army. Corps of Engineers. Pacific Ocean Division. III. U.S. Army Engineer Waterways Experiment Station. IV. Coastal Engineering Research Center (U.S.) V. Series: Technical report (U.S. Army Engineer Waterways Experiment Station) ; CERC-94-14. TA7 W34 no.CERC-94-14

Contents

Preface	viii
Conversion Factors, Non-SI to SI Units of Measurement	x
Executive Summary	xi
1—Introduction	1
Description of Harbor	1
The Problem	1
Purpose and Scope of Work	2
Background	4
Acceptance Criteria	9
Report Organization	10
2—Physical Model	11
Design and Appurtenances	11
Wave Climate	20
Longshore Currents	39
Wind Conditions	44
Test Program	46
3—Numerical Model	47
Model Description	47
Finite Element Grids	51
Test Procedures and Calculations	56
4—Navigation Study	61
Design Ship	61
Test Procedure	67
Test Results	72
Probability Assessment	80
Plan Summary	86
Surge Response of Moored Ship	87
5—Harbor Response	95
Wind-Wave Response	95
Long-Wave Response	101

6—Operational Considerations	135
7—Recommendations and Conclusions	139
References	143
Appendix A: Physical Model	A1
Appendix B: Wave Calibration	B1
Appendix C: Longshore Current Calibration	C1
Appendix D: Numerical Model	D1
Appendix E: Design Ship	E1
Appendix F: Navigation Study	F1
Appendix G: Wind-Wave Response	G1
Appendix H: Long-Wave Response	H1
Appendix I: Notation	I1

List of Figures

Figure 1. Project location	1
Figure 2. Aerial photo of Barbers Point Harbor complex	2
Figure 3. Entrance channel configurations	4
Figure 4. Prototype gauge locations	7
Figure 5. Physical model of Barbers Point Harbor	11
Figure 6. Construction crew working on north end of marina	12
Figure 7. Physical model schematic	13
Figure 8. Model wave gauge locations	17
Figure 9. Photograph of harbor gauges	18
Figure 10. Photograph of entrance channel and barge basin gauges	18
Figure 11. Triaxial ultrasonic current meter	19
Figure 12. Percentage and cumulative wave period distribution	23
Figure 13. Percentage and cumulative wave height distribution	23
Figure 14. S_{xy} array joint distribution of wave height and period	24
Figure 15. S_{xy} array directions	25
Figure 16. Wave directions in previous laboratory studies	25
Figure 17. Eight target prototype directional spectra	31
Figure 18. Eight measured model directional spectra	35

Figure 19.	Resonant response of outer region	38
Figure 20.	Prototype measurement locations	39
Figure 21.	Current histograms	40
Figure 22.	Current roses for offshore and channel locations	41
Figure 23.	Current calibration results	44
Figure 24.	Simulated wind effects	46
Figure 25.	Finite element grid for existing harbor	52
Figure 26.	Finite element grid for test plan 1c	53
Figure 27.	Finite element grid for test plan 4c	54
Figure 28.	Finite element grid for test plan 6c	55
Figure 29.	Numerical model output locations	57
Figure 30.	Numerical model output locations for expanded harbor	58
Figure 31.	Model C9 container ship	63
Figure 32.	Six degrees of ship motion	64
Figure 33.	Equilibrium conditions for a ship	65
Figure 34.	Professor Bratteland and model C9 container ship	67
Figure 35.	Ship transit through channel	71
Figure 36.	Acceptance criteria	72
Figure 37.	Navigation test results	75
Figure 38.	Problem areas along entrance channel	76
Figure 39.	Observed ship speeds	77
Figure 40.	Dye measurements at station 30	79
Figure 41.	Probability assessment for C9 navigation	86
Figure 42.	Free body diagram of ship in surge	87
Figure 43.	Surge natural period of C9 container ship	91
Figure 44.	Surge response of a ship	92
Figure 45.	Normalized wind-wave heights for the existing depth plans	97
Figure 46.	Normalized wind-wave heights for the deeper depth plans ..	97
Figure 47.	Measured wind-wave heights for test plan 1a	99
Figure 48.	Measured wind-wave heights for test plan 1c	99
Figure 49.	Measured wind-wave heights for test plan 4c	100
Figure 50.	Measured wind-wave heights for test plan 6c	100

Figure 51.	Harbor mode shapes	103
Figure 52.	Transfer functions for test plan 1a	106
Figure 53.	Transfer functions for test plan 1c	108
Figure 54.	Transfer functions for test plan 4c	109
Figure 55.	Transfer functions for test plan 6c	110
Figure 56.	Amplitude contour plots for test plan 1a	112
Figure 57.	Amplitude contour plots for test plan 1c	113
Figure 58.	Amplitude contour plots for test plan 4c	114
Figure 59.	Phase plots for test plan 1a	115
Figure 60.	Phase plots for test plan 1c	116
Figure 61.	Phase plots for test plan 4c	117
Figure 62.	Transfer functions for harbor expansion east location	120
Figure 63.	Transfer functions for harbor expansion north location	121
Figure 64.	Transfer functions for harbor ferry location	122
Figure 65.	Transfer functions for barge north location	124
Figure 66.	Transfer functions for barge south location	125
Figure 67.	Transfer functions for marina entrance location	126
Figure 68.	Transfer functions for marina west location	127
Figure 69.	Transfer functions for marina north location	128
Figure 70.	South corner transfer functions for test plan 1a	130
Figure 71.	South corner transfer functions for test plan 1c	131
Figure 72.	South corner transfer functions for test plan 4c	132
Figure 73.	South corner transfer functions for test plan 6c	133
Figure 74.	Locations of C9 moored ship potential surge problems	137

List of Tables

Table 1.	Barbers Point Harbor Test Plans	3
Table 2.	Important Events Affecting Prototype Measurements	9
Table 3.	Linear Array Gauge Coordinates	16
Table 4.	Minilab Calibration Coefficients	19
Table 5.	Buoy Percentage Distribution of Wave Height and Period	21
Table 6.	S_{xy} Joint Distribution of Wave Height and Period	22

Table 7.	Selected Prototype Wave Conditions	26
Table 8.	Operational Prototype Gauges	26
Table 9.	Simulated Target Wave Conditions	33
Table 10.	Measured Model Wave Parameters	37
Table 11.	Extreme Currents	40
Table 12.	Current Conditions for Navigation Tests	42
Table 13.	Percentage Frequency of Wind Speed and Direction	45
Table 14.	Estimated Wind Forces and Moments	46
Table 15.	Grid Descriptions	56
Table 16.	Wave Period Increments	56
Table 17.	Bottom Friction Coefficients	60
Table 18.	Inbound Test Conditions	68
Table 19.	Outbound Test Conditions	69
Table 20.	Acceptable/Unacceptable Inbound and Outbound Results ...	74
Table 21.	Float Measurements at Station 30	78
Table 22.	Comparison of Dye and Float Current Velocities	80
Table 23.	Environmental Regional Probabilities	81
Table 24.	Probability of Ship Being Present P(s)	83
Table 25.	Unacceptable Navigation Fraction	84
Table 26.	Recurrence Intervals for Unacceptable Events	85
Table 27.	Surge Natural Period of Moored C9 Container Ship	91
Table 28.	Harbor, Barge Basin, and Marina Modes	111

Preface

A request for physical and numerical model investigations of eight proposed modifications to the Barbers Point Harbor, Oahu, Hawaii, was initiated by the U.S. Army Engineer Division, Pacific Ocean (POD) in coordination with the Harbors Division, Department of Transportation, State of Hawaii (DOT). Authorization for the U.S. Army Engineer Waterways Experiment Station (WES), Coastal Engineering Research Center (CERC), to perform the study was subsequently granted by Headquarters, U.S. Army Corps of Engineers (HQUSACE). Physical and numerical model tests were conducted at WES during the period September 1990 to June 1992.

Mr. Michael J. Briggs, Wave Processes Branch (WPB), Wave Dynamics Division (WDD), was principal investigator for the study with responsibility for the overall study and physical model tests. Ms. Linda S. Lillycrop, Prototype Measurement and Analysis Branch (PMAB), Engineering Development Division, (EDD), had responsibility for the numerical model implementation. Direct supervision was provided by Mr. Dennis G. Markle, Chief, WPB, and general supervision by Mr. C. E. Chatham, Jr., Chief, WDD, Mr. Charles C. Calhoun, Jr., Assistant Director, CERC, and Dr. James R. Houston, Director, CERC.

Numerous individuals contributed to the successful completion of this project. Mr. David McGehee, PMAB, furnished background information on the field measurements. Mr. David A. Daily, WES Instrumentation Services Division, maintained the directional spectral wave generator, instrumentation, and associated electronics. Mr. Larry A. Barnes, WPB, interfaced with the WES shops in the construction of the physical model. Mr. Ernie Smith, Wave Research Branch, WDD, designed and supervised construction of the physical model from the bathymetric charts of the harbor. Mr. Frank Sargent, WPB, performed initial design of the longshore current-generating system and procurement of the model container ship. Mr. Hugh F. Acuff, WPB, assisted with calibration and testing. Ms. Debra R. Green, WPB, conducted tests, analyzed data, and assisted in report preparation. Mr. Gordie Harkins, WPB, supervised data collection, performed data analysis, and co-authored portions of this report. Dr. Edward F. Thompson, Research Division, assisted in implementation of the numerical model and co-authored portions of this report.

Special thanks are extended to Ms. Michele Okihiro, Scripps Institution of Oceanography, for analyzing prototype data and participating in early planning discussions. Professor Eivind Bratteland, Norwegian Institute of Technology, was on sabbatical during the last year of the study and was responsible for the longshore current and model ship calibration, and conducted and analyzed the navigation study tests. Captains Fred Hoppe and Jean-Louis LePendu, Harbor Pilots from the state of Hawaii, provided valuable confirmation of model response and results based on their experience as port pilots at Barbers Point Harbor.

Prior to the model investigation, representatives from CERC visited the Barbers Point Harbor site and several planning meetings were held at CERC. During the course of the investigation, liaison was maintained by means of conferences, telephone communications, and monthly progress reports. Sponsor representatives who visited WES during the course of the study included Mr. Stan Boc, POD, and Messrs. Calvin Tsuda, Harry Murakami, Robert Nagao, Fred Nunes, and Elton Teshima, all of DOT.

At the time of publication of this report, Dr. Robert W. Whalin was Director of WES. COL Bruce K. Howard, EN, was Commander.

The contents of this report are not to be used for advertising, publication, or promotional purposes. Citation of trade names does not constitute an official endorsement or approval of the use of such commercial products.

Conversion Factors, Non-SI to SI Units of Measurement

Non-SI units of measurement can be converted to SI (metric) units as follows:

Multiply	By	To Obtain
acres	4,046.873	square meters
degrees (angle)	0.01745329	radians
feet	0.3048	meters
horsepower (550 foot-pounds (force) per second)	745.6999	watts
inches	2.54	centimeters
inches	25.4	millimeters
kips (force)	4.448222	kilonewtons
knots (international)	0.5144444	meters per second
miles (U.S. nautical)	1.852	kilometers
pounds (force)	4.448222	newtons
pounds (force) per square inch	6.894757	kilopascals
pounds (force) per square inch	0.006894757	megapascals
pounds (mass)	0.4535924	kilograms
square feet	0.09290304	square meters
square inches	6.4516	square centimeters
tons (force)	8.896444	kilonewtons

Executive Summary

Introduction

Through the state of Hawaii's planning process, the need for Barbers Point Harbor to accommodate larger ships and increase the number of available berths was identified. Modifications to the harbor, including widening the entrance channel, and deepening (from 38 ft to 45 ft) and expanding the harbor basin (an 1,100-ft by 1,100-ft area on the northeast side of the harbor) were proposed to address these needs. Physical and numerical (computer) model studies to evaluate the technical feasibility and optimize the design of these modifications were conducted from September 1990 to June 1992 by the U.S. Army Corps of Engineers at the U.S. Army Engineer Waterways Experiment Station, Coastal Engineering Research Center, Vicksburg, Mississippi. In addition to physical and computer model studies, navigation studies were also conducted using a scale model C9 container ship in the physical model. The studies were jointly funded by the state of Hawaii and the Corps of Engineers.

Study Results

Entrance channel

Widening or flaring the channel helped navigation but allowed more wind-wave and long-period (surge) energy into the harbor. Flaring only the outer 1,000 ft of the channel improved navigation without significantly increasing wave energy entering the harbor. Construction of the 450-ft jetty along the north side of the channel improved wind-wave conditions within the harbor, especially at the barge basin, and eliminated an existing crosscurrent at the shoreline.

Harbor basin

Expanding the harbor improved wind-wave conditions in the interior part of the harbor. Wind-wave conditions in the barge basin remained unchanged from the existing conditions. The combination of the jetty and deeper harbor with the harbor expansion significantly improved wind-wave conditions

throughout the harbor (including the proposed ferry terminal site) and barge basin.

The harbor expansion significantly improved surge conditions in the harbor. Deepening the harbor and adding the jetty had a minimal effect on harbor surge response. Surge conditions in the barge basin were not noticeably affected by the harbor expansion, harbor deepening, or the jetty.

West Beach Marina

The recommended modifications to Barbers Point Harbor significantly improved wind-wave conditions in West Beach Marina over existing conditions. A slight improvement in surge conditions was observed.

Ship surge response

Barbers Point Harbor experiences natural resonance modes, which cause standing waves to occur under certain long-period ocean wave conditions. If a ship is docked at a location in the harbor where the wave-induced currents from these long waves are present (i.e. nodal points), it can experience an undesirable surge response, which makes cargo handling difficult. Possible actions to remedy the effects of this surge include proper ballasting as the ship is offloaded, adjustments to the tension in the mooring lines, and modifications to the mooring line configuration.

Model performance

Final physical and numerical models behaved realistically when compared to actual field observations at Barbers Point Harbor. There is a high level of confidence in the predictions made by these models.

Limitations

Wave energy input to the models was based upon 4 years of field data. Because of the limited data set, probabilities of actual critical wave occurrences were not calculated.

Navigation tests were conducted using a model container ship. Since different hull shapes "feel (react to) the entrance channel" in different ways, the navigation test cannot be said to apply equally to all types of ships.

Recommendations

Recommended modifications to Barbers Point Harbor include flaring the outer 1,000 ft of the entrance channel from 450 ft wide to 750 ft wide, deepening the channel to 49 ft, constructing a 450-ft jetty along the north side of the entrance channel, deepening the harbor to 45 ft, and dredging a 1,100-ft by 1,100-ft expansion area in the harbor basin.

Effects of future modifications to the harbor should be evaluated using the validated HARBD numerical model.

The authors recommend long-term wave gauging to calculate critical wave occurrences and to provide real-time offshore wave measurements for use in the actual day-to-day operations of the harbor.

1 Introduction

Description of Harbor

Barbers Point Harbor, Hawaii, is located on the southwest coastline of Oahu (Figure 1). Figure 2 shows that the harbor complex presently consists of an entrance channel, deep-draft harbor, barge basin, and a resort marina (often referred to as the West Beach Marina). The parallel entrance channel is 450 ft¹ wide, 3,100 ft long, and 42 ft deep (mean lower low water (mllw)). The deep-draft harbor basin is 38 ft deep, 2,200 ft wide, and 2,000 ft long, covering an area of 92 acres. Rubble-mound wave absorbers line approximately 4,600 linear feet of the inner shoreline of the harbor basin. The barge basin, located just seaward of the harbor on the south side of the entrance channel, is poorly sheltered from incident wave energy. It is 220 ft by 1,300 ft and 23 ft deep. The West Beach Marina was built to the west of the deep-draft harbor. It shares the same entrance channel, is 15 ft deep, and covers approximately 20 acres. The marina was designed to accommodate 350 to 500 pleasure boats.

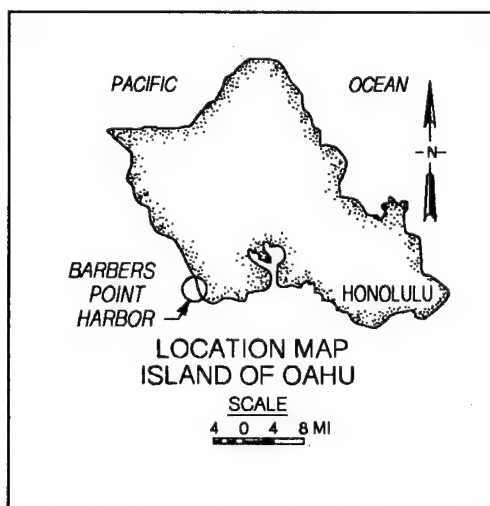


Figure 1. Project location

The Problem

The deep-draft harbor was originally designed to accommodate vessels with a length of 720 ft, a beam of 95 ft, and a loaded draft of 34 ft. Changing economics necessitate the use of bigger ships to transport cargo in the Pacific Rim routes. The state of Hawaii Department of Transportation (DOT) decided on the C9 class container ship as the "design" ship for the next century.

¹ A table of factors for converting non-SI units of measurement to SI units is presented on page x.



Figure 2. Aerial photo of Barbers Point Harbor complex

However, the C9 is too large for routine use in the existing harbor. Thus, the harbor and entrance channel require changes.

As waves travel into harbors from deep water, nonlinear processes transfer energy from the wind-wave frequencies to long waves with periods on the order of several minutes and wavelengths much longer than the wind waves. If the periods of these long waves correspond with natural (resonant) periods of the harbor, strong harbor oscillations can be induced, which can produce dangerous mooring conditions and structural damage within the harbor. On February 8, 1988, a Coast Guard vessel was in the process of entering the Marisco, Ltd. dry dock when they both sustained damage due to long-period harbor motions and other contributing factors (Noda and Associates 1988). Thus, the existing harbor has experienced some harbor oscillation problems, which should be addressed in evaluating any proposed modifications.

Purpose and Scope of Work

The purpose of this study was to evaluate eight proposed modifications of the harbor to accommodate the larger "design" vessel. Both physical and numerical model investigations were conducted at the U.S. Army Engineer Waterways Experiment Station's (WES's) Coastal Engineering Research Center (CERC) in Vicksburg, MS, between September 1990 and June 1992. A

remote-controlled, scale model of the C9 "design" vessel was used to conduct navigation tests for a range of wave and longshore current conditions.

Proposed harbor modifications included (a) deepening the harbor, (b) expanding the harbor, (c) widening and deepening the entrance channel, and (d) constructing an entrance jetty. Table 1 describes the changes for each of the eight proposed test plans.

Table 1 Barbers Point Harbor Test Plans							
Test Plan	Entrance Channel				Deep-Draft Harbor		
	Width	Depth	Config.	Jetty	Depth	Expansion	S. Corner
1a	450	42	Parallel	None	38	No	Existing
1c	450	42	Parallel	None	38	Yes	Square
2c	450	42	550' Flare	None	38	Yes	Square
3a	550	42	Parallel	None	38	No	Existing
3c	550	42	Parallel	None	38	Yes	Square
4c	450	49	750' Flare	450'	45	Yes	Square
5c	450	49	750' Flare	225'	45	Yes	Square
6c	450	49	750' Flare	None	45	Yes	Square
Notes: 1. Test plan 1a = Existing harbor. 2. Config. = Configuration or alignment of channel sides. 3. Existing = Existing conditions in prototype harbor. 4. Square = When harbor expansion is included, south corner is opened to 90 deg. 5. 550' Flare = Linearly flared channel sides from 450 ft at station 33 (shoreline) to 550 ft width at station 0 (channel entrance). 6. 750' Flare = Linearly flared channel sides from 450 ft at station 10 to 750 ft width at station 0.							

The first five test plans were built with the present prototype harbor depth of 38 ft and entrance channel depth of 42 ft. Water depth was increased by 7 ft throughout the harbor basin and entrance channel in the last three plans. To be conservative, the tide range of 2 ft was not included in the tests. All water depths were relative to mllw.

The proposed harbor expansion consists of an 1,100-ft by 1,100-ft additional berthing area in the northeast corner of the harbor basin. The "c" and "a" suffixes to the plan name designate configurations with and without this expansion, respectively.

A schematic of the different entrance channel configurations is shown in Figure 3. The first two plans (1a and 1c) had the existing channel configuration with parallel side walls and a 450-ft width. The third plan (2c)

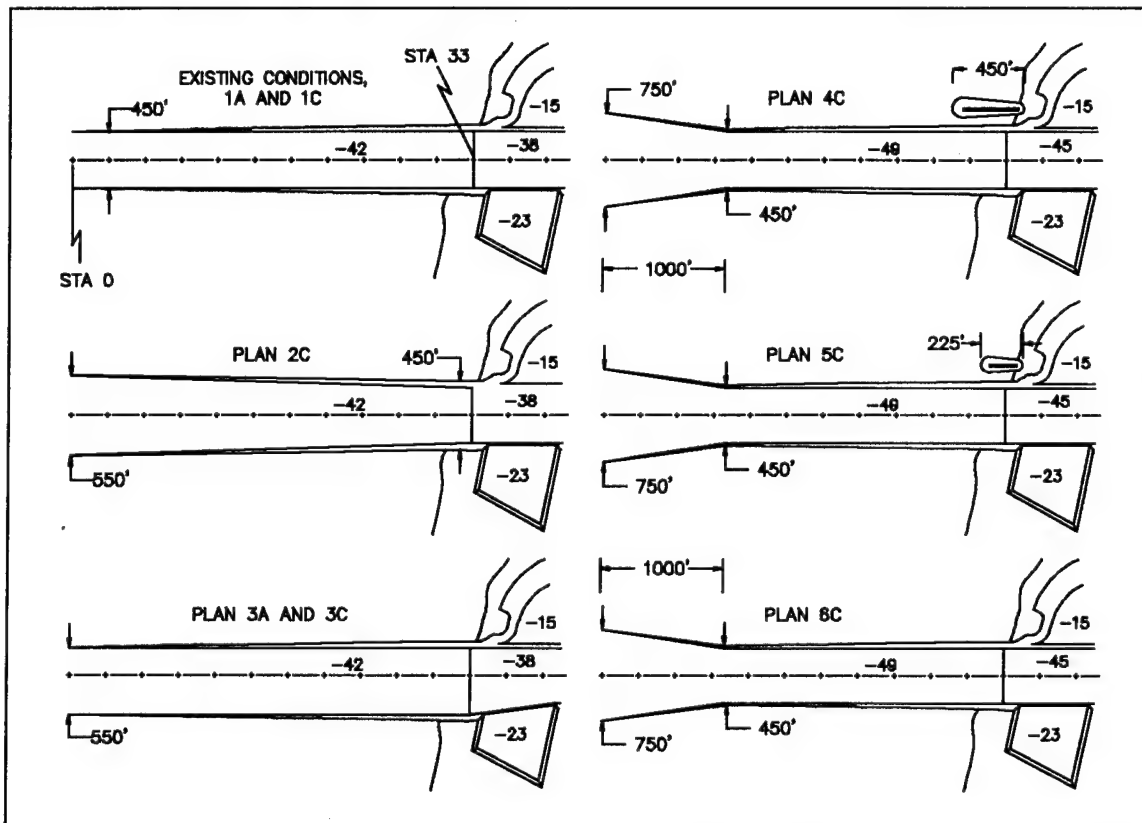


Figure 3. Entrance channel configurations

investigated the effect of flaring the channel from 550 ft at the channel opening to the existing 450 ft at the shoreline, approximately 3,300-ft shoreward. The channel side walls were again parallel, with a 550-ft constant width in the fourth and fifth plans (3a and 3c). The last three plans (4c, 5c, and 6c) had a 750-ft-wide flare in the outer 1,000 ft of the entrance channel, tapering to the existing 450-ft-wide parallel channel.

Finally, the length of the shore-connected jetty varied in each of the last three plans, ranging from a 450-ft-long jetty to no jetty.

Background

History

Initial planning for a harbor at Barbers Point began as early as 1958 when the U.S. Congress passed a resolution recommending that a feasibility study be conducted to determine the need and viability for a second port on Oahu. Based on a survey study completed by the Corps of Engineers, Congress authorized construction of Barbers Point Harbor as a part of the Rivers and Harbors Act of 1965. Alternative design evaluations were initiated in 1967,

including hydraulic model tests on a series of alternative harbor configurations with a view towards developing a technically sound harbor configuration for deep-draft vessels. The location of the harbor was predicated on availability of lands for support facilities and, to a major degree, the industrial growth pattern for Oahu.

Construction of the first phase of the total harbor development was initiated following award of a \$47-million contract in March 1982 to Peter Kiewit Sons, Inc. The dedication ceremony was held on August 30, 1985, at the site. Since that time, the state of Hawaii has completed a 1,600-ft pier, paved back-up areas, storage areas, and an access road in March 1990.

Previous hydraulic studies

Before construction of the deep-draft harbor was initiated, a physical model study was conducted at Look Laboratory at the University of Hawaii from 1967 to 1968 (Palmer 1970). The purpose of the model was to (a) study wave action in the proposed deep-draft harbor and barge basin, (b) develop an optimum design for wave absorbers in the harbor entrance and within the harbor basin, (c) study circulation and pollution potential in the harbor, and (d) develop plans to provide suitable navigation conditions in the entrance channel and mooring conditions in the proposed harbors. Results of the study indicated that wave absorbers placed along the sides of the basin would provide adequate protection for mooring and navigation.

Three-dimensional and two-dimensional tests were conducted by the University of Hawaii (Lee 1985) at Look Laboratory prior to construction of the West Beach Marina (WBM), to verify the proposed design concepts of the marina. Objectives of the three-dimensional tests were to test the wave characteristics of three proposed entrances: (a) an entrance perpendicular to the entrance channel of the deep-draft harbor, (b) a channel parallel to the deep-draft harbor, and (c) an entrance channel separate from that of the deep-draft harbor. The purpose of the two-dimensional study was to evaluate reflection characteristics of various structures in the basin including revetments, vertical walls, and igloo wave absorbers. Igloos are a specific type of vertical absorber and were considered in front of vertical walls in the marina basin and in the entrance of WBM as an alternative to a spending beach.

Results of the three-dimensional study indicated that a marina entrance perpendicular to the entrance channel of the deep-draft harbor was superior to the other entrance channel configurations. Tests conducted with a perpendicular alignment, both with and without igloos, showed: (a) wave heights less than the maximum allowable limit of 2.0 ft within the marina, (b) reduction of wave heights at berthing sites in the deep-draft harbor and barge harbor, and (c) relatively safe transit of yachts into the marina under these wave conditions. Two-dimensional tests indicated that a spending beach would be more effective in the entrance than igloos. The igloos were effective for wave periods of 6 sec and shorter, but less effective for longer wave periods.

Previous numerical studies

A post-authorization study of Barbers Point Harbor indicated a need for a basin larger than the original design. The harbor needed to accommodate 720-ft-long container vessels as well as 900-ft-long vessels projected to use the facility in the future. Based on results from the 1968 hydraulic model study, a new plan consisting of a 94-acre, 38-ft-deep basin, with a 4,280-ft-wide, 38- to 42-ft-deep entrance channel was developed. At the request of the U.S. Army Engineer Division, Pacific Ocean (POD), WES conducted a numerical harbor oscillation study of this proposed harbor plan during the period January to April 1977 (Durham 1978). The purpose of this study was to investigate harbor oscillations excited by waves with periods from 15 sec to 27 min and to ensure that no undesirable oscillations were introduced in the barge basin.

A hybrid finite element model developed by Chen and Mei (1974) was used to evaluate long-period response of the proposed deep-draft harbor. This linear, long-wave model allowed arbitrary configurations and variable bathymetry. The harbor response was calculated for each incident wave condition with results available for wave height amplification factors at each nodal point and current velocities at each element centroid. At the time of the study, the hybrid element model was the only numerical harbor oscillation model available with the capability to economically calculate resonance effects in large complex harbors. Amplification peaks predicted by the numerical model were larger than the peaks actually occurring in nature because the model neglected all dissipative processes except energy radiation from the harbor. The model, however, did adequately predict the relative severity of various modes of oscillation. This numerical model was the forerunner of the HARBD numerical model used in this study and described in detail in Chapter 3 of this report.

The finite element grid included the deep-draft harbor, entrance channel, and barge harbor. Total number of elements and nodes were 2,334 and 1,277, respectively. For each incident wave condition, wave height amplification factors were saved from 30 nodes: 18 in the deep-draft harbor, 5 in the entrance channel, and 7 in the barge harbor. Test conditions consisted of incident waves from a direction parallel to the axis of the entrance channel (approximately 225.0-deg azimuth) with periods from 15 sec to 27 min.

Twenty-five resonant modes of oscillation ranging from 19.4 to 799.0 sec were identified. The Helmholtz mode for the deep-draft harbor occurred at 799.0 sec (13.32 min). This mode exhibited amplification factors from 7.5 to 8.5 throughout the harbor. Resonant modes were also identified at wave periods of 145.0, 129.5, 107.2, and 81.9 sec, with amplification factors ranging from 4.35 to 14.45. These modes were close to the 120-sec (2-min) mode observed to excite the barge harbor. The remaining resonant modes occurred between 63.0 and 19.4 sec.

Prototype measurements of waves

Prototype measurements of waves were made in Barbers Point Harbor between July 1986 and March 1990 as part of the Monitoring Completed Coastal Projects (MCCP) Program and the Coastal Data Information Program (CDIP), a network of real-time wave gauges jointly sponsored by the Corps of Engineers, the California Department of Boating and Waterways, and the Scripps Institution of Oceanography (SIO). Figure 4 shows the selected sites in the main harbor, entrance channel, and the nearshore region. Bottom-mounted pressure gauges were used to minimize interference with navigation. A Waverider wave buoy (not shown) was located approximately 1 mile offshore in 600 ft of water.

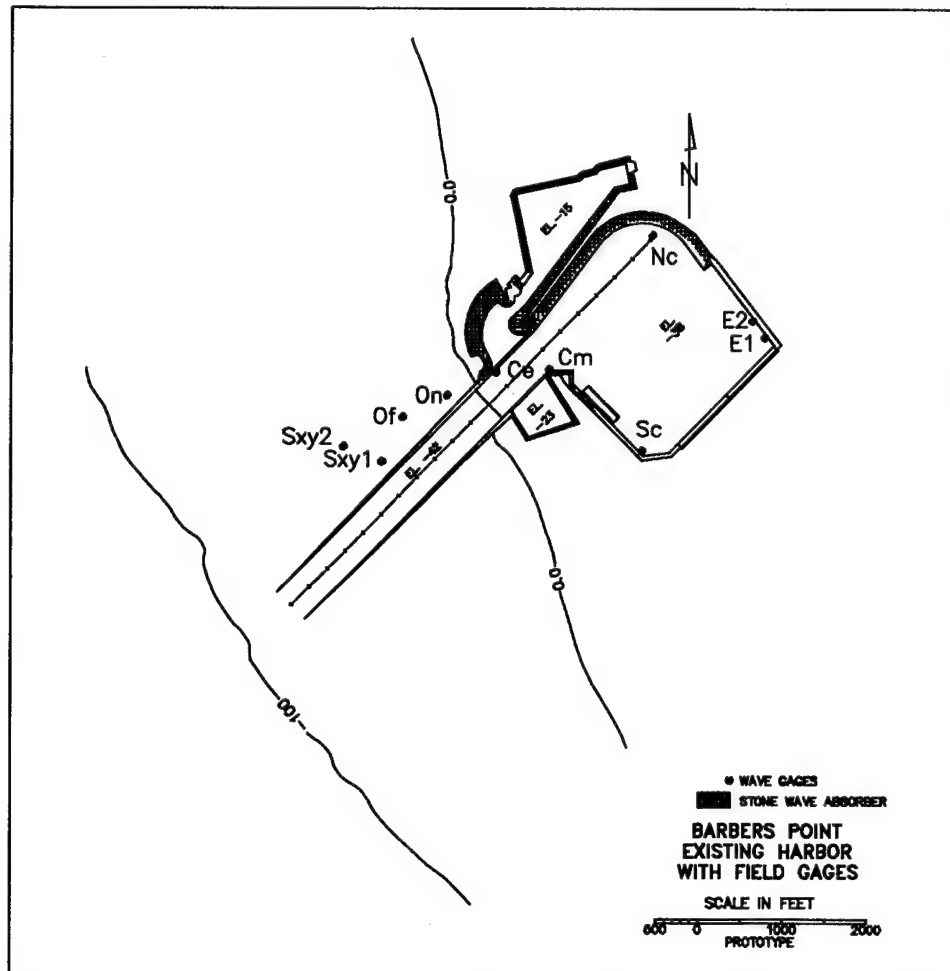


Figure 4. Prototype gauge locations

A four-gauge S_{xy} array was used offshore to measure incident directional spectra conditions in 27.5 ft of water. Individual gauges were used elsewhere to measure frequency spectra. Other offshore gauges included the offshore (Of) and onshore (On) gauges, both located shoreward of the S_{xy} gauge. Channel entrance (Ce) and channel mid-point (Cm) gauges were located in the

entrance channel, where navigation conditions were a consideration. Finally, a gauge was located in the south (Sc) corner of the harbor to measure anticipated maximum amplification factors.

A sampling scheme that collected both wind waves (energy) and long-period waves (surge) was designed. Initially, energy and surge were obtained from separate records collected by each sensor: 1,024 samples at 1.0 Hz for the energy, and 2,048 samples at 0.125 Hz for the surge. After January 1989, a system upgrade permitted a single record of 4.6 hr at 0.5 Hz inside the harbor (8,192 samples) or 1.0 Hz outside the harbor (16,384 samples) to be collected by each sensor.

Sampling interval was controlled by varying the call-up schedule in the software. The standard interval was every 6 hr in summer, and every 3 hr in winter. A threshold routine was built into the system that automatically switched the interval back to 3 hr if significant wave height exceeded 1 m offshore, or 30 cm in the harbor. On the 3-hr schedule, the enhanced sampling scheme provided a continuous record.

The time series signal recovered at the central computer was converted to a pressure time series using appropriate calibration coefficients. It was spectrally analyzed, using linear wave theory, to produce frequency spectra for the single sensors and directional spectra for the S_{xy} array. Quality control functions, including spike removal, detrending, and editing were performed daily. Analyzed data were available on-line from the CDIP database and printed summaries were provided in monthly reports.

The S_{xy} , Ce, Cm, and Sc gauges were installed in July 1986. The S_{xy} gauge experienced two major data gaps from cable failures when vessels pulling barges snagged the cable with their tow bridles. This problem was eliminated by moving the shore station to the navigation aid and rerouting the cable away from the entrance channel. Data from the second position of the S_{xy} (S_{xy2} in Figure 4) was believed to be more reliable because it was farther from the edges of the entrance channel and any refractive effects that might have influenced the first position of the array. Construction in the harbor caused longer gaps in the Sc gauge. In January 1989, additional sensors were installed in the north (Nc) and east corners to improve spatial resolution. The east corner gauges are labeled E1 and E2 to differentiate the two locations. At this time, the entire system was upgraded to the longer sampling scheme. Table 2 summarizes these and other important events that affected prototype measurements in Barbers Point Harbor.

Background summary

An MCCP report by Lillycrop et al. (1993b) summarizes the field monitoring program and physical and numerical model studies that have been conducted to date for Barbers Point Harbor. The report describes (a) previous physical and numerical model studies conducted in the planning stages of the

Table 2 Important Events Affecting Prototype Measurements	
Date	Event Description
July 1986	Data collection begins
February 8, 1988	Marisco event, dry dock breaks mooring
June 1988	Sxy ₂ operational
December 20, 1988	102 pier test piles installed
February 1, 1989	Pier installation begins
April 1989	East corner gauge fails
May 1989	Channel entrance gauge fails
July 1989	West Beach Marina opens
July 7, 1989	Pier complete
October 1989	Ec ₂ , second location for east corner gauge
March 1990	Data collection ends

harbor, (b) state-of-the-art physical and numerical model studies used to estimate harbor response in the existing harbor complex, (c) a field monitoring program for collecting wind wave and long-period waves outside and inside the harbor, (d) intercomparison among previous and current model studies and field data relative to harbor response and deepwater and nearshore coupling between infragravity and wind waves, and (e) evaluation of the effectiveness of the existing rubble-mound wave absorber in dissipating wave energy inside the harbor.

Acceptance Criteria

Prototype measurements were used to calibrate the numerical model and verify the physical model at selected locations within the harbor. Numerical model results were used to assist the physical model in the selection of test conditions; incident wave conditions having little effect on the harbor were not tested. The physical model provided an opportunity to test wave conditions which were not measured in the field, but were of interest from a design standpoint. The physical model data set was used to verify the numerical model results for the proposed modifications. Thus, the presence of all three types of data was very beneficial in testing the proposed modifications and optimizing the final design of the harbor.

Model test results were used to determine the best design for the harbor based on the following criteria: (a) acceptable navigation conditions for the design ship entering and leaving the harbor based on relatively extreme or rare wave events, (b) minimum wind-wave and long-wave action within the harbor

and barge basin boundaries, and (c) minimum adverse effects on the marina and the proposed ferry terminal site in the deep-draft harbor.

Report Organization

This report describes physical and numerical model investigations of the harbor and model ship response. Chapter 2 describes the physical model effort including design, instrumentation, wave climate, longshore currents, wind conditions, and the test program. A description of the numerical model and finite element grids is presented in Chapter 3. The navigation study is described and results are presented in Chapter 4. The harbor response to wind and long waves is presented in Chapter 5. Chapter 6 discusses operational considerations and recommendations. Finally, recommendations and conclusions are presented in Chapter 7.

Appendix A provides data on the physical model, including gauge locations, and feedback and command channel numbers. Wave calibration is described in Appendix B, while Appendix C describes longshore current calibration. Finite element grids for the numerical model are contained in Appendix D, and Appendix E contains performance characteristics for the prototype C9 ship. Appendix F provides data on the navigation study and Appendix G contains wind-wave response data. Long wave response data are contained in Appendix H.

2 Physical Model

Design and Appurtenances

Model design

An undistorted, three-dimensional model of Barbers Point Harbor (Figure 5) was constructed at a model-to-prototype scale $L_r = 1:75$, in accordance with Froude scaling laws (Stevens et al. 1942). It was patterned after earlier physical model studies by Palmer (1970) and Lee (1985). The nearshore area extends to the 100-ft mllw contour and includes approximately 3,500 ft on either side of the entrance channel. Total area of the model was over 11,000 ft². The model scale was selected to allow proper reproduction of significant harbor features, typical storm waves and longshore currents, and the design container ship (Briggs, Lillycrop, and McGehee 1992). Model and prototype lengths scale as L_r , areas as L_r^2 , and time and velocity as $\sqrt{L_r}$.

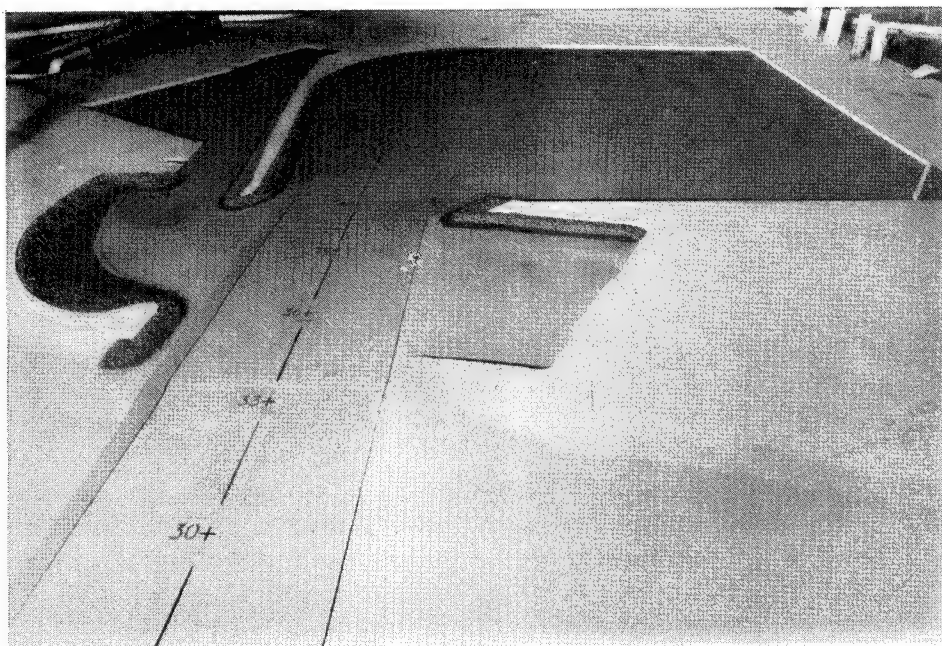


Figure 5. Physical model of Barbers Point Harbor

The model was constructed using templates, sand filler, and a 2-in. mortar cap to mold the contours (Figure 6). A unique aspect of the physical model was the use of concrete slices, which were removed or added to the entrance channel and deep-draft harbor to accommodate the desired changes in depth and wall geometry.



Figure 6. Construction crew working on north end of marina

Wavemaker

Waves were generated with a unique wavemaker, which can make waves from many different directions at once, typical of those occurring in nature. The directional spectral wave generator (DSWG) is an electronically controlled, electromechanical system, designed and built by MTS Systems Corporation, Minneapolis, MN. It is 90 ft long and consists of 60 paddles, each 1.5 ft wide and 2.5 ft high. The four portable modules, consisting of 15 paddles each, allow all or part of the DSWG to be moved to other model studies with relative ease. Each wave paddle is independently driven at its joint by a 3/4-hp electric motor operating in piston mode. This configuration, along with flexible plastic plate seals between the paddles, produces a smoother, cleaner wave form (Outlaw and Briggs 1986, Harkins 1991).

Typical peak wave periods are 1.00 to 3.00 sec, with longer and shorter periods possible. The range of strokes is ± 6 in., corresponding to a ± 10 -V input signal. Offset angles between paddles can be continuously varied within the range of 0 to 180 deg using the "snake principle" to produce directional waves at angles approaching ± 90 deg for most wave periods.

The DSWG was aligned parallel to the 100-ft contour, at approximately 325 deg relative to north. This alignment permitted the greatest range of wave conditions and directions. The basin sides and rear were lined with wave absorbers and the northwest side was open to an adjacent basin to minimize reflections and cross-basin oscillations (Figure 7).

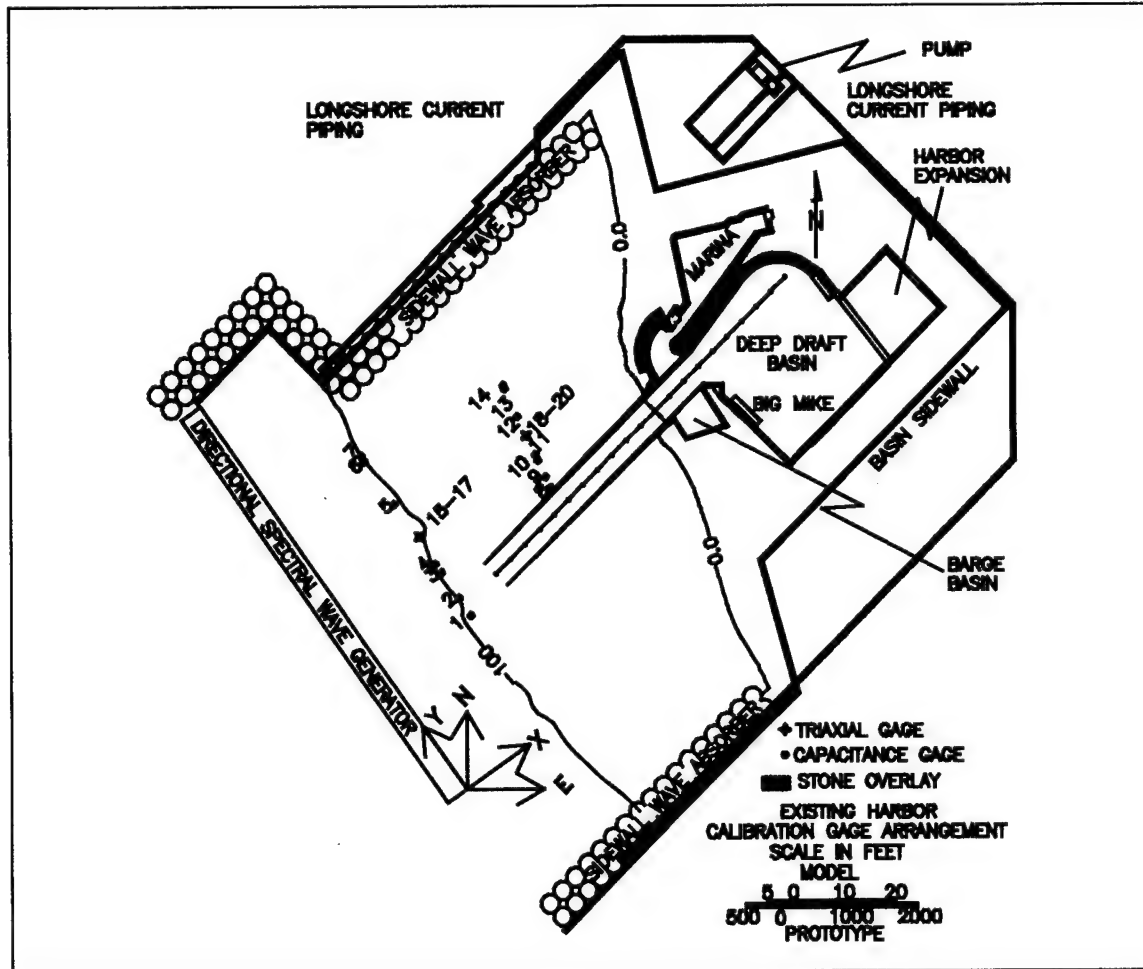


Figure 7. Physical model schematic

Longshore current-generating system

A 30-hp, 2,500-gal/min pump was used to generate longshore currents from northerly and southerly directions (Figure 7). Troughs were built into the sides of the physical model to accommodate 8-in.-diam PVC piping, which terminated in multiport diffusers with 1-in.-diam holes with variable spacing from the 10-ft contour to the 100-ft contour. Crossflow was customized by placing rubber stoppers in the diffuser ports to redistribute the flow, while maintaining a sufficient number of open ports so that their combined cross-sectional area was equal to that of the 8-in. manifold.

Flow was controlled by an orifice plate and a manometer setup to ensure repeatability. The closed loop system was reversed using a series of shunt valves, designed to minimize hydraulic head losses.

Three short training walls were added to both trenches to ensure uniform flow over the shallow-water areas of the model. Without the walls, the flow tended to go down the trenches, around the toe of the slope, and back up the opposite trench. Wave absorber material was added to the seaward side of these walls to minimize reflections during wave generation.

Computer support

A Digital VAX 11/750 minicomputer was used to control the DSWG. It performs digital-to-analog conversion for the 60 paddles at run time, monitors paddle displacement and feedback, calibrates wave gauges, and digitizes the measured data. A Digital VAX 3600 minicomputer was used to do preliminary analysis of the measured wave data. A third computer, a CRAY Y-MP supercomputer, was used to calculate control signals for the wavemaker and to conduct more advanced data analysis. All three computers can communicate with one another through a fiber-optic network.

Wave gauges

Calibration arrays. Two linear arrays of capacitance wave gauges were used to calibrate the control signals for each wave condition (Figure 7). The offshore gauge array (OGA) was parallel to the 100-ft contour at a heading of 325 deg relative to north, parallel to the DSWG. The nearshore gauge array (NGA) was parallel to the 27.5-ft contour at a heading of 335 deg, and centered about the location of the second location of the prototype S_{xy} directional wave gauge (i.e. S_{xy2} in Figure 4). The linear array provides superior resolution capability for wave components at or near the same frequency and slightly different direction. The seven gauges in each linear array comprise a "2-3-1-7-5-1/2" linear array patterned after the larger linear array design of Oltman-Shay at CERC's Field Research Facility (Oltman-Shay 1987).

A well-designed linear array must have a total length equal to the largest wavelength (i.e. lowest frequency) at the largest angle expected. It also must be short enough to avoid aliasing the higher frequency, smaller wavelength components. Spatial aliasing occurs when half the wavelength of the highest frequency wave does not exceed the distance between sensors. When this happens, it is impossible to discern the smaller wave from the longer wave. Thus, there is a classic tradeoff between the longest array to optimize resolution of the low-frequency components and the shortest spacing to minimize aliasing of the high-frequency waves. The secret to this tradeoff is to select a minimum distance between two sensors that minimizes aliasing at the high-frequency cutoff desired while simultaneously providing an overall length that optimizes resolution at the low-frequency cutoff. By clever arrangement

of a limited number of gauges, both objectives can be achieved. Rather than spacing the gauges a uniform distance apart, they are spaced at multiples of a unit "lag" length based on the criteria above. Thus, all wavelengths between the smallest and longest are covered by combinations of different gauges. For the 2-3-1-7-5-1/2 array (i.e. gauges spaced 2 lag lengths, 3 lag lengths, etc.), wave periods with half wavelengths equal to 1, 2, 3, 4, 5, 6, 7, 8, 11, 12, 13, 16, and 18 lags are discernable. The 1/2 lag separation is intended more to improve the resolution of the high-frequency components than to add to the overall array length.

The procedure consists of calculating the depth-limited wavelength for the low- and high-frequency cutoffs desired. Local (x/y) and global (N/E) coordinate systems are shown in Figure 7. The origin is at the beginning of paddle 1 of the DSWG. Wave direction is measured clockwise from north. The y-axis wave number component k_y is calculated as

$$k_y = k \sin \theta \quad (1)$$

where wave number $k = 2\pi/L$ and a maximum wave direction to the linear array of $\theta = 20$ deg was assumed. The corresponding y-axis wavelength component L_y is then

$$L_y = \frac{2\pi}{k_y} \quad (2)$$

Finally, the array length capable of resolving this wavelength is equal to one third to one half of L_y . Based on this procedure, a lag spacing of 1.0 ft was selected for the NGA array and 2.0 ft for the OGA array. These "lags" give total array lengths of 18.5 ft and 37.0 ft for the NGA and OGA arrays, respectively. Table 3 lists the x/y and N/E axis coordinates for the OGA and NGA arrays.

Test gauges. Subsequent to calibration, wave gauges were placed in the harbor to match the placement of prototype wave gauges and to obtain additional information at critical places in the model. Figure 8 shows the 22 locations used in this study. The first 10 positions (i.e. S_{xy1} , S_{xy2} , Of, On, Ce, Cm, Nc, E1, E2, and Sc) correspond to the field locations (Okiihiro 1991).

Twelve additional wave gauges were positioned throughout the model to record harbor response at important locations. Three gauges were located in the entrance channel, two in the barge basin, two in the expansion, one at the proposed ferry terminal, one in the center of the harbor, and three in the marina. Figure 9 is a photograph of the harbor gauges looking toward the DSWG from the back of the expansion area. Figure 10 is a close-up of the entrance channel and barge basin gauges, again looking toward the DSWG.

Table 3
Linear Array Gauge Coordinates

Gauge	X-DSWG	Y-DSWG	North	East
OGA Linear Array				
1	20.00	27.00	33.58	0.90
2		31.00	36.86	-1.40
3		37.00	41.78	-4.84
4		39.00	43.41	-5.99
5		53.00	54.88	-14.02
6		63.00	63.07	-19.75
7		64.00	63.89	-20.33
NGA Linear Array				
8	48.05	38.75	59.30	17.14
9	48.40	40.72	61.12	16.29
10	48.92	43.67	63.83	15.02
11	49.09	44.66	64.74	14.60
12	50.31	51.55	71.09	11.64
13	51.18	56.48	75.62	9.53
14	51.26	56.97	76.07	9.32

Three gauges were located in a 3-gauge Goda array in the entrance channel, to measure reflection coefficients. They were labeled C4, C5, and C6 (C5 is located north-east of gauge C4, but is not shown in Figure 8 for clarity). The spacing between gauge pairs C4 and C5 and C4 and C6 satisfies the following equation:

$$\frac{\Delta x}{0.45} < L < \frac{\Delta x}{0.05} \quad (3)$$

The two gauges in the barge basin were located in the north (Bn) and south corners (Bs). Two gauges were placed in the proposed harbor expansion: one each in the east (Ex2) and north (Ex3) corners. In the harbor, two additional gauges were placed in key locations. The state of Hawaii has future plans to develop a ferry terminal to transport rush-hour commuters from Barbers Point Harbor to downtown Honolulu. A wave gauge labeled Hf was positioned at the proposed location of the ferry terminal. A second gauge labeled harbor middle (Hm) was positioned in the center of the harbor. Finally, three gauges were positioned in the

marina: one in the marina entrance (Me), one in the west corner (Mw), and one in the north corner (Mn).

Channel numbers corresponding to these gauge locations for each test plan, along with feedback and command channel numbers for DSWG paddle 8, are shown in Appendix A. For the existing harbor configuration, three gauge configurations were used. The first configuration, 1a-1, was for tests conducted in May 1991 with the dry dock in its original position prior to the "Marisco" incident. Incident conditions at the S_{xy2} location were not measured because calibration phase results were available. The second configuration, 1a-2, is an artificial setup to add incident conditions from the S_{xy2} location to data files from configuration 1a-1. Seven NGA gauges were added to the beginning of the data files for each wave case and the gauges were renumbered. The third configuration, 1a-3, was for tests conducted in February 1992 with the dry dock in the post-Marisco position on the south side of the harbor. The total number of gauges changes by two, depending on whether the harbor expansion gauges are included.

Measurement rods on the gauges had a variable length depending on the water depth. They were calibrated each day prior to conducting tests. A Jordan controller stepper motor was used to automatically raise and lower the

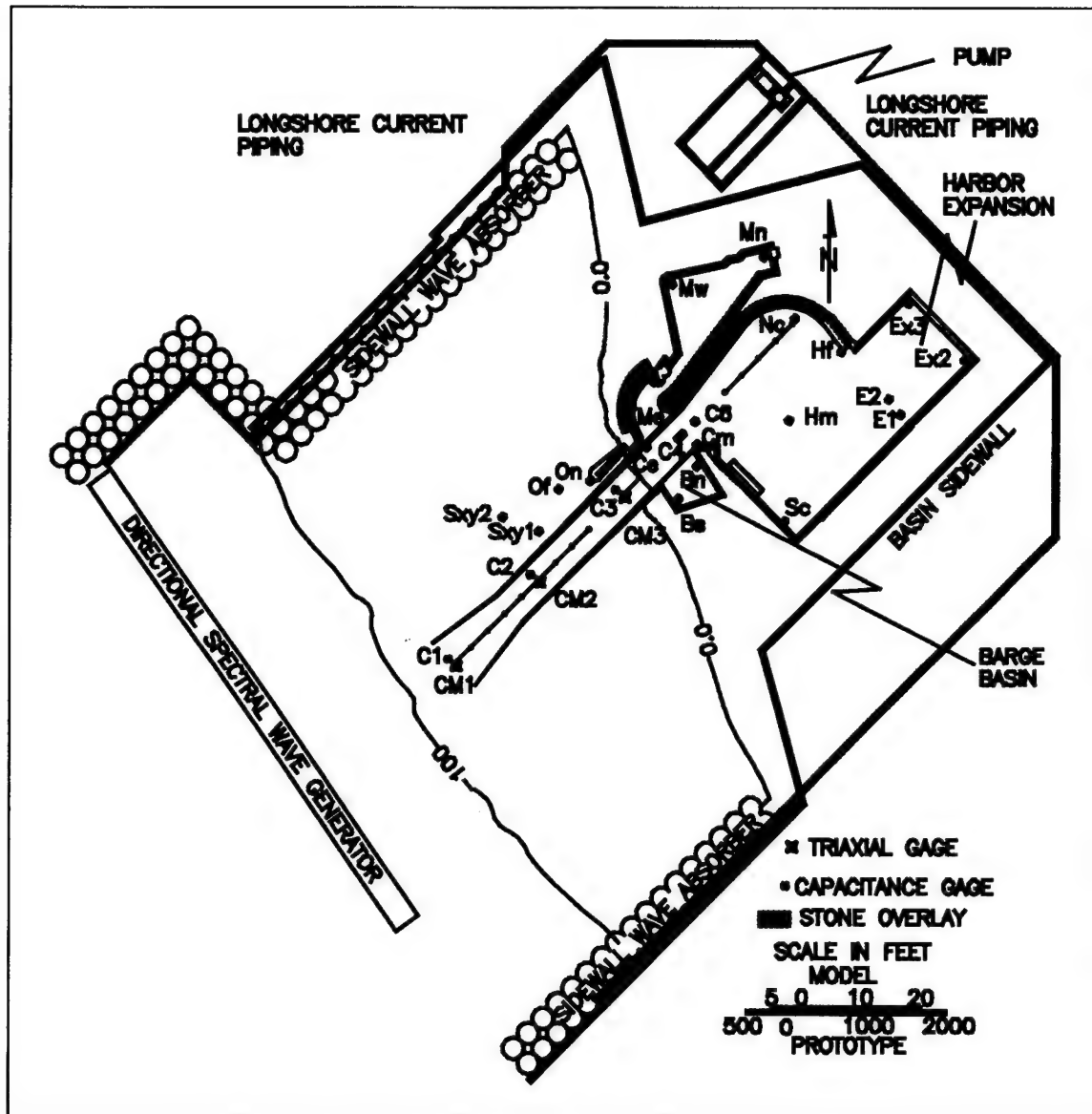


Figure 8. Model wave gauge locations

rod through a series of 11 steps to obtain calibration coefficients using a least squares linear or quadratic fit. This averaging technique, using 21 voltage samples per gauge, minimizes the effect of slack in the gear drives and hysteresis in the sensors.

Current meters

Two triaxial, ultrasonic current meters were used to measure water particle and longshore current velocities (Figure 11). One was embedded in each linear array during the calibration phase of the wave cases (channel

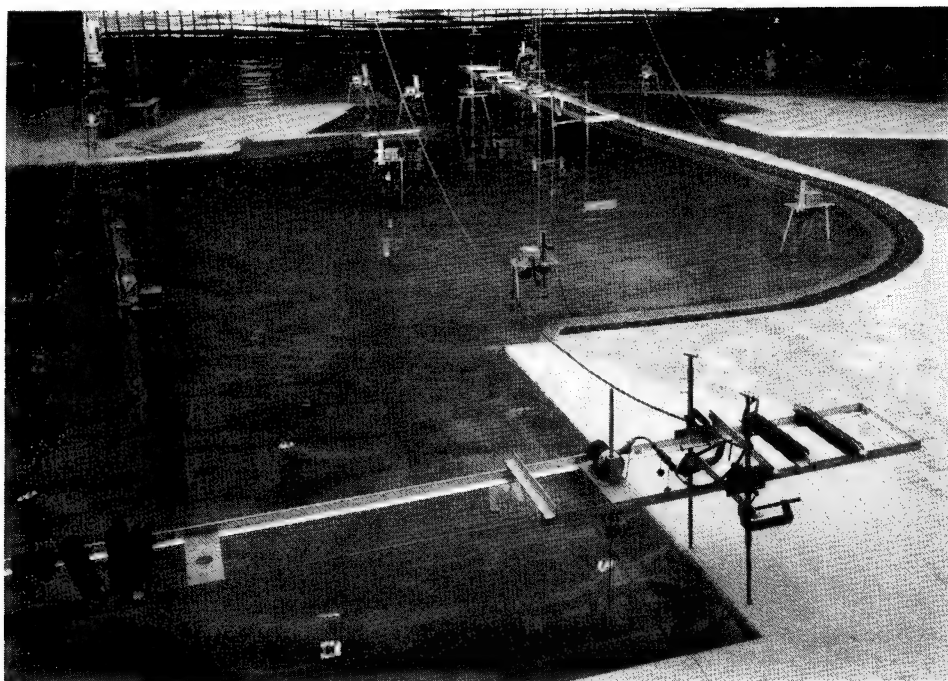


Figure 9. Photograph of harbor gauges



Figure 10. Photograph of entrance channel and barge basin gauges

numbers 15-17 and 18-20 in Figure 7) to measure the directional wave spectra. They were also used to calibrate the longshore currents.

These current meters are manufactured by Sensordata A/S, Bergen, Norway, as the Minilab SD-12 system. Outstanding features of these units include a low threshold velocity, wide dynamic range, high bandwidth, small dimensions, high linearity, modular design, and easy computer interfacing. The system consists of a display unit, an instrument cable, a probe housing, and the 3-axis probe. The display unit contains the power supply, processing circuits, digital displays, and terminals for analog and RS-232C formatted signals. The 32.8-ft-long, polyurethane instrument cable connects the display unit to the probe housing with a waterproof termination. The probe housing contains the acoustic processing circuits and attaches directly to the 3-axis probe. It has a diameter of 2.4 in. and a length of 1.31 ft. Connected to the probe housing with an underwater connector is the 3-axis probe. It consists of three orthogonal pairs of 2- by 5-mm piezoelectric 4-Mhz transducers mounted on a stem or riser. The net acoustic path length is 1.2 in.

These current meters were calibrated by Sensordata in Norway and require no further correction unless the probes are altered. Calibration coefficients are used to convert the recorded voltage to velocity in engineering units. Extensive trial-and-error tests in Vicksburg showed that for low velocities where $1 \text{ V} = 0.33 \text{ fps}$ (typical of laboratory tests), a gain of 10 should be used. A gain factor of 1 can be used when higher velocities are expected, where $1 \text{ V} = 3.3 \text{ fps}$. Slope C and intercept D calibration coefficients for a gain of 10 for the x-, y-, and z-axes are listed in Table 4. Values are shown for all three current meters even though only two were used at any one time during this study.

Figure 11 shows the directions of positive flow for the x-, y-, and z-axes of the current meters. The top of the "U-shaped" support frame of the current meters was positioned at mid-depth to ensure that the probes would not become exposed as the wave troughs passed overhead. To minimize potential interference from this support frame, the closed end of the "U" was positioned downstream of the wave flow. The x-axis of the current meter was aligned with south so that positive flow

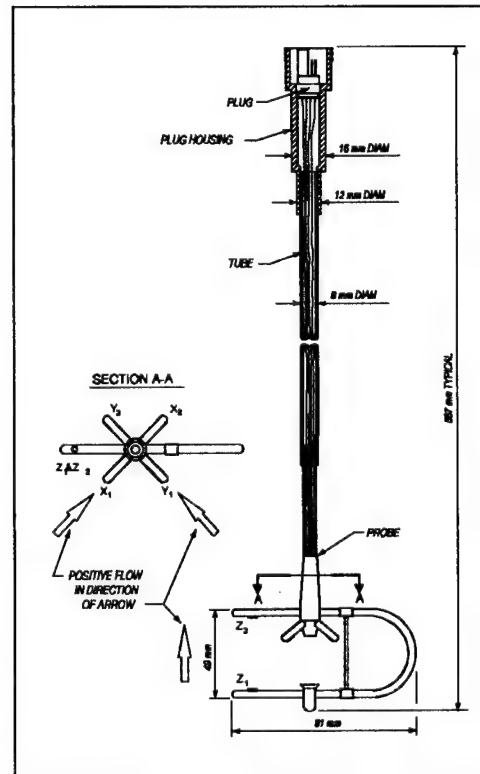


Figure 11. Triaxial ultrasonic current meter

Table 4
Minilab Calibration Coefficients

Probe	Axis	Gain x 10	
		Slope C	Intercept D
1	X	8.26833	-0.14884
	Y	8.21639	-0.28392
	Z	8.18854	-0.17383
2	X	7.48054	-0.13462
	Y	7.55591	-0.09624
	Z	8.18854	-0.17383
3	X	7.68047	-0.07629
	Y	7.71735	-0.13066
	Z	8.18854	-0.17383

was to the north. The y-axis of the current meter was aligned with east so positive flow was to the west.

The current meter orientation angles required to transform the measured angles to the global coordinate system was 180 deg. The direction relative to the global N/E coordinate system θ_g is obtained from the current meter direction θ_{cm} by

$$\theta_g = 180^\circ - \theta_{cm} \quad (4)$$

Flow occurs from the southeast to the northwest in the first quadrant in the current meter coordinate system, measured counterclockwise from the positive x-axis. It is transformed to the second quadrant of the global coordinate system, measured clockwise from north. Similarly, flow from the northeast to the southwest in the second quadrant of the current meter coordinate system is transformed to the first quadrant of the global system.

Water level controller

Water depth was maintained within ± 0.001 ft of the desired level by an automatic water level float and solenoid control valve.

Wave Climate

Prototype wave conditions

Barbers Point Harbor is subject to waves approaching the Hawaiian Islands from the northwest and the southwest. Wave approach from the west is rare but does occur during Kona (local) storms, and the island of Oahu blocks the easterly trade wind waves from impacting the harbor. The largest waves occur during the winter months and are caused by a north swell generated in the Northwest Pacific.

Table 5 and Table 6 are joint distributions of wave peak period and significant wave height for the buoy (Bu) and S_{xy} array gauges, respectively. These data are from annual reports published by the CDIP, according to Scripps Institution of Oceanography analysis procedures. The buoy table is in percentages, whereas the S_{xy} data are given in number of occurrences. Buoy measurements are from June 1986 to January 1990. Array data are from July 1986 to March 1990. Peak period values represent center band periods. Significant wave height values were originally sorted into 1.0-ft-wide bins for the buoy station and 0.5-ft-wide bins for all other gauges. These 0.5-ft-wide bins were combined into 1.0-ft-wide bins for the array data for ease of comparison with the buoy data.

Table 5 Buoy Percentage Distribution of Wave Height and Period											
Hs ft	Peak Period, sec									Sum	%
	22+	20	17	15	13	11	9	7	5		
10+			1	2						3	0.1
9				1	4	1		3		9	0.2
8		5	6	4	6	2	2	2		27	0.7
7		4	3	20	8	9	6	9	1	60	1.6
6		4	8	33	30	29	16	13		133	3.6
5		1	22	79	92	49	35	35	6	319	8.6
4		11	62	173	237	176	145	208	37	1049	28.2
3		10	47	182	384	307	306	527	87	1850	49.8
2			4	16	65	55	44	60	18	262	7.1
1							4			4	0.1
Sum		35	153	510	826	628	558	857	149	3716	
%		1.0	4.1	13.7	22.2	16.9	15.0	23.1	4.0		100.0

Figures 12 and 13 illustrate percentage and cumulative distributions for both buoy and array locations for wave period and wave height, respectively. "Percentage" curves for the buoy and array are smaller than the "cumulative" curves in each figure. Differences in wave period are probably due to nonlinear energy transfers between the buoy and array locations as the waves shoal and break. Differences in observed wave heights are due to wave breaking.

Model wave conditions

Selection criteria. Model wave conditions from the available prototype data were selected based on (a) obtaining the largest wave heights and a representative range of wave period and direction within model constraints, (b) preference given to the time after the marina opened in July 1989 and the second S_{xy} directional gauge was installed, and (c) maximum number of operational field gauges for comparisons.

Figure 14 shows the joint distribution of wave height and period from Table 6 for the S_{xy} array. Inspection of this figure indicates that most waves at the S_{xy} had a peak period between 9 and 15 sec and wave heights between 1 and 3 ft. Table B1 in Appendix B lists the distribution of wave periods for all wave heights for the buoy, offshore, and onshore gauges, in addition to the two S_{xy} locations. The change in wave period as the water depth decreases can be seen from this table.

Table 6 S _{xy} Joint Distribution of Wave Height and Period														
Region	H _s ft	Peak Period, sec										SUM	%	CUM%
		22+	20	17	15	13	11	9	7	5				
A	10								1			1		
	9			1	1			1	1			4	0.1	100
	8			3	2	2	1	5	1			14	0.4	99.9
	7		1	3	7	8	1	1	11	3		35	1.0	99.5
	6		3	4	8	6	6	3	17	3		50	1.4	98.5
	5			13	32	40	23	6	8	2		124	3.5	97.1
B	4		1	26	64	120	85	14	9	19		338	9.4	93.6
	3	1	18	62	144	298	397	116	33	47		1116	31.2	84.2
	2		24	105	250	310	484	308	55	260		1796	50.3	53.0
C	1		2	1	8	13	9	13	4	45		95	2.7	2.7
	SUM	1	49	218	516	797	1006	467	140	379		3573		
	%		1.4	6.1	14.4	22.3	28.2	13.1	3.9	10.6			100	
	CUM%		100	98.6	92.5	78.1	55.8	27.6	14.5	10.6				

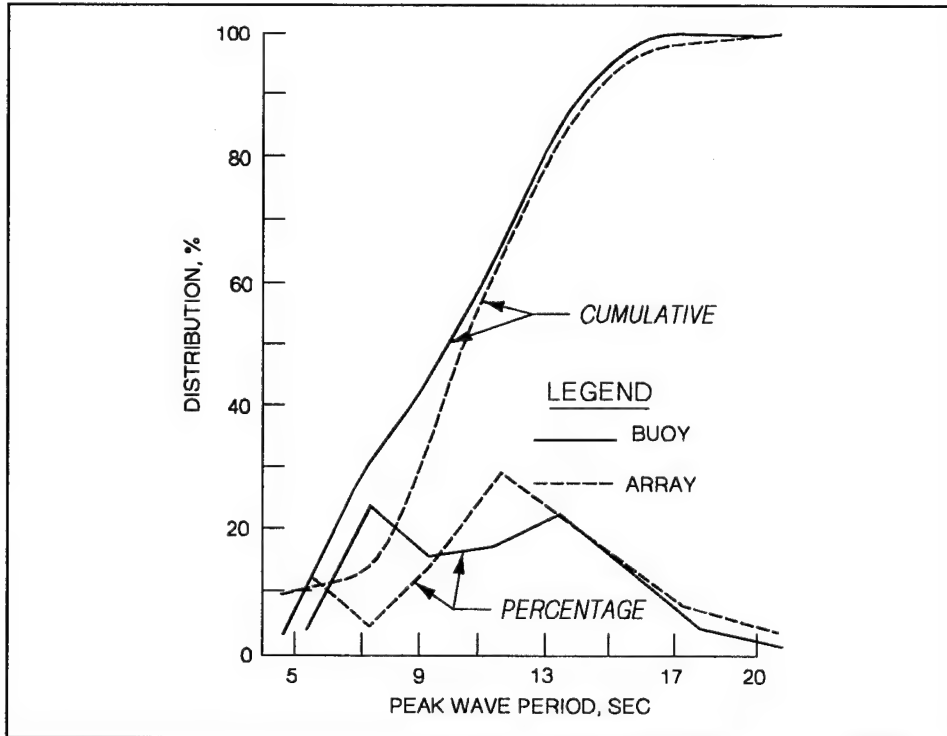


Figure 12. Percentage and cumulative wave period distribution

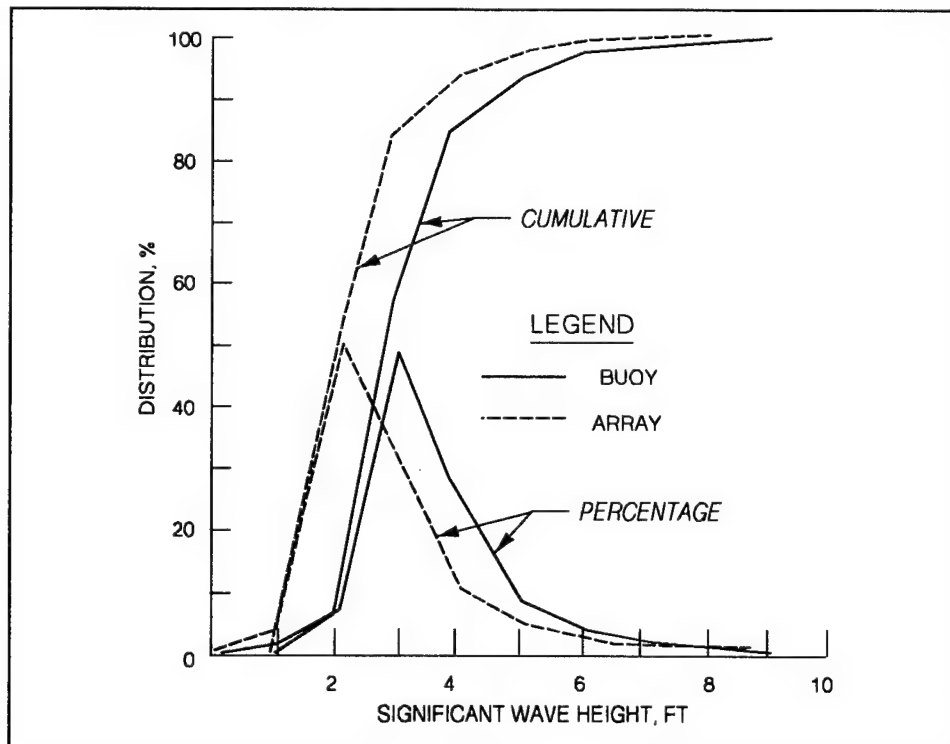


Figure 13. Percentage and cumulative wave height distribution

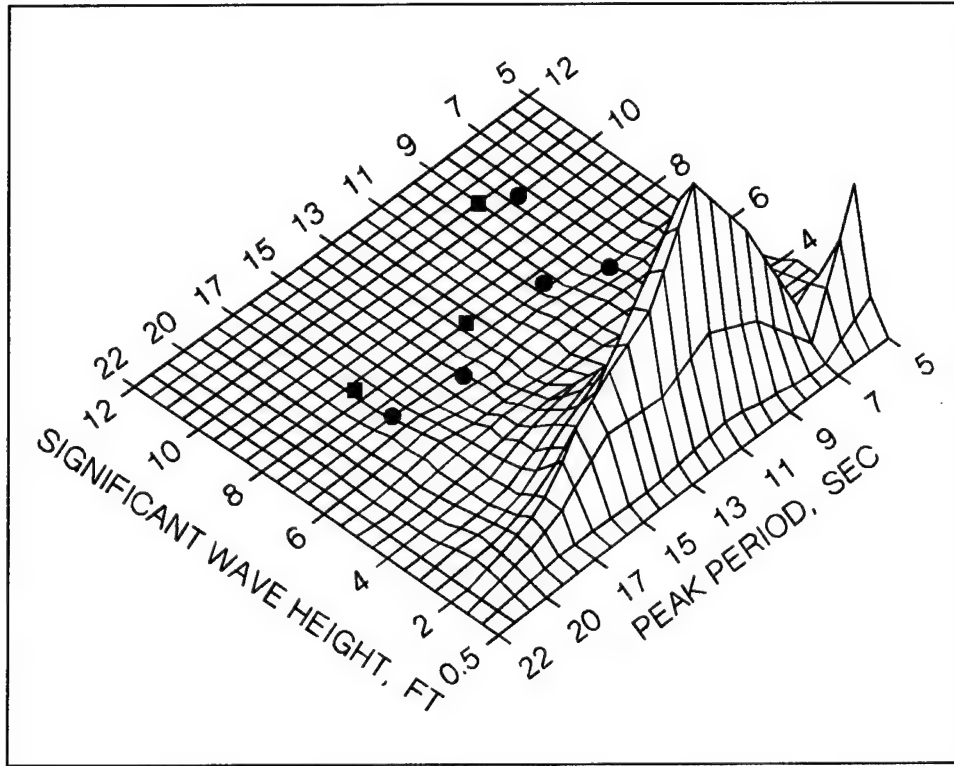


Figure 14. S_{xy} array joint distribution of wave height and period

Figure 15 shows the distribution of mean wave directions measured at the S_{xy} array by SIO. The mean and ± 1 standard deviation range of directions are shown for the different center band wave periods. Four different time windows are shown for each wave period, reflecting the change in array position and downtime. Figure 16 shows the different wave directions modeled in the two previous Look Laboratory physical model tests. Note that the entrance channel is aligned approximately with S45W.

With this wave information from the prototype measurements, the eight wave conditions listed in Table 7 were selected for harbor response and navigation tests in the physical model. Simulated wave periods, heights, and directions range from 6 to 18 sec, 7 to 10 ft, approach angles of S28W to west (S86W), and directional spreading up to 10 deg, respectively. The range of directions is within the limits shown on Figure 15. The water level for all tests was mllw.

Each case is representative of wave conditions that could have occurred before or after opening of the marina. Thus, for comparisons of long wave harbor response, all cases were tested in the physical model with the marina open, even for the existing harbor plan 1a.

The first four wave cases are after the S_{xy} had been moved to its second location. The last four cases were measured when it was in the first location. Table 8 lists the gauges that were operational during each wave case.

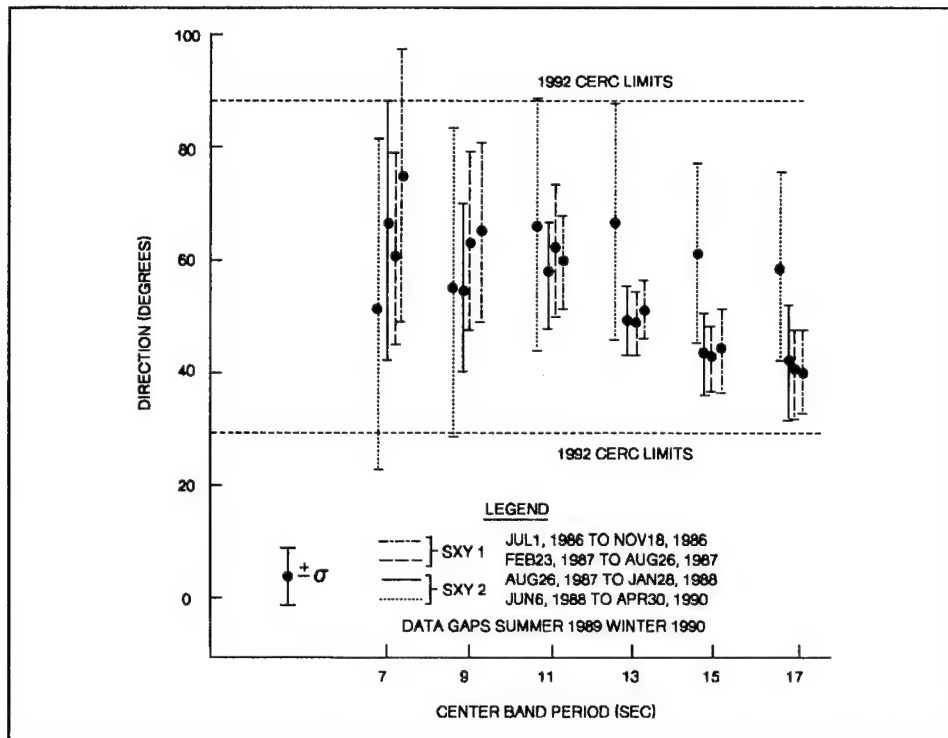


Figure 15. S_{xy} array directions

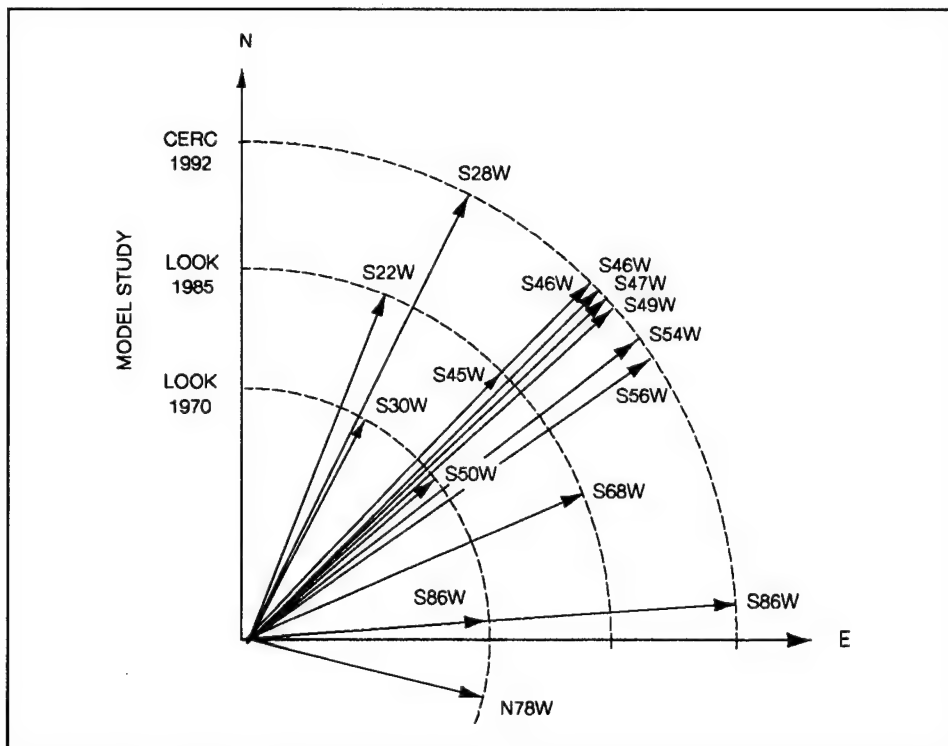


Figure 16. Wave directions in previous laboratory studies

Table 7
Selected Prototype Wave Conditions

No.	Date	Time	Peak Period sec	Significant Wave Ht ft	Average Direction deg	Range of Directions deg	Case Name
1	Nov 16 89	1306	10-12	7.0	86	33-101	BPS210
2	Nov 4 88	1600	6-8	9.8	45	45-86	BPS220
3	Mar 2 89	0704	6-8	7.0	28	28-59	BPS230
4	Mar 3 89	0104	8-10	7.4	54	38-92	BPS240
5	Nov 3 86	1439	8-10	10.0	56	44-59	BPS150
6	Jan 21 88	2006	16-18	7.8	46	46-77	BPS160
7	Jan 22 88	0806	14-16	8.1	47	43-68	BPS170
8	Jan 23 88	0206	12-14	7.1	49	37-62	BPS180

Table 8
Operational Prototype Gauges

No.	Sxy	Of	On	Ce	Cm	Nc	Ec	Sc
1	2	x			x	x	2	x
2	2			x	x			
3	2	x	x	x	x			x
4	2	x	x	x	x			x
5	1			x	x			
6	1			x	x			x
7	1			x	x			x
8	1			x	x			x

Notes:

1. 1 = First position.
2. 2 = Second position.

These eight wave cases are shown as dots and squares in Figure 14. All eight waves represent rare events because of their large wave heights. Joint distribution of wave height and period was divided into three regions, A, B, and C, reflecting frequency of occurrence and severity of wave conditions (see Table 6). This division was done to facilitate probability assessment of the navigation test results (see Chapter 4). Demarcation between regions is a stepwise function based on the fact that shorter wave periods require higher wave heights to pose the same navigation hazards.

Target directional spectra. Measured pressure time series for each of the gauges of the S_{xy} array were obtained from SIO on 9T magnetic tape for each wave case. Appendix B describes the data retrieval and analysis procedure used by CERC to convert these pressure time series to surface elevation time series.

Surface elevation time series were then input into a program to calculate the directional wave spectra $S(f,\theta)$. The Cray Y-MP supercomputer was used to calculate these $S(f,\theta)$ in the frequency domain using a double summation,

random phase method with deterministic amplitudes (Briggs, Borgman, and Outlaw 1987; LeMehaute and Hanes 1990).

The $S(f,\theta)$ is parameterized as the product of a frequency spectrum $S(f)$ and a directional spreading function $D(f,\theta)$ as

$$S(f,\theta) = S(f) D(f,\theta) \quad (5)$$

where

f = frequency

θ = wave direction

The frequency spectrum and spreading function are subject to the following constraints:

$$S(f,\theta) = \int_0^{2\pi} S(f,\theta) d\theta \quad (6)$$

$$\int_0^{2\pi} D(f,\theta) d\theta = 1 \quad (7)$$

The spectral formulation of the problem is discussed in the paragraphs which follow. A Fourier series expansion of the directional spectrum is first calculated. This procedure is based on the relation that the auto spectra $S_{ii}(f)$ and cross-spectra $S_{ij}(f)$ between all pairs of surface elevation time series can be expressed as a linear combination of the directional components of $S(f,\theta)$ at that frequency. If the wave elevation time series $\eta(x,y,t)$ at DSWG paddle location (x,y) and time t is defined as

$$\eta(x,y,t) = 2 \int_0^{\infty} \int_0^{2\pi} A(f) \exp(-i\Phi) \exp(i\phi) \quad (8)$$

where

Φ = independent random phase, uniformly distributed on $(0,2\pi)$

$\phi = kx \cos \theta + ky \sin \theta - 2\pi ft$

$i = \sqrt{-1}$

k = wavenumber, $2\pi/L$

and the amplitude function $A(f)$ is defined by

$$A(f) = \sqrt{2S(f,\theta)dfd\theta} \quad (9)$$

Then, a system of equations for the spectral matrix of $S_{ii}(f)$ and $S_{ij}(f)$ in terms of $S(f,\theta)$ is

$$S_{ii}(f) = \int_0^{2\pi} S(f,\theta) d\theta \quad (10)$$

$$S_{ij}(f) = \int_0^{2\pi} S(f,\theta) \exp(iB_{ij}) d\theta \quad (11)$$

where

$$B_{ij} = \kappa X_{ij} \cos \theta + \kappa Y_{ij} \sin \theta$$

$$X_{ij} = x_i - x_j$$

$$Y_{ij} = y_i - y_j$$

x = x-axis gauge coordinates at location i or j

y = y-axis gauge coordinates at location i or j

The cross-spectrum $S_{ij}(f)$ is composed of real co-spectra C_{ij} and imaginary quadrature components Q_{ij} .

The first step in solving the system of equations above is to estimate the $S_{ii}(f)$ for each of the N gauges in the S_{xy} array. A combined best estimate $\bar{S}(f)$ is obtained using a harmonic mean.

$$\bar{S}(f) = \left[\prod_{i=1}^N S_{ii}(f) \right]^{1/N} \quad (12)$$

The directional spreading function is initially approximated by a truncated Fourier series expansion of $L = 5$ harmonics. The $D(f,\theta)$ is then defined by

$$D(f,\theta) = \frac{1}{2\pi} + \sum_{l=1}^L a_M(f) \cos(l\theta) + b_M(f) \sin(l\theta) \quad (13)$$

where

$a_M(f)$ = real Fourier coefficient of the spreading function

$b_M(f)$ = imaginary Fourier coefficient of the spreading function

The next step was to calculate measured autospectral and cross-spectral density estimates for each gauge and each gauge pair, respectively. Data were zero-meaned, tapered by a 10-percent cosine bell window, and Fourier transformed using a "235" Fast Fourier Transform. Then a Gaussian smoothing function was used to smooth the estimates with an effective prototype bandwidth $B_e = 0.01$ Hz between lower $f_l = 0.001$ Hz and upper $f_u = 0.40$ Hz cutoff frequencies. This procedure is like "band averaging" since raw spectral estimates are smoothed in the frequency domain. However, it tends to give a smoother transition since it is more of a weighted moving average in that overlapping is used. The Gaussian smoothed line spectra \bar{S}_m for each frequency $m\Delta f$ is defined by

$$\bar{S}_m = \frac{\sum_{j=-J}^J w_j S_{m-j}}{\sum_{j=-J}^J w_j} \quad (14)$$

where w_j is a weighting function, and S_{m-j} is the raw autospectral or cross-spectral estimate at frequency $(m-j)\Delta f$. The equivalent number of Gaussian smoothed frequencies was 25 and 49 for the cases with 1,024 and 2,048 points, respectively. This is a considerably greater number than a comparable frequency domain band-averaging procedure.

Thirty equally spaced frequencies between 0.01 and 0.30 Hz were selected to define the frequency spectrum. Table B3 compares peak frequency and period for corresponding prototype and model conditions.

Significant wave height H_o was equal to four times the standard deviation of the time series of water surface wave elevation σ_η . An average was calculated for the number of gauges used to calculate the directional spectrum. Only three of the four gauges in the S_{xy} array were used because of data collection problems with the fourth gauge. Gauges 2 through 4 were used for all wave cases except for the fifth case. In this case, gauges 1, 2, and 4 were used.

$S_{ii}(f)$ for each gauge are inserted into the left-hand side of Equation 10. They are also substituted into Equation 12 to calculate $S_{ij}(f)$. $S_{ij}(f)$ are calculated for each pair of gauges and substituted into the left-hand side of Equation 11. The estimate of $S(f)$ and the parameterized directional spreading function $D(f, \theta)$ are substituted into the right-hand side of Equation 11 for $S(f, \theta)$. Thus, for $N = 3$ gauges, a set of $N^2 = 9$ simultaneous linear equations (i.e. N autospectral equations of the form of Equation 10 and $N(N-1)/2$ pairs of cross-spectral equations of the form of Equation 11) were solved for the full-circle Fourier coefficients a_M and b_M of the spreading function. A least

squares Fourier transform method for numerical integration was used to solve the set of available equations. A vector linear regression model inverts the matrix containing the spreading coefficients of $D(f, \theta)$.

Finally, a maximum likelihood method (MLM) algorithm was used to improve $D(f, \theta)$ because the initial estimate is distorted due to truncation of the Fourier series. This method gives a higher resolution estimate of $D(f, \theta)$ with the least amount of error. A directional resolution $\Delta\theta = 2.5^\circ$ (i.e. 144 increments in 360 deg) was used for the directional spreading function estimates. Once $a_M(f)$ and $b_M(f)$ are obtained, the mean wave direction $\theta_m(f)$ at each frequency f is calculated from the first harmonic $a_1(f)$ and $b_1(f)$ coefficients as

$$\theta_m(f) = \arctan\left[\frac{b_1(f)}{a_1(f)}\right] \quad (15)$$

The mean of all $\theta_m(f)$ over all frequencies equals the overall mean wave direction or peak wave direction $\bar{\theta}$.

A directional spread or standard deviation of the spreading function $\sigma_m(f)$ was calculated to give a relative indication of the width of the directional distribution. It is defined by

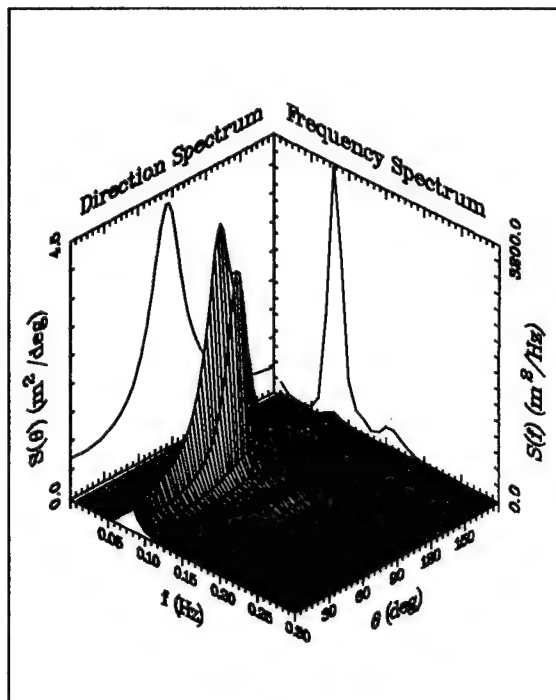
$$\sigma_m(f) = \sqrt{-2 \ln[\pi \sqrt{a_1^2(f) + b_1^2(f)}]} \quad (16)$$

Figure 17 shows target directional spectra for each wave case using the CERC analysis. The right vertical panel shows the frequency spectrum obtained by summing energy at each frequency over all directions. The left rear panel is the direction spectrum obtained in a similar manner, except that direction is held fixed and energy is summed over all frequencies. Frequency and directional lines have uniform spacing of 0.01 Hz and 2 deg, respectively.

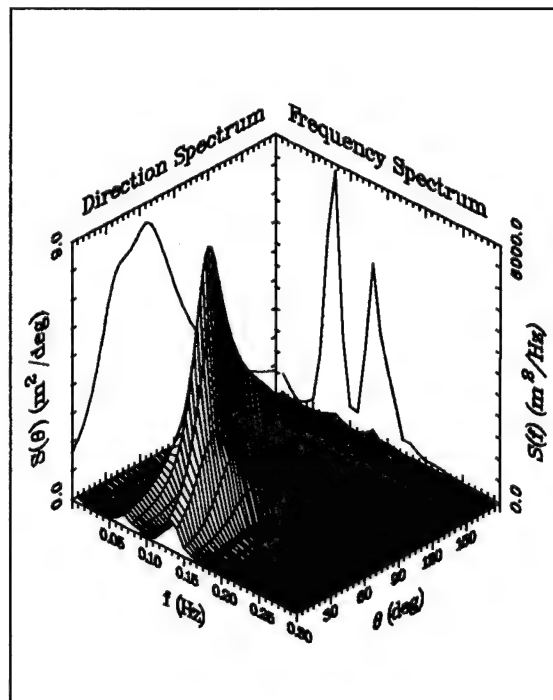
Table 9 lists the simulated target wave conditions from the CERC directional analysis. Because of differences in the analysis routines between SIO and CERC, there are some slight differences in wave height and direction that are not considered significant. A ninth wave condition, W9, was added to simulate less severe wave conditions in the navigation tests.

Control signal simulation. The directional spectrum in the form of the calculated frequency spectrum $S(f)$ and spreading function $D(f, \theta)$, was then input into another program to simulate a stroke time series for each of the 61 paddles of the DSWG for each wave case. The $S(f)$ was calculated at the same 30 discrete frequencies between 0.01 Hz and 0.30 Hz used for the target spectra. Similarly, $D(f, \theta)$ was estimated at 2.5-deg increments.

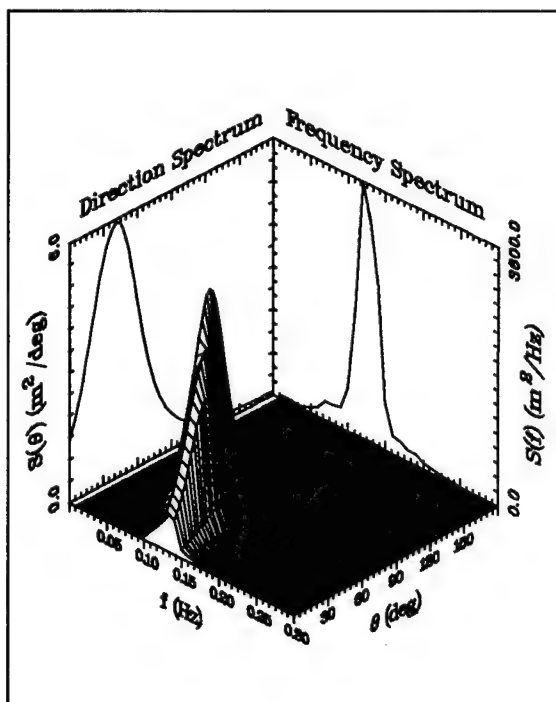
The digital-to-analog (D/A) rate for the DSWG is 20 Hz, corresponding to a time increment $\Delta t = 0.05$ sec. Equivalent prototype time series durations of



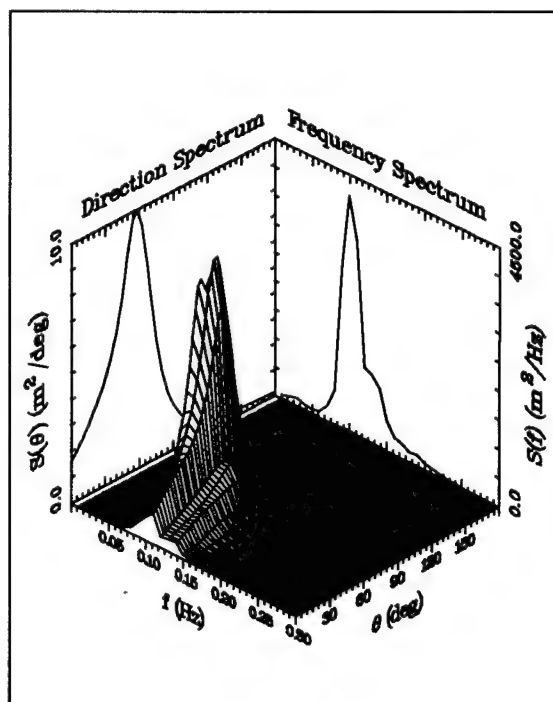
a. Case 1, BPS210, Gauges 2-4



b. Case 2, BPS220, Gauges 2-4

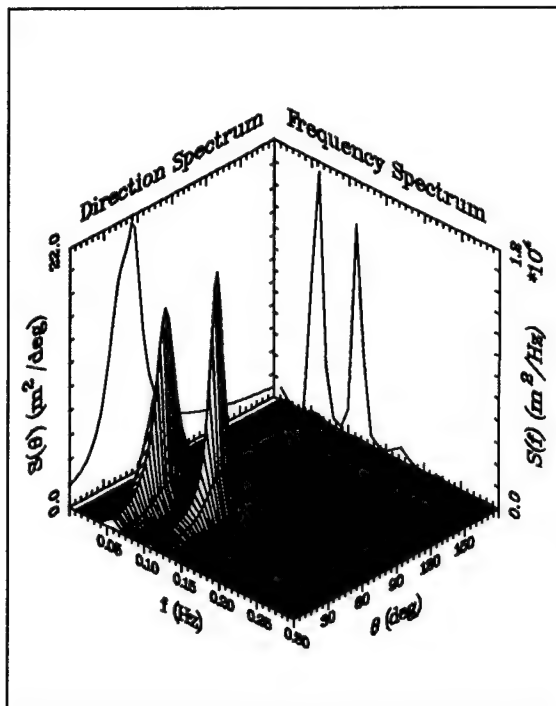


c. Case 3, BPS230, Gauges 2-4

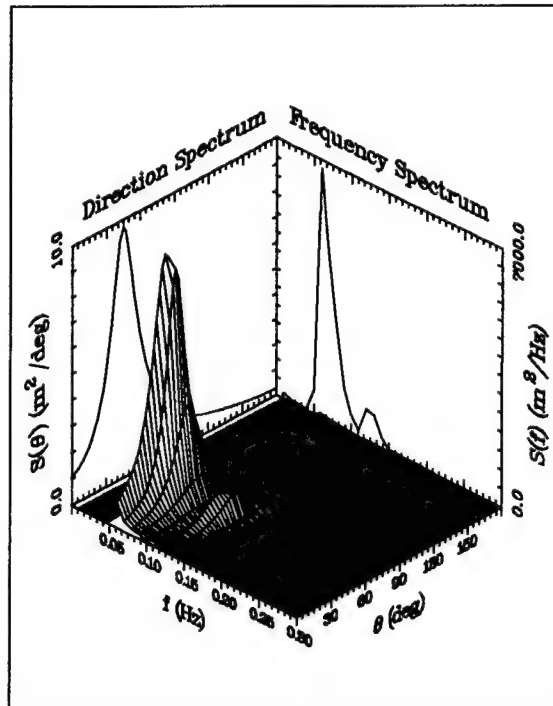


d. Case 4, BPS240, Gauges 2-4

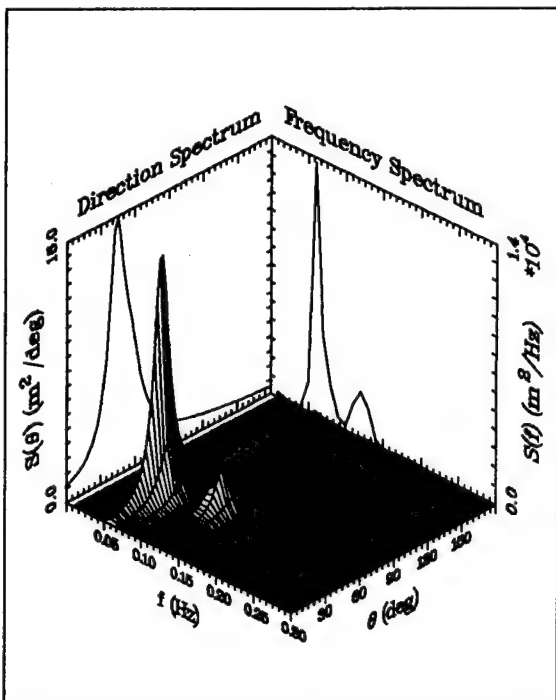
Figure 17. Eight target prototype directional spectra (Continued)



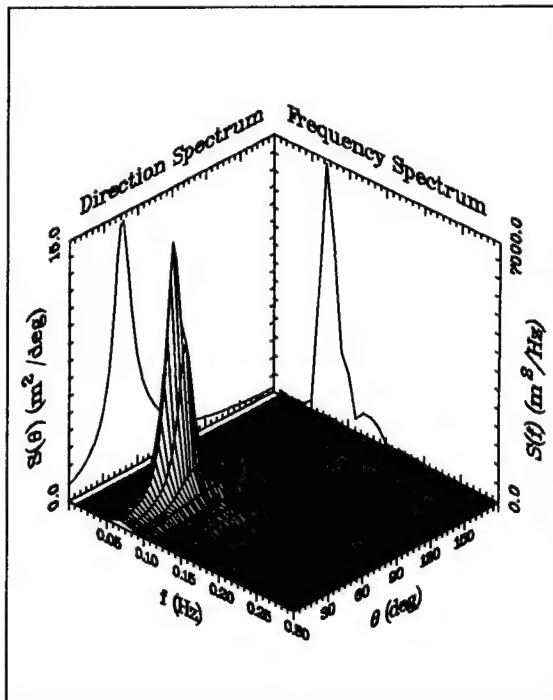
e. Case 5, BPS150, Gauges 1, 2 & 4



f. Case 6, BPS160, Gauges 2-4



g. Case 7, BPS170, Gauges 2-4



h. Case 8, BPS180, Gauges 2-4

Figure 17. (Concluded)

6.01 hr (i.e. 50,000 points, 41.7 min model) were created for each paddle. Data were again zero-meant, tapered by a 10-percent cosine bell window, and Gaussian smoothed with an effective bandwidth of 0.01 Hz between $f_l = 0.0001$ Hz and $f_u = 0.35$ Hz. These control signals were then stored on 9T magnetic tapes for later calibration.

Data sampling. Experiments were conducted by starting the 9T magnetic tape containing the control signal and waiting 10 sec to allow a common starting point for repeat tests. The DSWG was not actually making waves until this instant in time. Then, a 10-sec hardware ramp was automatically activated on the control signal to bring the DSWG on-line smoothly and prevent damage. Higher frequency wave components travel slower than lower frequency components. Thus, prior to sampling all gauges at 10 Hz (i.e. time increment $\Delta t = 0.10$ sec) for 40 min (i.e. 24,000 points), a total waiting time of 25 sec (i.e. 5 additional sec) was observed to allow these slow-moving components to reach the farthest gauges in the harbor.

Control signal calibration. An iterative calibration procedure was used to correct the control signals to match target parameters using the NGA linear array. In the first step, all wave conditions were measured and compared to the target spectra and a transfer function or response amplitude operator (RAO) was calculated and applied to correct the control signal for each wave condition. In subsequent steps, the wave conditions were again measured and compared to the target conditions. Usually, one or two iterations were sufficient to correct variations in peak period, wave height, and frequency and directional spectral shape. The final step was to apply a gain factor at run time to adjust only the wave height. This gain was used for all future tests for each wave case.

The $RAO_i(f)$ for each gauge in the NGA is calculated in the frequency domain as the ratio of the autospectra $S_{ii}(f)$ to the target spectral shape $S_p(f)$

$$RAO_i(f) = \sqrt{\frac{S_{ii}(f)}{S_p(f)}} \quad (17)$$

An average RAO from all seven gauges in the NGA array was used. Calculated RAO values outside f_l and f_u cutoff frequencies were set to 1.0 because of low signal-to-noise ratios. Also, RAO's greater than 100.0 or less than 0.01

Table 9
Simulated Target Wave Conditions

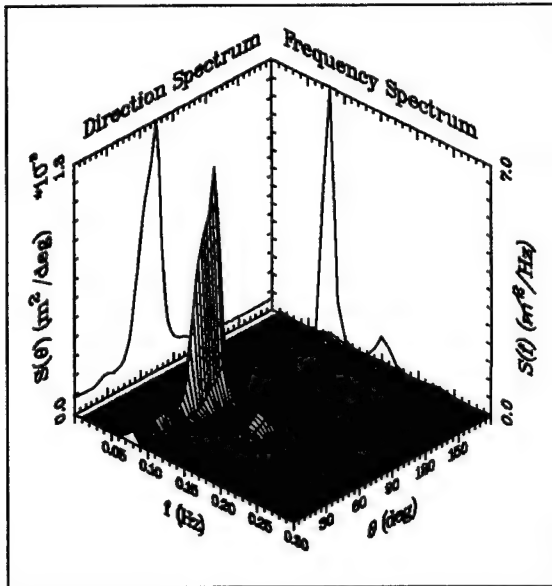
No.	Peak Period sec	Significant Wave Ht ft	Average Direction deg	Spread deg
1	12.6	7.1	80	15
2	7.7	9.8	38	17
3	8.3	7.1	45	19
4	10.0	7.4	63	16
5	9.1	10.2	58	7
6	16.7	6.5	43	14
7	16.7	8.2	43	9
8	14.2	7.1	45	9
9	12.6	4.4	80	15

were set to these respective upper and lower limit values. Once the RAO is calculated, control signals are Fourier transformed to the frequency domain, divided by the appropriate RAO at each frequency, and then transformed back to the time domain to form the corrected control signal.

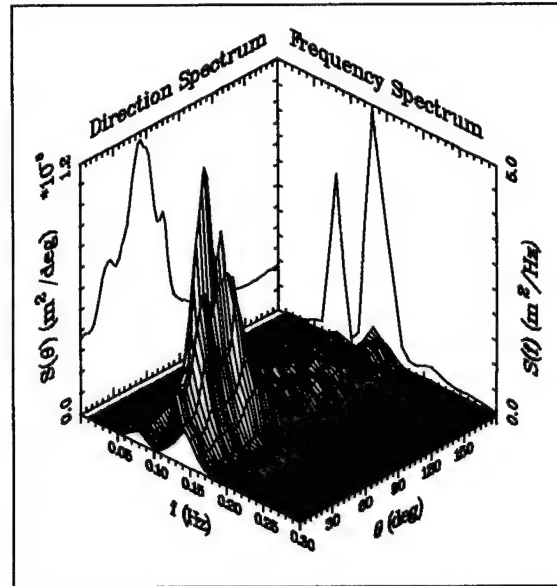
The DSWG has specified limits on displacement, velocity, and acceleration of the individual paddles. For some of the larger wave heights, these limit values were often exceeded in the control signals. Prior to running the tests, the control signals were checked for exceedance of these paddle limits and corrected if necessary. Typical locations of these exceedances were at the peaks and troughs (and corresponding positive and negative flanks) of large waves. The procedure consisted of rounding these peaks or troughs to lower values within the thresholds. If a value exceeded the threshold, a new value equal to half the distance between the threshold and the previous value was substituted. This procedure was used on successive steps until the exceedance was remedied. Because threshold values are based on a displacement less than the maximum, the procedure usually converged after one or two iterations.

Measured water surface elevation time series from the NGA array were again analyzed using the directional spectral analysis procedure. The equivalent prototype data records of 5.8 hr (i.e. 24,000 points, 40-min model) were zero-meaned, tapered, and Gaussian smoothed with a bandwidth of $B_e = 0.01$ Hz. Thirty frequency bands between 0.01 and 0.30 Hz and directional increments of 2.5 deg were again used. An average depth of 30 ft was assumed for the NGA linear array. The directional spreading function was normalized by its peak value. The spread was then calculated as half the width at the 50-percent level of the spreading function.

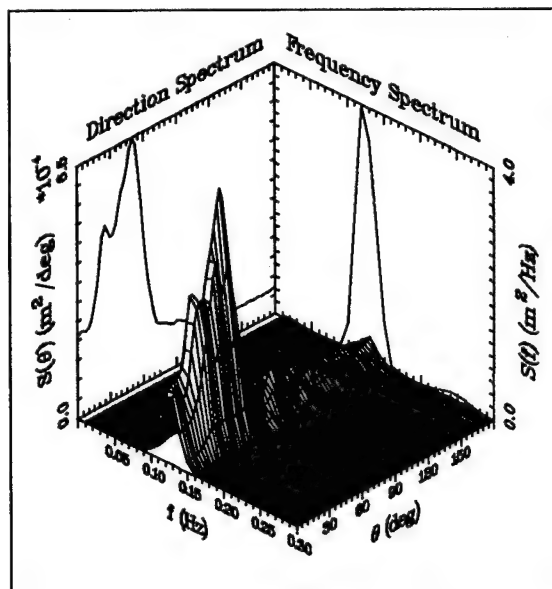
Figure 18 shows the measured directional spectra from the NGA array for the eight wave cases. Case W9 was not calibrated, but was reduced by applying a gain factor at run time to case W1. Table 10 lists the measured wave parameters for comparison with Table 9. Figures B3-B10 show target and measured frequency spectra and directional spreading at the peak frequency for the eight wave cases, respectively. In general, agreement between measured and corresponding target directional spectra in Figure 17 is very good, especially for the bimodal cases W2 and W5. The root mean square error for wave period σ_T between the CERC target and measured values was 1.2 sec. This means the error between the measured and target values for all wave cases was no more than 1.2 sec, an excellent match. The correlation coefficient for wave period r_T between these two was 0.97, also confirming the excellent match. For wave height, the $\sigma_H = 0.3$ ft and the $r_H = 0.98$. These two statistical parameters again show an excellent match between the measured and target wave height values for all wave cases. Agreement between measured and target wave directions was also very good. The $\sigma_\theta = 6$ deg and $r_\theta = 0.93$. Finally, for the directional spread, $\sigma_\phi = 5^\circ$ and $r_\phi = 0.48$. The correlation coefficient is not very good because the measured directional spreads in cases W7 and W8 were 9 deg wider than their target spreads. This was felt to be a reasonable agreement considering the resolution of the wave gauge linear array and the analysis program.



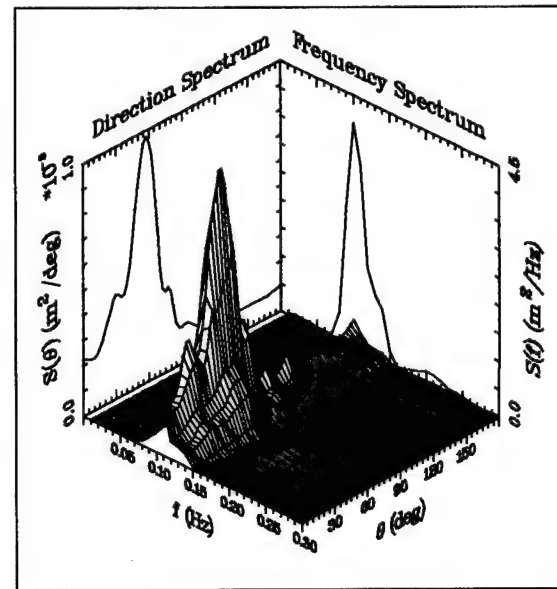
a. Case 1, BPS211, NGA array



b. Case 2, BPS221, NGA array

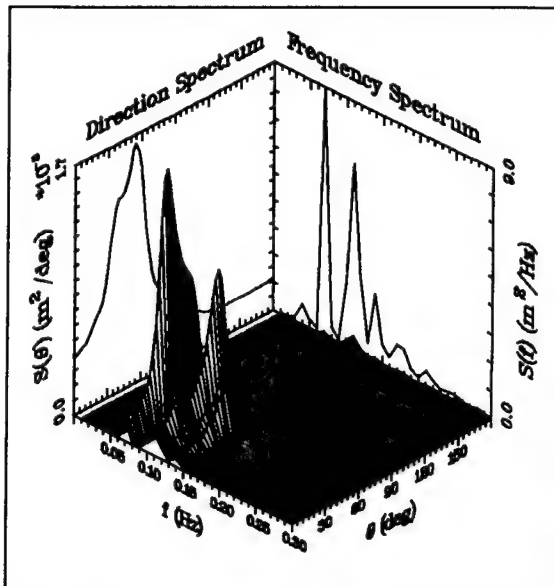


c. Case 3, BPS231, NGA array

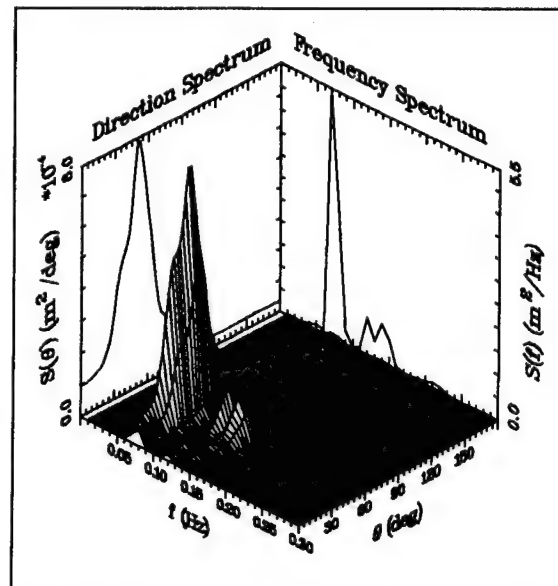


d. Case 4, BPS241, NGA array

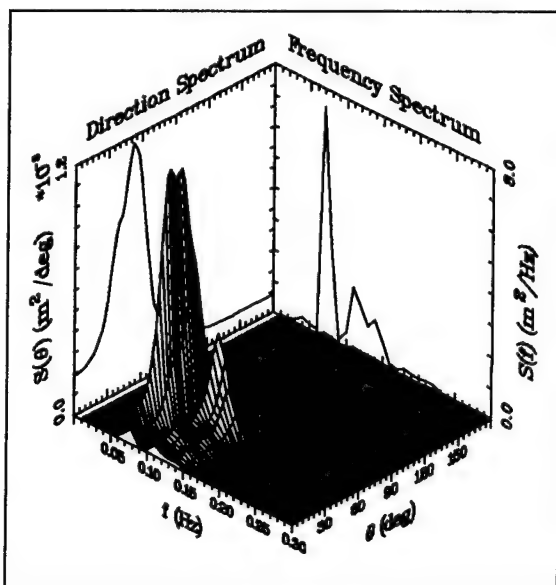
Figure 18. Eight measured model directional spectra (Continued)



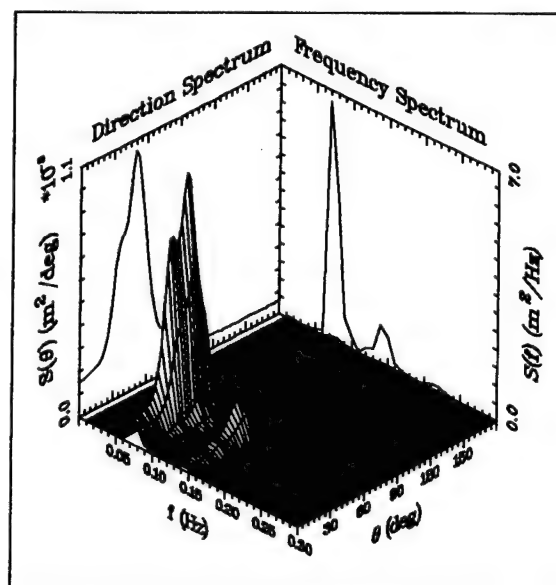
e. Case 5, BPS151, NGA array



f. Case 6, BPS161, NGA array



g. Case 7, BPS171, NGA array



h. Case 8, BPS181, NGA array

Figure 18. (Concluded)

Free long wave tests. Free or spurious long waves (FLW) are generated when first-order wave theory is used for calculating the wavemaker control signal. Boundary conditions at the wavemaker cannot be satisfied for the second-order bound waves, which are associated with the occurrence of wave groups. These FLW are the sum of waves of different origin including parasitic, displacement, and local disturbance components. Amplitude of the FLW is smaller than the bound wave, with opposite phase and faster speed. These waves may cancel or reinforce each other

and can have much higher reflection coefficients (i.e. order of 40 to 50 percent) than the desired wind waves. Stroke limitations of the DSWG make the use of second-order wave theory impractical for generating the control signals. However, the long-wave components were modeled as accurately as possible within the constraints of the RAO transfer functions described above. This procedure is similar to the iterative one used by Fittschen and Scheffer (1987) for correcting FLW. Good agreement between target and measured directional spectra was regarded as an indication of minimization of these unwanted components.

A series of FLW tests were conducted to establish the influence of the outside region, or open sea, portion of the model on the interior harbor response. Because of basin boundaries, an open sea condition is not exactly modeled in the laboratory. These tests were designed to show if waves at the natural period of oscillation of the outer region (i.e. between the shoreline and the DSWG) were unduly influencing the inner harbor response.

Monochromatic long waves of normal incidence with a period corresponding to the natural period of oscillation of the outside region of the model were tested for one to five cycles to see if a steady state oscillation was reached inside the harbor before reflected waves from outside contaminated the forcing function. Because the DSWG makes an angle to the shoreline (i.e. wider at one end than at the other end), model resonant periods were calculated at the narrow and wide ends and at the center of the DSWG. Figure 19 shows a cross section of the outer region of the model with a flat section adjacent to the DSWG and a sloped section to the shoreline.

Table 10
Measured Model Wave Parameters

Test Case	Equivalent to Prototype				Gain	Case Name
	Peak Period sec	Signif. Wave Ht. ft	Ave. Dir. deg	Spread deg		
W1	12.6	7.2	75	11	0.85	BPS211
W2	7.7	9.6	48	24	1.18	BPS221
W3	8.3	7.0	50	21	0.97	BPS231
W4	10.0	7.4	60	12	0.93	BPS241
W5	9.1	10.6	58	10	0.87	BPS151
W6	14.2	6.7	53	17	0.64	BPS161
W7	14.2	8.6	40	18	0.78	BPS171
W8	14.2	7.7	50	15	0.70	BPS181

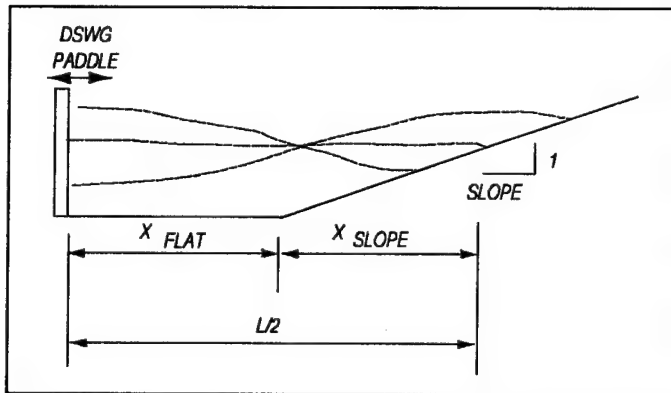


Figure 19. Resonant response of outer region

The natural period of oscillation for the flat section T_{flat} is given by

$$T_{flat} = \frac{x_{flat}}{C} \quad (18)$$

where

x_{flat} = distance between DSWG and toe of slope, ft

$C = \sqrt{gh}$ = wave celerity for shallow water, ft/sec

g = gravity, 32.2 ft/sec²

h = constant water depth, ft

The resonant period for the sloped section, T_{slope} is defined by

$$T_{slope} = \int_0^{x_{slope}} \frac{dx}{C(x)} = \int_0^{x_{slope}} \frac{dx}{\sqrt{gh(1 - \frac{x}{x_{slope}})}} \quad (19)$$

where

x = dummy variable of integration

$$x_{slope} = h * \text{slope}$$

= distance between the toe of the slope and the shoreline, ft

Carrying out the integration for T_{slope}

$$T_{slope} = \frac{2x_{slope}}{C} \quad (20)$$

The natural period of the basin T_{basin} is the sum of the natural periods for the flat T_{flat} and sloped T_{slope} sections. Calculated T_{basin} at the narrow, center, and wide ends of the basin were 16, 20, and 24 sec (corresponding to 138, 173, and 208 sec in the prototype), respectively. The effect of these waves was negligible for the main harbor, indicating that the reflected waves from the outer region would not contaminate the harbor response during actual testing. The marina, however, did show a resonant response, especially noticeable along the back wall of the marina. The walls are not covered with wave absorber in this region of the marina. This behavior indicated that the marina's natural periods coincide with these periods of the outer region of the

model and that the marina can be expected to resonate in this manner in the prototype.

Longshore Currents

Prototype current conditions

Prototype currents were measured over a 65-day period from July 29, 1988, to October 3, 1988, at three locations (Sea Engineering, Inc. 1988, 1991). The offshore current meter B was 5,200 ft seaward at the south channel line, at a depth of 30 ft in 120 ft of water (Figure 20). Two current meters were located 300 ft north of the entrance channel. The first location A was placed 1,800 ft from the shoreline at a depth of 12 ft in 24 ft of water. It was moved on September 13 to location A', 2,700 ft offshore at a depth of 18 ft in 30 ft of water. Measurements were taken at channel location A from July 29 to September 13 and location A' from September 13 to October 3. These meters were placed at mid-depth in the water column to measure currents which could affect the ship below the waterline. Surface drogue samples were also taken on two dates and confirmed the current meter results.

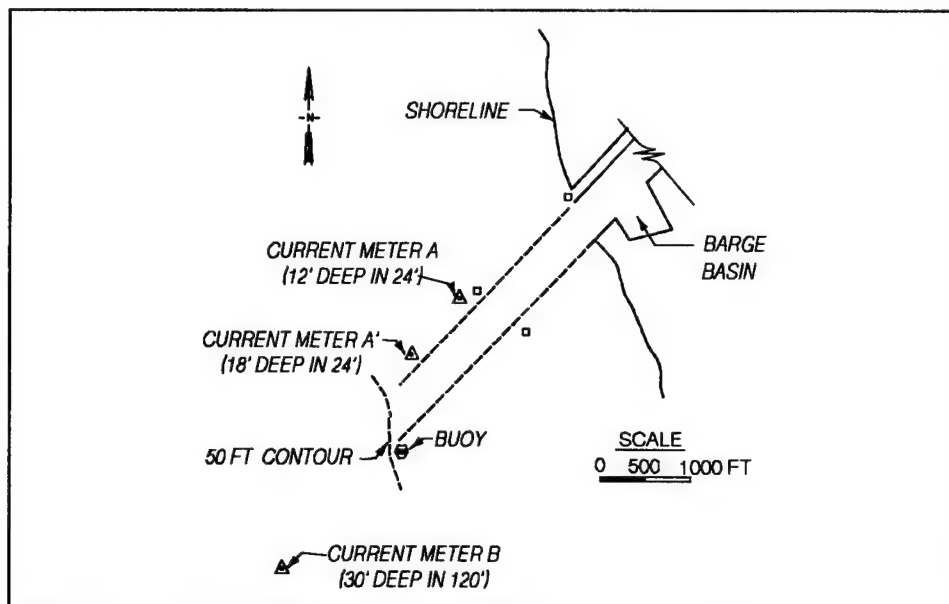


Figure 20. Prototype measurement locations

Samples were recorded at 7.5-min intervals and vector averaged over 0.5-hr intervals. Figure 21 shows current histograms in percentage of observations for the three current meter locations. The offshore location B is shown on the left and the two channel locations are shown on the right. Table 11 lists the percent of time a current exceeds a particular velocity for the three locations. Maximum observed currents were 1.6 knots and 0.8 knots for the offshore B and channel locations, respectively. Current roses are shown in Figure 22.

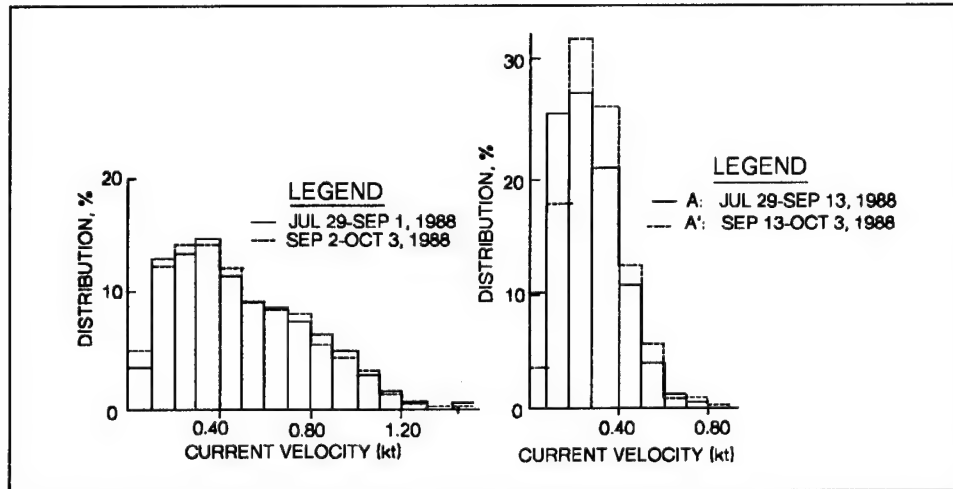


Figure 21. Current histograms

Table 11 Extreme Currents		
Location	Velocity knots	Percent Exceedance
Offshore B	0.6	33.0
	1.0	5.0
	1.4	0.2
	1.6	Max
A	0.5	6.6
A'	0.5	8.3
A & A'	0.6	2.2
	0.7	0.5
	0.8	Max

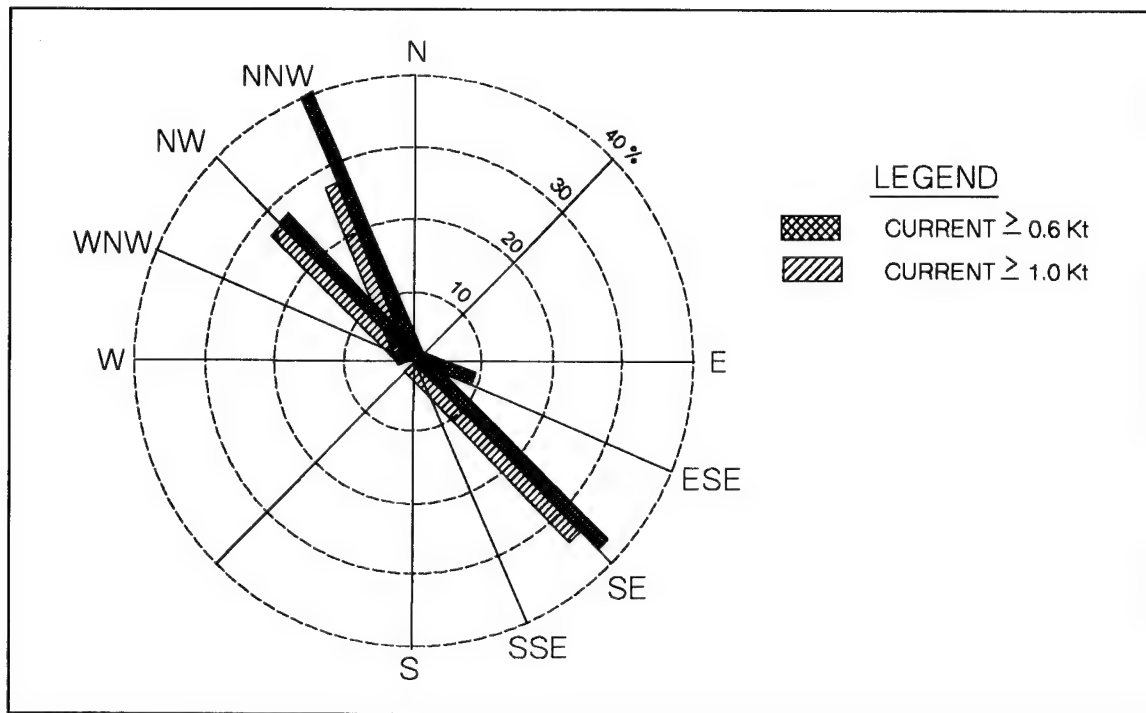
Figure 22a shows current speeds and directions in two speed ranges for the offshore B location. Figure 22b shows currents greater than or equal to 0.5 knots for the channel A and A' locations. Current directions show the direction from which the current was flowing.

Measured field data indicated a bidirectional, tidally driven, longshore current flowing parallel to the bottom contours (Sea Engineering, Inc. 1991). In general, channel currents are less than half the offshore current velocity, and can flow in the opposite direction. The boundary between the offshore and channel regimes is generally just seaward of the channel entrance, at the 50-ft contour. At the offshore B location, dominating currents are from the northwest (329 deg) and southeast (132 deg). At the channel A and A' locations for velocities exceeding

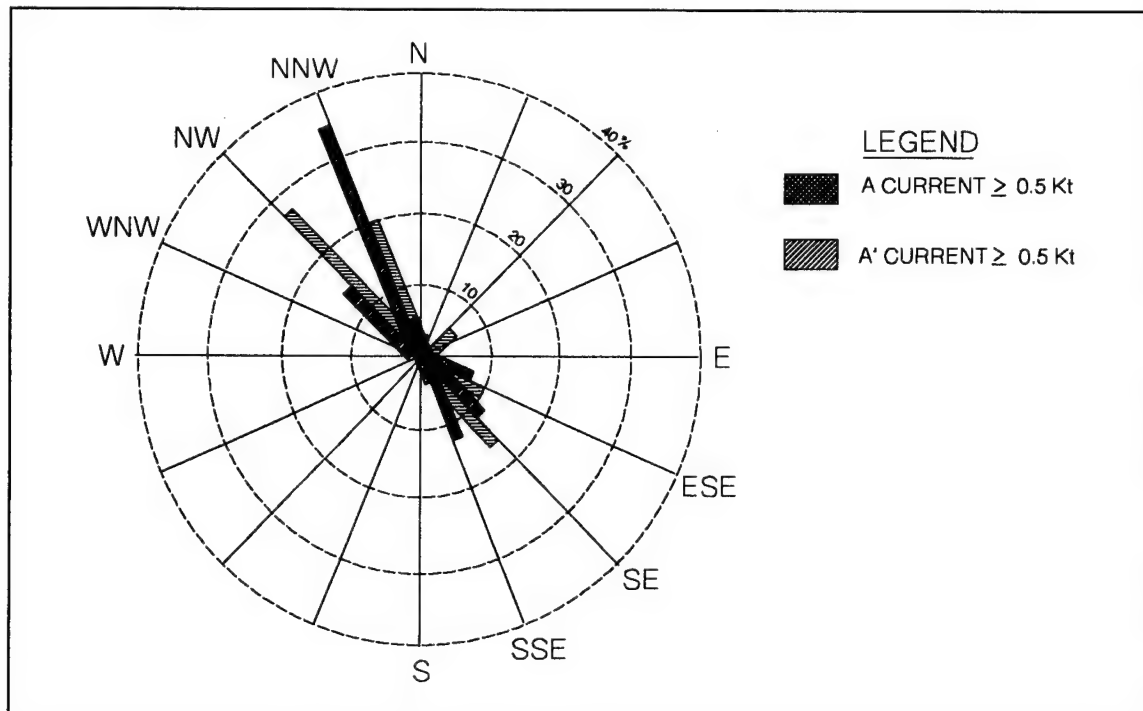
0.5 knots, the dominating current is from the northwest (331 deg) two-thirds of the time and from the southeast (130 deg) only one-third of the time. Moving closer in to shore from location A' to A, the current shifts slightly to the north and south. The highest current velocities tended to occur with the end of flood or ebb tidal cycles. Current reversals were reported and confirmed by local maritime personnel. However, these reversals do not generally occur in conjunction with the highest current velocities.

Model current conditions

Based on these prototype measurements, current conditions shown in Table 12 were selected for the navigation tests. Similar to the procedure used



a. Offshore location B



b. Channel locations A and A'

Figure 22. Current roses for offshore and channel locations

for the waves (see Table 6), currents from the "A," "B," and "C" regions were identified for both the offshore and channel locations. These three regions correspond to "average," "normal," and "extreme" conditions. Demarcation between regions was based on the frequency of occurrence and severity of current conditions. Prototype and model current velocities are listed for currents from both northerly (CN) and southerly (CS) directions. The "average" condition is actually 20 percent above the average recorded currents and corresponds to conditions frequently occurring in the prototype. Ninety-four percent of the time, currents would fall in this region and these conditions must be easily handled by ships entering and leaving the harbor. The "normal" condition represents a current which could occur 440 hr a year, or a little more than once a day. Currents in this region would be exceeded only 5 percent of the time. An "extreme" condition would occur less than once a month with a level of exceedance less than 0.1 percent of the time. Currents greater than the "extreme" could occur annually, but design for safe navigation under these conditions would not be considered economically feasible.

Table 12
Current Conditions for Navigation Tests

Test Case	Current Region	Description	Prototype knots	Model ft/sec	Manometer	
					North	South
Offshore Location B						
CN1, CS1	C	Average	0.60	0.11		
CN2, CS2	B	Normal	1.00	0.19		
CN3, CS3	A	Extreme	1.50	0.28		
A & A' Channel Locations						
CN1, CS1	C	Average	0.35	0.07	1.2	1.9
CN2, CS2	B	Normal	0.50	0.09	1.6	2.6
CN3	A	Extreme	0.80	0.15	3.0	
CS3			0.65	0.12		3.5
CN4, CS4	B	Region B	0.40	0.08	1.4	2.3
Notes: 1. CN = Current from north CS = Current from south 2. Highest value obtainable with current from south						

Because channel conditions are most important for navigation and offshore measurements were in deeper water than the limits of the physical model, only channel current conditions were modeled. A series of trial-and-error runs were made by adjusting the flow rate and plugging and unplugging various combinations of diffuser ports until a reasonably uniform representation of the long-shore current over the entire channel length was achieved. Appendix C

contains schematics of the north and south side diffuser settings for currents from the north and south. The manometer setting (see Table 12) was varied to define a range of current velocities from both the north and south directions. Since the waves were small when the currents were measured, the addition of the water particle velocities to the current distribution was not deemed necessary. All calibration tests were conducted without waves. Dye was used to visualize the flow patterns. Generally, the highest current velocities occurred offshore near the channel entrance and behind a small bar located 1,500 to 1,800 ft from shore. Current speed decreased gradually toward shore.

Next, two triaxial current meters were positioned at the A and A' locations to determine current speed and direction. Because waves were very small during the prototype current measurements, all model current calibration was performed without waves. Long test series, equivalent to 5 hr in the prototype (35 min model), were collected to establish the time necessary to reach and maintain steady-state conditions. Current speeds and directions were averaged over 30-min intervals (3.5 min model) for both locations A and A'. Current speeds were very stable and uniform. Current directions from the south exhibited more variability than those from the north, but were within acceptable limits. Model directions for the south current were 20 to 30 deg more from the south than the prototype. Some of this variability could be due to the fact that the currents were calibrated without waves. Addition of the wave orbital velocities would probably have had a stabilizing effect on currents from the south, turning them more towards the north, in agreement with the prototype observations. Based on these results, values in the range between 1 and 2 hr were selected for further calibration.

Average current speed and direction were also calculated using floats over a 1.6-ft-long stretch between the edge of the entrance channel and location A'. The float measurements were close enough to location A' without unduly influencing the current meter measurements. This was judged to be an acceptable compromise considering an ideal situation would have been synoptic measurements at the same location for both floats and current meters. Readings were averaged over 4 or 5 runs.

Figure 23 compares average current meter velocity and direction for the A and A' locations to the float measurements. The top part of Figure 23 shows the current velocity for currents from the north and south. The bottom part of the figure shows the current directions from the south and north. Both are plotted against manometer setting, which controls the flow rate through the pump. Based on these results, the manometer settings listed in Table 12 were selected to achieve target current conditions.

Possible explanations for the observed variations between the float and current meter measurements are the differences in measurement depths and averaging time. Also, as the current reaches the edge of the entrance channel, current velocities tend to drop off.

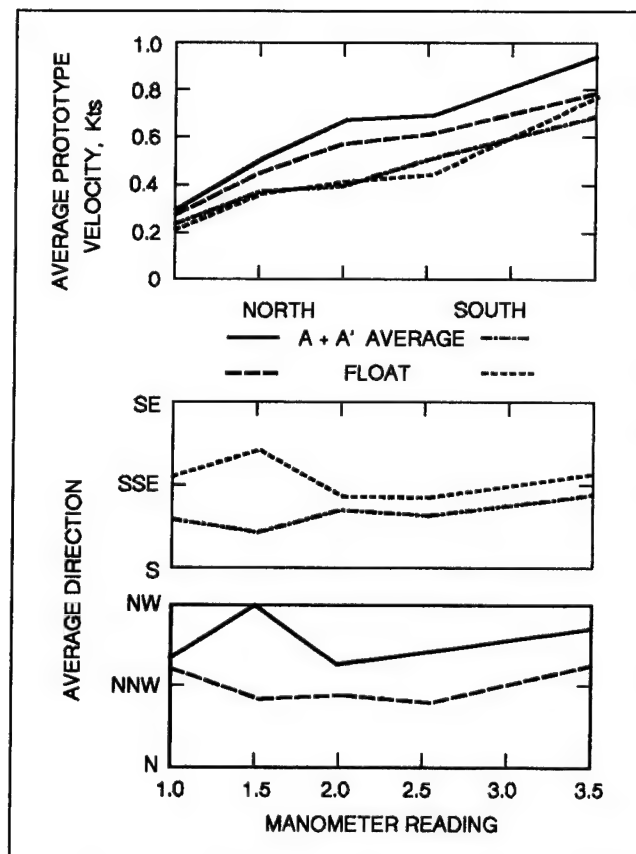


Figure 23. Current calibration results

Wind Conditions

Prototype wind conditions

Wind information was obtained from a 19-year dataset collected at the Barbers Point Naval Air Station from 1949 to 1967. Table 13 lists percentage frequency of wind speed and direction based on this data set. Wind speed is given in nine categories from Beaufort 1 (B1) to Beaufort 9 (B9). Wind directions are listed in 16 sectors of 22.5 deg width.

Winds less than B3, 7 to 10 knots, have a negligible impact on navigation. The interval between 17 and 21 knots corresponds to B5, or fresh breeze, and is a critical level for large wind-area vessels such as the design container ship. The range from 34 to 40 knots corresponds to B8, gale, and is the limiting wind condition for container handling operations and will often cause the container ship to leave the berth for safety reasons.

Thirty-eight percent of the observations are from the NE sector with a mean wind speed of 8.9 knots. The four sectors comprising the northeast quadrant (i.e., N, NNE, NE, and ENE) account for 76.6 percent of the total winds. Thus, approximately 40 weeks a year, the wind comes from this quadrant with a dominant direction of N65E. The entrance channel is aligned within this quadrant.

Approximately 6.4 to 7 percent of the observations are for wind speeds greater than B5 and they occur more from the NE and ENE than the average of all observations. This percentage corresponds to a total time of 24 to 25 days a year.

Model wind conditions

Winds were classified into "A," "B," and "C" regions for probability assessment of the navigation test results using a procedure similar to that used for waves (Table 6) and currents (Table 12). Only winds greater than B5, region "A" or "extreme" winds, were tested in the navigation model tests. A two-speed, 12 volts direct current fan was placed on the deck of the model

Table 13
Percentage Frequency of Wind Speed and Direction

Direction	Wind Speed, knots (Beaufort Scale)									Total Percent	Mean Wind Speed
	1-3 (B1)	4-6 (B2)	7-10 (B3)	11-16 (B4)	17-21 (B5)	22-27 (B6)	28-33 (B7)	34-40 (B8)	41-47 (B9)		
N	0.3	1.3	1.4	0.4	0.0	0.0				3.5	7.3
NNE	0.8	4.3	6.7	2.3	0.3	0.0	0.0			14.5	8.2
NE	3.6	9.8	13.6	8.4	2.5	0.3	0.0			38.1	8.9
ENE	2.4	4.4	5.9	5.5	1.9	0.4	0.0			20.5	9.6
E	0.5	1.2	1.8	1.2	0.4	0.1	0.0		0.0	5.1	9.3
ESE	0.1	0.4	1.0	0.8	0.1	0.0	0.0			2.4	9.7
SE	0.1	0.5	1.3	1.0	0.1	0.0	0.0	0.0		3.1	9.8
SSE	0.1	0.4	0.8	0.4	0.1	0.0	0.0	0.0		1.7	9.2
S	0.1	0.6	0.9	0.4	0.1	0.0	0.0	0.0		2.2	8.6
SSW	0.1	0.3	0.6	0.2	0.0	0.0	0.0	0.0		1.3	8.6
SW	0.1	0.4	0.7	0.3	0.0	0.0	0.0	0.0		1.6	8.7
WSW	0.0	0.2	0.4	0.2	0.1	0.0	0.0			1.0	9.5
W	0.1	0.4	0.6	0.3	0.0	0.0	0.0			1.4	8.7
WNW	0.1	0.2	0.3	0.1	0.0	0.0				0.7	8.5
NW	0.1	0.2	0.1	0.1	0.0					0.5	6.7
NNW	0.1	0.2	0.1	0.0	0.0	0.0				0.3	6.0
Calm										2.0	
Total Number of Observations = 152,671.											
Note: Based on hourly observations at Barbers Point NAS, 1949-1967.											

ship to qualitatively simulate wind effects. It was positioned at a 30-deg angle to the ship's longitudinal axis and 1.0 ft forward of the center of gravity (Figure 24). This positioning gave the required force and moment for a constant wind of 21 knots, between Beaufort 5 and 6. The high speed setting of the fan matched the model thrust of 0.13 lb required to simulate this wind speed.

Constant wind force was calculated by assuming an asymmetrical distribution of containers, stacked five high on the forward half of the ship only. A wind direction of 65 deg (i.e. N65E) and yaw angle of 10 deg gave an effective angle of 30 deg between the ship's longitudinal axis and the wind. A

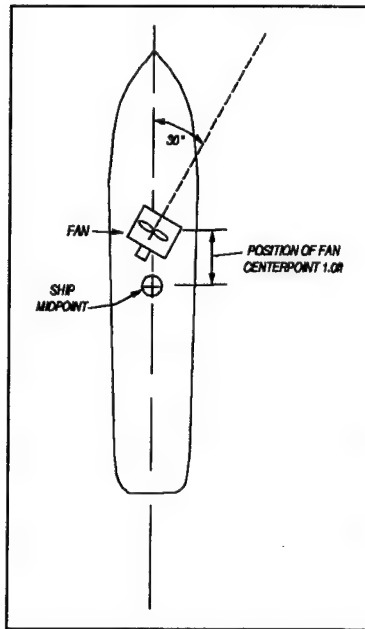


Figure 24. Simulated wind effects

factor of 1.20 was applied to the wind velocity to account for gustiness. Table 14 lists prototype and model forces and moments for Beaufort 5, 6, and 8 winds.

Test Program

The physical model test program consisted of three phases: (a) calibration, (b) navigation, and (c) harbor response. The purpose of the calibration phase was to verify incident wave and current conditions and model ship response. In the navigation phase, the model ship was used to evaluate navigation conditions in six of the eight test plans (Plans 1c and 3a were omitted). If these tests proved successful, then the harbor response phase was conducted. In this phase, the harbor response to wind- and long waves was measured for each test plan using the capacitance wave gauges.

Table 14					
Estimated Wind Forces and Moments					
Wind	Velocity kts	Prototype		Model	
		Force kips	Moment ft-kips	Force lb	Moment in-lb
Beaufort 5 Fresh Breeze	20	45	1,700	0.10	0.7
Beaufort 6 Strong Breeze	25	68	2,600	0.16	1.0
Beaufort 8 Gale	40	175	6,800	0.42	2.6

3 Numerical Model

Model Description

The numerical harbor wave-response model, HARBD, was used to estimate wave oscillations in Barbers Point Harbor for the existing configuration (test plan 1a) and seven proposed design modifications (test plans 1c, 2c, 3a, 3c, 4c, 5c, and 6c) to the harbor. HARBD is a steady-state finite element model that calculates linear wave oscillations in harbors of arbitrary configuration and variable bathymetry. Effects of bottom friction and boundary absorption (reflection) are included. Bottom friction is assumed to be proportional to flow velocity with a phase difference. Boundary reflection is based on a formulation similar to the impedance condition in acoustics and is expressed in terms of the wave number (i.e. wavelength) and reflection coefficient of the boundary. The model uses a hybrid element solution method which involves the combination of analytical and finite element numerical solutions to determine the response of a harbor to an arbitrary forcing function. A more complete description of the model and its limitations is given in the subsection titled "Model formulation."

Background

HARBD was originally developed for long-period harbor oscillations and was adapted for wind waves (i.e. short-period waves) by Houston (1981). Mathematical formulations and numerical schemes are described in detail in Chen (1984, 1986) and a user's manual (Chen and Houston 1987) is available. The model is accessible through the Coastal Modeling System (CMS) at CERC and a CMS user's manual (Cialone et al. 1991) is available. The CMS is based on WES's CRAY-YM-P supercomputer.

The HARBD model has been tested and compared with known analytical solutions for a number of cases and the results were excellent (Chen 1984, Chen and Houston 1987). It has been applied in assessing the design or modification of the existing Barbers Point Harbor, Oahu, Hawaii (Durham 1978, Lillycrop and Briggs 1992); Agat Harbor, Guam (Farrar and Chen 1987); Kawaihae Harbor, Hawaii, Hawaii (Lillycrop, Bratos, and Thompson 1990); and Maalaea Harbor, Maui, Hawaii (Lillycrop et al. 1993a). The HARBD

model was used in conjunction with a physical model to study the effects of entrance channel dredging at Morro Bay Harbor, California (Kaihatu, Lillycrop, and Thompson 1989), harbor resonance at Los Angeles-Long Beach Harbor, California (Sargent 1989), and optimal wave protection at Fisherman's Wharf, San Francisco, California (Bottin, Sargent, and Mize 1985). The HARBD numerical model was used to design coastal structures to provide optimal wave protection at Green Harbor, Massachusetts (Weishar and Aubrey 1986) and Los Angeles-Long Beach Harbor, California (Houston 1976). It was used to estimate wave conditions in Indiana Harbor, Indiana, during a study of sediment disposal alternatives (Clausner and Abel 1986). Finally, HARBD was compared to laboratory data collected from the physical model study of Barcelona Harbor, Buffalo, New York (Crawford and Chen 1988) with encouraging results.

Model formulation

In model formulation for arbitrary depth water waves (i.e., shallow, intermediate, and deepwater waves), the water domain is divided into near and semi-infinite far regions. The near region includes the harbor and all marine structures and bathymetry of interest and is bounded by an artificial 180-deg semi-circular boundary offshore of the harbor entrance. The far region is an infinite semicircular ring shape bounded by the 180-deg semicircular boundary of the near region and the coastline. The semi-infinite far region extends to infinity in all directions and is assumed to have a constant water depth and no bottom friction (Chen and Houston 1987). The finite near region, which contains the area of interest, is subdivided into a mesh of non-overlapping triangular-shaped elements. The length of side of each element is determined from the desired grid resolution and design wave parameters. Water depth and bottom friction coefficient are specified at the centroid of each element, and a reflection coefficient is assigned to each element along the solid, near region boundaries. The model requires a wave period and direction as input. The solution consists of an amplification factor (i.e., the ratio of local wave height to incident wave height) and a corresponding phase angle for each grid point in the near region. Phase angle represents the difference in phase between the grid point and the incident wave. Contour plots of the amplification factors and corresponding phase angles are used to determine the oscillation patterns occurring throughout the harbor.

The governing partial differential equation is derived through application of linear wave theory to the continuity and momentum equations. All dependent variables are assumed to be periodic in time with angular frequency ω . These steps yield the following generalized Helmholtz equation (Chen 1986) in which the velocity potential ϕ is solved

$$\nabla(\lambda c c_g \nabla \phi) + \frac{c c_g}{c} \omega^2 \phi = 0 \quad (21)$$

where

∇ = horizontal gradient operator

λ = complex bottom friction factor

c = wave phase velocity = (ω/κ)

c_g = wave group velocity = $[c/2\{1 + (2\kappa h/\sinh 2\kappa h)\}]$

ω = angular frequency

ϕ = velocity potential

h = water depth

The wave number is obtained from the dispersion relation

$$\omega^2 = g\kappa \tanh(\kappa h) \quad (22)$$

where g = acceleration due to gravity.

The complex bottom friction factor λ is assumed proportional to the maximum velocity at the bottom and is defined as

$$\lambda = \frac{1}{1 + \frac{i\beta a_o}{h \sinh \kappa h} \exp(i\gamma)} \quad (23)$$

where

$$i = \sqrt{-1}$$

β = dimensionless bottom friction coefficient that can vary spatially

a_o = incident wave amplitude

γ = phase shift between stress and flow velocity

The effects of bottom friction do not necessarily need to be included in the general solution. This is accomplished by setting $\beta = 0$, which results in $\lambda = 1$, and Equation 21 reduces to an expression that excludes bottom friction.

For the absorptive boundary condition along the solid harbor boundaries, the model adopts the impedance condition used in acoustics in terms of the boundary reflection coefficient K_r expressed as:

$$\frac{\partial \phi}{\partial n} - \alpha \phi = 0 \quad (24)$$

with

$$\alpha = i\kappa \frac{1 - K_r}{1 + K_r} \quad (25)$$

where

α = dimensional coefficient related to the boundary reflection

n = unit-normal vector directed outward from the fluid domain

Similar to the friction coefficient, when $K_r = 1$, then $\alpha = 0$ and Equation 24 reduces to a zero velocity potential normal to the boundary (Sargent 1989). This infers a perfectly reflecting boundary condition.

A hybrid element method is used to solve the boundary value problem of Equation 21. In this solution, a conventional finite element approximation is used in the finite near region, while an analytical solution with unknown coefficients is used to describe the semi-infinite far region. Conditions in the near and far regions must be matched along the artificial semicircular boundary. This requirement is met by HARBD routines, which automatically match the solutions, using the stationarity of a functional, to a series of Hankel functions, which give the solution for the semi-infinite far region (Farrar and Chen 1987). The hybrid element numerical techniques used in the formulation are discussed in greater detail in Chen and Mei (1974).

The HARBD model is intended to simulate waves that can be adequately described by the governing generalized Helmholtz equation, (Equation 21). Therefore, HARBD does not simulate nonlinear processes such as wave breaking, wave transmission and overtopping of structures, entrance losses, steep bathymetric gradients, and wave-wave and wave-current interaction. Fortunately, these limitations are not dominant for many harbors and HARBD can be applied with some degree of confidence. Since nonlinear processes

naturally occur in the prototype, these effects must be considered in interpretation of results.

Finite Element Grids

The finite element grid generated to predict the harbor resonance modes for the existing harbor (test plan 1a) is shown in Figure 25. Numerical grids for test plans 1c, 4c, and 6c are shown in Figures 26, 27, and 28, respectively. Finite element grids for the other four test plans are contained in Appendix D. All grids include the entrance channel, barge basin, deep-draft basin, and marina (WBM). The additional 1,100-ft by 1,100-ft berthing area is included when appropriate.

The artificial semicircular offshore boundary extends to the Sxy array gauge location, approximately 2,000 ft offshore. A seaward extension of twice the entrance distance is sufficient to adequately model the wave response inside a harbor. However, the grid boundary for this study extended to the location of the Sxy array gauge location to an attempt to investigate model predictions and measured prototype wave conditions. Investigations with extending the HARBD boundary and bathymetric changes in the offshore area determined the HARBD model was not sensitive to boundary changes this distance seaward of the harbor entrance. Therefore, effects of proposed modifications on the entrance channel, such as flaring, were quantified through the physical model observations and measurements, rather than the numerical model.

Grid bathymetry was obtained from POD hydrographic surveys relative to mllw. Simulations of the seven proposed design modifications were conducted through alteration of the existing grid to include the proposed modifications.

The original grid for the existing configuration (Figure 25) was designed with a grid resolution, the length of side of each element, equal to approximately one-sixth of the local wavelength, based on linear wave theory using a wave period of 10 sec and the deep-draft basin depth of 38 ft. In calibrating the model with prototype measurements and available physical model predictions, grid resolution was refined in the barge basin and marina to obtain six elements per wavelength resolution in shallower water. The refined grids improved the accuracy of the numerical model predictions in these areas. Total numbers of elements (triangles), nodes (triangular corners), and boundary elements are given in Table 15.

To compare numerical model predictions to prototype measurements and physical model predictions, and to assist in identifying the harbor resonant modes, numerical model output locations were selected coincident with prototype and physical model wave gauge locations. Several additional locations were selected to investigate wave propagation through the entrance channel, in the marina, and the expansion area. An output location is an area consisting of a specified number of elements from which the mean value of the results of those elements is calculated. Twenty-eight output locations were selected for

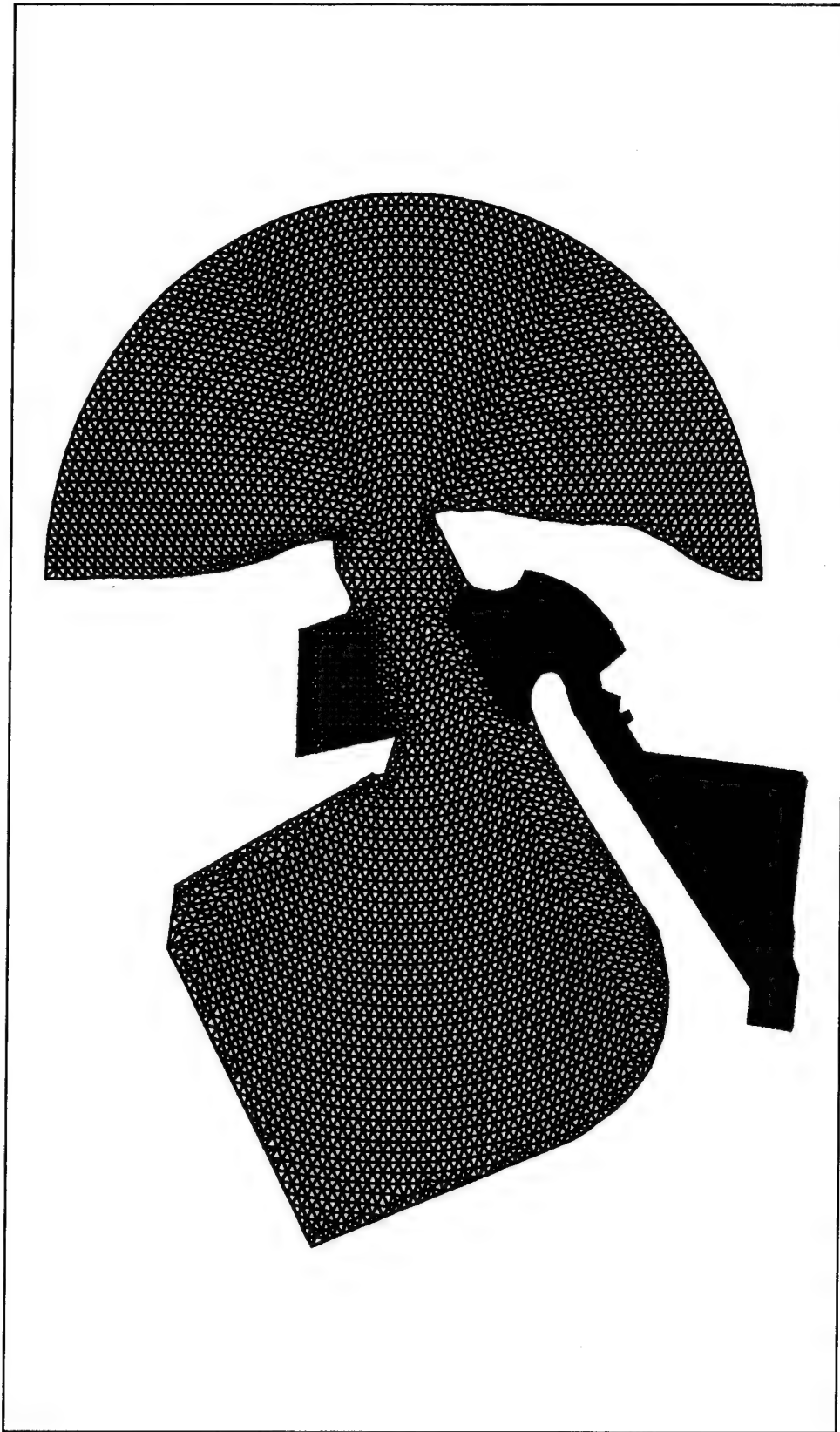


Figure 25. Finite element grid for existing harbor

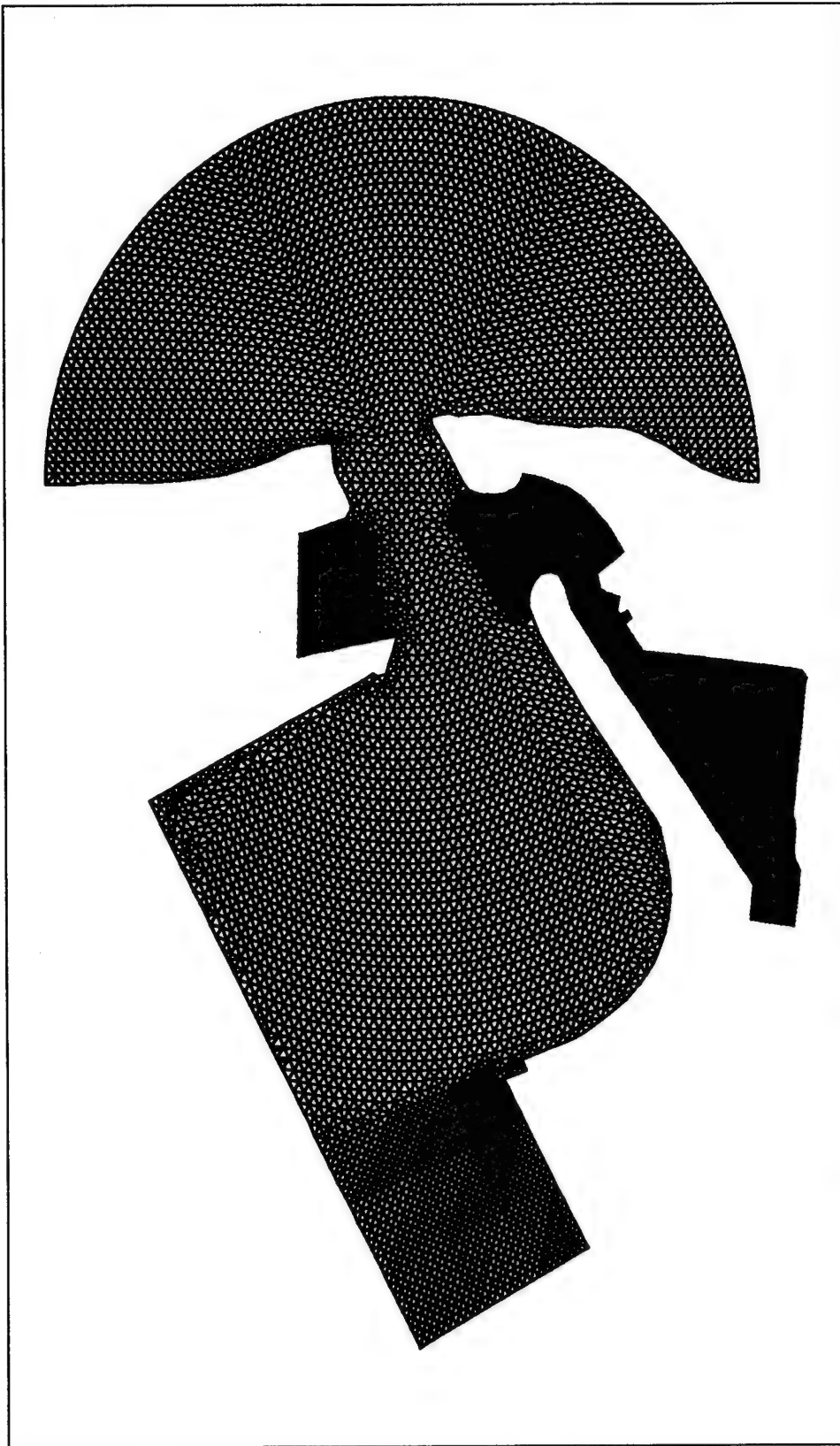


Figure 26. Finite element grid for test plan 1c

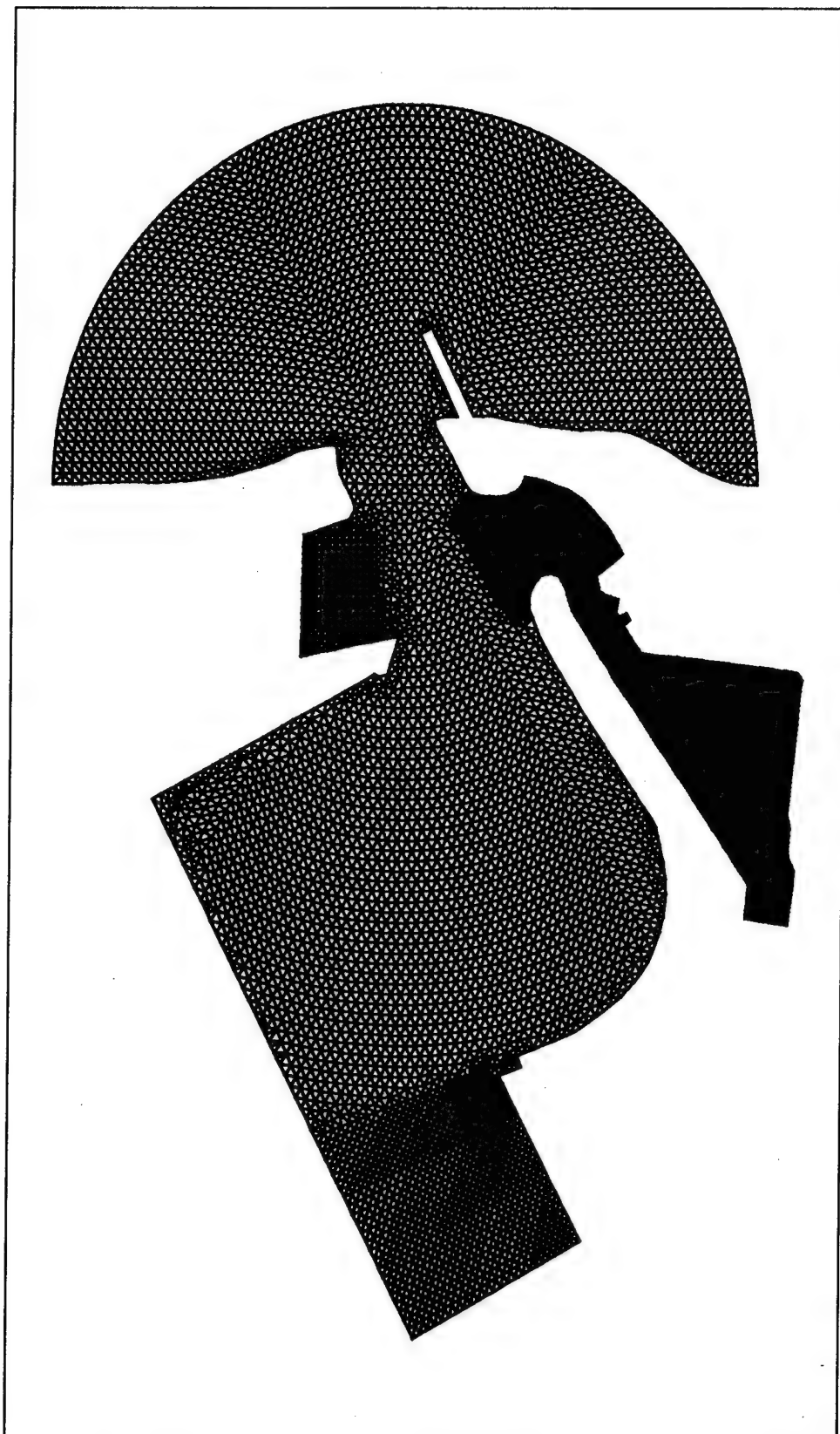


Figure 27. Finite element grid for test plan 4c

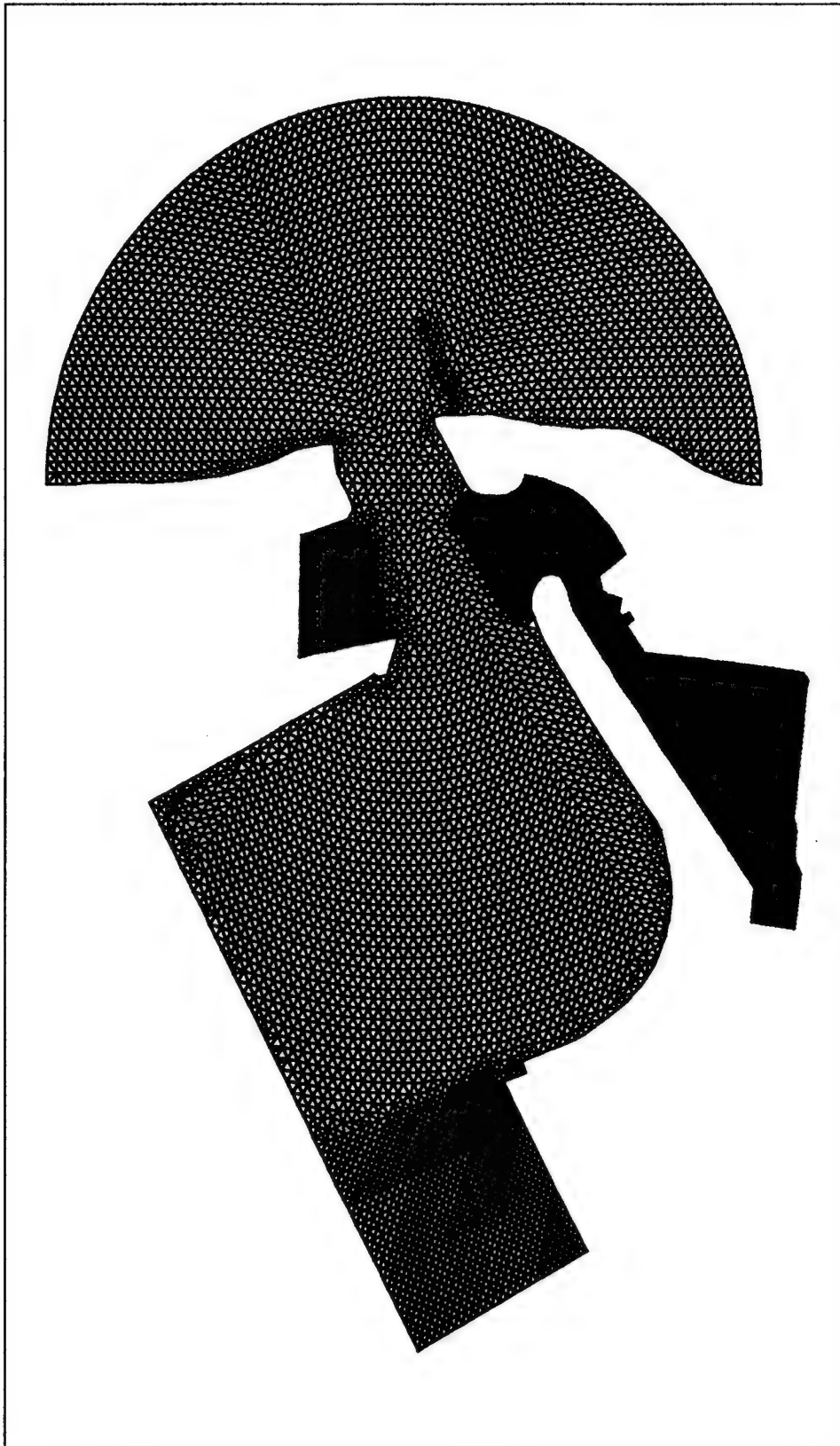


Figure 28. Finite element grid for test plan 6c

Table 15 Grid Descriptions			
Design Plan	No. of Elements	No. of Nodes	Boundary Elements
1a	11,694	6,155	503
1c	13,087	6,890	570
2c	13,097	6,890	570
3a	11,694	6,155	503
3c	13,097	6,890	570
4c	13,088	6,897	593
5c	13,108	6,903	585
6c	13,136	6,910	571

harbor configurations which excluded the harbor expansion (test plans 1a and 3a) and 33 output locations were selected for those design plans which included this expansion. The locations were selected by CERC, POD, and the Hawaii DOT, and are shown for the two configurations in Figures 29 and 30. Output locations coincident with the prototype and physical model gauge locations can be identified by referring to Figures 4 and 8, respectively. Wave height amplification factors and phase angles calculated from the numerical model were also obtained over the entire harbor domain for use in determining oscillation patterns and magnitudes of wave height amplification occurring during harbor resonance.

Test Procedures and Calculations

Prior to this study, calibration of the numerical model with prototype measurements was conducted through the MCCP. Initially, the model was tested with wave period increments ΔT for the range of wave periods listed in Table 16. These wave periods and ΔT were selected to coincide with those

Table 16 Wave Period Increments	
ΔT sec	Range of Wave Periods sec
1.0	15.0 - 68.0
2.0	70.0 - 100.0
2.5	102.5 - 200.0
5.0	205.0 - 360.0
10.0	360.0 - 720.0
20.0	740.0 - 1620.0

used in the numerical model study conducted during the design phase of the existing harbor (Durham 1978). Analysis of the prototype data indicated that no significant resonance modes existed for wave periods smaller than 50 sec. Therefore, future comparisons with prototype and physical model data were done with a high-frequency cutoff of 50 sec.

The incident wave angle was chosen perpendicular to the bottom contours. Analysis of the prototype data was made without regard for wave direction and directional spreading. Preliminary tests with HARBD showed insignificant differences in results from variable wave directions for the long wave periods considered. The physical model later showed some variability in the

measured transfer functions for the eight different wave conditions, as a function of wave direction and directional spreading. However, the general trend appeared to be present for all cases and an average transfer function was considered representative. Additional discussion is contained in Chapter 5.

The HARBD model was tested with complete boundary reflection and no bottom friction since these modeling capabilities were not available during the design study of the existing harbor.

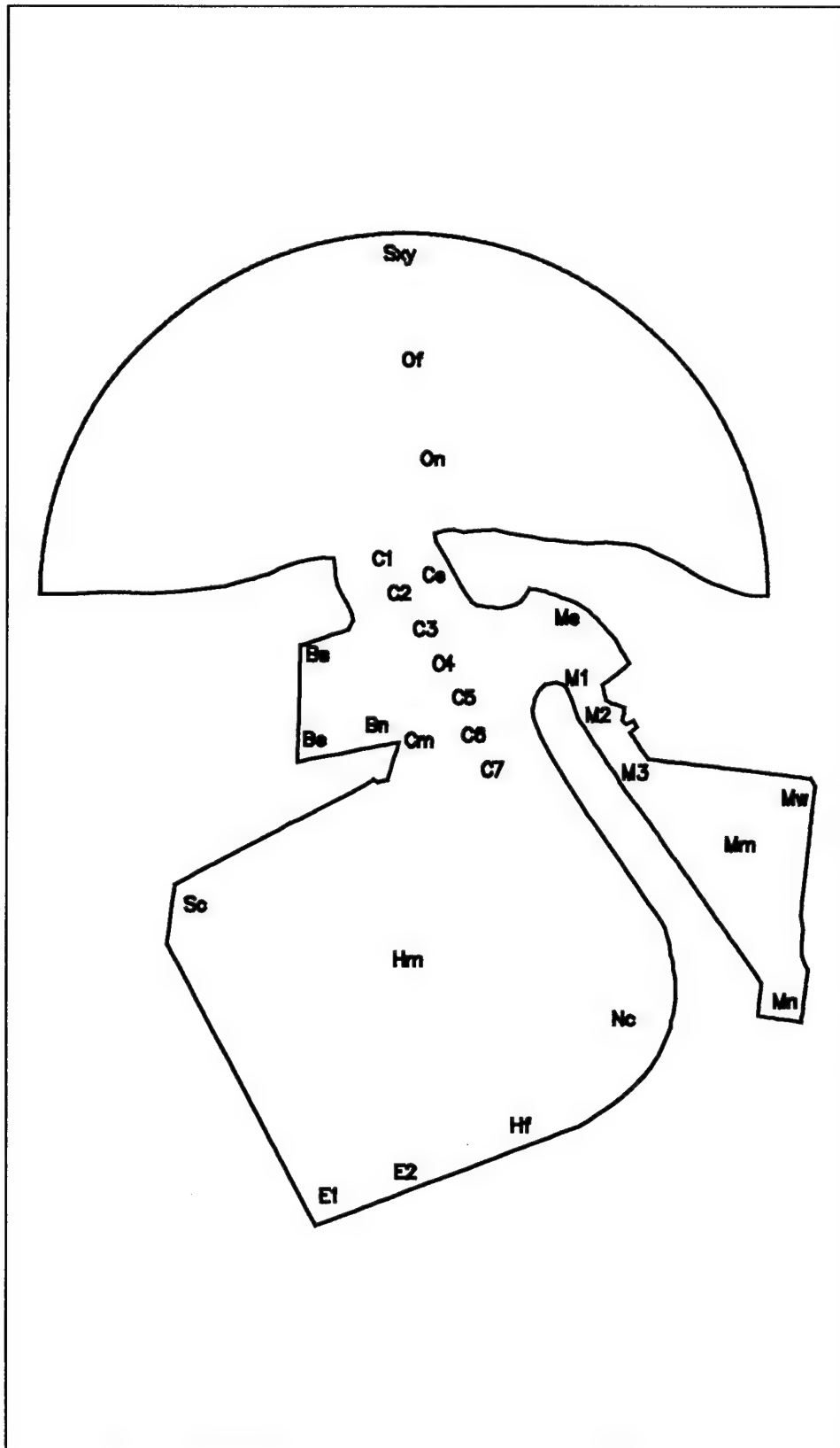


Figure 29. Numerical model output locations

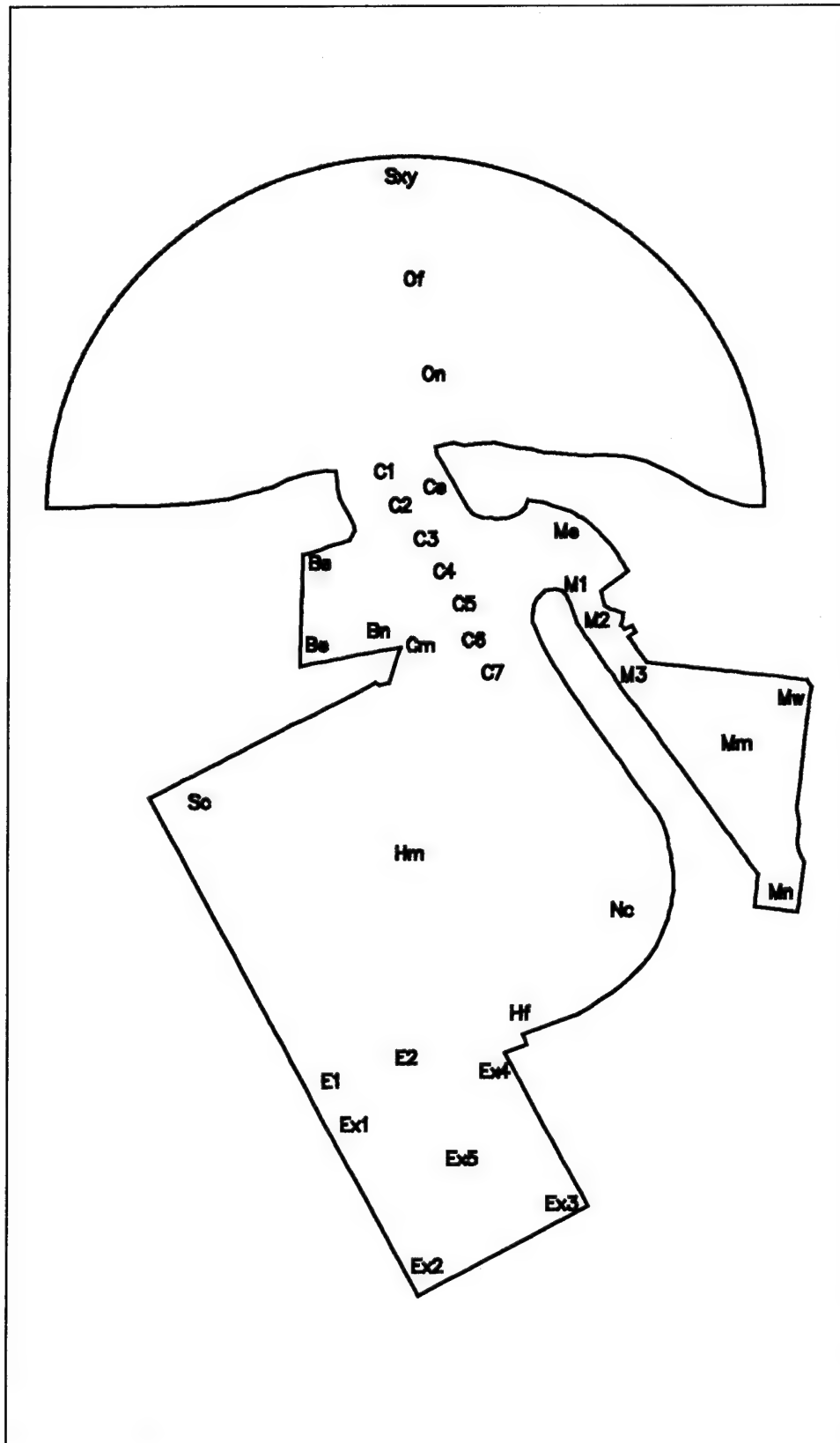


Figure 30. Numerical model output locations for expanded harbor

After comparison with the prototype measurements, it was determined that the numerical model was not predicting several modes of oscillation identified in the prototype measurements. Since the prototype measurements were analyzed at a frequency of 0.000122 Hz (1/8196.7 sec), numerical model input frequencies were increased to three times the frequencies of the analyzed prototype measurements or 0.0004069 Hz (1/24,576 sec). This was done in an effort to avoid missing numerical model peak frequencies which were not coincident with the prototype resonant frequencies. The model then correctly predicted the resonant modes of oscillation identified in the prototype measurements; however, the frequencies were slightly offset. Also, the magnitude of wave height amplification factors was larger in the numerical model predictions than in the prototype measurements. This was due to the assumption that no energy losses were considered in these simulations (i.e., no bottom friction and perfect boundary reflection). Also, as the frequency increased, or wave period decreased, numerical model amplitudes increased because dissipative effects become more dominant with shorter wave periods.

With the numerical model properly predicting the resonant modes of oscillation identified in the prototype measurements, the next task was to accurately predict the magnitudes of wave height amplification. The HARBD model computes a standing wave for a given frequency. For a low frequency, or very long wavelength, the entire harbor responds as if it were a reflecting wall. A standing wave against a reflecting wall has a height of twice the incident wave. Therefore, the low-frequency wave height amplitudes predicted by HARBD for input frequencies between 0.000122-Hz (8,196 sec) and 0.001343-Hz (745 sec) were divided by two. Only the Helmholtz mode (or pumping mode of the harbor) was affected by this criteria because the wavelength of this wave encompasses the entire domain of the harbor and outer region to the S_{xy} gauge.

The model was then tested at 0.0004069-Hz (1/24,576-sec) frequency increments with varying bottom friction coefficients. The resulting wave height amplifications from each test were compared with prototype measurements to investigate the reduction of wave energy due to the increase of bottom friction. This procedure was repeated until an accurate match of wave height amplification between the model predictions and prototype measurements was possible. The range of frequencies and wave periods and the corresponding bottom friction coefficients used to reduce the wave energy in the numerical model are given in Table 17.

The HARBD numerical model has two free parameters which can be adjusted to match prototype data: bottom friction and reflection coefficients. Boundaries for these long-period waves were felt to be nearly perfectly reflecting. The bottom friction coefficients, however, should be a function of the type of bottom material as a function of the wave period and corresponding wavelength. Therefore, the bottom friction coefficients were varied to calibrate the model predictions to the measured prototype values at each frequency peak or mode.

Table 17
Bottom Friction Coefficients

Period Increments $T_1 - T_2$ sec	Frequency Increments $f_1 - f_2$ Hz	Friction Coefficient β
8192.02 - 744.73	0.000122 - 0.001343	0.0000
682.67 - 546.13	0.001465 - 0.001831	0.0000
512.00 - 204.80	0.001953 - 0.004883	0.0012
199.81 - 130.83	0.005005 - 0.007644	0.0025
128.00 - 106.39	0.007813 - 0.009399	0.0050
105.03 - 102.40	0.000952 - 0.009766	0.0100
101.14 - 66.06	0.009887 - 0.015138	0.0150
65.54 - 57.29	0.015258 - 0.017455	0.0200
56.89 - 49.95	0.017578 - 0.020020	0.0300

Once the bottom friction coefficients were identified for the range of wave periods tested, the model was tested using the identified coefficients for each wave period or frequency. Since the numerical model was tested at three times the frequency of the analyzed prototype measurements, results were averaged over wave periods one increment above and one increment below the prototype frequencies. This was done so that numerical frequencies matched those of the prototype. Averaging the results had little effect on the numerical predictions. Once calibrated, the modifications to the harbor were modeled at the prototype frequency increments to reduce necessary CPU and run time. All

tests were run on the WES CRAY YM-P supercomputer.

Wave height amplifications in the marina and the barge basin were of concern due to the large magnitudes occurring in those areas. Since those areas are shallower than the deep-draft basin, the numerical model grid was refined in the marina and the barge basin to assure the accuracy of the numerical model predictions.

Finally, the numerical model calibration was checked against the prototype measurements and the physical model results for the existing harbor configuration (test plan 1a). This comparison was excellent and is discussed in Chapter 5. With the numerical model calibrated, the refined grid was then modified to include the next proposed design modification, test plan 1c, and the model was retested and results compared with the physical model calculations. This procedure was continued for all seven proposed design modifications.

4 Navigation Study

Navigation testing in a physical model is a demanding task, involving a number of factors that can influence the outcome. Some of the more important are (a) physical model scale, boundaries, and limitations; (b) realistic simulation of environmental conditions including wind, wave, and currents; (c) accurate modeling of ship dimensions and performance characteristics; (d) correct application of ship operating procedures relative to vessel speed, engine power, and rudder angle; (e) experience of model ship operator; (f) selection of criteria for evaluating ship navigability in entrance channel; and (g) other factors not reproduced in the model such as tugs, etc. A quantitative evaluation of a harbor's navigability is not possible. The results always include some scale effects due to the model and subjective assessment of the person(s) conducting and evaluating the tests. The paragraphs below describe the attempts which were made to minimize the impact of these factors during the Barbers Point tests. Then, discussions of the navigation results, problem areas along the entrance channel, probability assessment of the results, and surge response of the moored ship are presented.

Design Ship

Prototype C9 container ship

Barbers Point Harbor was designed for C7-class vessels with a length of 720 ft, beam of 95 ft, and loaded draft of 34 ft. Since the original design, economics has gradually dictated construction of larger vessels to transport cargo. A ship simulation study (Marine Safety International 1988) of the harbor was conducted for American President Lines (APL) using a third-generation, C8-class container ship with a length of 787 ft, beam of 100 ft, draft of 40 ft, and container capacity of 2,000 twenty-foot equivalent units (TEU). The study indicated that only operations with minimum waves and currents less than 1 knot (plus several other constraints) would be acceptable for safe entry of C8-class ships.

Through discussions with the state of Hawaii, the C9-class container ship was chosen for the navigation study. The President Lincoln was built in the early 1980's and is currently one of the larger container ships on the Pacific

Rim trade routes. The ship has a length of 860 ft, beam of 106 ft, fully loaded draft of 39 ft, and capacity of 2,900 TEU. The scantling draft is 35 ft and the design draft for speed and maneuvering tests is 30 ft. Fully loaded displacement is 55,000 long tons (lt) with a light ship operational weight of 20,000 lt. Gross and net tonnage are 41,000 and 31,000 lt, respectively. The rated horsepower of the ship was 43,200 bhp.

Performance characteristics for the prototype C9 ship are given in Appendix E. Revolutions per minute (rpm's) and corresponding speed for different engine orders are listed in Table E1. Turning circle parameters illustrated in Figure E1 are given in Table E2. Table E3 lists crash stop times and distances. Crash stops are to be avoided as the ship is out of control during these maneuvers. Finally, Table E4 lists bow thruster performance characteristics. The bow thruster is less effective as the ship's forward or reverse speed increases.

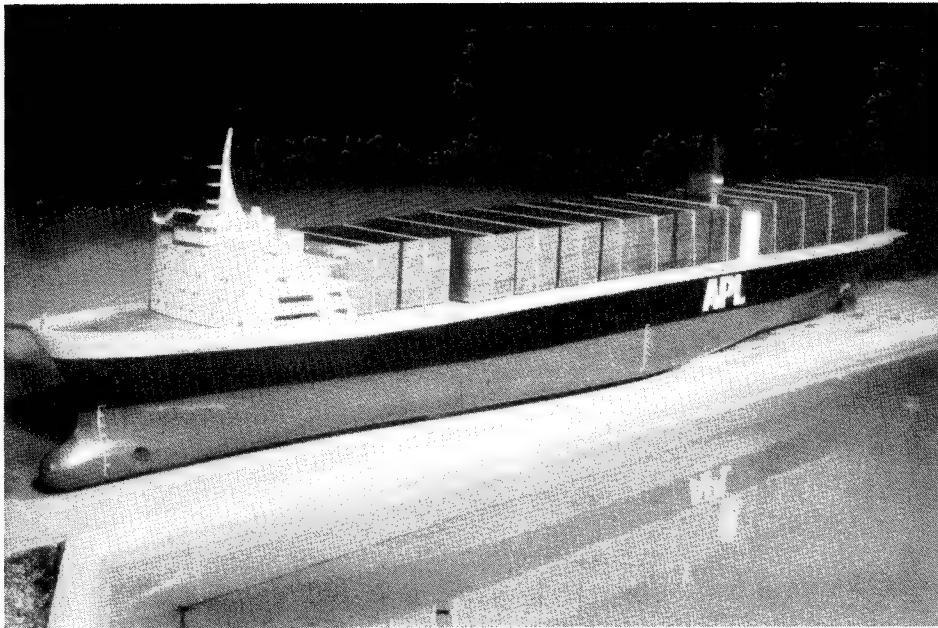
Model C9 container ship

The model C9 container ship was constructed by Mr. Bill Sturdivant, Jackson, MS, at the same 1:75 scale as the physical model using drawings supplied by APL. Figure 31 shows two views of the model ship. It had a length of 11.5 ft, beam of 17 in., and a scantling draft of 5.6 in. A 12-V engine powered the scaled propeller and bow thruster. Forward and reverse speeds, rudder angle, and bow thruster direction and speed were remote controlled.

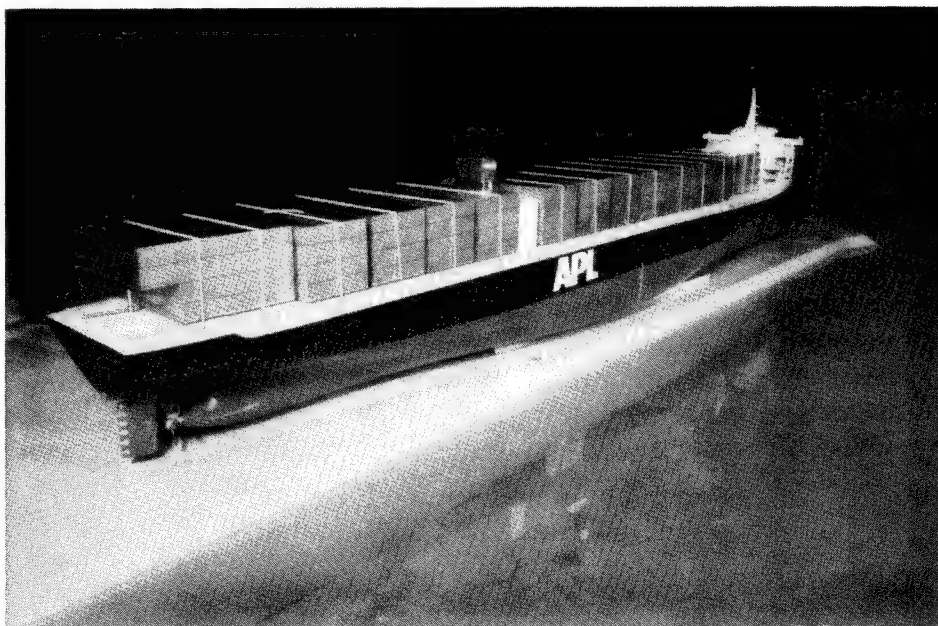
An accelerometer was mounted inside the model ship in an attempt to indicate possible contact with the channel bottom and sides during transit. The self-contained piezo-resistive accelerometer triggered a 12-vdc lamp mounted on the ship's superstructure. Tuning of the accelerometer's sensitivity proved to be difficult, however. If the accelerometer was too sensitive, reversing the engine power, applying the bow thruster, or waves could trigger a false alarm. If not sensitive enough, the light would not turn on when the ship contacted the channel. The final tuning required contact near the accelerometer location in the middle of the ship to register. In the end, more confidence was placed in visual observations and video recordings of the ship transits to indicate groundings than the accelerometer. Additional accelerometers mounted in the ship's bow and stern might alleviate this problem in future studies. Figure E2 shows a circuit diagram of the accelerometer system.

Model ship calibration

The scale model C9 container ship was calibrated to closely reproduce prototype response to various external forces. Static and dynamic balancing were performed for the most important parameters only. These included ship loading to scantling draft, metacentric height, roll period, forward speed to full ahead, reverse speed to full astern, rudder angle to reproduce turning circle maneuvers, and bow thruster performance.



a. Front view



b. Rear view

Figure 31. Model C9 container ship

In the prototype ship, the displacement is approximately 50,000 lt for the scantling draft of 35 ft. This places the center of gravity 42 ft above the keel and 10 ft aft of the center line. The model ship without ballast weighed 116 lb. An additional 146 lb of lead weights were placed along the port and starboard sides to simulate the required model displacement of 262 lb, equivalent to the prototype displacement of 50,000 lt and scantling draft of 35 ft. This draft was used for all navigation tests. The bottoms of these 1.5-in.-thick, 1.5-in.-wide, and 3.5-in.-long weights were positioned 7 in. above the keel and 4 in. inboard from the outside edge of the ship.

Figure 32 illustrates the six degrees of freedom of a ship. Surge, sway, and heave are the translational modes in the x, y, and z directions, respectively. Roll, pitch, and yaw are the rotational motions about the x, y, and z axes, respectively. The x coordinate lies along the longitudinal axis of the ship, the y coordinate is the transverse axis, and the z coordinate is the vertical axis.

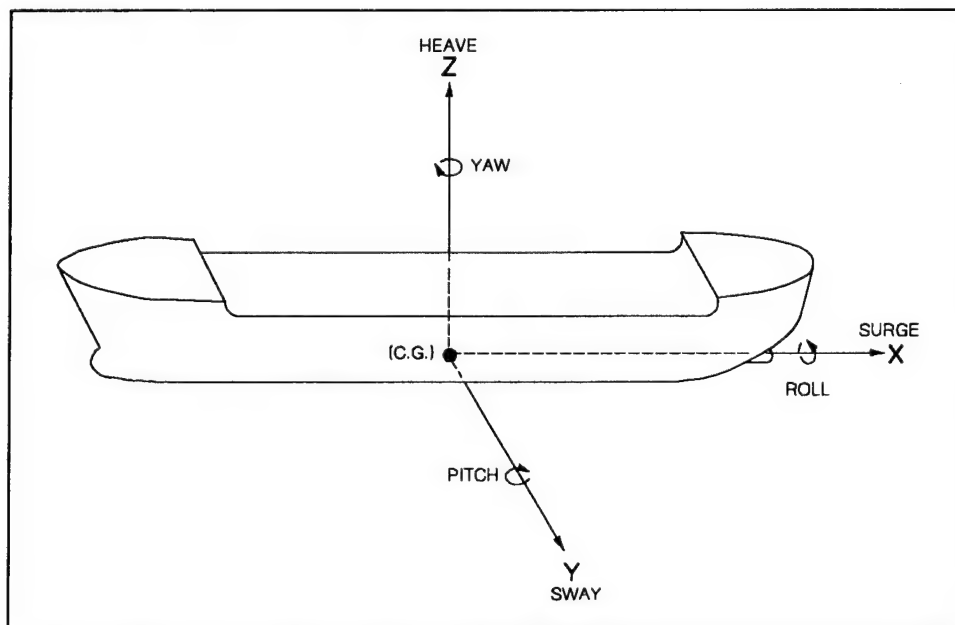


Figure 32. Six degrees of ship motion

Figure 33 is a cross section through the center of the ship (i.e. the Y-Z plane) illustrating the surface stability of a ship. The left side shows conditions of static equilibrium and the right side shows conditions of free unrestrained rolling. The condition of static equilibrium is based on Archimedes principle: the weight of the ship and cargo W equals the weight of the water displaced by the ship B . The center of gravity (CG) is usually located along the vertical axis of the ship, approximately midway in the cargo from the bottom of the ship. As previously stated, the CG for the C9 at a draft of 35 ft is located 10 ft aft of the vertical axis and 42 ft above the keel. The center of

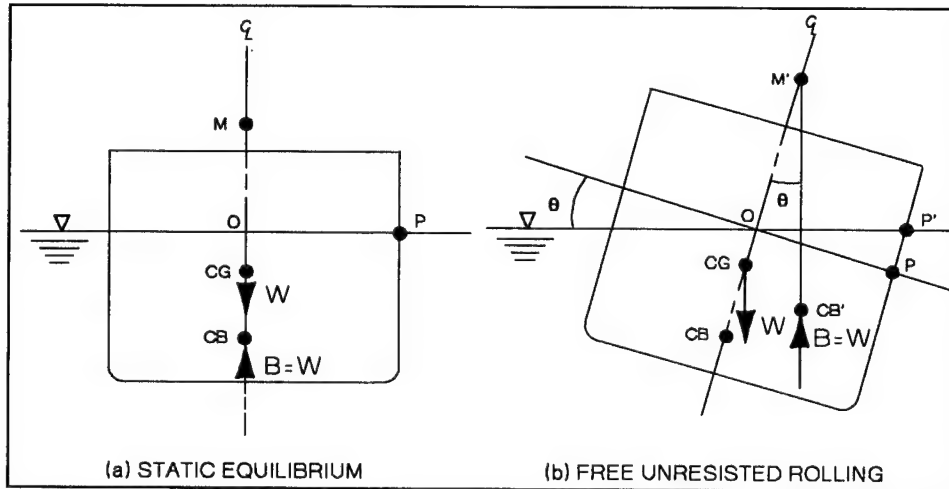


Figure 33. Equilibrium conditions for a ship

buoyancy (CB) is the center of gravity of the fluid displaced by the ship. The CB is positioned along the vertical axis of the ship during static conditions. It may be located above or below the CG.

The condition of stability of a ship is not necessarily to have the CB above the CG, but rather to have the metacenter M above the CG. The metacentric height \overline{gm} is the distance from the CG to M. When the ship rolls, the CB moves out to a new position, which is no longer in line with the CG and the vertical axis of the ship. The intersection of the vertical from the new CB' with the vertical axis defines the location of M. For the prototype President Lincoln, \overline{gm} is approximately 3.3 ft with a corresponding model value of 0.53 in.

The righting moment of the ship in roll is a function of the weight of the displaced water (i.e. weight of the ship and cargo) W , the angle of roll θ , and the metacentric height \overline{gm} . It is given by

$$M_{Roll} = W \overline{gm} \sin \theta \quad (26)$$

According to Berteaux (1976), the theoretical natural roll period T_{Roll} is defined by

$$T_{Roll} = 2\pi \sqrt{\frac{I_v}{W \overline{gm}}} \quad (27)$$

where

$$I_v = \text{virtual moment of inertia} = I + I_a$$

$$I = \text{moment of inertia of the water plane}$$

I_a = added mass moment of inertia of the water entrained by the ship's rotation

An empirical formula for T_{Roll} as defined by APL (1991) is

$$T_{Roll} = \frac{C B}{\sqrt{gm}} \quad (28)$$

where

C = conversion factor = 0.44

B = ship beam = 106 ft

This gives a roll period of 26 sec for the prototype. The model roll period of 3 sec is computed by dividing the prototype value by the square root of the scale factor (i.e. $\sqrt{L_r} = \sqrt{75} = 8.66$). A roll period of 3 sec was measured in the model, matching the target value.

Model maneuvering tests were conducted in water depths ranging from three to six times the ship's draft, approaching deepwater conditions. A comparison of prototype and model ship speed for different engine orders is given in Table E5. The "Nav Full" ahead condition was not calibrated because it is only used once underway in the open ocean, a condition that was not modeled. Different rpm settings were recorded for the model because of differences in the model propeller. In general, the model matched the prototype speeds within 10 percent.

Table E6 compares model and prototype turning circle advance and tactical diameters for half speed ahead (see Figure E1 for definitions). Agreement was within 3 percent. Finally, Table E7 compares bow thruster performance between the model and prototype at zero ship speed. Model results are the average for both directions of turning. Again, model agreement was within 5 percent.

Model ore carrier

The C9 container ship model was used during the majority of the tests. A few demonstration tests with an existing Great Lakes ore carrier were performed to qualitatively assess the effect of a different hull shape. An ore carrier has larger block coefficients (i.e., drag), less power, smaller rudders, slower response, larger metacentric heights, and faster roll periods than a container ship.

This model ore carrier was built to a scale of 1 model to 100 prototype. For the 1 to 75 scale used in this study, the corresponding dimensions of this model were as follows: length = 750 ft, beam = 79 ft, and draft = 20.7 ft. Because of these scale differences, the ship's response could not be correctly

reproduced. Also, the overall size of this vessel was much smaller than projected ships in Barbers Point Harbor.

Test Procedure

Six of the eight test plans (all except 1c and 3a) were tested in the model with varying combinations of waves, currents, and winds. The navigation tests were run in two series depending on the operator of the model ship: staff or pilot. The staff series were conducted by Professor Eivind Bratteland, on sabbatical from the Norwegian Institute of Technology (Figure 34). A local harbor pilot, familiar with conditions at Barbers Point, conducted the pilot series on two occasions. The first pilot tests were conducted by Capt. Fred Hoppe for test plan 1a. The second pilot tests were conducted by Capt. Jean-Louis LePendu for test plans 4c and 6c. During these tests, the pilot either gave orders on the engine and rudder settings (as in real life) or verified the actions of Professor Bratteland. The pilots were able to bring their real world experience from Barbers Point and other harbors to validate and further calibrate operating procedures and navigation assessment for the model ship.

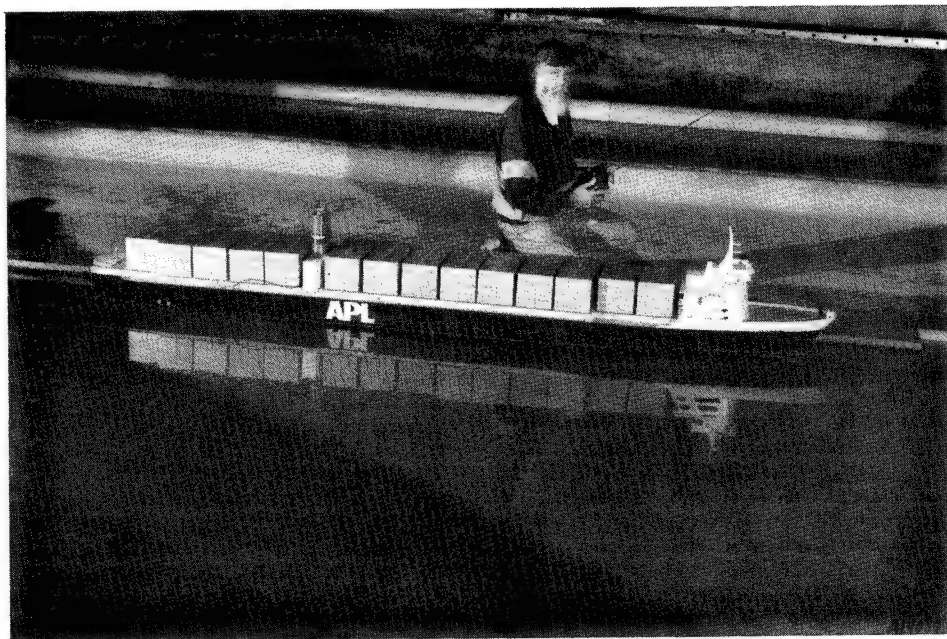


Figure 34. Professor Bratteland and model C9 container ship

Table 18 lists the wave, current, and wind test conditions for the inbound runs for all test plans. The number of individual runs for each test plan are also given. Table 19 lists the test conditions for the outbound runs for test plan 1a. Total inbound and outbound runs were 414 and 75, respectively.

Test plan 1a was the most extensively tested (both inbound and outbound runs with the ship were made). First, the model ship was run in the

Table 18
Inbound Test Conditions

Test No.	Wave Condit.	Current Condit.		Wind Con.	Number of Runs by Test Plan									Tot.
		North	South		1a	1ap	2c	3c	4c	4cp	5c	6c	6cp	
1	1				1	3	3	3	3	5	3	3	0	24
2		2			2	3	3	3	3	0	3	3	0	20
3			2		1	3	3	4	3	5	3	3	8	33
4		2		5	1	0	3	3	3	0	3	3	0	16
5		3			2	6	3	3	3	5	4	3	0	29
6			3		1	4	0	0	0	0	0	0	0	5
7	2				1	0	0	0	0	0	0	0	0	1
8		2			1	0	0	0	0	0	0	0	0	1
9			2		1	0	0	0	0	0	0	0	0	1
10	3				1	0	0	0	0	0	0	0	0	1
11		2			1	0	0	0	0	0	0	0	0	1
12			2		1	0	0	0	0	0	0	0	0	1
13	4				1	0	0	0	0	0	0	0	0	1
14		2			1	0	0	0	0	0	0	0	0	1
15			2		1	0	0	0	0	0	0	0	0	1
16	5				3	3	3	3	3	5	3	4	0	27
17		2			1	3	3	3	3	0	3	3	0	19
18			2		1	3	3	3	3	5	3	3	0	24
19		2		5	1	0	3	3	3	0	3	3	0	16
20		3			0	0	3	3	3	5	3	3	0	20
21	6				1	0	0	0	0	0	0	0	0	1
22		2			1	0	0	0	0	0	0	0	0	1
23			2		1	0	0	0	0	0	0	0	0	1
24	7				1	3	3	3	3	5	3	3	0	24
25		2			2	3	3	3	3	0	3	3	0	20
26			2		1	3	3	3	3	5	3	3	3	27
27		2		5	1	0	3	3	3	0	3	3	0	16
28		3			0	5	3	3	3	5	3	3	0	25
29	8				1	0	0	0	0	0	0	0	0	1
30		2			1	0	0	0	0	0	0	0	0	1
31			2		1	0	0	0	0	0	0	0	0	1
32		2		5	1	0	0	0	0	0	0	0	0	1
33	9	4			0	0	0	0	45	5	0	0	0	50
34			4		0	0	0	0	0	0	0	0	3	3
Total:					35	42	45	46	90	50	46	46	14	414

Note:

1. Suffix "p" is for pilot tests.
2. Wave, current, and wind codes correspond to codes in Tables 9, 12, and 13.

Table 19
Outbound Test Conditions

Test No.	Wave Condit.	Current Condition		Wind Cond.	No. Runs		Total	Comments
		North	South		1a	1p		
1	1				1	3	4	
2		2			2	3	5	
3			2		1	3	4	
4		2		5	1	0	1	No wind
5		3			2	6	8	
6			3		1	4	5	
7	2				1	0	1	
8		2			1	0	1	
9			2		1	0	1	
10	3				1	0	1	
11		2			1	0	1	
12			2		1	0	1	
13	4				1	0	1	
14		2			1	0	1	
15			2		1	0	1	
16	5				3	3	6	
17		2			1	3	4	
18			2		1	3	4	
19		2		5	1	0	1	No wind
20	6				1	0	1	
21		2			1	0	1	
22			2		1	0	1	
23	7				1	3	4	
24		2			2	3	5	
25			2		1	3	4	
26		2		5	1	0	1	No wind
27		3			0	4	4	
28	8				1	0	1	
29		2			1	0	1	
30		2		5	1	0	1	No wind
Total:					34	41	75	
Note:								
1. Suffix "p" is for pilot tests.								
2. Wave, current, and wind codes correspond to codes in Tables 9, 12, and 13.								

waves-only condition for all eight region A (i.e. extreme) wave cases (Table 6) to establish baseline response conditions for the ship. Next, north and south longshore currents from region B (i.e. CN2 and CS2, Table 12) were combined with each of the eight wave cases for inbound and outbound ship runs. Based on these results, only wave cases W1, W5, and W7 (Table 10) were retained. Then, a region B (i.e. Beaufort 5, Table 14) wind was combined with the region B current from the north and four wave cases (wave case W8 was also tested) to evaluate the qualitative effect of winds on the ship. Finally, extreme currents from the north (i.e. CN3) were combined with wave cases W1 and W7. An extreme current from the south (i.e. CS3) was combined with wave case W1 only. Not all of these combinations were run for both staff/pilot operator series.

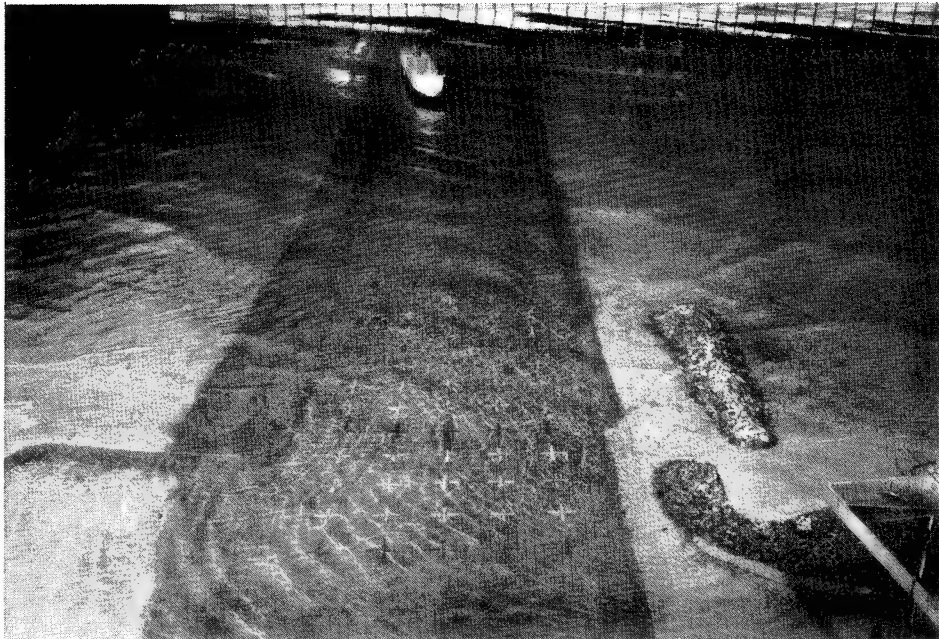
During tests for plan 1a, it was determined that inbound runs were significantly more difficult than outbound runs. Generally, ship speed tended to be somewhat higher for outbound runs, and any problems arising during the transit could easily be corrected by increasing speed and rudder action. This finding was supported by the harbor pilots. Hence, only inbound runs were conducted for subsequent test plans.

For the remaining test plans, only tests with wave cases W1, W5, and W7 were run. The same procedure as before was followed. Wave-only runs were made first, followed by waves and currents from the north (CN2) and waves and currents from the south (CS2). Then, region B winds were combined with CN2 currents and each of the three wave cases. Finally, waves and CN3 north currents were tested with the inbound ship. For test plan 4c, a region B wave case, W9, was tested in combination with a region B current from the north and south (i.e. CN4 and CS4).

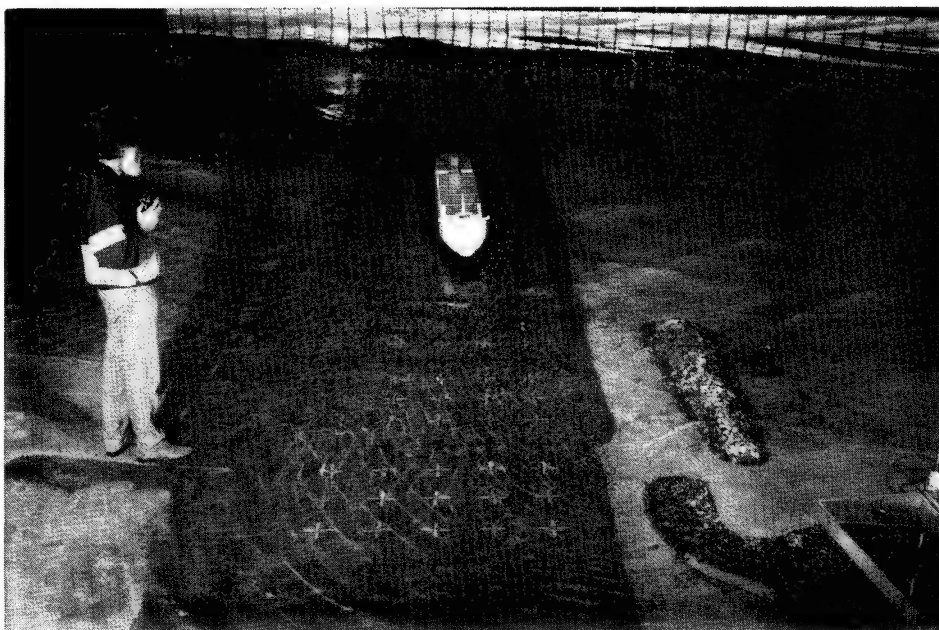
A typical sequence of the ship entering and traversing the channel is shown in Figure 35 for test plan 4c. Although Professor Bratteland is shown piloting the model ship from shore, he usually followed alongside on a catwalk that was parallel to the channel.

Test criteria

Figure 36 illustrates the criteria used to judge the success of a run. The channel width in this figure is the width of the entrance channel at the waterline. The slope of the channel sides was 1 to 1, so it decreased below the waterline to the bottom of the channel. To impose a more conservative evaluation, the ship's curvature below the waterline was not taken into account. An acceptable run occurred if the ship did not get within half a beam width (i.e. $B/2$) of the channel sides. If the clearance between the ship and the bank was less than this amount or the ship touched the bottom or side of the channel, an unacceptable run was recorded. The ship's stern position relative to the side was judged to be less critical as long as it did not touch the bottom or side, since the ship would be pulling away from any possible danger.



a. Ship entering channel



b. Ship approaching jetty

Figure 35. Ship transit through channel

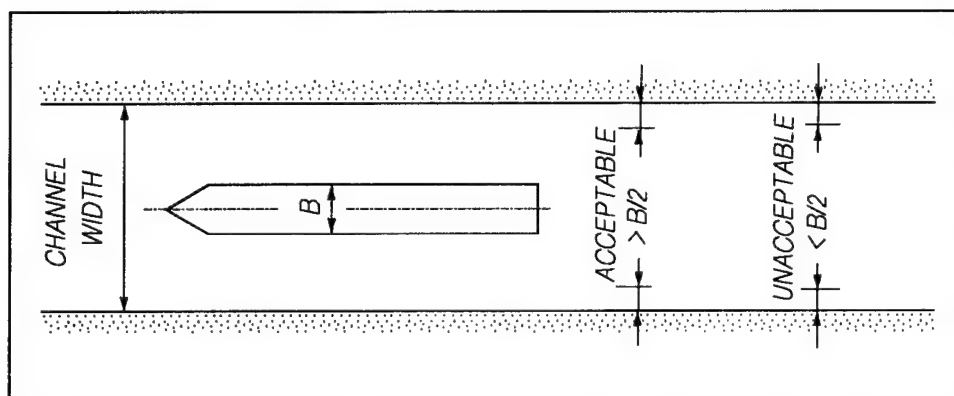


Figure 36. Acceptance criteria

Onsite recorded data. The ship operator recorded the following information based on his observations: (a) ship behavior entering the entrance channel, traversing it, and exiting it; (b) ship trackline through the channel, including possible contact with the bottom or sides; (c) applied engine power and rudder angle, both number of changes and level; (d) average ship speed from the channel entrance to the shoreline; (e) maneuvering and stopping conditions once inside the deep-draft harbor during inbound runs; and (f) overall safety rating. Appendix F summarizes navigation study data and Figure F1, "Barbers Point Navigation Tests," shows a blank form used to record this information.

Video recordings. An overhead, black and white video camera recorded each of the runs for later viewing and evaluation. This was felt to be the most objective evaluation because it was easy to examine runs in more detail and rerun interesting segments for more thorough review.

Test Results

Acceptable cases

Data were recorded on the blank forms (Figure F1) for all inbound runs for each test plan during the staff series. These data were collated and summarized for the six test plans in Tables F1 to F6, respectively. Table F7 is the navigation test summary for the outbound runs for test plan 1a. Region B waves (Table 6) and currents (Table 12) were recorded in test plan 4c (i.e. recommended plan) and are summarized in Table F8. For the pilot series of test plan 4c, recorded data are listed in Table F9.

Next, results were grouped into number and percentage of acceptable and unacceptable runs for each environmental condition for all test plans. Data were further separated into staff/pilot operator series and onsite/video evaluation criteria. Tables F10 to F15 summarize these results for all inbound runs

for each of the six test plans, respectively. Region B tests with the container ship and ore carrier are also shown for test plans 4c and 6c (container ship only). Finally, Table F16 shows these results for the outbound runs for test plan 1a.

Navigation test results for all environmental conditions were summed for each test plan and are shown for inbound and outbound runs in Table 20. Again, they are shown for staff/pilot series and onsite/video evaluation criteria. Wave region A or B is also shown for test plans 4c and 6c. Video rankings from the staff operator series for the inbound runs for each test plan are shown in Figure 37.

Generally, onsite evaluation ratings gave slightly better (i.e. more positive) results than video evaluations. Similarly, staff series rankings were somewhat less critical than pilot series ratings. Part of this variability was due to the subjective nature of the evaluations and part was due to more experience with the model by the staff. In all cases the pilot results confirmed the results from the staff, within reasonable levels of statistical uncertainty. The number and level of engine power and rudder angle changes were considered realistic by the harbor pilots. For test plan 1a, video analysis showed that 42 percent of the runs were unacceptable. The pilot confirmed this low ranking with 64 percent receiving unacceptable ratings. From a purely navigational point of view, test plan 4c gave the best overall results. For region A waves (Table 6), 93 percent of the runs were in the acceptable category. Again, the pilot confirmed this rating with 82 percent receiving acceptable rankings. Both staff/pilot operator series ranked region B waves as nearly 100 percent acceptable. Rankings for test plan 6c were not as good as test plan 4c, but were much improved over test plan 1a for the existing harbor. Staff and pilot operator ratings in the acceptable category were 89 percent and 73 percent, respectively.

The few runs with the ore carrier in region B waves demonstrated no appreciable navigation problems. The more extreme wave conditions representative of region A would probably cause more difficulties. No statistical estimates can be drawn from such a low number of tests, especially since this model was not scaled properly for this study.

Problem areas

Figure 38 shows locations along the channel where the ship experienced problems during inbound and outbound transit. The number of unacceptable occurrences are plotted versus entrance channel station numbers. The channel entrance is defined as station 0, while the start of the harbor basin is approximately 4,100 ft away at station 41. Channel station numbers are given in hundreds of feet.

Figure 38a compares inbound and outbound runs for the existing harbor. Separate groupings are shown for inbound staff/pilot operator series and video

Table 20
Acceptable/Unacceptable Inbound and Outbound Results

Test Plan	Wave Region	Operator	Evaluation	Acceptable		Unacceptable		Total Runs
				No.	%	No.	%	
Inbound Runs								
1a	A	Staff	Onsite	18	51	17	49	35
			Video	19	58	14	42	33
		Pilot	Video	15	36	27	64	42
2c	A	Staff	Onsite	44	98	1	2	45
			Video	38	84	7	16	45
3c	A	Staff	Onsite	43	93	3	7	46
			Video	36	78	10	22	46
4c	A	Staff	Onsite	44	98	1	2	45
			Video	42	93	3	7	45
		Pilot	Onsite	31	69	14	31	45
			Video	37	82	8	18	45
	B	Staff	Onsite	45	100	0	0	45
			Video	43	96	2	4	45
		Pilot	Video	5	100	0	0	5
			5c	A	Staff	Onsite	39	85
Video	39	85				7	15	46
6c	A	Staff	Onsite	45	98	1	2	46
			Video	41	89	5	11	46
		Pilot	Video	8	73	3	27	11
	B	Pilot	Video	3	100	0	0	3
Total:		Staff	Onsite	278	90	30	10	308
			Video	258	84	48	16	306
		Pilot	Onsite	31	69	14	31	45
			Video	68	64	38	36	106
Outbound Runs								
1a	A	Staff	Onsite	30	97	1	3	31
			Video	33	97	1	3	34
		Pilot	Video	28	68	13	32	41

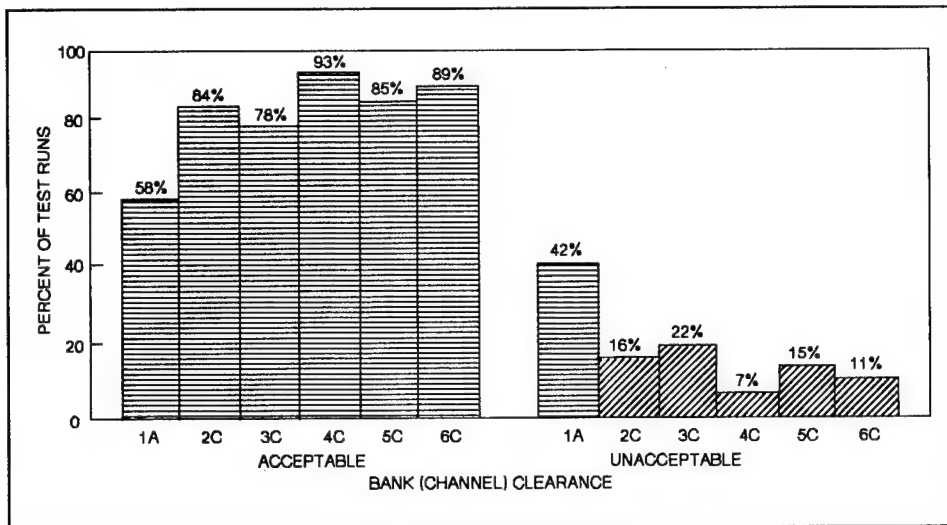


Figure 37. Navigation test results

evaluation of inbound and outbound runs. The outer 1,000 ft typically caused the most problems for inbound runs. These tests clearly demonstrated the importance of achieving a proper vessel approach to the channel entrance. In this respect, the model obviously has boundary restrictions offshore influencing the navigation and maneuvering of the vessel. However, the harbor pilots confirmed that real-life approaches often demand entering the channel in a curved trajectory over a fairly short distance. During the model tests, it was decided that a realistic approach was to line up the ship outside the channel in a reasonable position for entering the channel. If the ship initially entered the channel poorly, the test was aborted and rerun.

Figure 38b compares inbound runs for the proposed modifications for staff/pilot operator series and onsite/video evaluation criteria. Problems with the outer 1,000 ft of the channel were significantly improved by flaring or widening the entrance channel in this region. The other "hot spot" was at station 41, where the channel joins the main harbor. As a result of previous maneuvers, the ship would sometimes tend to shear to starboard with the stern turning too close into the south bank as it crossed into the harbor. Test plan 4c was the only plan that improved this condition.

Ship speed

Ship speed through the entrance channel was calculated based on the average travel time to traverse the full channel from the entrance at station 0 to the shoreline at station 33, a distance of 3,300 ft. Ship speeds were generally higher in the outer part of the entrance channel, decreasing towards shore. Figure F2 shows the corresponding model and prototype times required for different prototype ship speeds. Figure 39 shows average ship speeds during channel transit from the model tests for staff/pilot operators for each test plan. Test plan 4cB corresponds to the generic tests with the region B wave cases

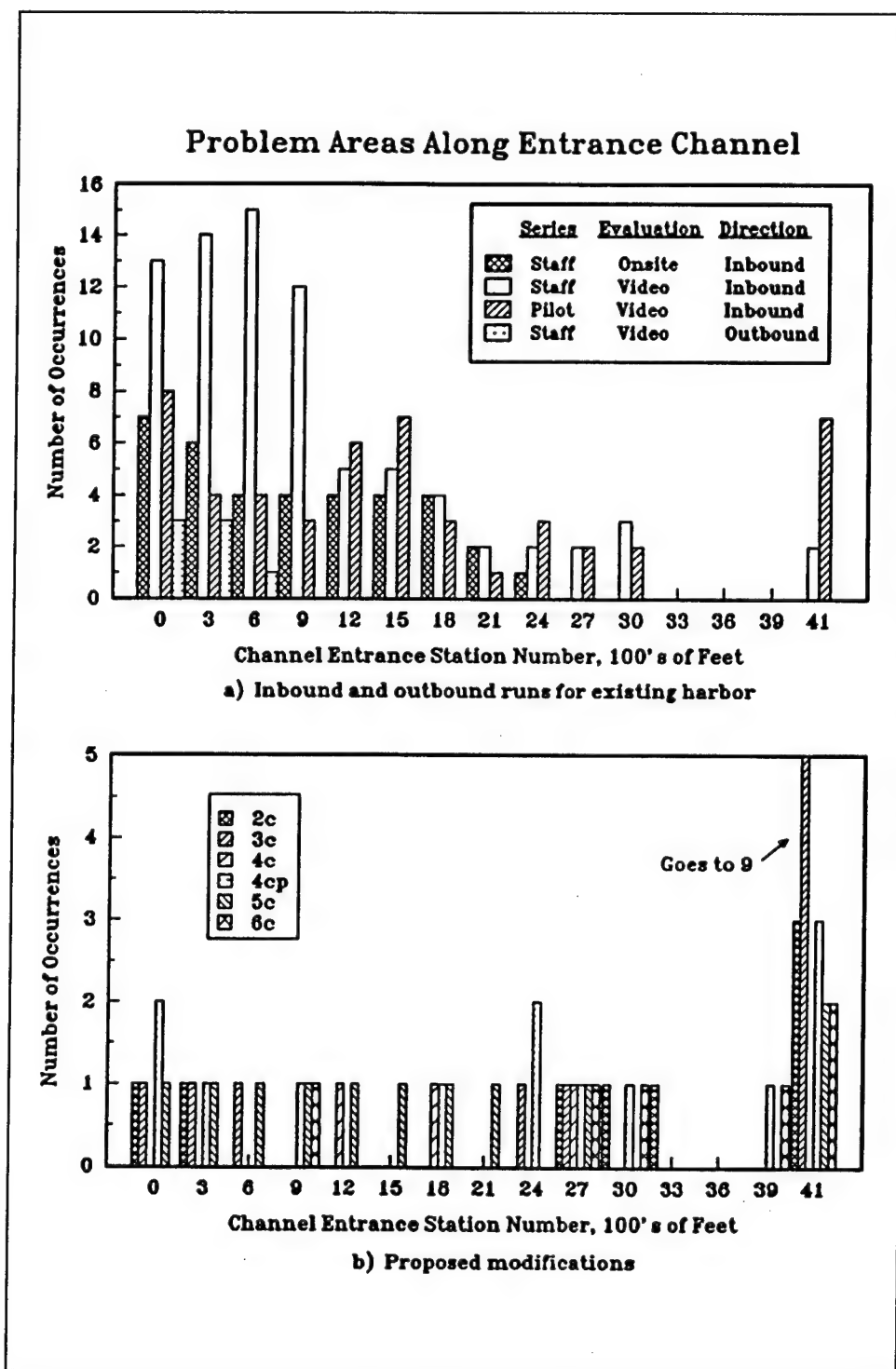


Figure 38. Problem areas along entrance channel

for the recommended plan. Upper and lower speed limits in prototype knots are also shown. The average speed for all staff tests was approximately 5.2 knots, with a range between 3.5 and 7.3 knots. The average speed for the two pilot test series (i.e. 1ap and 6cp) was 6.2 knots, with a range between 3.8 and 9.0 knots. Even though the pilot series speeds were higher than the staff series, all values were considered realistic by the harbor pilots. Outbound runs (for the staff series) were slightly higher than the inbound runs because the

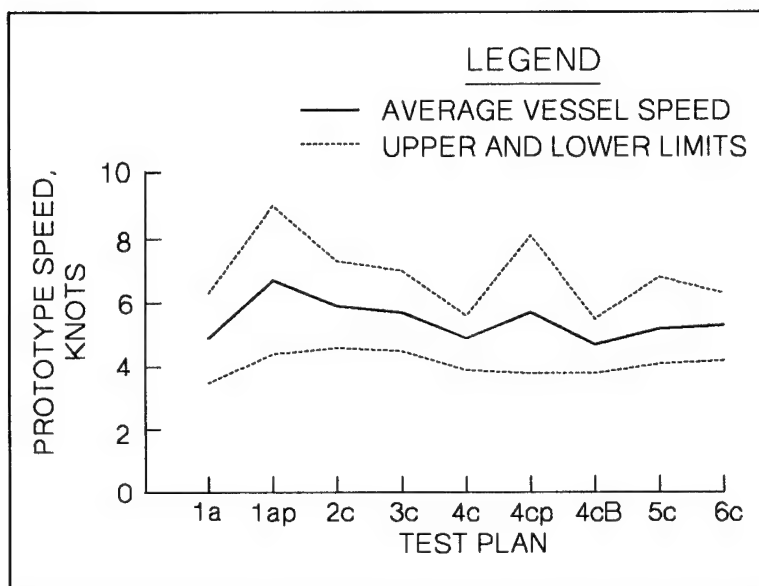


Figure 39. Observed ship speeds

ship did not have to come to a stop at the end of the transit. Average speeds were 5.3 knots, with a range between 3.5 and 6.6 knots. For inbound runs, higher speeds were generally required for more difficult situations or inexperience with the model. Low ship speeds when entering the channel could actually cause problems, depending on the wave conditions. The low ship speeds recorded for test plan 4c are indicative of the ease of transiting the channel.

Nearshore currents

Crosscurrents in the nearshore region between stations 24 and 36 (i.e. 2,400 and 3,600 ft from the channel entrance) have been observed in the prototype. These currents can lead to hazardous conditions as the ship makes the transition from the open ocean to the sheltered part of the entrance channel. One of the benefits of the shore-connected jetty is the reduction of these currents in the inner part of the channel. Float and dye tests were conducted in test plans 4c, 5c, and 6c to evaluate the effect of the jetty on these nearshore currents.

Float measurements were taken 5 min after dye measurements. For current-only cases, the current was run for 10 min before the dye was introduced and 15 min before the floats. For wave and currents, the current was started 5 min before the waves. Dye and floats were then introduced after 10 and 15 min, respectively.

Table 21 shows float measurements over the upper 10 ft of the water column at station 30. Average speed and direction and minimum and maximum speed are listed for five combinations of wave and current for the three test plans. Figure 40 is a schematic of the dye measurements for the three

Table 21						
Float Measurements at Station 30						
Test Case	Jetty	Wave & Current Test Conditions	Prototype Currents			
			Average		Speed, kts	
			Speed kts	Direction deg	Min	Max
6c	None	CN2	0.052	320	One reading	
		W1	0.814	130-140	0.69	0.94
		W1 + CN2	0.675	105-135	0.45	1.14
		W1 + CS2	0.589	135-145	0.45	1.06
		W5 + CN2	0.520	95-145	0.35	1.07
5c	225 ft	CN2	0.052	320	One reading	
		W1	0.658	130-135	0.59	0.71
		W1 + CN2	0.606	105-135	0.49	0.78
		W1 + CS2	0.225	135-165	0.14	0.36
		W5 + CN2	0.346	50-135	0.24	0.50
4c	450 ft	CN2	0.000	No float measurements		
		W1	0.658	125-135	0.50	1.02
		W1 + CN2	0.225	105-145	0.16	0.45
		W1 + CS2	0.191	105-145	0.00	0.52
		W5 + CN2	0.312	85-135	0.23	0.59

jetty configurations at station 30. These values were calculated from video recordings of the dye spread with time. Finally, Table 22 gives a comparison of these dye and float current velocities. The values for "Average - CN2" listed at the bottom of the table are averages for only the cases with waves and waves and currents. Current magnitudes for the CN2 current are not included in this average.

In general, float velocities are higher than dye measurements. Current speed and direction vary over time in the prototype and model. Some of the observed differences can be explained by the fact that the float measurements were begun 5 min later than the dye measurements. Dye measurements generally fall within the maximum and minimum float velocities shown in Table 21.

Differences between test plans 5c (225-ft jetty) and 6c (no jetty) are minimal. The 450-ft jetty in test plan 4c, however, did significantly improve current conditions in this inner part of the entrance channel, especially between station 30 and shore. Thus, from a navigational point of view, the 450-ft jetty will be very beneficial. The jetty will make it possible to start the harbor approach procedures at an earlier point in the channel, 450 to 600 ft further

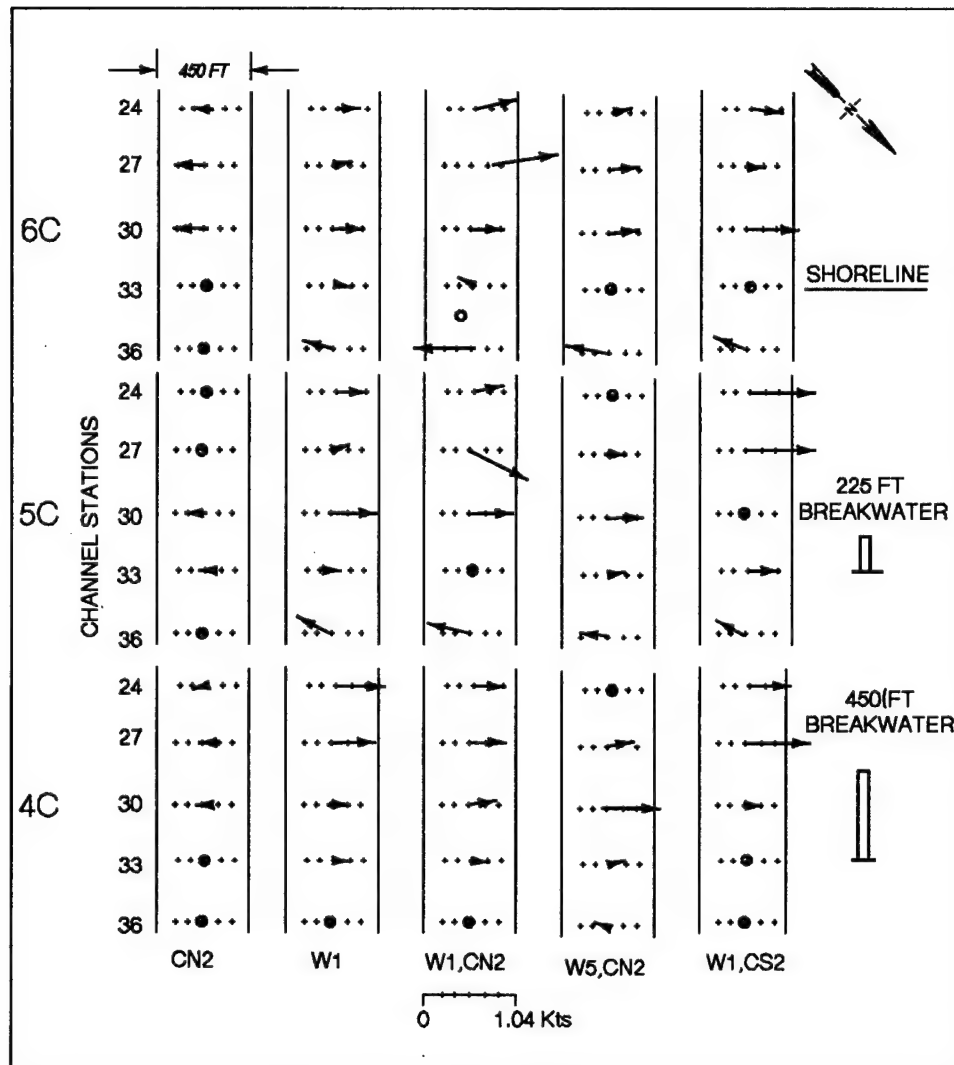


Figure 40. Dye measurements at station 30

seaward. This will permit a somewhat higher ship speed, if necessary, because the effective stopping distance in the harbor has been increased by this amount.

Wind effects

The dominant wind, aligned with the channel, proved to be beneficial, as it provided a constant force for the ship to steer against, which meant the ship's rpm (i.e., control and maneuverability) could be maintained. Cross winds, fluctuating winds, and gustiness were not tested. These conditions could pose a problem for high ship yaw angles and winds from the east.

Table 22
Comparison of Dye and Float Current Velocities

Wave & Current Test Conditions	Plan 6c		Plan 5c		Plan 4c	
	Float kts	Dye kts	Float kts	Dye kts	Float kts	Dye kts
CN2	0.05	0.38	0.05	0.24	0.0	0.0
W1	0.81	0.42	0.66	0.52	0.66	0.26
W1 + CN2	0.68	0.36	0.61	0.50	0.23	0.35
W1 + CS2	0.59	0.55	0.23	0.00	0.19	0.23
W5 + CN2	0.52	0.40	0.35	0.40	0.31	0.59
Average - CN2	0.66	0.43	0.47	0.36	0.35	0.36

Probability Assessment

The previous sections described how different entrance channel configurations were tested for a selected group of environmental conditions. Percentages of unacceptable navigation for this limited data will now be converted into a statistical representation of the expected number of accidents based on frequency of occurrence or recurrence intervals. Criteria for rating the various channel configurations must include a probability assessment of all possible environmental conditions and vessel densities. The probability of unacceptable navigation in a harbor is defined as

$$P(T_i) = P(e_i) * P(s) * P(g_i) \quad (29)$$

where

$P(T_i)$ = probability for unacceptable navigation in environmental domain i

$P(e_i)$ = probability for environmental conditions in domain i to occur

$P(s)$ = probability for ship to be present in the entrance channel for inbound or outbound run

$P(g_i)$ = fraction of unacceptable navigation conditions or groundings in domain i as assessed in physical model tests

This formulation assumes that each of these events is independent, a reasonable assumption for the relatively short Barbers Point entrance channel. From a statistical point of view, the probability of two independent events to occur is the product of their individual probabilities. For two conditions that are completely dependent, the probability of occurrence is the probability of one of the events to occur since they will always occur together.

Environmental domains

Environmental domains are necessary to accurately define the different combinations of waves (Table 6), currents (Table 12), and winds (Table 14) which might be present when the ship is transiting the entrance channel. The first domain (domain A) is composed of extreme or rare environmental conditions that have a low frequency of occurrence. They might be expected to occur 3 to 5 percent of the time, or once a month. The upper boundary to this domain is the limiting condition where ships would not attempt to enter the harbor, such as during a storm or typhoon. The second domain (domain B) is characterized by frequently occurring environmental conditions, which would influence navigation. They are the normal conditions the ship encounters on a weekly basis. The last domain (domain C) is the "no problem" domain, which has a negligible influence on navigation. It has the highest frequency of occurrence.

The value assigned to $P(e_i)$ for each environmental domain was based on an assessment of the relative importance of waves, currents, and winds in each domain. First, each of these environmental conditions was divided into A, B, and C regions of severity, as was done for the overall environmental domain (see Chapter 2). Table 23 lists the probabilities for waves $P(w_i)$, currents $P(c_i)$, and winds $P(wi_i)$ in each region from Chapter 2, where subscript $i = A, B, \text{ or } C$.

In environmental domain A, waves were selected as the dominant navigation consideration. Currents from regions A and B and winds from region B were combined with these extreme waves in the physical model tests. Since current and wind effects were included in these test conditions, these environmental conditions were considered completely dependent and the probability assigned to this environmental domain was equal to the probability for waves $P(w_A)$. In environmental domain B, a combination of waves and currents was judged to be important. Therefore, in the model tests, waves and currents from region B were combined. These two environmental conditions were assigned a level of dependence less than complete dependence. It was no longer necessary for currents to be present whenever waves were present. Waves were still judged to be dominant, but currents acting alone were also assumed to have a significant effect on navigation. A factor of $C = 0.7$ was assumed and used to multiply the probability for waves in region B, $P(w_B) = 0.284$, to reflect this dependent relationship between waves and currents. Thus, the resultant probability for environmental domain B was $P(e_B) = C * P(w_B) = 0.199$. Finally, domain C was assumed to be independent of environmental conditions and a probability for unacceptable navigation due to other factors was assumed.

Table 23
Environmental Regional Probabilities

Region	Wave	Current	Wind
A	.021	.005	.010
B	.284	.177	.065
C	.695	.818	.925

Vessel density

The number of ship calls to a harbor is a random process, independent of environmental conditions, and can be characterized by a Poisson distribution. This distribution can be used to evaluate the probability of having a certain number of arrivals within a specified interval of time (i.e. yearly). Large ports might have a continuous flow of ships in transit, whereas Barbers Point can expect only a limited number of arrivals and departures because of the small number of berths. The assumption of independence is valid as long as the time between ship arrivals is greater than the expected duration of environmental conditions. Seasonal and weather effects have been neglected. The same number of ships are expected to call each year, without any time dependence due to weather delays.

The existing harbor has berthing space for two ships of the size tested in this study. Although the planned harbor expansion will provide four additional berths, a total of only four berths were assumed for the expanded harbor. This was felt to be a reasonable estimate of the harbor's utilization with C9 container ships. If all six berths were used, the probabilities of groundings would increase slightly. The inclusion of smaller vessels using these berths would decrease the probabilities of grounding because these smaller vessels would have more clearance and be easier to maneuver. The scope of this study did not include physical model tests with smaller vessels, so grounding information is not available.

A realistic estimate of normal utilization for the existing harbor is 100 ship calls per year. This assumes 1 ship arrives each week for each berth, based on reasonable loading and unloading times. Full utilization of the existing harbor is 200 ships per year, or 2 ships per week. For the expanded harbor, normal utilization of the harbor would be 200 ships per year. Medium utilization would be 300 ships per year, or 1.5 ships per week. Full utilization would be 400 ships per year, or 2 ships per week. Finally, maximum utilization would be 500 ships per year, equivalent to 2.5 ships per week. These values of vessel density are based on international statistics for ports and harbors.

Table 24 lists the probabilities of a ship being present in the entrance channel for various vessel densities or harbor utilization levels. A one-way transit time of 15 min is assumed for inbound or outbound runs based on an average ship speed of 3 knots. The one-way $P(s)$ listed is equal to the one-way transit time divided by the total time (i.e. 25/8760).

Unacceptable navigation

The probabilities of unacceptable navigation or groundings $P(g_i)$ in domains A and B were calculated from the physical model results. Comparisons were made between recommended plan 4c and existing plan 1a. Percentages of unacceptable navigation for staff/pilot operator series for these two test plans from Table 20 were used to calculate a "best," "average," and "worst" case

scenario. The net $P(g_i)$ for a round trip was the sum of inbound and outbound probabilities. Table 25 summarizes these probabilities for unacceptable navigation to occur. The $P(g_i)$ for the "best" case was the minimum percentage of unacceptable navigation recorded in the model tests for both staff/pilot operator series and onsite/video evaluation criteria. Similarly, the $P(g_i)$ for the "worst" case was the maximum percentage recorded. The intent of these two cases was to bracket the range of observed unacceptable navigation percentages.

The "average" $P(g_i)$ was the average of these two values. For example, for inbound runs for test plan 1a in domain A, the unacceptable percentages observed by the staff/pilot operator series were 49, 42, and 64 percent (Table 20). Therefore, the "best" $P(g_A) = 0.42$, the "worst" $P(g_A) = 0.64$, and the "average" $P(g_A) = 0.53$. The same procedure was followed for the inbound runs in test plan 4c.

Outbound runs were only tested in the existing plan 1a in domain A. Since they were judged to be easy, the same values were used in plan 4c. This is thought to be a conservative assumption because the changes to the entrance channel will probably make outbound runs easier.

In domain B only inbound runs for recommended plan 4c were conducted. The percentages ranged from 0 to 4 percent (Table 20). A conservative value of 1 percent was selected for the "best" inbound case. For the outbound probability for plan 4c, a value equal to the inbound probability was selected based on a comparison between inbound and outbound probabilities in domain A for plan 4c.

No domain B navigation tests were conducted for existing plan 1a. Therefore, inbound and outbound probabilities were estimated from the domain A results. For the inbound runs shown in Table 25, plan 1a probabilities for unacceptable navigation were 2 to 20 times greater than plan 4c probabilities. The domain A "best," "average," and "worst" probabilities were divided by factors of 4, 3, and 2, respectively. For example, the "best" $P(g_B) = P(g_A)/4 = 0.42/4 = 0.11$, "average" $P(g_B) = P(g_A)/3 = 0.53/3 = 0.18$, and "worst" $P(g_B) = P(g_A)/2 = 0.64/2 = 0.32$. The ratio of outbound to inbound probabilities for test plan 1a were the same as in domain A. For example, the outbound "best" $P(g_B) = 0.11 * (0.03/0.42) = 0.01$.

Table 24
Probability of Ship Being Present P(s)

No. of Ship Calls Per Year	Utilization	1-Way Transit Time hours	Total Time hours/year	1-Way P(s)
Existing harbor, 2 berths				
100	Normal	25	8760	0.003
200	Full	50	8760	0.006
Expanded harbor, 4 berths				
100	Low	25	8760	0.003
200	Normal	50	8760	0.006
300	Medium	75	8760	0.009
400	Full	100	8760	0.011
500	Maximum	125	8760	0.014

Table 25
Unacceptable Navigation Fraction

Region	Test Cond.	Ship Run	P(g)	
			Plan 1a	Plan 4c
A	Best	In	0.42	0.02
		Out	0.03	0.03
		Total	0.45	0.05
	Ave	In	0.53	0.17
		Out	0.17	0.17
		Total	0.70	0.34
	Worst	In	0.64	0.31
		Out	0.32	0.32
		Total	0.96	0.63
B	Best	In	0.11	0.01
		Out	0.01	0.01
		Total	0.11	0.02
	Ave	In	0.18	0.02
		Out	0.06	0.02
		Total	0.23	0.04
	Worst	In	0.32	0.04
		Out	0.16	0.04
		Total	0.48	0.08

Total probability

The total probability of unacceptable navigation conditions $P(T)$ is the sum of the individual probabilities for each domain.

$$P(T) = P(T_A) + P(T_B) + P(T_C) \quad (30)$$

where

$P(T_A)$ = probability for unacceptable navigation in domain A

$P(T_B)$ = probability for unacceptable navigation in domain B

$P(T_C)$ = probability for unacceptable navigation in domain C

As mentioned earlier, unacceptable navigation in domain C was due to circumstances other than environmental conditions. Therefore, a value of $P(T_C) = 6.0 \times 10^{-5}$ was assigned to this domain. This value is based on worldwide experience and represents a ship accident six times every 100,000 years or once every 16,667 ship calls.

Recurrence intervals

Table 26 summarizes recurrence intervals for plans 1a and 4c for the different levels of port utilization. The number of calls and years between unacceptable navigation events or accidents are listed for the "best," "average," and "worst" case scenarios. Figure 41 illustrates the number of years between accidents for the two test plans.

A simple spreadsheet program was written to calculate the values listed in Table 26. First, the probabilities for unacceptable navigation from Equation 29 were calculated for inbound and outbound ship runs for each domain using values from Tables 23, 24, and 25. Next, total probability was calculated using Equation 30. Finally, the number of calls and years between unacceptable navigation events were calculated from this total probability.

An example of the "best" case scenario with 100 ships per year for test plan 1a will help clarify this procedure. For domain A inbound ships, the total probability $P(T_A)_{In} = 0.021 \times 0.003 \times 0.42 = 2.5 \times 10^{-5}$. For outbound ships, the total probability $P(T_A)_{Out} = 0.021 \times 0.003 \times 0.03 = 0.2 \times 10^{-5}$. Thus, the domain A total probability $P(T_A) = 2.7 \times 10^{-5}$. Similarly, for domain B

Table 26
Recurrence Intervals for Unacceptable Events

Ships/Year	Test Cond.	Probabilities, x 10**-5				Between Unacceptable Navigation Events	
		P(TA)	P(TB)	P(TC)	P(T)	Calls	Years
Test Plan 1a, Existing Harbor							
100	Best	2.7	6.4	6.0	15.1	6,631	66
	Average	4.2	13.2	6.0	23.4	4,267	43
	Worst	5.8	27.2	6.0	39.0	2,565	26
200	Best	5.4	12.8	6.0	24.2	4,139	21
	Average	8.4	26.5	6.0	40.9	2,447	12
	Worst	11.5	54.5	6.0	72.0	1,389	7
Test Plan 4c, Recommended Plan							
100	Best	0.3	1.1	6.0	7.4	13,451	135
	Average	2.0	2.3	6.0	10.3	9,702	97
	Worst	3.8	4.5	6.0	14.3	6,986	70
200	Best	0.6	2.3	6.0	8.9	11,276	56
	Average	4.1	4.5	6.0	14.6	6,843	34
	Worst	7.6	9.1	6.0	22.6	4,419	22
300	Best	0.9	3.4	6.0	10.3	9,706	32
	Average	6.1	6.8	6.0	18.9	5,285	18
	Worst	11.3	13.6	6.0	30.9	3,232	11
400	Best	1.2	4.5	6.0	11.7	8,520	21
	Average	8.2	9.1	6.0	23.2	4,305	11
	Worst	15.1	18.2	6.0	39.3	2,547	6
500	Best	1.5	5.7	6.0	13.2	7,592	15
	Average	10.2	11.3	6.0	27.5	3,632	7
	Worst	18.9	22.7	6.0	47.6	2,102	4

inbound ships, $P(T_B)_{In} = 0.284 * 0.7 * 0.003 * 0.11 = 6.0 \times 10^{-5}$. For out-bound ships, $P(T_B)_{Out} = 0.284 * 0.7 * 0.003 * 0.01 = 0.4 \times 10^{-5}$. Total domain B probability $P(T_B) = 6.4 \times 10^{-5}$. The domain C total probability $P(T_C) = 6.0 \times 10^{-5}$, a constant for both inbound and outbound ship runs. Total probability $P(T)$ for all three domains is 15.1×10^{-5} . Inverting this probability results in a total of 6,631 ship calls between unacceptable navigation events or accidents. This corresponds to one accident every 66 years for 100 ships calling the port every year.

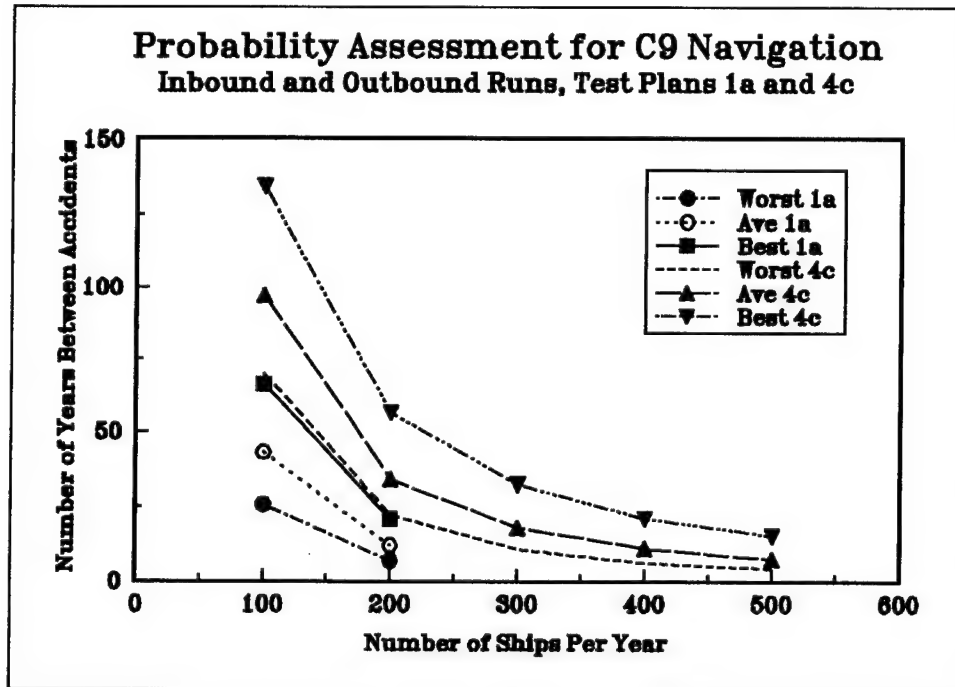


Figure 41. Probability assessment for C9 navigation

Plan Summary

Existing channel width and depth (Plan 1a), although adequate for current ship traffic, would be unacceptable for safe navigation for the larger C9 container ship. Problem areas along the channel are the outer 1,000 ft and inner 450-600 ft adjacent to the shoreline. Linear flaring of the channel from 450 ft at the harbor entrance to 550 ft at the channel entrance (Plan 2c) improved navigation conditions significantly. Navigation conditions for Plan 3c with an increased parallel channel width of 550 ft were comparable to Plan 2c with the flared channel. Deepening the channel and flaring the outer 1,000 ft of the channel from 450 ft to 750 ft (Plans 4c, 5c and 6c) was near optimum as it improved channel entry by allowing the ship to align itself with the channel. The recommended plan is Plan 4c, with the 450-ft-long, shore-connected, rubble-mound jetty on the north side of the entrance channel. It gave the best overall navigation results and the jetty shelters the ship from crosscurrents near the harbor entry, which tend to yaw the ship into the harbor basin.

Videotapes from selected navigation test runs for each test plan were edited and combined in a 35-min "Barbers Point Navigation Study" videotape. Table F17 lists test plan, starting times, test ID, wave and current parameters, overall maneuvering rating, and comments for the 25 cases summarized in this video. Copies of this video can be obtained on request from CERC.

Surge Response of Moored Ship

Surge natural period

For container ships surge, sway, and roll are the most pertinent parameters of concern when moored at a dock or quay. Ranges of allowable movements for container ships have been given by Bruun (1990). If the natural period of the ship corresponds to a harbor resonance mode and the ship is moored in the vicinity of the node, excessive ship motion can prevent loading and unloading of the ship for a number of days. In some cases, extensive damage to the ship and pier can result if the mooring lines fail.

The motion of a ship in surge can be described by the motion of a linear system with a single degree of freedom. Figure 42 is a free body diagram of a ship in surge motion.

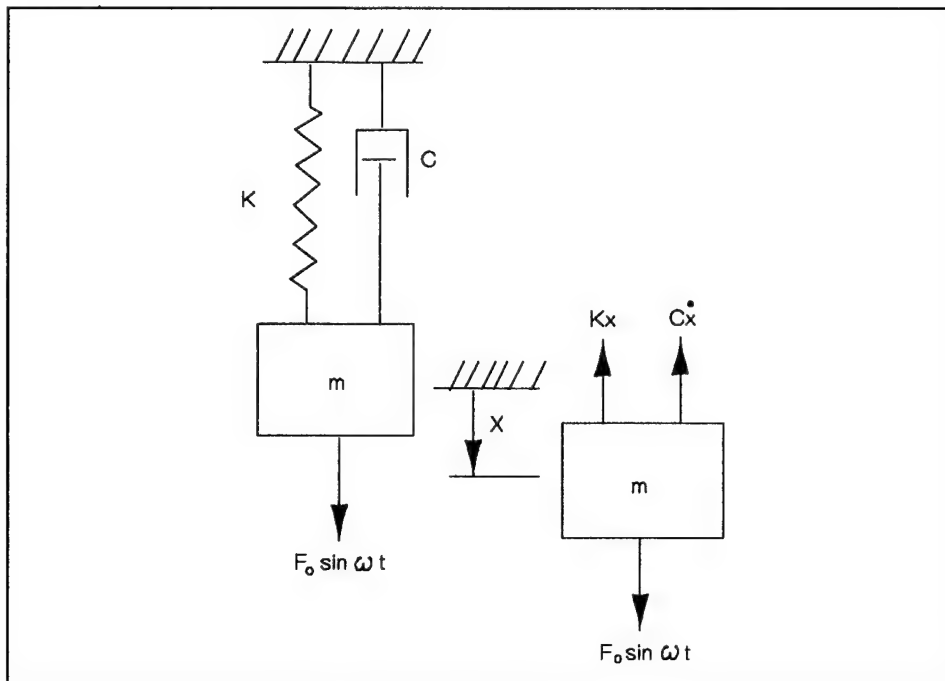


Figure 42. Free body diagram of ship in surge

The following second-order differential equation is obtained from Newton's law

$$m_v x'' + cx' + kx = F_0 \sin \omega t \quad (31)$$

where

m_v = virtual mass of system, lb-sec²/ft

c = damping coefficient

k = stiffness, effective spring constant of mooring lines, lb/ft

x = displacement in surge, ft

x' = velocity in surge, ft/sec

x'' = acceleration in surge, ft/sec²

F_0 = exciting force, lb

ω = radian frequency, rad/sec

Restoring or reaction forces due to the change in position, velocity, and acceleration of the ship from equilibrium are assumed linear and are shown on the left side of the equation. The exciting force on the right side of the equation is due to the drag force of the water flowing past the ship. The motion of the ship in surge is assumed to be independent of other directions of motion. Damping is assumed to be small for the low frequency motions of a ship in surge.

The system's natural frequencies and mode shapes of vibration can be obtained by solving for the free response of the system without damping. Equation 1 reduces to the homogeneous equation

$$m_v x'' + kx = 0 \quad (32)$$

Solving the above equation for the undamped natural period in surge T_s results in

$$T_s = 2 \pi \sqrt{\frac{m_v}{k}} \quad (33)$$

The virtual mass of the ship m_v is the sum of the actual mass or displacement of the ship m and the added mass m_a due to inertial effects of the water entrained with the ship. For a ship in surge, m_a is approximately 15 percent of the actual mass

$$m_v = m + m_a = 1.15m \quad (34)$$

Operational weights for the C9 container ship range from light ship displacement of 19,877 lt to fully loaded displacement of 54,978 lt.

For a taut mooring line in which sag is negligible, longitudinal extension Δl is proportional to the longitudinal force or tension T and the properties of the mooring line. If deflections are small, the effective spring constant k for a mooring line is defined by

$$k = \frac{T}{\Delta l} = \frac{E_c A_c}{l} \quad (35)$$

where

T = axial tension in the mooring line, lb

E_c = equivalent modulus of elasticity, Young's modulus, psi

A_c = cross-sectional area of the mooring line, in²

l = length of the mooring line, ft

This formulation assumes that cable dynamics can be neglected, and that the natural frequency of the mooring line in longitudinal and transverse vibration is much higher than the surge frequency of the ship.

The total mooring line stiffness is the vector sum of the stiffness from all lines in the mooring system. The mooring line system will typically consist of eight lines in a symmetrical pattern, four from the bow and four from the stern of the ship. The first line on both bow and stern is the breast line. It is perpendicular to the ship and dock and is assumed to provide no restoring force in surge. However, it is very beneficial because it presses the ship against the dock and fenders. Two head lines make an angle of 60-70 deg to the breast line and go forward from the bow. Two stern lines are analogous to the head lines, but originate from the stern of the ship. These four lines are assumed to be 100 ft long between ship and dock attachment points. The fourth line on the bow and stern is the spring line. It makes an angle of 85 deg to the breast line and goes toward midships. These two lines can vary in length from 100 to 200 ft. The spring lines, in combination with the breast lines, provide the most efficiency for ship mooring. Since mooring lines have no compressive strength, only one head and spring line provides any restoring force, regardless of the direction of the ship surge. The deck of the C9 is assumed to be 23 ft above the dock at the bow and 15 ft at the stern.

Typical mooring lines used for the C9 are 7-1/2 in. circumference (2.5-in. diam) Karat Estalon fiber ropes and 8-in. circumference (2-5/8-in.-diam)

dacron ropes.¹ Karat lines are manufactured by Columbian Rope Company, Guntown, MS, under license from Akzo, Holland. Estalon is a fiber which is a copolymer of polyester and polypropylene. Karat ropes are used for the head and spring lines; dacron is used for the breast lines. Minimum and average breaking strengths for Karat ropes are 118,260 lb and 131,400 lb, respectively.² Elongation at 20 percent of ultimate strength for new, unused rope is 6 to 8 percent. At a loading of 75 percent, elongation is 15 percent. These elongation values would decrease for previously elongated ropes (i.e. used) which have been pulled to 50 percent of minimum breaking force. Used ropes would provide a stiffer mooring, giving a slightly smaller surge natural period.

Therefore, the natural period of a moored ship in surge is a function of displacement, and number, type, length, size, and tension of the mooring lines. Table 27 and Figure 43 give natural periods of a ship in surge for different mooring configurations. Values are given for constant mooring line tensions from 15 to 25 tons for ship displacements from light operational to fully loaded conditions. The average strength at breaking of this mooring line material is assumed to be approximately 50 percent that of nylon, which has the largest strength of synthetic fiber ropes. Strength depends on the material, size, and construction of the rope. The equivalent modulus of elasticity for nylon is 100,000 psi. Thus, the assumed value for $E_c = 60,000$ psi. The load in percent is the ratio of tension to the minimum breaking strength. The elongation in percent is proportional to this load.

Thus, natural period can vary depending on the ship's displacement and the mooring line tension. Adjustments in the tension can be made to accommodate changing wind and wave conditions during berthing at Barbers Point.

Dynamic response

The dynamic response of a moored ship in surge can be estimated if it is assumed that it follows a Rayleigh probability density function. Statistical expectations of means and maxima can be computed if the mean square value of response in surge is measured or computed using probabilistic theory. The ship's response in surge to a random seaway is assumed to be linear.

The procedure is illustrated in Figure 44 for an arbitrary ship. First, a representative sea spectrum $S_w(\omega)$ is selected. Next, a response amplitude operator or transfer function $H_s(\omega)$ is calculated from the equations of motion for the ship in surge. It is the ratio of the Fourier transform of surge motion to the Fourier transform of the force profile and is defined by

¹ Facsimile, 19 February 1993, R. Stanley, "C9 class containerships, mooring arrangements and lines," American President Lines, Ltd., Oakland, CA.

² Facsimile, 22 February 1993, J. E. Richardson, Jr., "Technical data karat (Estalon)," Columbian Rope Company, Rohnert Park, CA.

Table 27 Surge Natural Period of Moored C9 Container Ship												
Weight lt	Virtual Mass lb-sec^2/ft	Tension tons	Load %	Elong %	Head/Stern Line			Spring Line			k net lb/ft	Ts sec
					No.	l ft	k head lb/ft	No.	l ft	k spr lb/ft		
19,877	1,590,160	15	25.4	8.8	2	100	6,294	1	150	2,253	8,547	86
		20	33.8	10.7			6,902			2,470	9,373	82
		25	42.3	12.0			7,693			2,753	10,447	78
38,000	3,040,000	15	25.4	8.8			6,294			2,253	8,547	118
		20	33.8	10.7			6,902			2,470	9,373	113
		25	42.3	12.0			7,693			2,753	10,447	107
54,978	4,398,240	15	25.4	8.8			6,294			2,253	8,547	143
		20	33.8	10.7			6,902			2,470	9,373	136
		25	42.3	12.0			7,693			2,753	10,447	129

Notes:

1. Minimum breaking strength, lb = 118260.
2. Head/stern line vertical angle, deg = 11.
3. Spring line vertical angle, deg = 6.

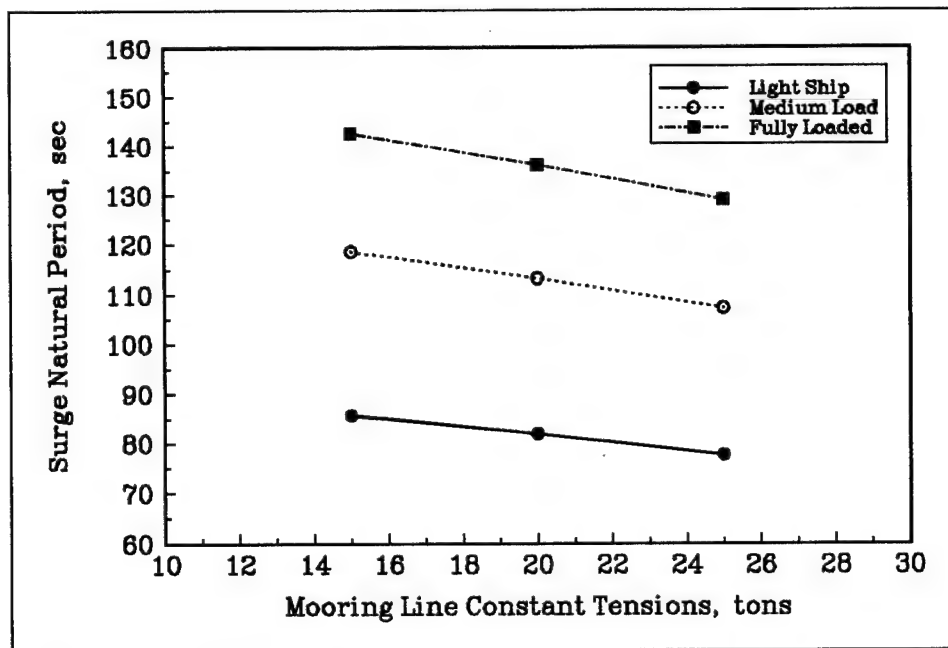


Figure 43. Surge natural period of C9 container ship

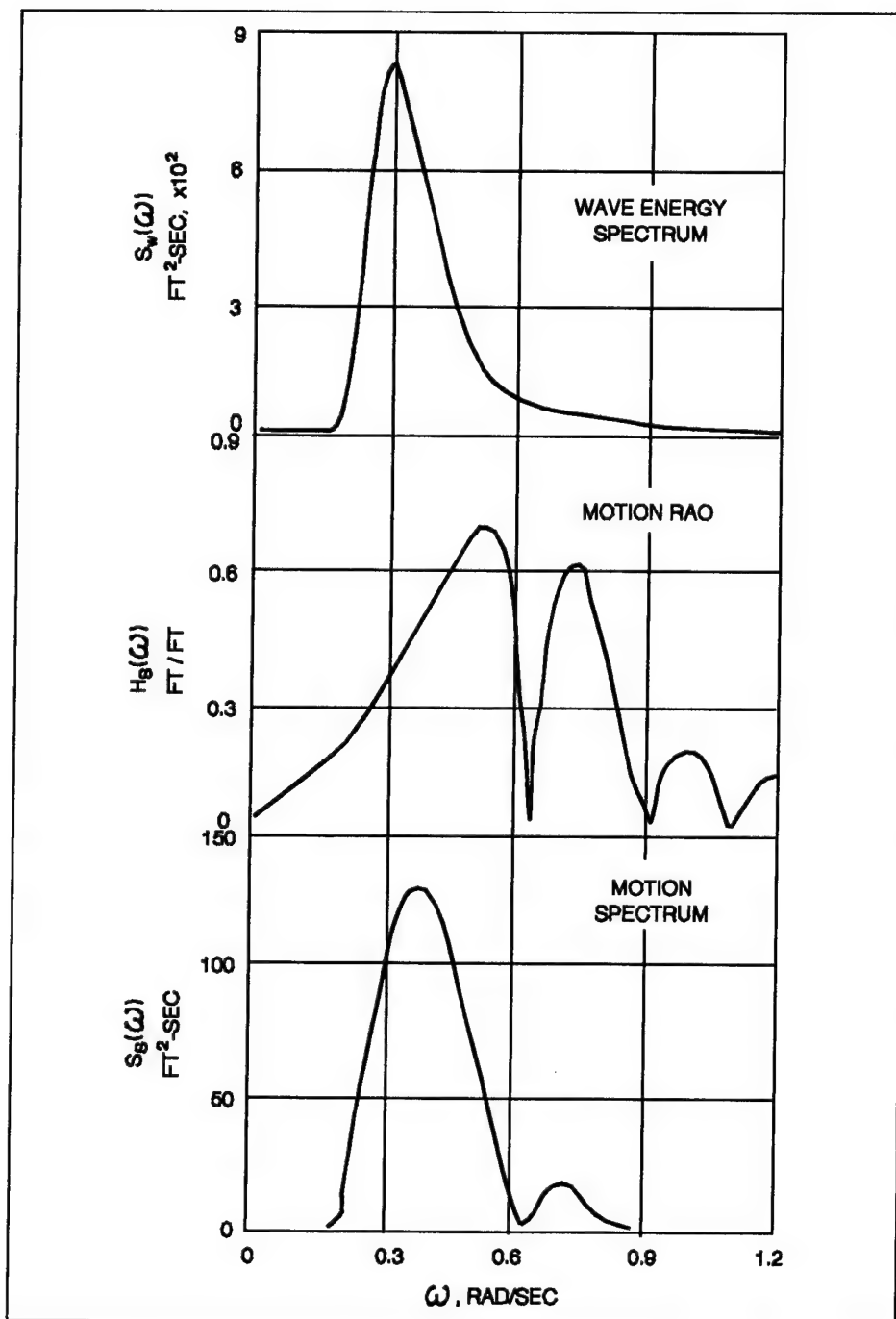


Figure 44. Surge response of a ship

$$H_s(\omega) = \frac{\frac{x''}{H/2}}{\sqrt{(\omega_n^2 - \omega^2)^2 + (2\xi\omega_n\omega)^2}} \quad (36)$$

where

$H_s(\omega)$ = response amplitude operator in surge, ft/ft

x'' = average acceleration of the displaced fluid, ft/sec

H = wave height, ft

ω_n = natural frequency, rad/sec

ω = radian frequency, rad/sec

ξ = damping factor, ratio of damping C to critical damping C_c

For a ship in surge the damping is assumed to be small and can be approximated by $\xi = 0.1$. Average acceleration of the displaced fluid x'' can be calculated from linear wave theory and is given by

$$x'' = \frac{Hg}{2D} \frac{\sinh \kappa d - \sinh \kappa s}{\cosh \kappa d} \frac{\sin \kappa l}{\kappa l} \quad (37)$$

where

d = water depth, ft

s = distance between bottom and keel of ship, ft

l = length of ship, ft

The response spectrum of the ship in surge $S_s(\omega)$ is then defined by

$$S_s(\omega) = [H_s(\omega)]^2 \cdot S_w(\omega) \quad (38)$$

and has units of $\text{ft}^2\text{-sec/rad}$. The mean square value or zeroth moment of the surge response m_{0s} is obtained by integrating $S_s(\omega)$ over all frequencies

$$m_{0s} = \int_0^{\infty} S_s(\omega) d\omega \quad (39)$$

Since this is the area under the surge response spectrum, the significant surge $s_{1/3}$ can be calculated as

$$s_{1/3} = 4 \sqrt{m_{0s}} \quad (40)$$

Appropriate Rayleigh coefficients can be used to estimate other statistical surge distances.

This procedure can be used to predict the dynamic response of the C9 container ship and other moored ships in surge using stochastic methods. Significant surge (like a significant wave height) can be estimated from the response amplitude operator for the ship and representative sea states. Thus, for a particular sea state, the ship's dynamic response in surge could be estimated, much like a "cause and effect" relationship.

5 Harbor Response

The wave climate found in a harbor can be divided into short- and long-period waves. For simplicity, waves shorter than 25 sec ($f = 0.04$ Hz) will be classified as short-period or wind waves. These higher frequency waves affect the mooring and operation of small boats. As waves travel into harbors from deep water, nonlinear processes transfer energy from the wind wave frequencies to long waves with periods on the order of several minutes and wavelengths much longer than the wind waves. Other sources of these long-period waves are tsunamis, meteorological disturbances, and internal waves (Okhihiro 1993). If the periods of these long waves correspond with natural (resonant) periods of the harbor, strong harbor oscillations can be induced, which can produce dangerous mooring conditions, structural damage, and sediment deposition or erosion within the harbor.

Wind-Wave Response

Test plan comparison

Procedure. A number of different analytical techniques exist for comparing the changes in wave climate inside the harbor for different plans. One method involves comparing the wave height inside the harbor for the existing plan with the wave height of the alternative plans. A good wave height parameter to use for spectral seas is the H_{m0} value, defined as four times the square root of the zeroth moment m_0 . The zeroth moment is the variance of the wave elevation defined as

$$\sigma^2 = m_0 = \int_{f_l}^{f_u} S(f) df \quad (41)$$

Thus, wave height is calculated by summing the energy under the spectral curve within the lower and upper cutoff frequencies. Values of $f_l = 0.04$ Hz and $f_u =$ three times the peak frequency value were selected.

H_{m0} values were calculated for each of the eight wave conditions for each test plan. Wave height values at each gauge location were then normalized by the corresponding test plan 1a wave height except for the two expansion gauges. Since no expansion gauges were present for the existing test plan 1a, expansion gauges from test plan 1c were used to normalize these gauges in the other test plans. Normalized H_{m0} values for the eight wave conditions were then averaged for each test plan. Thus, a variety of wave conditions are represented in these normalized H_{m0} wave heights because the eight wave conditions included a variety of wave periods and directions.

By comparing the ratio of the H_{m0} values for the alternative plans versus the H_{m0} values for the existing plan at a particular location, the change in wave energy is apparent. If

$$\frac{H_{m0}(\text{alternative plans})}{H_{m0}(\text{existing plan})} > 1, \quad (42)$$

then there is more energy in the harbor for the alternative plan at that location. Normalized H_{m0} values greater than one indicate an increase in wind-wave energy relative to the existing harbor. Likewise, values less than one indicate a decrease in wind-wave energy. One would like to see values less than or equal to one for all gauge locations.

Existing depth plans. Normalized H_{m0} values for each location for the four plans with the existing water depth are shown in Figure 45. There are only three curves for the two expansion gauges (Ex2 and Ex3) because test plan 1c was normalized by itself. The effect of expanding the harbor (test plan 1c) was minimal. The only significant changes occurred for the two east corner (E2 and E1) and south corner (Sc) locations. For E1 and E2, the decrease in wave height is probably attributable to the change in distance from the reflecting sidewalls. The Sc gauge shows that there may be some trapping of the wave energy in the expanded area. Flaring the channel in test plan 2c increased wave heights up to 10 percent for those locations near the harbor entrance. For test plan 2c the effect of the expansion is again evident in interior harbor gauges E1, E2, and Sc, although not as great because the flare lets more energy into the harbor. Widening the channel to 550 ft in test plans 3a and 3c, while simplifying navigation into the harbor, increased wave heights up to 40 percent at some locations. Gauges located in the channel (C6), north corner (Nc), harbor ferry (Hf), and barge basin (Bn and Bs) show a 25-percent increase in wave height. Wind-wave energy inside the marina has increased 10 to 20 percent. The effect of the expansion in test plan 3c is evident in gauges E1, E2, and Sc, where there is the usual decrease in wave height.

Deeper depth plans. Figure 46 shows normalized H_{m0} values for the gauges in the three plans, with the 7-ft increase in the channel and harbor depth. Test plans 4c, 5c, and 6c gave the best results, with reductions in wind-wave energy up to 70 percent and an overall decrease in wave height of

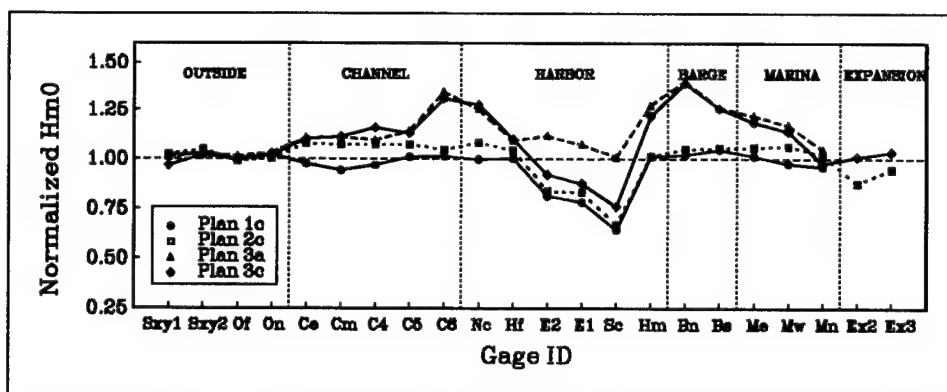


Figure 45. Normalized wind-wave heights for the existing depth plans

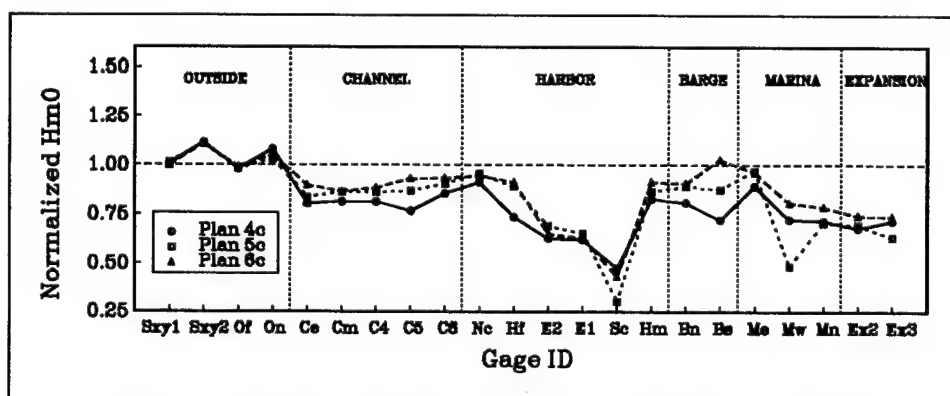


Figure 46. Normalized wind-wave heights for the deeper depth plans

approximately 15 percent in the barge basin. There were only small changes between the three plans because of changes in the jetty length.

The increase in water depth and the flare in the outer 1,000 ft of the channel appear to have refracted energy away from the harbor. Waves in the deeper channel travel faster than the adjoining waves on either side of the channel. Unless the wave direction is aligned with the channel, wave energy tends to be transported out of the channel. The effect of the added flare is to get the wave energy into the channel sooner and effectively out of the channel faster. The primary purpose of the jetty was to act as a barrier to the cross-currents near the channel entrance because they are a hindrance to harbor navigation. An added benefit of the jetty is a reduction in wind-wave energy inside the harbor. In general, wave heights decreased as jetty length increased. Thus, test plan 4c appears to be the best alternative plan because it reduces the wind-wave energy in the harbor more than the other plans.

Predicting wind-wave response

Based on the eight wave cases used in this study, the harbor master could predict what type of wind-wave conditions to expect at different locations in the harbor for various incident waves. The eight wave cases represented a range of frequency spectral shapes, wave direction, and directional spreading (see Chapter 2). Cases BPS231 (wave case W3) and BPS241 (wave case W4) had unimodal (i.e. one mode or peak) frequency spectra. The other six wave cases had bimodal (i.e. two modes) frequency spectra. Wind-wave energy in cases BPS221 (W2) and BPS151 (W5) was almost equally split between swell (wave period greater than 10 sec) and sea components. Six wave cases were predominately composed of swell energy: BPS211 (W1), BPS241 (W4), BPS151 (W5), BPS161 (W6), BPS171 (W7), and BPS181 (W8). The overall mean wave direction for wave case BPS211 was from the west. Wave cases BPS241 and BPS151 were from the southwest, and the rest were parallel to the entrance channel. Although none of the eight wave cases were truly unidirectional, they all had relatively narrow directional spread except for wave cases BPS221 and BPS231.

Figure 47 shows the wind-wave response of the existing harbor (i.e. test plan 1a) for each of the eight wave cases. The format of these graphs is similar to Figures 45 and 46, except that measured wave heights are normalized by the wave height at the second S_{xy} location (S_{xy2}). The eight wave cases are grouped according to whether they were measured in the prototype at the first or second S_{xy} location. The two expansion gauges (Ex2 and Ex3) are set to zero because they were not present for the existing plan. Figures 48, 49, and 50 show the corresponding wind-wave response for test plans 1c, 4c, and 6c, respectively. Plots for the remaining test plans are contained in Appendix G (Figures G1 to G4).

These figures illustrate the variability in wind-wave energy inside the harbor as a function of wave condition. Generally, wave heights are larger in the entrance channel and barge basin than in the harbor, marina, and expansion for all wave conditions. The largest harbor response is for wave case BPS211. This wave was composed of swell energy from the west with relatively narrow directional spreading. The response of the channel and barge basin to wave case BPS221, although generally less than BPS211, is appreciable. In test plans 4c and 6c, the channel responds more to this wave than to BPS211. This wave was composed of nearly equal amounts of sea and swell energy with broader directional spreading coming parallel to the channel. In the marina, wave case BPS211 is still the largest, but BPS161 also pumps in a significant amount of wind-wave energy, especially for the existing harbor. Wave case BPS161 is similar to BPS211 except that its wave direction is parallel to the entrance channel.

Based on this limited data set, the harbor master can expect the largest wind waves in the harbor when waves are coming from the west. Addition of the 450-ft-long jetty should help reduce this wind-wave energy in the harbor.

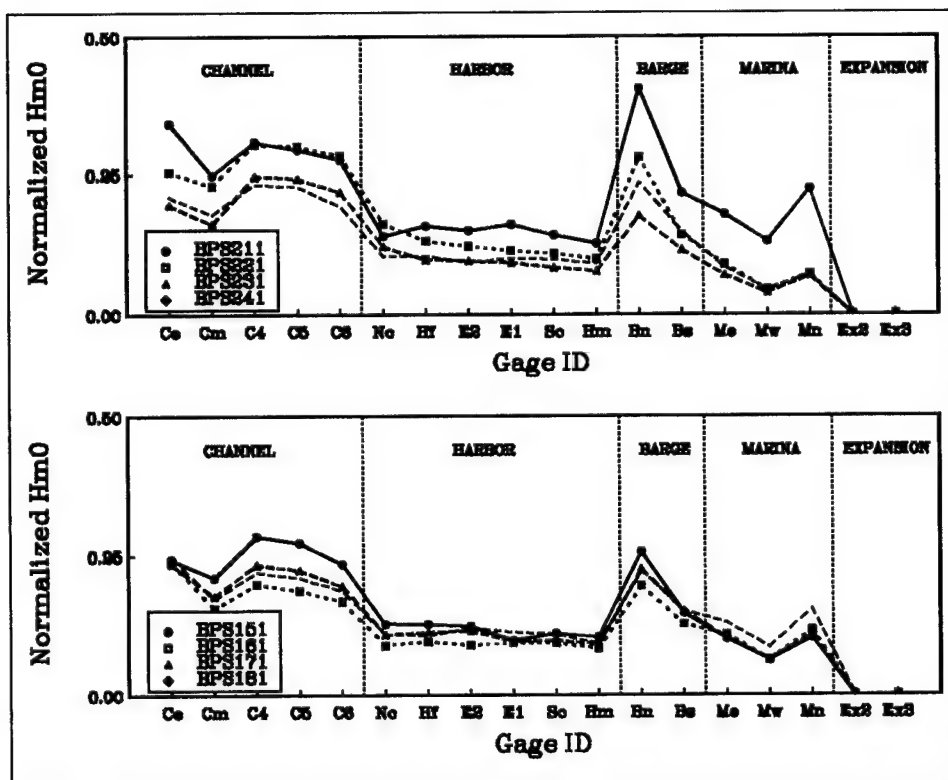


Figure 47. Measured wind-wave heights for test plan 1a

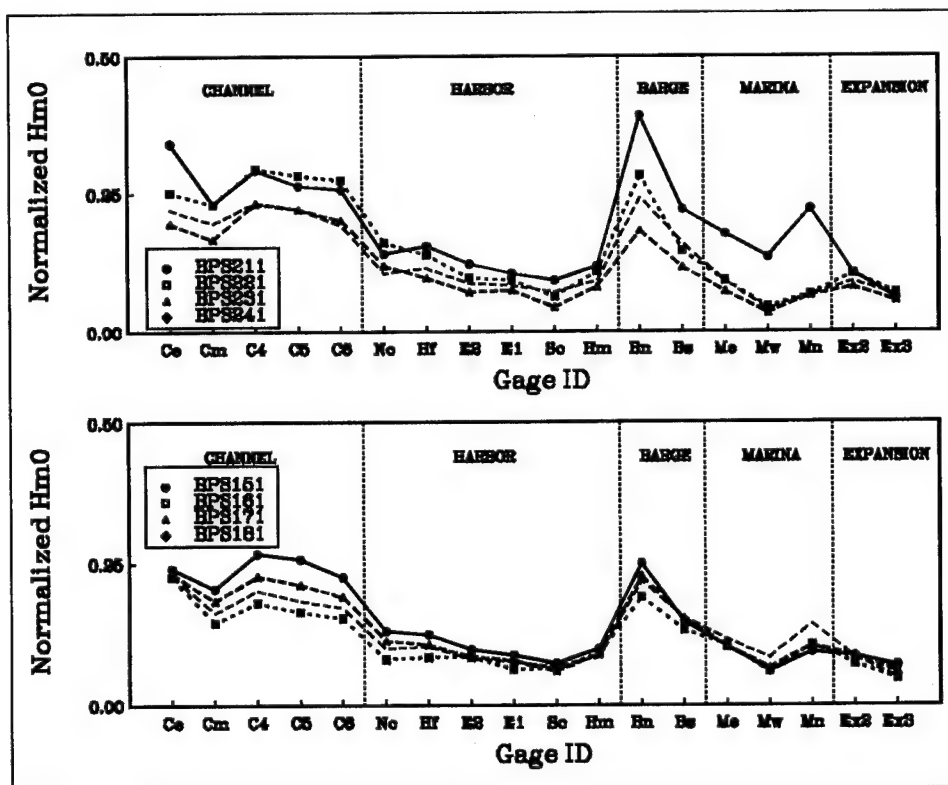


Figure 48. Measured wind-wave heights for test plan 1c

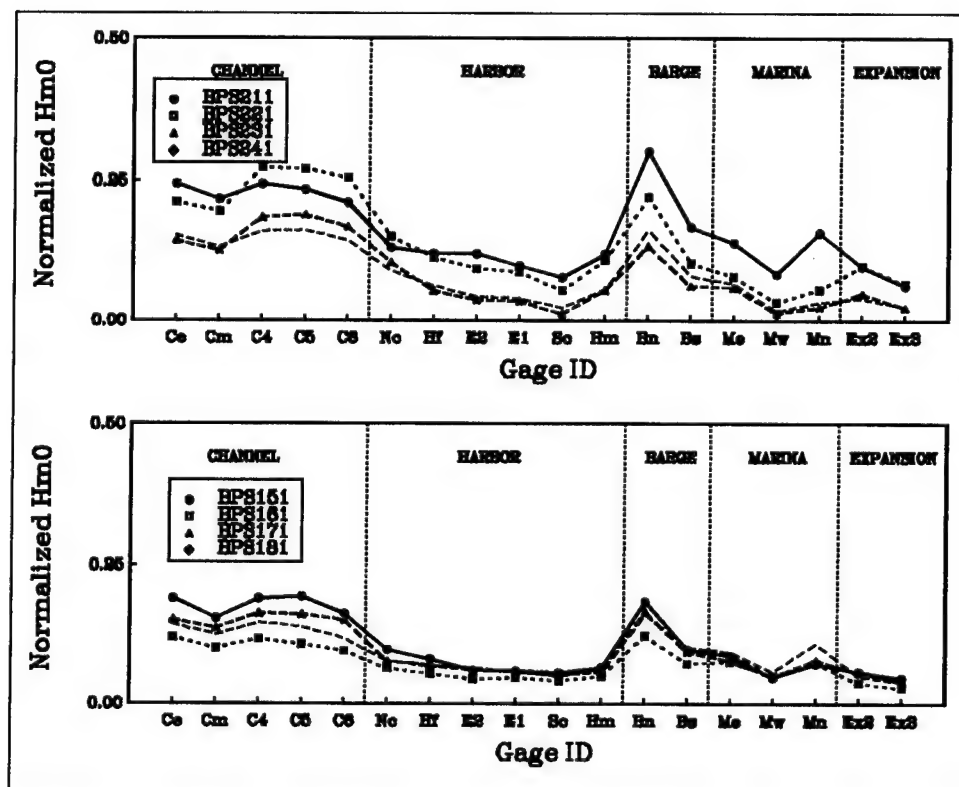


Figure 49. Measured wind-wave heights for test plan 4c

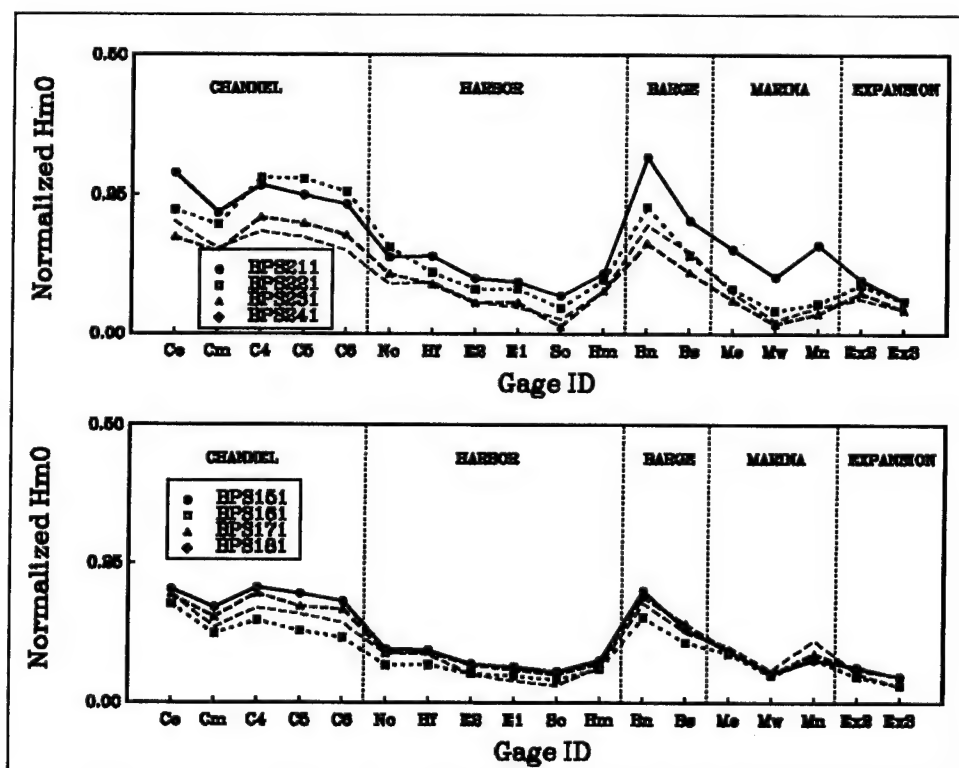


Figure 50. Measured wind-wave heights for test plan 6c

In addition to these eight wave cases, 36 empirical wave cases were tested in the physical model as part of an expanded research effort. These wave cases covered a range of directional spectral parameters: half were unidirectional and half had directional spreading. All were unimodal with narrow and broad frequency spreading representative of sea and swell conditions. These data should complement the eight wave cases and provide further insight into the wind-wave response of the harbor.

Long-Wave Response

Harbor resonance

Harbor resonance (also known as seiche, surge, or resonant oscillations) is the phenomenon that occurs when the amplitude of oscillation inside a harbor increases as it is stimulated at its resonant frequencies. Examples of resonance in everyday life are a child "pumping" his legs in time with the oscillations of a swing, causing it to go higher or an opera singer shattering a crystal glass because the sound matches the glass's resonant frequency.

Okihiro, Guza, and Seymour (1992) postulate that both bound and free infragravity waves are the forcing function for harbor resonance at Barbers Point Harbor. Infragravity waves are long-period waves in the range of 25 to 200 sec on the Pacific coast. Infragravity wave heights are much smaller than wind-wave heights, typically only 10 percent. Bound infragravity waves are nonlinearly forced by and coupled to wave groups. Bound long waves appear to be the controlling mechanism when swell energy outside the harbor is large (Bowers 1977, Mei and Agnon 1989, Wu and Liu 1990). For this condition, it may be possible to predict harbor resonance given wind-wave spectrum outside the harbor. Okihiro, Guza, and Seymour (1992) found that directional spreading in the wind-wave spectrum affects the amount of bound wave energy present in the infragravity band. In deep water, a broad directionally spread wind-wave spectrum can force more bound wave energy than a unidirectional spectrum. In shallow water, however, the opposite effect is observed. More bound energy is present in a unidirectional spectrum than a directionally spread spectrum. Okihiro, Guza, and Seymour also found that wind-wave energy present at swell frequencies produces more bound wave energy than the equivalent amount of energy in sea frequencies.

Recent research (Okihiro, Guza, and Seymour 1992; Elgar et al. 1992; Herbers et al. 1992; Bowers 1993) indicates that free long waves, in the form of leaky or edge waves, are important and may contribute the bulk of infragravity energy in depths corresponding to the S_{xy} location. Leaky waves are generated in shallow water and reflected or radiated seaward to the open ocean. Edge waves are generated and radiated seaward like leaky waves but become trapped on the continental shelf due to reflection and refraction, and propagate in the longshore direction. Bound waves may even be a source of free infragravity waves in shallow water. The discontinuity of the bound infragravity waves across the harbor mouth may nonlinearly generate free

infragravity waves. These free waves would then have comparable energy to bound long waves from outside the harbor.

Outside Barbers Point Harbor, Okihiro and Seymour (1992) found a near-shore coupling between infragravity and wind-wave energy, with a larger infragravity wave height for swell conditions than for higher frequency sea waves. Inside the harbor, they found that infragravity wave heights were highly correlated with infragravity wave heights measured outside the harbor. Furthermore, infragravity wave heights increased as swell energy increased outside the harbor.

A harbor has certain resonant frequencies or periods at which it oscillates in a standing wave pattern. These resonant frequencies are a function of harbor size, shape, and water depth. Historically, these resonant frequencies have been referred to as eigenfrequencies, from the German word "eigen" meaning "characteristic." For Barbers Point Harbor, these resonant periods are 1 min and longer.

The shape of the vibration is called the eigenfunction or mode shape. Each eigenfrequency has a corresponding eigenfunction. Harbors have more than one eigenfrequency and eigenfunction. One characteristic mode might be established along the longitudinal dimension of the harbor, another along the transverse or width dimension, while another might be established along the diagonal dimension. The set of eigenfrequencies and eigenfunctions is usually called eigenmodes, or normal modes of oscillation of a harbor. The eigenfunction of the lowest eigenfrequency or fundamental frequency describes half a wave across a dimension of the harbor. Doubling the fundamental frequency produces the second harmonic. This is the eigenfrequency that describes a full wave between ends of the harbor. The third harmonic occurs when the harbor vibrates so that it completes a wave and a half between the ends. Its frequency corresponds to three times the fundamental frequency. In general, harbor resonance can occur whenever a harbor dimension (i.e., length across the harbor or diagonal) equals a multiple of half a wavelength of a resonant frequency.

Another characteristic of resonant modes is the increase in nodes and antinodes within the harbor as the resonant period decreases (i.e. resonant frequency increases). For example, Figure 51 illustrates the fundamental, second, and third mode shapes for a harbor with a closed basin. These wave profiles are typical of standing wave patterns due to perfect reflection from a vertical wall. Although not exact for Barbers Point, they give a qualitative idea of what the different mode shapes are like. The first mode has one node in the center of the basin and one antinode at each wall. The length of the basin in this direction corresponds to half a wavelength. The water surface appears to pivot about the nodal point in the middle of the basin. Displacements at the two antinodes are 180 deg out-of-phase with each other at any instant in time; a positive water level on one side of the nodal point is matched by an equivalent negative water level on the other side of the nodal point. The water surface at the antinodes goes from its highest to lowest values over half a wave

period. There is no flow through the wall, so the horizontal velocity is zero at the antinode locations. Horizontal flow is greatest at the nodal point, a fact that influences surge and sway motions of moored ships.

The second mode has two nodes and three antinodes. The nodes are evenly spaced in the basin and the additional antinode is located in the center of the basin. Water surface displacement is in phase for the two antinodes at the walls and 180 deg out of phase for the center antinode. The two nodal points again pose the greatest problem for ship surge and sway motions.

Similarly, the third mode is one-and-a-half wavelengths long and has three nodes and four antinodes. Higher modes follow the same pattern of increasing wavelengths, and nodal and antinodal points across the harbor.

Analysis methods

Prototype and physical model. Transfer function estimates were used to identify resonant modes and the relationship between incident conditions outside the harbor (the input) to conditions inside the harbor (the output) for the prototype and physical model. Input was data from the S_{xy2} gauge and output was from the four corner locations in the harbor where gauges were placed. The transfer function is defined as

$$|\hat{H}(f)| = \frac{|\hat{G}_{xy}(f)|}{\hat{G}_{xx}(f)} \quad (43)$$

where $\hat{G}_{xy}(f)$ is the cross-spectral estimate between input x and output y channels and $\hat{G}_{xx}(f)$ is the auto-spectral estimate for the input x channel. The auto-spectral estimate is just the frequency spectrum for the S_{xy2} gauge for each wave case. Cross-spectral estimates are similar to autospectral estimates except that both input S_{xy2} and output harbor gauges are used in the calculation. For the transfer function for the south gauge (Sc), the cross-spectral estimate contains information from both the S_{xy2} and Sc gauges for each wave case.

The relationship of the transfer function estimate to unity is important. If the transfer function value is less than one at a particular wave period or

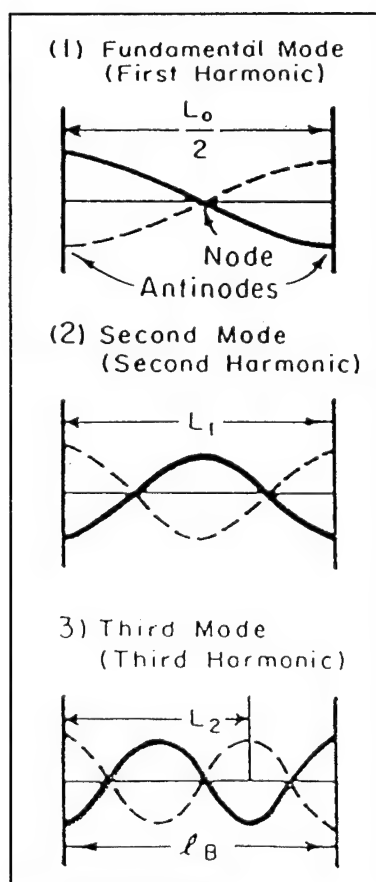


Figure 51. Harbor mode shapes

frequency, wave energy and corresponding wave height are smaller inside the harbor than outside. If the transfer function value is greater than one, then the wave height is higher inside the harbor, indicating a resonant mode. Energy levels within the harbor at these resonant periods can be on the order of 10 times greater than outside the harbor.

Prototype data from the period October 1989 to March 1990 were analyzed by Okihiro (1991). Synchronized time series records 2.3 hr (8,192 sec) in duration, collected four times a day, were ensemble averaged without band averaging to preserve the highest frequency resolution while achieving very high confidence in the estimates. For the frequency resolution of $\Delta f = 0.00012$ Hz (i.e. 1.0/8192 sec), typical degrees of freedom were $\nu = 116$ or 234. Degrees of freedom is a statistical measure of the confidence or accuracy of the calculated transfer function relative to its "true" value. These large values of degrees of freedom imply very high accuracy. The tide range at Barbers Point is on the order of 3 ft. As the water level in the harbor increases, the resonant peaks will tend to shift toward smaller periods. This will tend to give wider resonant peaks. To eliminate this phenomenon, Okihiro used results around the mid-tide level.

For the physical model, transfer function estimates (as a function of frequency) were calculated as the average of the ratios of cross-spectra and auto-spectra (Equation 43) for the eight wave cases for the 40-min-long model runs (5.8 hr prototype). Rather than digitally filtering the data, only long-wave frequency bands less than 50 sec were included in the calculations. Three bands were band averaged in the frequency domain to give a frequency resolution in model scale approximately equal to that of the prototype ($\Delta f = 3/2400 = 0.00125$ Hz model, $\Delta f = 0.000144$ Hz prototype). The degrees of freedom of these estimates are approximately $\nu = 48$, much less than the prototype transfer function estimates. Thus, accuracy of the physical model estimates is limited by the short duration of the data sets.

Numerical model. In the numerical model, wave amplification factors and phase values were calculated at the intersection of each grid line. Three-dimensional contour plots of the entire harbor were constructed for each test plan to display these amplification factors at each resonant period or frequency. These values are comparable to the results that would be given by the transfer function calculation. Normalized magnitudes were calculated from these amplitude factors at individual locations for comparison with the prototype and physical model transfer function estimates.

Phase plots indicate the relative phase shift between the incident wave at the S_{xy2} gauge and the wave at a particular location in the model. Since the numerical model is time independent, phase plots can be thought of as an instantaneous picture of the phase of the wave. They are useful in identifying the relative position of the free surface elevation and in identifying nodal lines (i.e. line of nodal points). For standing waves, the phase of the wave can be thought of as the level of the displaced water relative to the still-water level. In other words, areas with dark shading are in phase with each other and the

incident wave (i.e., water surface above still water level) and areas with light shading are out of phase with the dark-shaded areas (i.e., water surface below still-water level). Nodal lines are formed at the transition between positive and negative water levels and their corresponding positive and negative phase values. **The more abrupt the transition, the stronger the nodal line.** **Wave-induced water particle motion is perpendicular to the phase lines.** **It is this horizontal particle motion that causes a moored ship to rock back and forth and, when conditions are right, to break its moorings.**

Modal analysis

Model calibration. The first step in the modal analysis was to calibrate the numerical model and verify correct simulation of the physical model with prototype measurements for the existing harbor. Figure 52 compares resonant modes for the existing harbor from the physical and numerical models with the prototype. Normalized magnitude along the y-ordinate is based on the transfer function estimates for the physical model and the prototype data. For the numerical model, the normalized magnitude corresponds to the amplification factor previously described. The S_{xy2} location was used as the input and the four corners of the harbor were the output locations. Resonant modes in the harbor are identified by peaks greater than one in these transfer function estimates.

The most noticeable difference occurs between the physical model and the numerical model and prototype in the very long-period resonant peaks. The resonant mode with the longest period at 1,024 sec is the Helmholtz or pumping mode for the harbor because the water appears to move up and down in unison (i.e. in phase) throughout the harbor. The magnitude of this peak is smaller at the channel mid-point than at the three interior harbor locations, consistent with theory. The next peak at 630 sec corresponds to the Helmholtz mode for the marina. Physical model agreement is not as good for these two modes because the run length did not provide sufficient resolution to identify these modes after averaging for statistical confidence. In general, the physical model can resolve waves whose periods are less than 400 sec.

The last five modes at approximately 204, 132, 107, 85, and 57 sec correspond to resonant modes of the harbor, and are the ones of most interest. Agreement is very good for most of these modes between physical and numerical models and the prototype. This indicated that both physical and numerical models were calibrated well and would be good predictors for the proposed modifications. Additional description of these modes is given in the paragraphs which follow.

Harbor modes. Proposed modifications to the harbor involve changes in harbor dimensions and depth. These changes will affect the resonant modes. An increase in basin dimensions causes an increase in the resonant period to a larger value because a longer wavelength can fit within the basin. Conversely, an increase in water depth causes a shift in a resonant mode to a shorter

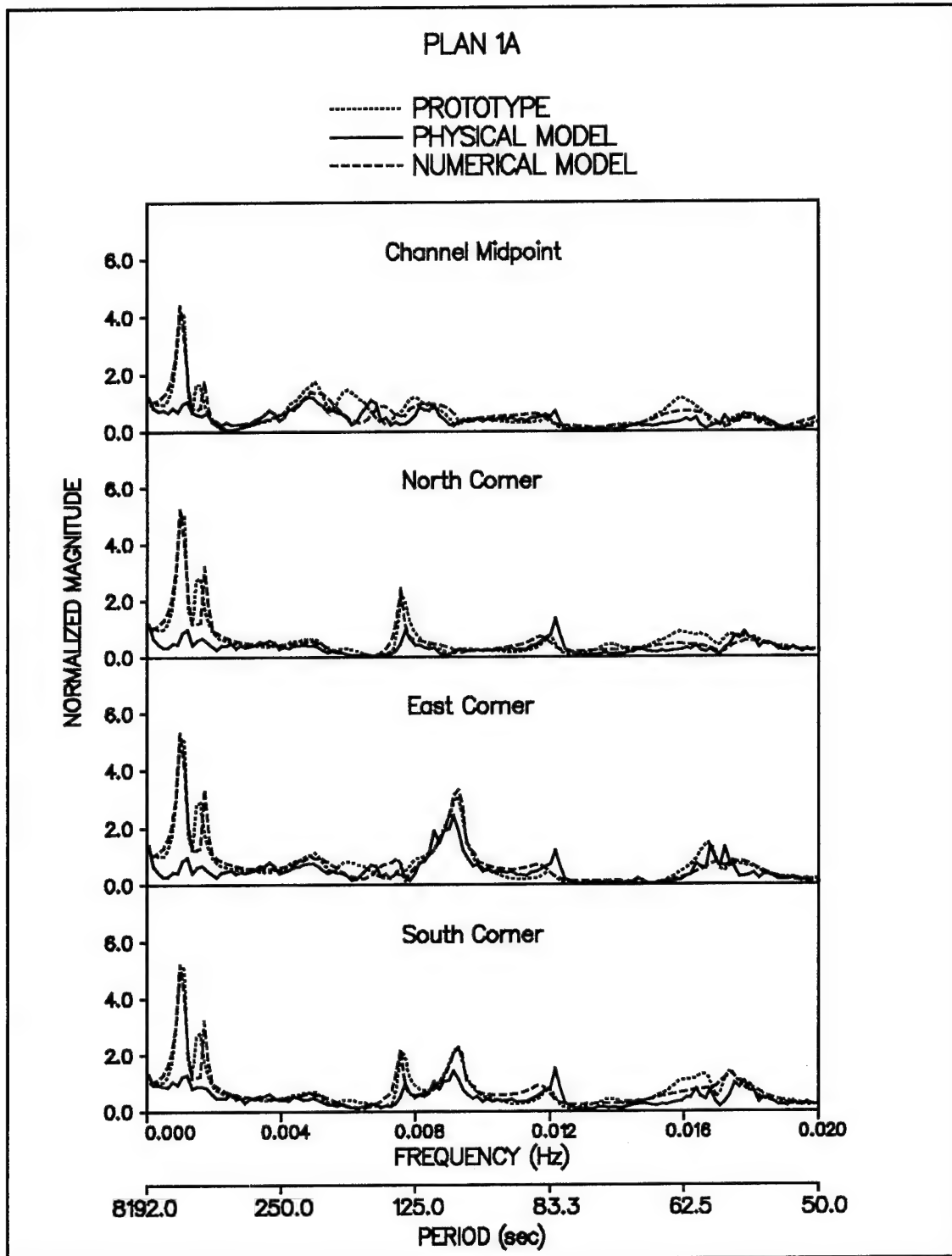


Figure 52. Transfer functions for test plan 1a
106

period. Since the wave travels faster as depth increases, wave period must decrease to keep the wavelength fixed (i.e. $L = CT$). Changes in the geometry may produce new modes that were not present prior to the harbor changes.

Physical and numerical model transfer function plots for test plans 1c, 4c, and 6c are shown in Figures 53, 54, and 55, respectively. Transfer functions for the existing plan 1a were shown in Figure 52. Transfer functions for the remaining test plans 2c, 3a, 3c, and 5c are contained in Appendix H (Figures H1 to H4, respectively). Agreement between the physical and numerical models is very good for all test plans.

Transfer functions for test plan 6c are not shown, but are very similar to those of test plan 4c, since there is no change in the harbor configuration or water depth between these two test plans. The effect of the jetty on long-wave harbor response is minimal because these long-period waves are not influenced by small rubble-mound structures. Therefore, in future discussions, it is assumed that the harbor response to test plan 6c is similar to that of test plans 4c and 5c.

From these transfer function plots, the harbor resonant modes listed in Table 28 were identified. Contour and phase plots were then generated by the numerical model for test plans 1a, 1c, and 4c at each resonant mode to illustrate the harbor response. The three contour plots are shown in Figures 56, 57, and 58, respectively. Maximum amplification values are annotated on the figures. The corresponding phase plots for these three test plans are given in Figures 59, 60, and 61, respectively. Amplitude contour plots for the five remaining test plans (2c, 3a, 3c, 5c, and 6c) are contained in Figures H5, H6, H7, H8, and H9, respectively. Figures H10-H14 show the corresponding phase plots for these five test plans.

The first resonant mode shown on the transfer function plots at approximately 1,024 sec is the Helmholtz mode (H_h). Because harbor size and water depth increase in test plans 1c and 4c, resonant period increases slightly, within the resolution of the analysis. This slight increase is shown by a "+" sign in Table 1 for these test plans. This mode generally does not endanger moored vessels because its period is too long and the water motion is in phase throughout the harbor (i.e., no nodal lines are present inside the harbor).

The fundamental harmonic mode along the east-west diagonal (H_{ew}) has a wavelength equal to twice the diagonal distance of the harbor between the east corner and the western side of the entrance channel. It is located at 204 sec in test plan 1a, 220 sec in test plan 1c, and 210 sec in test plan 4c. The resonant period increases because the harbor expansion increases the effective length of the harbor in this direction. The increase in depth in test plan 4c causes the resonant period to decrease slightly relative to test plan 1c. The magnitude of the transfer function is twice as large for test plan 1c as it is for test plans 1a and 4c. The one nodal line in this mode runs in the north-south direction. For the existing plan, it intersects the southwest wall in the vicinity of the "Big Mike" dry dock facility. For test plan 4c, the nodal line moves further into the

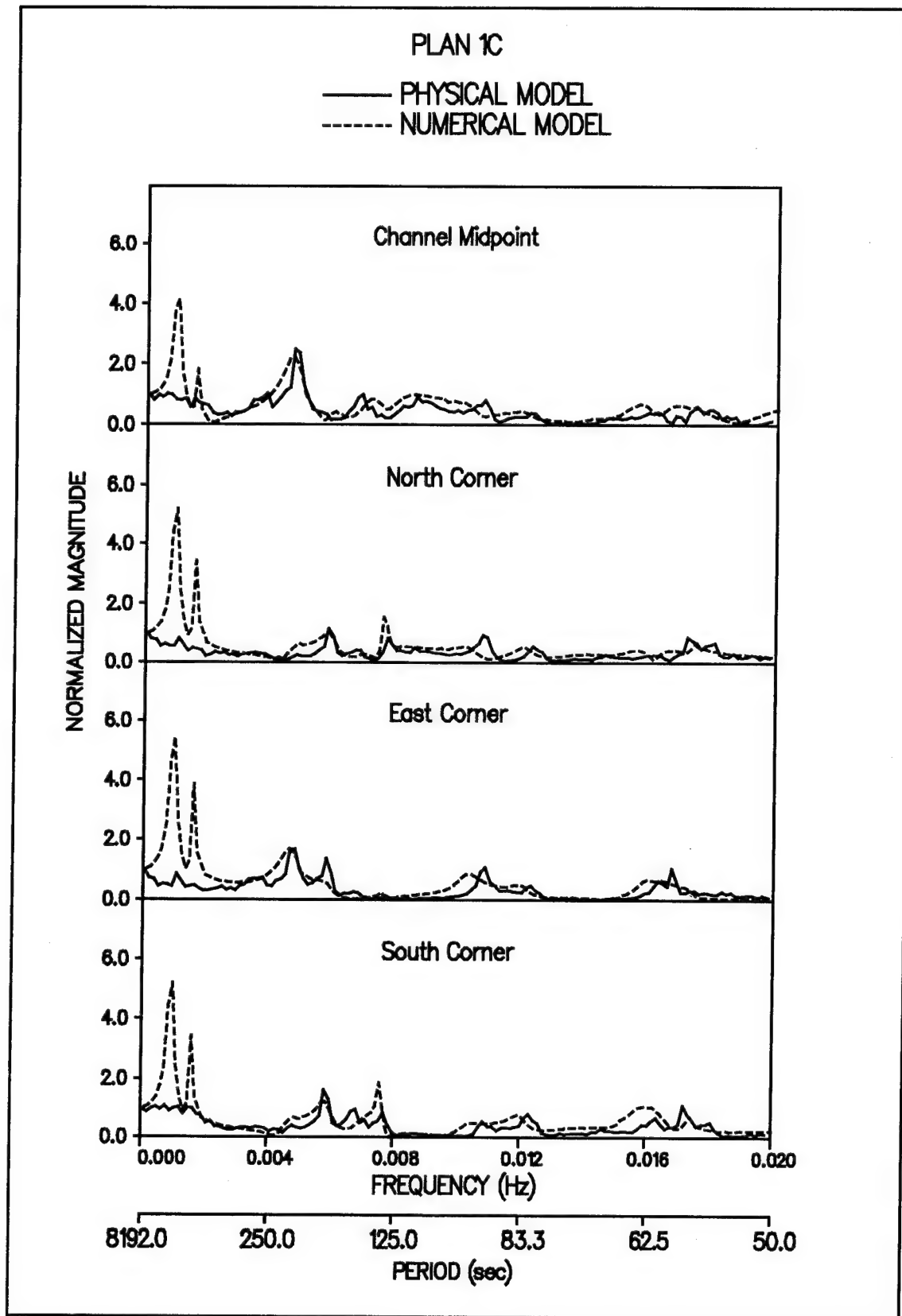


Figure 53. Transfer functions for test plan 1c

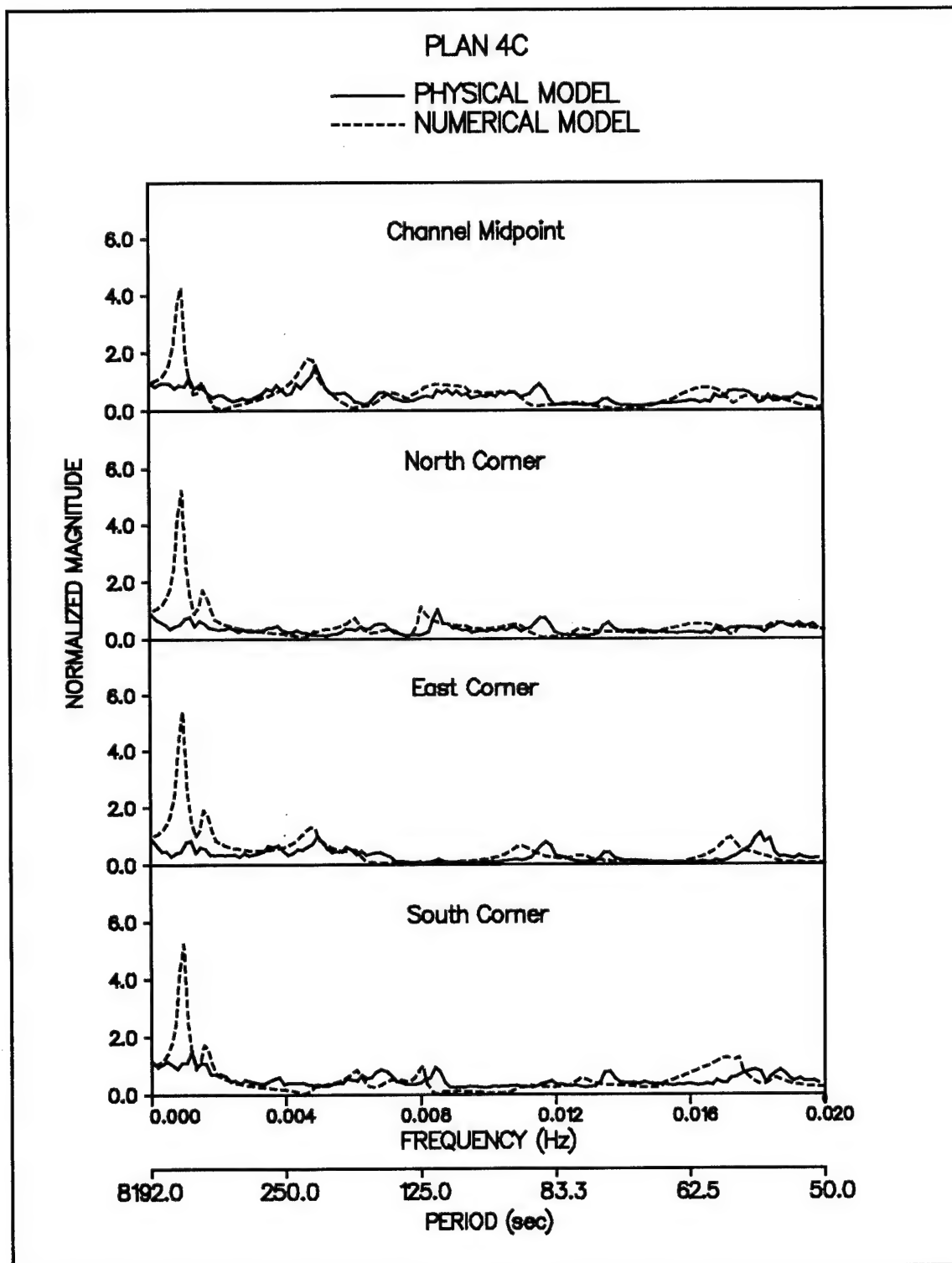


Figure 54. Transfer functions for test plan 4c

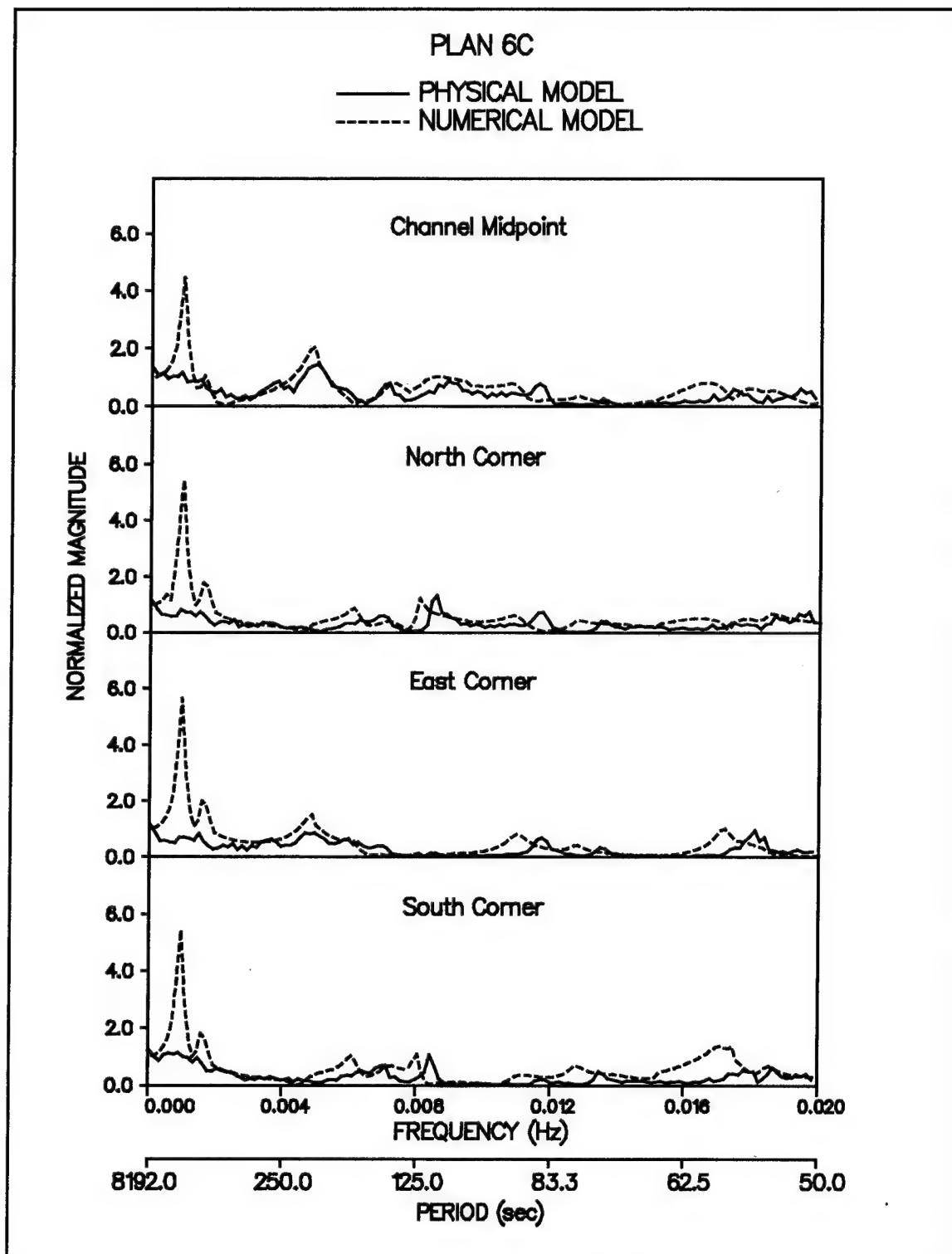


Figure 55. Transfer functions for test plan 6c

Table 28
Harbor, Barge Basin, and Marina Modes

Mode Description	Mode Label	Period, sec		
		Plan 1a	Plan 1c	Plan 4c
Harbor Modes				
Helmholtz	H_h	1024	1024+	1024+
Fundamental East-West	H_{ew}	204	220	210
Fundamental North-South	H_{ns}	132	132	124
Fundamental Length	H_l	107	170	163
Second North-South and	H_{ns2}	85	83	78
Second East-West	H_{ew2}	85	83	78
Second Length	H_{l2}	57	96	91
Third Length	H_{l3}	—	62	58
Barge Basin Modes				
First Width	B_{w2}	72	—	—
Marina Modes				
Helmholtz	M_h	630	630	630
Fundamental Length	M_l	167	167	167
Second Length	M_{l2}	125	125	125

basin, intersecting the southeast wall between the south and east corners. The surge analysis in Chapter 4 indicated that the natural periods in surge for the C9 container ship will be much less than the resonant period of this mode. Thus, even though the nodal line intersects the pier area, surge should not be a problem for the C9 container ship and similar vessels. Finally, this mode will not affect surge natural periods at 57 sec and 130 sec identified for the "Big Mike" dry dock facility during the Marisco event at its original position along the southeastern wall (Noda and Associates 1988).

The fundamental mode along the north-south diagonal (H_{ns}) occurs at 132 sec in test plans 1a and 1c, and 124 sec in test plan 4c. Amplitudes are largest in the north and south corners. The phase changes along the heavily shaded nodal line running east-west in the center of the harbor. Resonant peaks do not shift between test plans 1a and 1c since the north-south diagonal distance is unaffected by the expansion. The increase in depth in test plan 4c causes a shift to a slightly smaller period. Although this mode is in the range of the surge natural periods of the C9 container ship, it should not be a problem because the nodal lines do not intersect berthing areas along the southeast wall or, if they do, they are very weak.

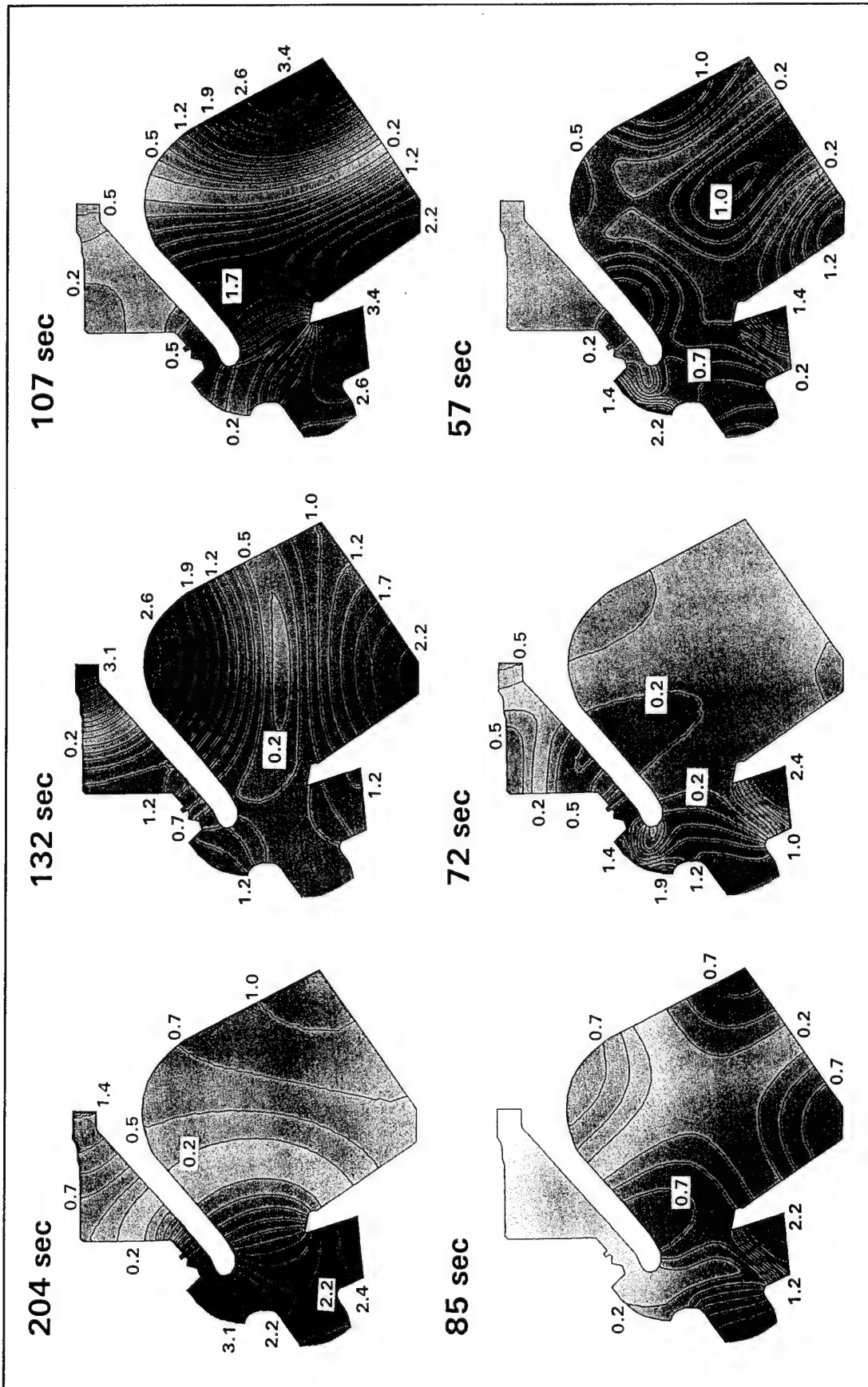


Figure 56. Amplitude contour plots for test plan 1a

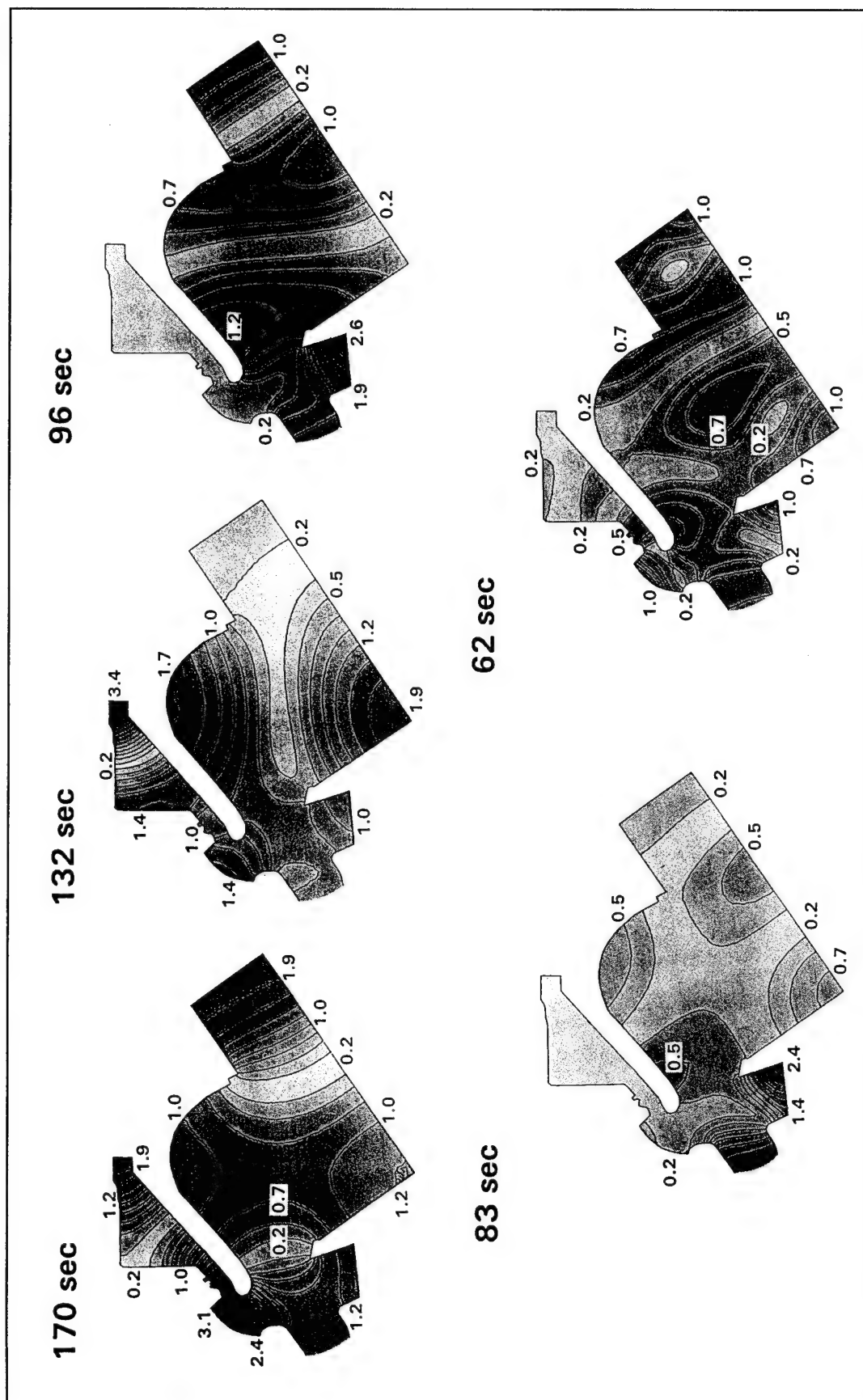


Figure 57. Amplitude contour plots for test plan 1c

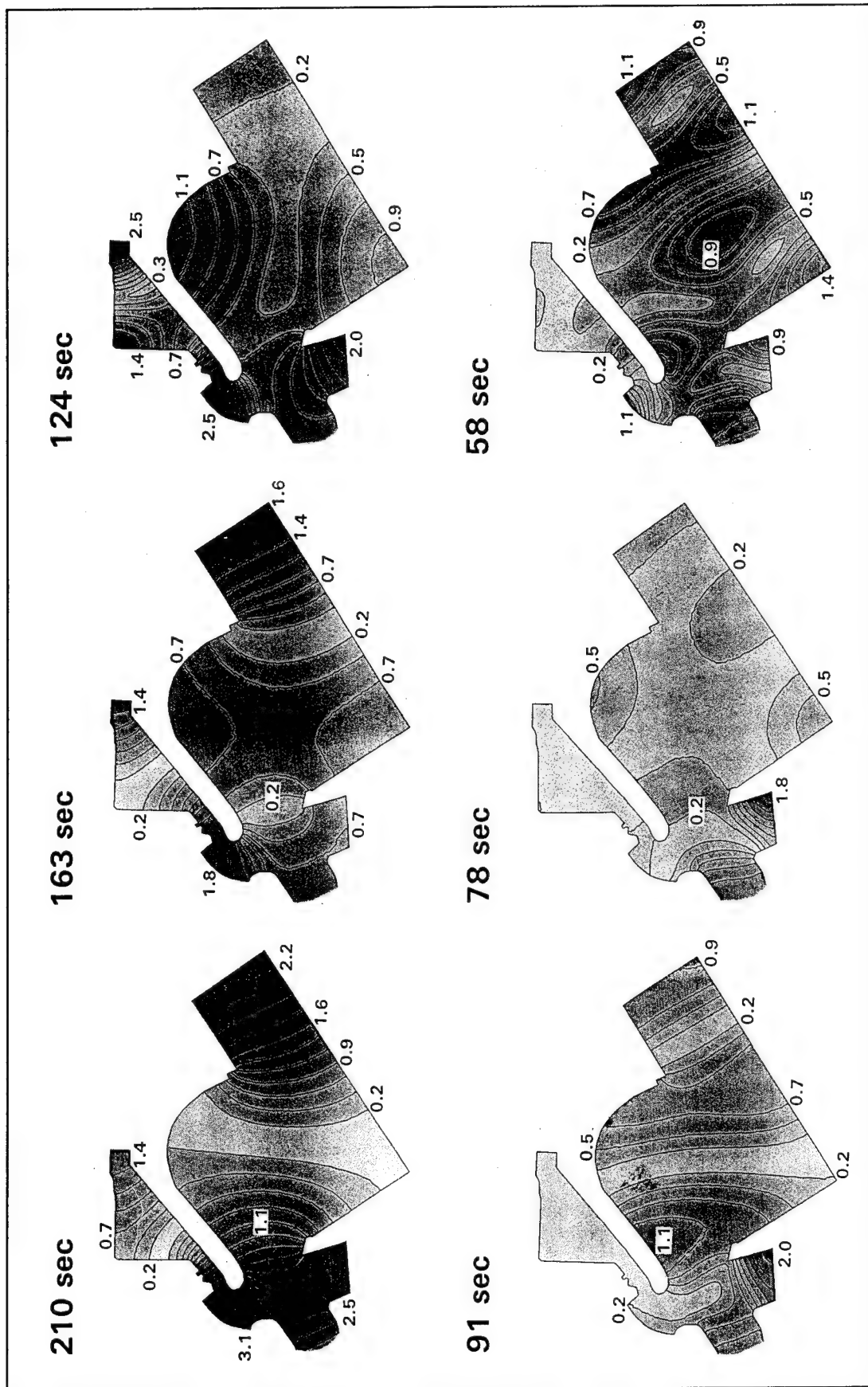


Figure 58. Amplitude contour plots for test plan 4c

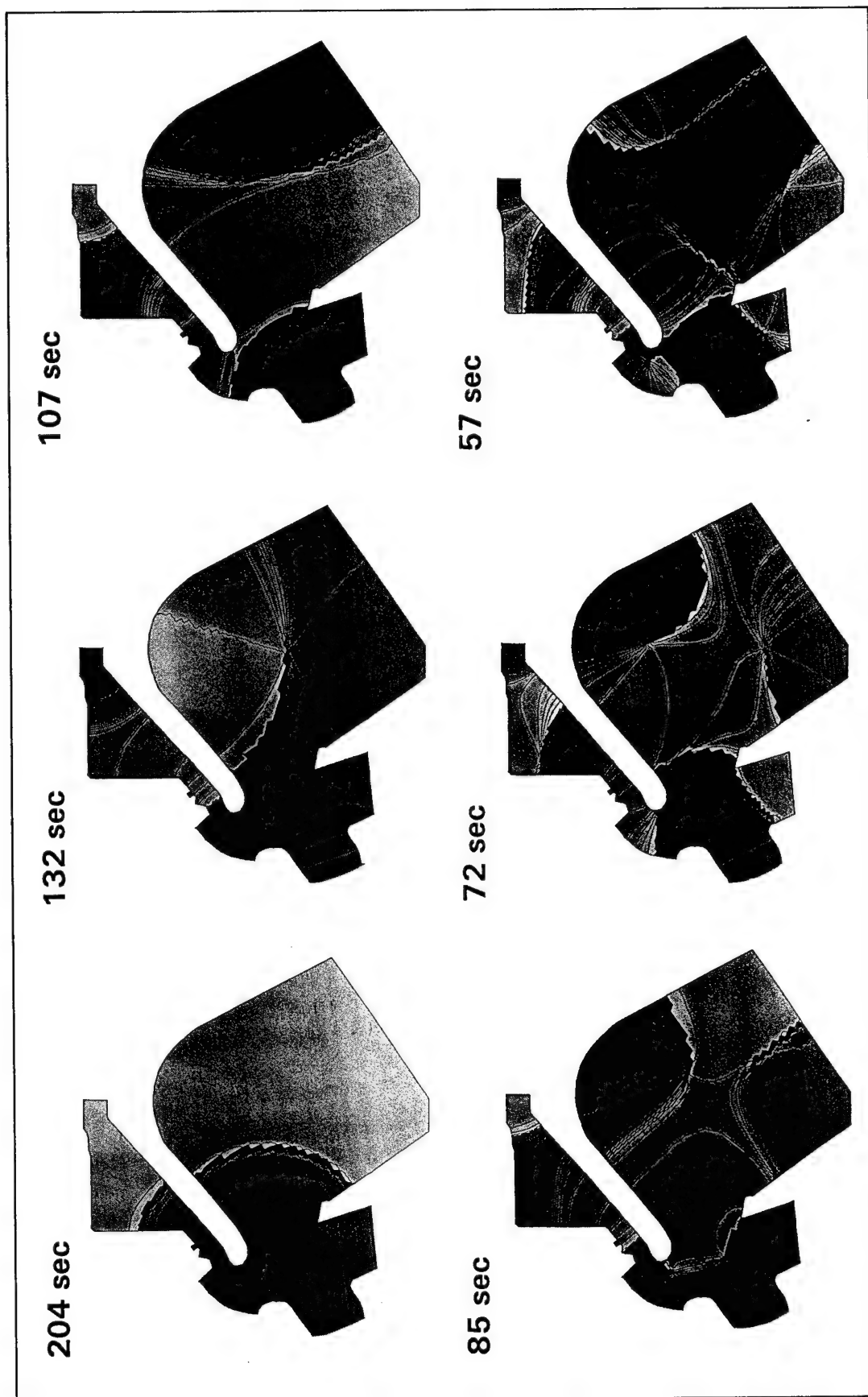


Figure 59. Phase plots for test plan 1a

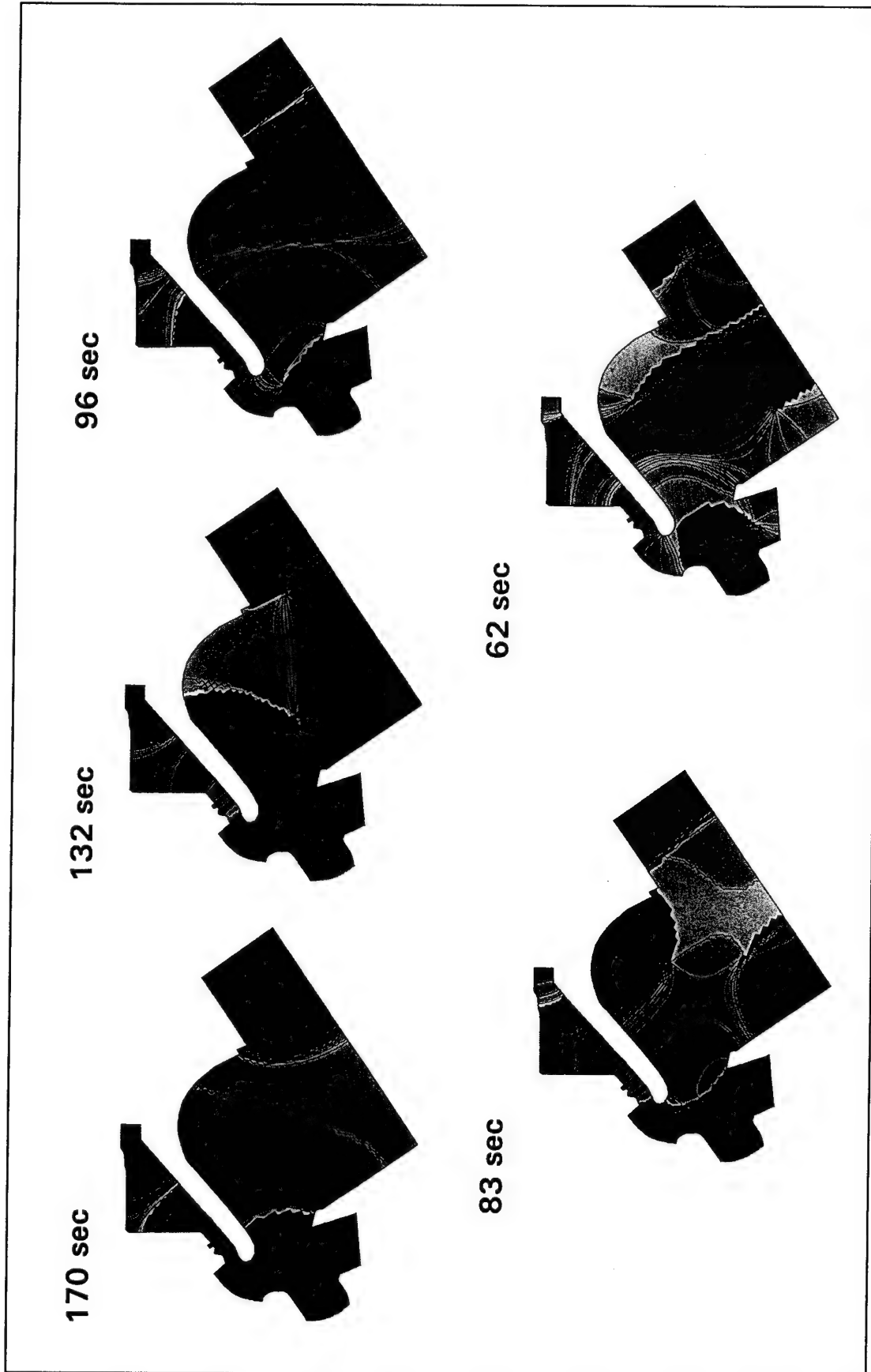


Figure 60. Phase plots for test plan 1c

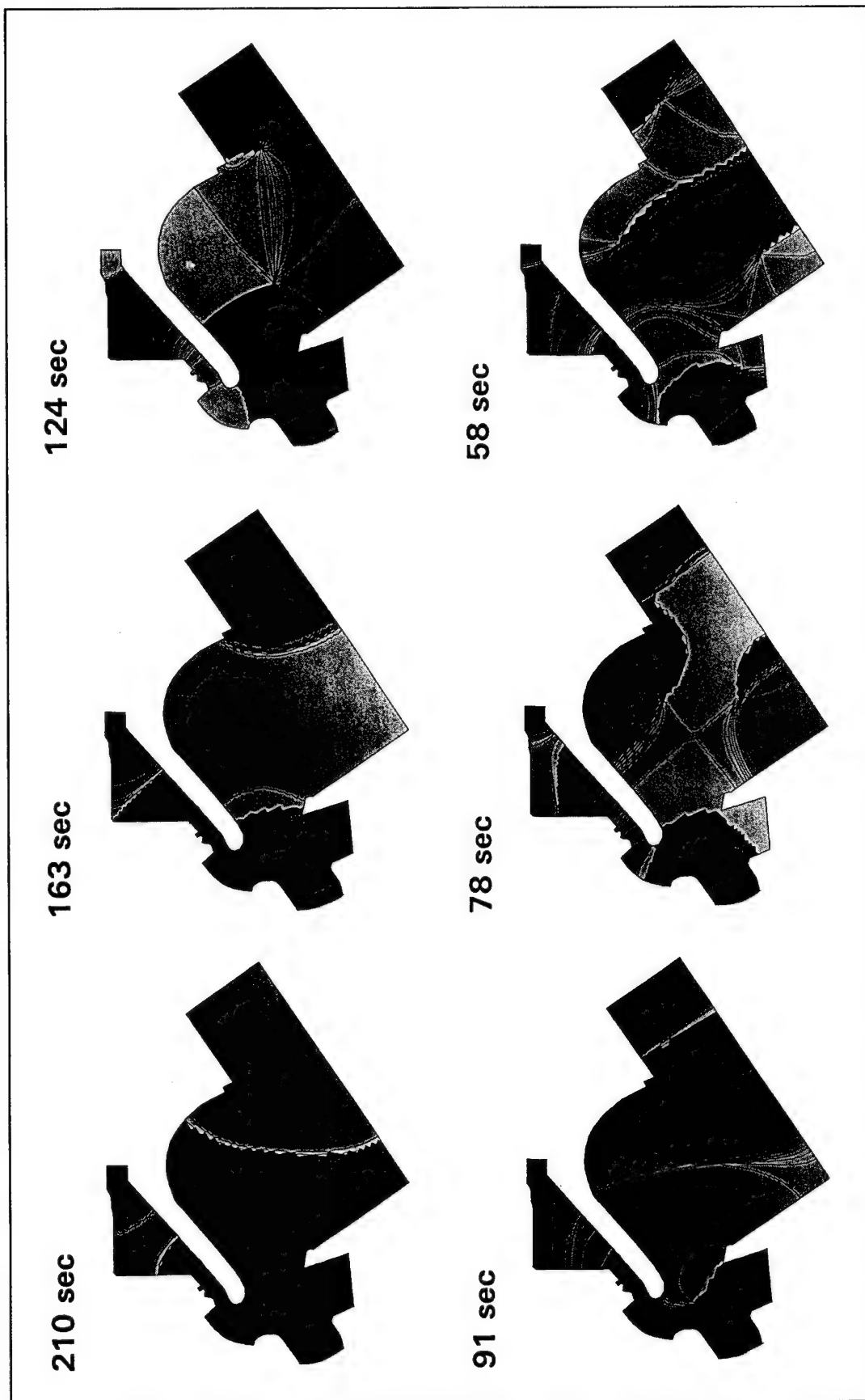


Figure 61. Phase plots for test plan 4c

The fundamental mode parallel to the length of the harbor is in the south-east direction (H_p) between the south and east gauges and occurs at 107 sec in test plan 1a, 170 sec in test plan 1c, and 163 sec in test plan 4c. The period of this mode changes drastically between test plans because the expansion adds 1,100 ft to the previous length of 2,000 ft, a 50-percent increase. Also, increasing the water depth in test plan 4c decreases the resonant period as before. The confusing amplitude and phase contours are due to the irregular shape of the basin with the expansion and the opening to the ocean. It is fairly well defined along the southeastern side of the basin because the reflecting endwalls are parallel over the 1,100-ft width of the expansion, reinforcing the standing wave pattern of a closed basin. Strong horizontal water particle motions exist at these locations because the gradient of the phase is large (i.e. intense shading of phase contours). For the existing harbor, a surge problem could potentially exist along the southeast wall for the C9 container ship in the process of loading/unloading (i.e. medium load). Since the container ships will probably exchange cargo for water ballast, this may never be a problem. Adding the expansion will shift the natural period to larger values, away from the surge period of the container ship.

The second harmonic along the north-south diagonal (H_{ns2}) occurs at 85 sec in test plan 1a, 83 sec in test plan 1c, and 78 sec in test plan 4c. This mode is combined with the second harmonic along the east-west diagonal (H_{ew2}). For both modes the harbor diagonal is equal to a whole wavelength. Water motion at the opposite corners is in phase, while the middle is out of phase. When the flow is up in the corners, it is down in the center of the harbor, and vice versa. These two second harmonics are out of phase with each other, so that the center is always a nodal point with no movement and the north and south corners are out of phase with the east and west corners. The intense shading of the nodal lines intersecting the southeastern wall is indicative of a potential problem for ships in surge, especially light ships that have been deballasted.

The second harmonic along the length of the harbor (H_{l2}) occurs at 57 sec in test plan 1a, 96 sec in test plan 1c, and 91 sec in test plan 4c. The harbor length in the southeast direction is equivalent to a full wavelength in this mode. Again, the change in modal period between test plans is due to the increase in the harbor length dimension because of the expansion and the increase in depth. Two nodal lines run parallel to the width dimension of the harbor and intersect the southeast wall. With the harbor expansion, the northern nodal line moves up into the expansion. Again, when the water motion is up in the corners, it is down in the middle, and vice versa. Because of the opening to the harbor, the pattern is not exact across the width of the harbor. The proximity of test plan 1c and 4c resonant periods to the surge natural periods for a light ship could pose a problem if the container ship is not ballasted properly.

The final harbor resonant mode is the third harmonic along the length of the harbor (H_{l3}) for test plans 1c and 4c. Because this mode occurs in the existing harbor at a much higher frequency, it is not shown. It occurs at 62 sec in test plan 1c and 58 sec in test plan 4c. The length dimension now

accommodates 1.5 wavelengths in this mode. Three nodal lines run parallel to the width dimension of the harbor. Four segments of the wave are present: two in phase and two out of phase. Adjacent segments are always out of phase. Even though the nodal lines intersect the southeastern wall, their resonant periods are too small to be a concern for ship mooring.

Harbor expansion modes. Transfer function estimates from the physical and numerical models for the harbor expansion east and north gauges (i.e. EX2 and EX3) are shown for test plans 1c, 4c, and 6c in Figures 62 and 63, respectively. The harbor expansion was only in these three test plans. The long-wave response at these locations is similar to that of the east corner of the harbor for each of the test plans, with slight differences due to the change in the harbor configuration.

Physical and numerical model results match reasonably well for resonant periods less than 400 sec. Again, the physical model does not replicate the Helmholtz mode. Physical model resonant periods are shifted to smaller periods relative to the numerical model predictions. Changes between the east and north locations are very slight, except for the highest mode at approximately 60 sec, which is shifted to a lower period for the east location. Some shifting of the two highest modes (i.e. approximately 100 sec and 60 sec, respectively) occurs between test plan 1c and test plans 4c and 6c.

Plans call for the C9 container ship and other large ships to use this area for berthing along two sides. Only resonant modes with intense nodal lines in the vicinity of the proposed berthing sites and resonant periods corresponding to ship natural periods in the range of 70 to 140 sec need be considered. Referring to Figure 60, only the fundamental north-south ($H_{ns} = 132$ sec), second length ($H_l = 96$ sec), and the second north-south and second east-west ($H_{ns2} = 83$ sec and $H_{ew2} = 83$ sec) are of possible interest. The densest nodal lines are associated with the two highest modes H_l and $H_{ns2} = H_{ew2}$. Water will flow parallel to the width (i.e. perpendicular to the nodal line) in the northeast direction at the proposed berthing site along the northeast wall. There does not appear to be a surge problem associated with berthing a ship along the northwest wall at the top of the proposed expansion. For test plan 4c (see Figure 61), the same modes ($H_{ns} = 124$ sec, $H_l = 91$ sec, $H_{ns2} = H_{ew2} = 78$ sec) are of interest. Again, only the two highest modes H_l and $H_{ns2} = H_{ew2}$ will pose a surge problem along the northeast wall. There might be a slight possibility of surge along the northwest wall if the ship's surge natural period corresponds with the 124 sec of the H_{ns} mode.

Harbor ferry modes. Transfer function estimates from the physical and numerical models are shown for test plans 1a, 1c, 4c, and 6c in Figure 64. The long-wave response at this location is similar to that of the north and east corners of the harbor because it is between them. Because the displacement (i.e. weight) of the ferry is so much less than the container ship, the natural periods of the ferry in surge and sway will be much less. Only resonant modes with intense nodal lines in the vicinity of the proposed harbor ferry site and resonant periods corresponding to the ship natural periods need be

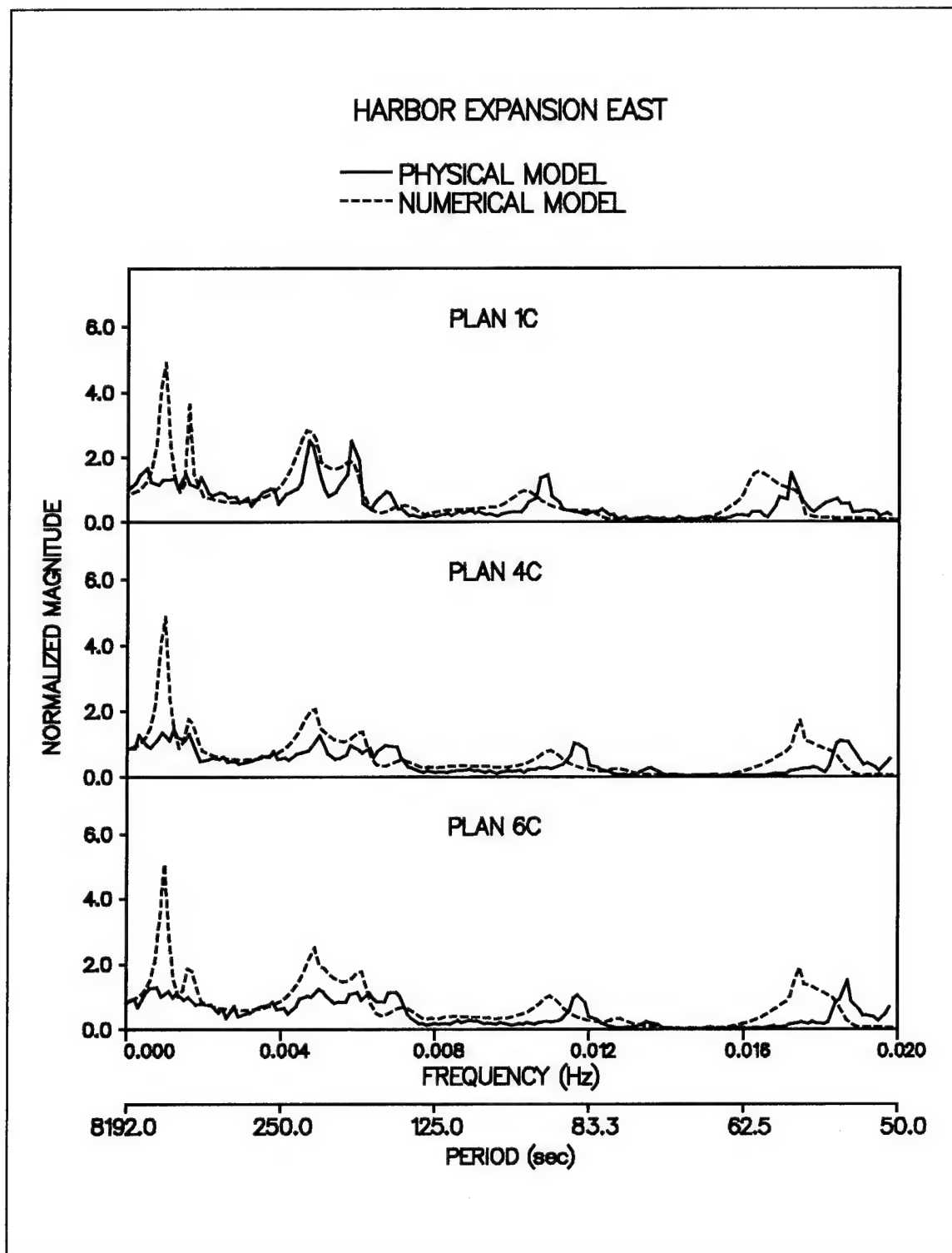


Figure 62. Transfer functions for harbor expansion east location

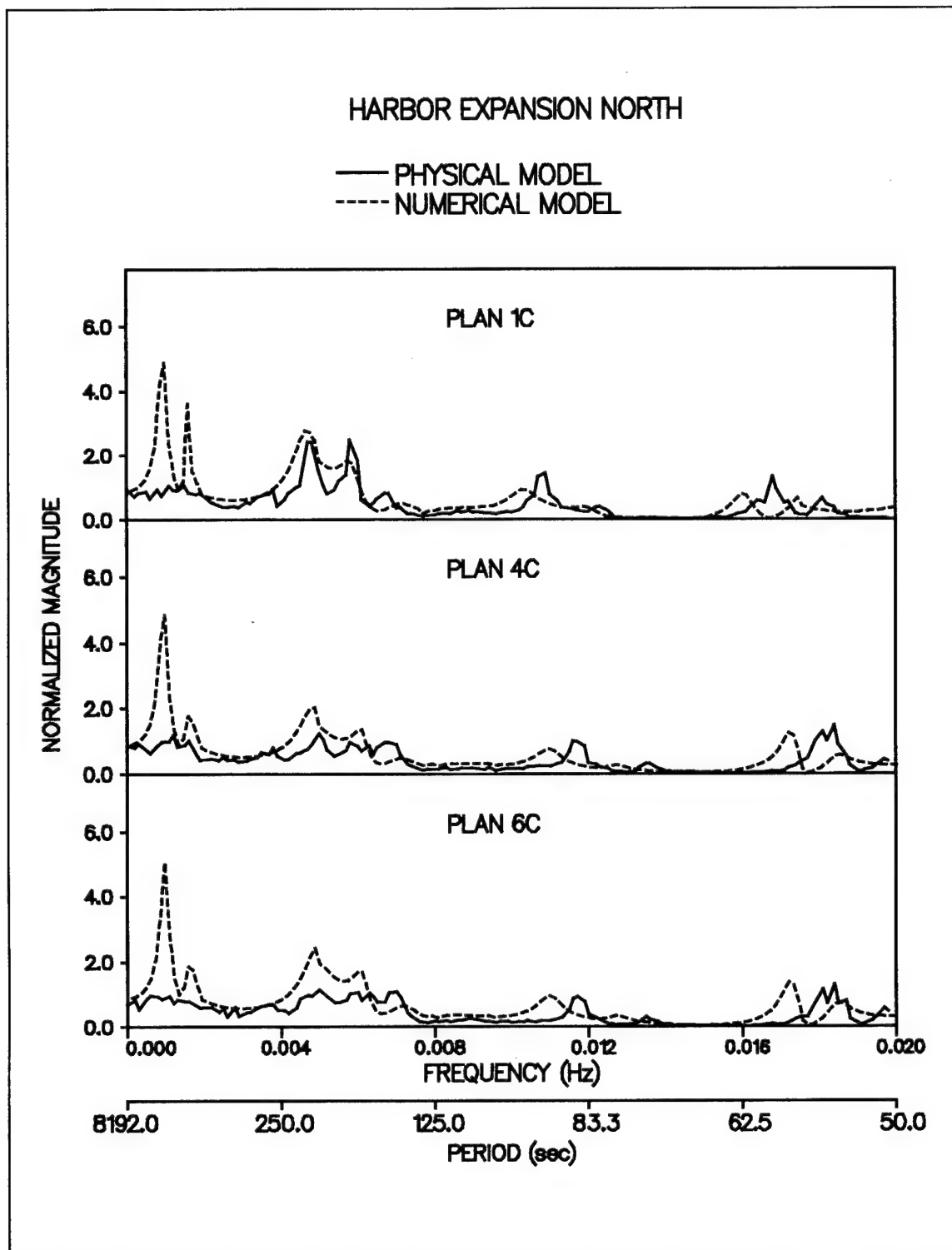


Figure 63. Transfer functions for harbor expansion north location

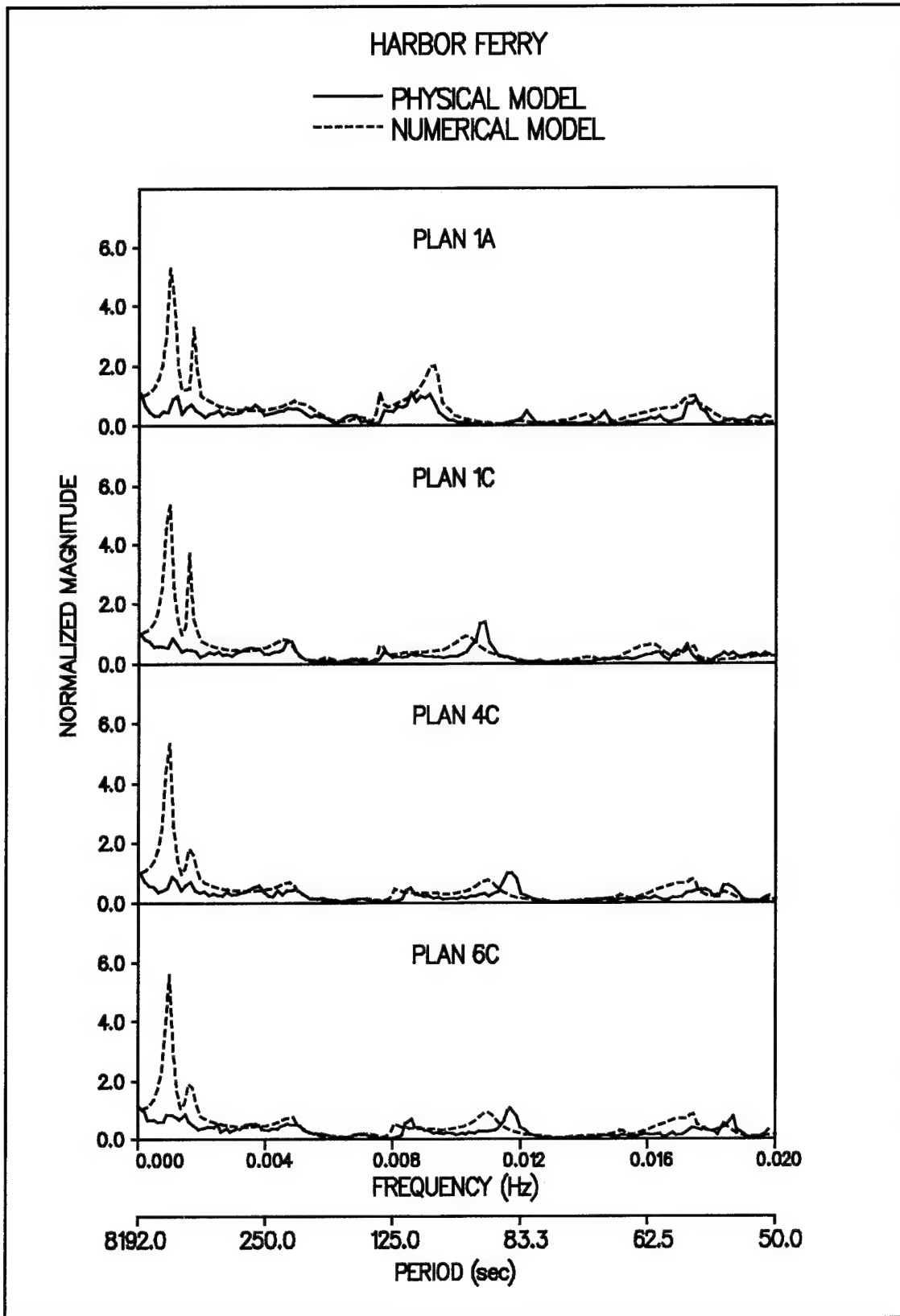


Figure 64. Transfer functions for harbor ferry location

considered. Thus, only the H_{ns2}/H_{ew2} mode, with resonant periods between 78 and 85 sec for the different test plans, is of possible interest. Water will flow parallel to the width (i.e. perpendicular to the nodal line) in the northeast direction at the proposed ferry site. Care should be taken to calculate the natural surge and sway periods of the ferry boat prior to making the final decision.

Barge basin modes. Physical and numerical model transfer function estimates for the four test plans for the north and south barge basin locations are shown in Figures 65 and 66, respectively. As before, physical and numerical models match reasonably well for resonant periods less than 400 sec. In the physical model, the resonant periods are slightly shifted and the transfer functions are smaller than corresponding numerical model predictions. Changes between the north and south locations are very slight. Some shifting of the resonant peaks occurs, but the overall effect on the long-wave response of the barge basin is not changed between test plans.

The harbor Helmholtz mode (H_h) is recorded by the two barge basin locations because it is an integral part of the harbor. Both fundamental and second harmonic east-west diagonal modes (i.e., H_{ew} and H_{ew2}) are present, with appropriate variation in modal period among test plans. Similarly, the fundamental and second harmonic length modes (i.e., H_l and H_{l2}) appear to be "felt" by the barge basin locations.

Additional resonant peaks are present at approximately 145, 125, and 72 sec. Some of these peaks are related to the marina response because of its proximity. In the existing harbor, the second harmonic along the barge basin width dimension (B_{w2}) occurs at 72 sec (see Figures 56 and 59). This mode interacts with the marina with a full wavelength between the southern wall of the barge basin and the northwestern wall of the marina at the entrance. Water flow is back and forth across the entrance channel.

Marina modes. Physical and numerical model transfer function estimates for the four test plans for the three marina locations, marina entrance (Me), marina west (Mw), and marina north (Mn), are shown in Figures 67, 68, and 69, respectively. Even though there is no change in the marina between test plans, some reduction in long-wave energy does occur. Again, agreement between physical and numerical models is good. Physical model peaks are shifted and their values are slightly smaller relative to the numerical model.

The Helmholtz mode for the marina (M_h) is at 630 sec. It is positioned next to the H_h mode at 1,024 sec. As mentioned previously, the physical model is usually not able to resolve these long-period peaks. Interestingly, the physical model was able to resolve the M_h mode for test plan 6c at the Mw and Mn gauges. Many of the harbor and barge basin resonant peaks are recorded by the marina locations. The harbor H_{ew} and the barge basin B_{w2} are the most noticeable.

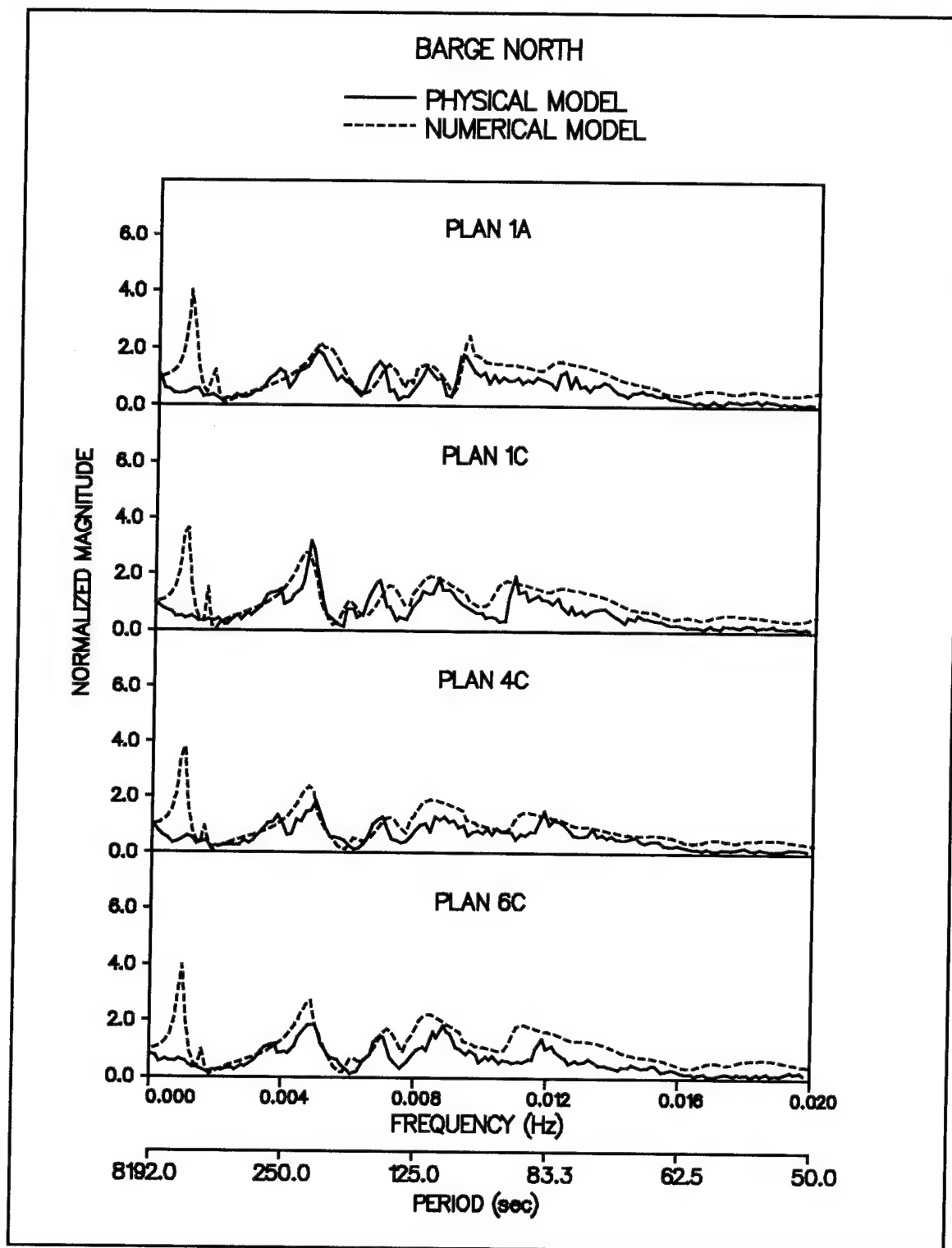


Figure 65. Transfer functions for barge north location

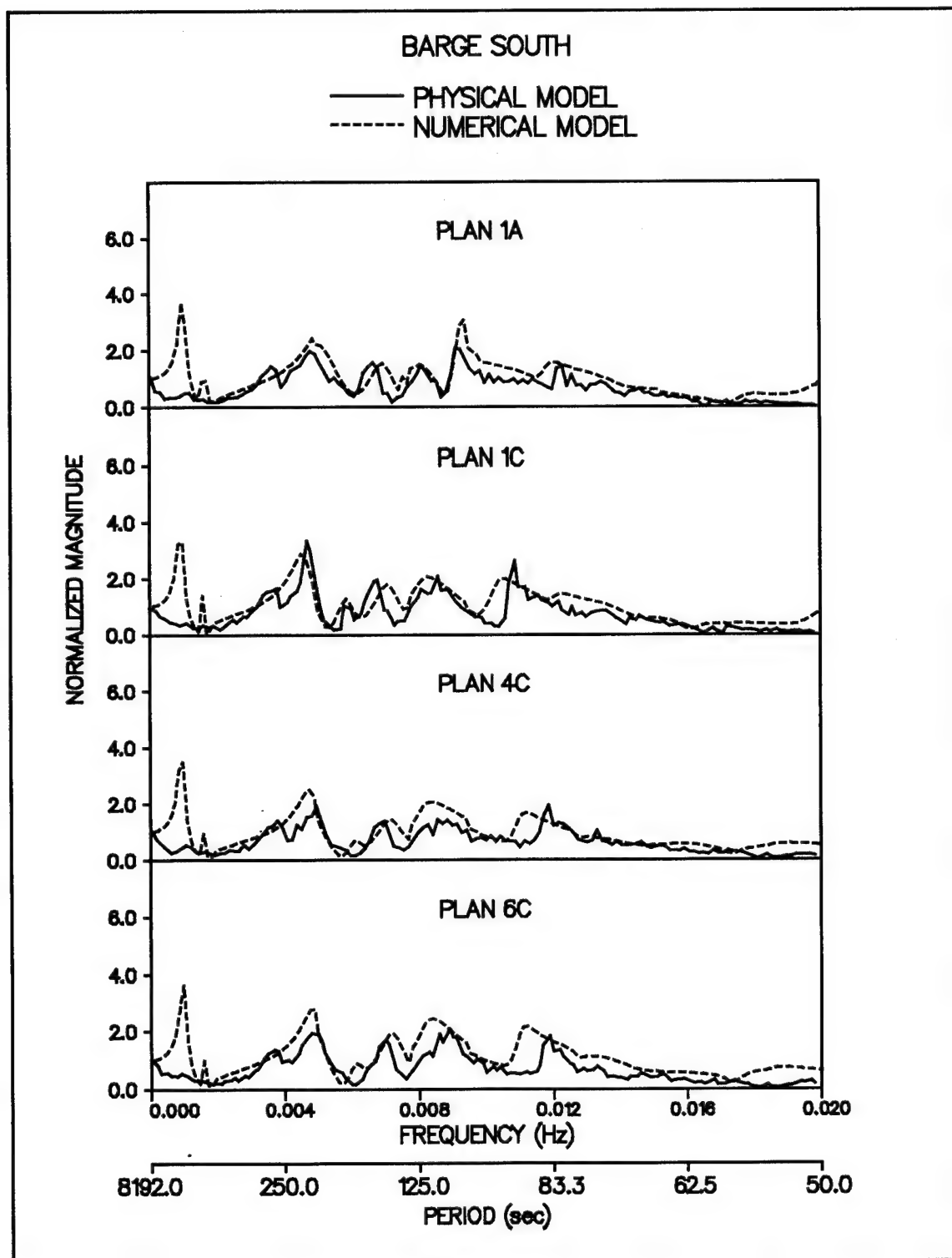


Figure 66. Transfer functions for barge south location

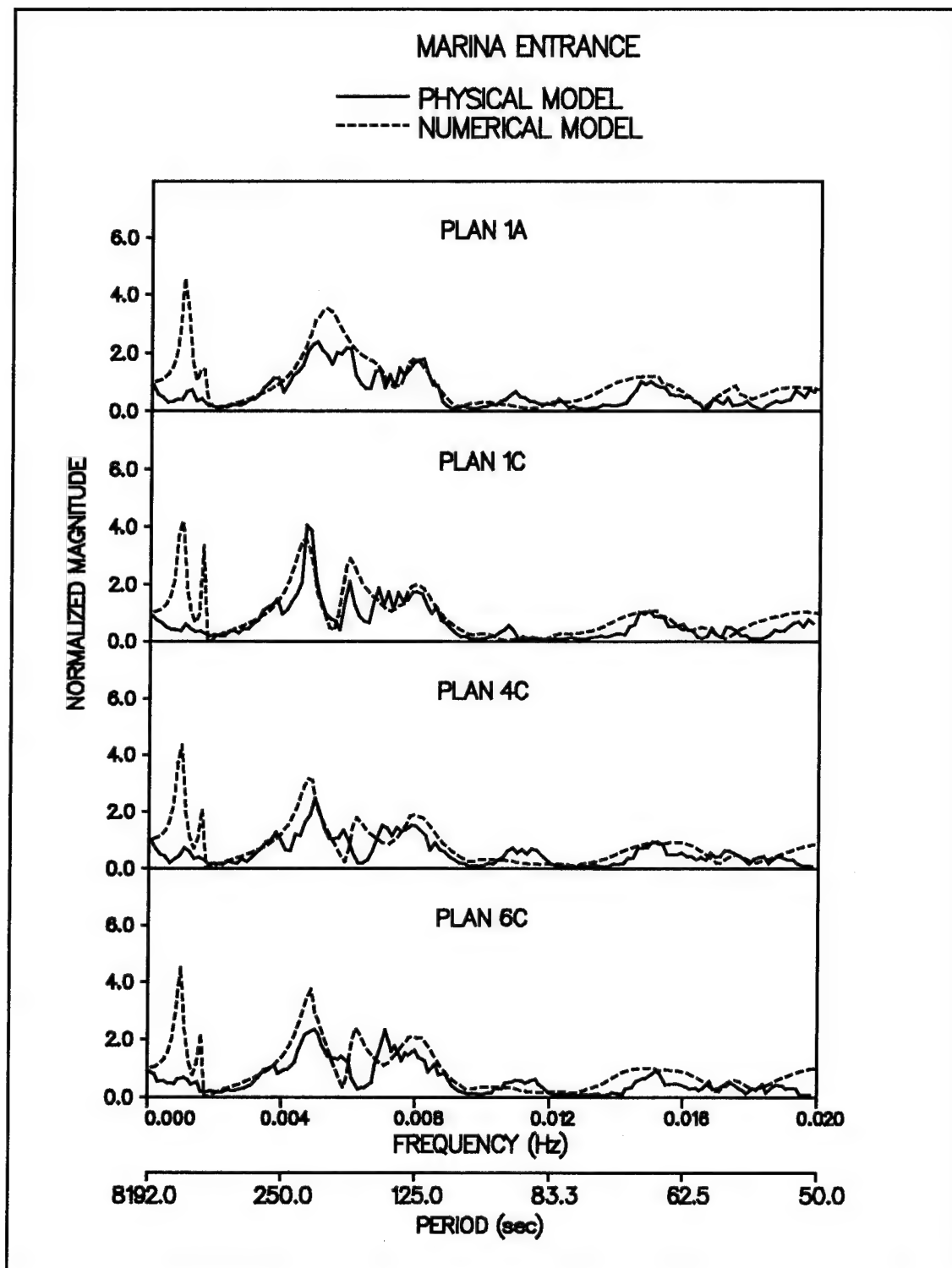


Figure 67. Transfer functions for marina entrance location

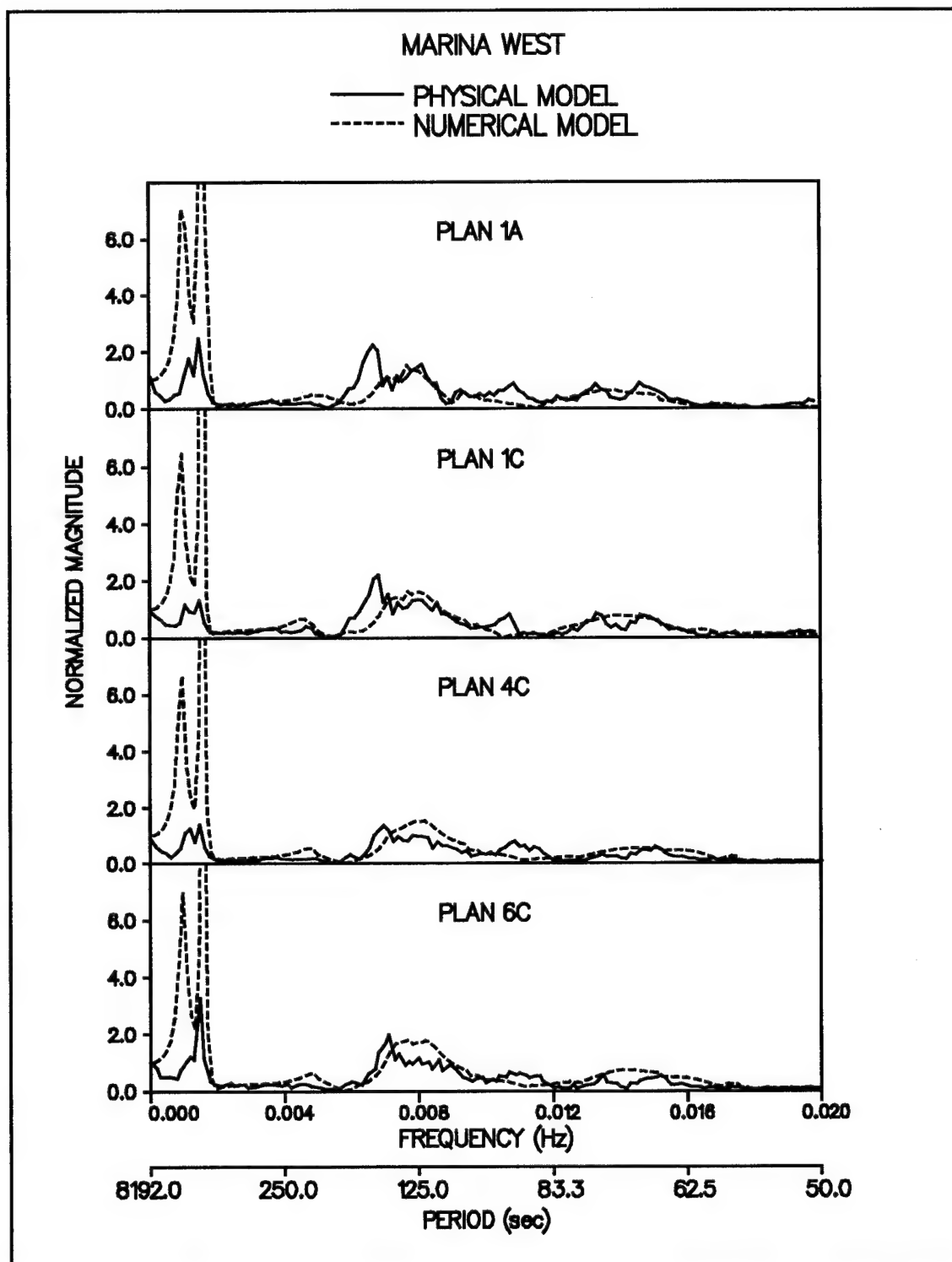


Figure 68. Transfer functions for marina west location

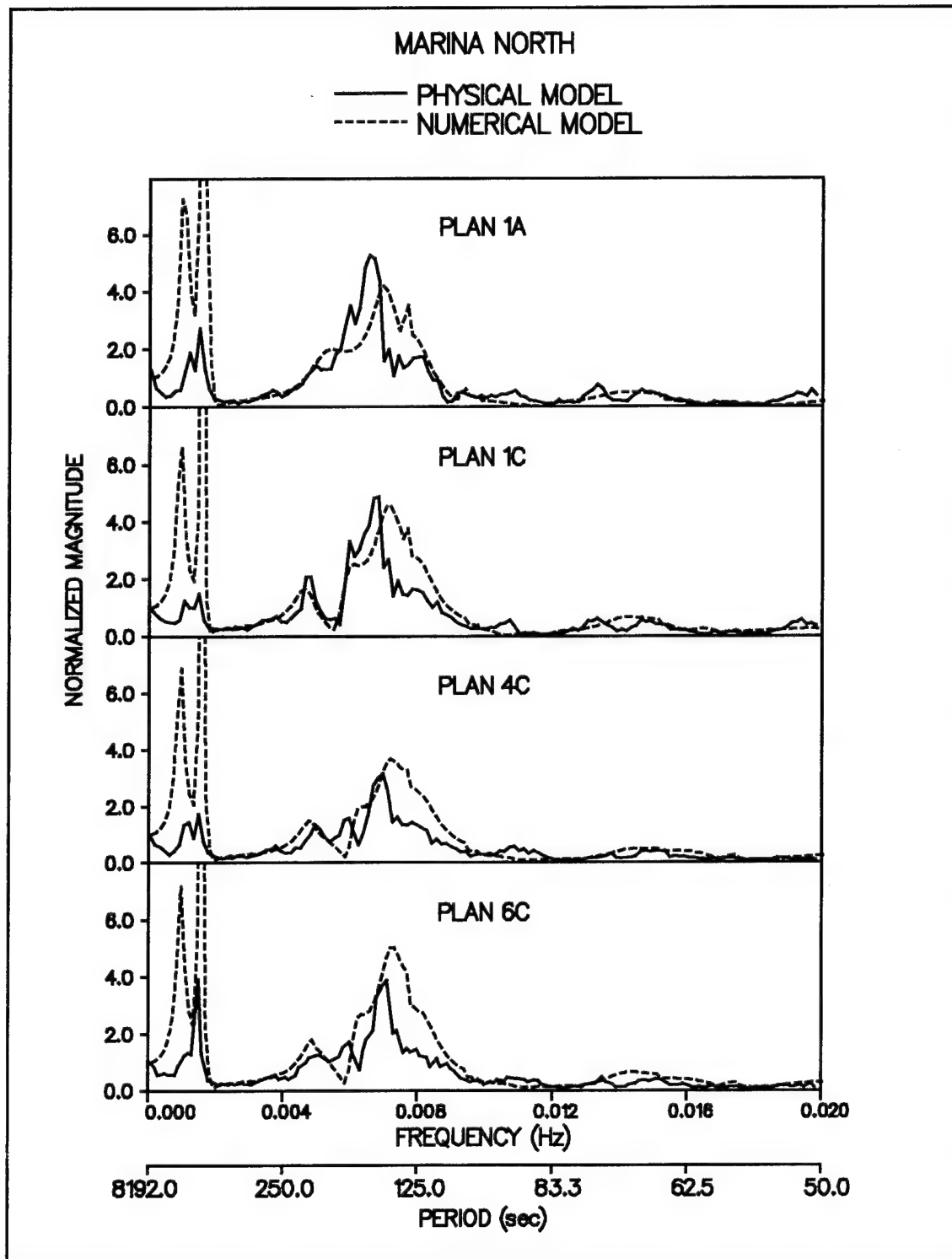


Figure 69. Transfer functions for marina north location

The fundamental length mode for the marina (M_0) occurs at 167 sec. Transfer functions at Me and Mn corners show a strong correlation and are out of phase at this period. The second harmonic (M_2) occurs at 125 sec. Transfer functions are strongly correlated at all three locations.

Predicting long-wave response

As mentioned previously, transfer function estimates for the physical model were averaged from the eight individual wave cases for comparison with the prototype and numerical model. Individual transfer functions for each of the wave cases in test plan 1a are shown in Figure 70 for the south corner (Sc). Individual transfer functions for test plans 1c, 4c, and 6c are shown in Figures 71, 72, and 73, respectively. They are grouped by wave case, with the functions from the second location at S_{xy2} in the top panel and those from the first location at S_{xy1} in the second panel. The average transfer function is repeated in the bottom panel. Transfer functions for the four corner gauges for each test plan are contained in H15 to H42.

These figures illustrate the variability in transfer function estimates as a function of wave condition. The general trend, as represented by the average, is present for the dominant modes for all wave conditions. However, different wave conditions appear to preferentially excite different modes in the harbor more than others. According to Okihiro, Guza, and Seymour (1992), bound infragravity energy is often a major component of the infragravity energy present at Barbers Point Harbor, especially when most of the wind-wave energy is swell. Under these conditions, the harbor response to long waves should be greater for unidirectional waves than those with broad directional spreading.

As mentioned previously, the eight wave cases represented a range of frequency spectral shapes, wave direction, and directional spreading. Six wave cases were predominately composed of swell energy: BPS211 (wave case W1), BPS241 (W4), BPS151 (W5), BPS161 (W6), BPS171 (W7), and BPS181 (W8). The overall mean wave direction for wave case BPS211 was from the west. Wave cases BPS241 and BPS151 were from the southwest, and BPS161, BPS171, and BPS181 were parallel to the entrance channel. All six of the cases with predominant swell energy had relatively narrow directional spread.

In general, the harbor response is greater for these six cases with dominant swell energy and narrow directional spreading, in agreement with Okihiro, Guza, and Seymour's (1992) observations. Figure 70 shows that the existing harbor responds more (i.e. larger transfer function) at the fundamental length mode H_1 at 107 sec to the unimodal BPS241 and bimodal BPS151 than the other wave cases. Some discrepancies do exist, however. Wave case BPS231, with sea energy predominant and broad directional spreading, excited the harbor more than the other wave cases at the second north-south mode (H_{ns2})

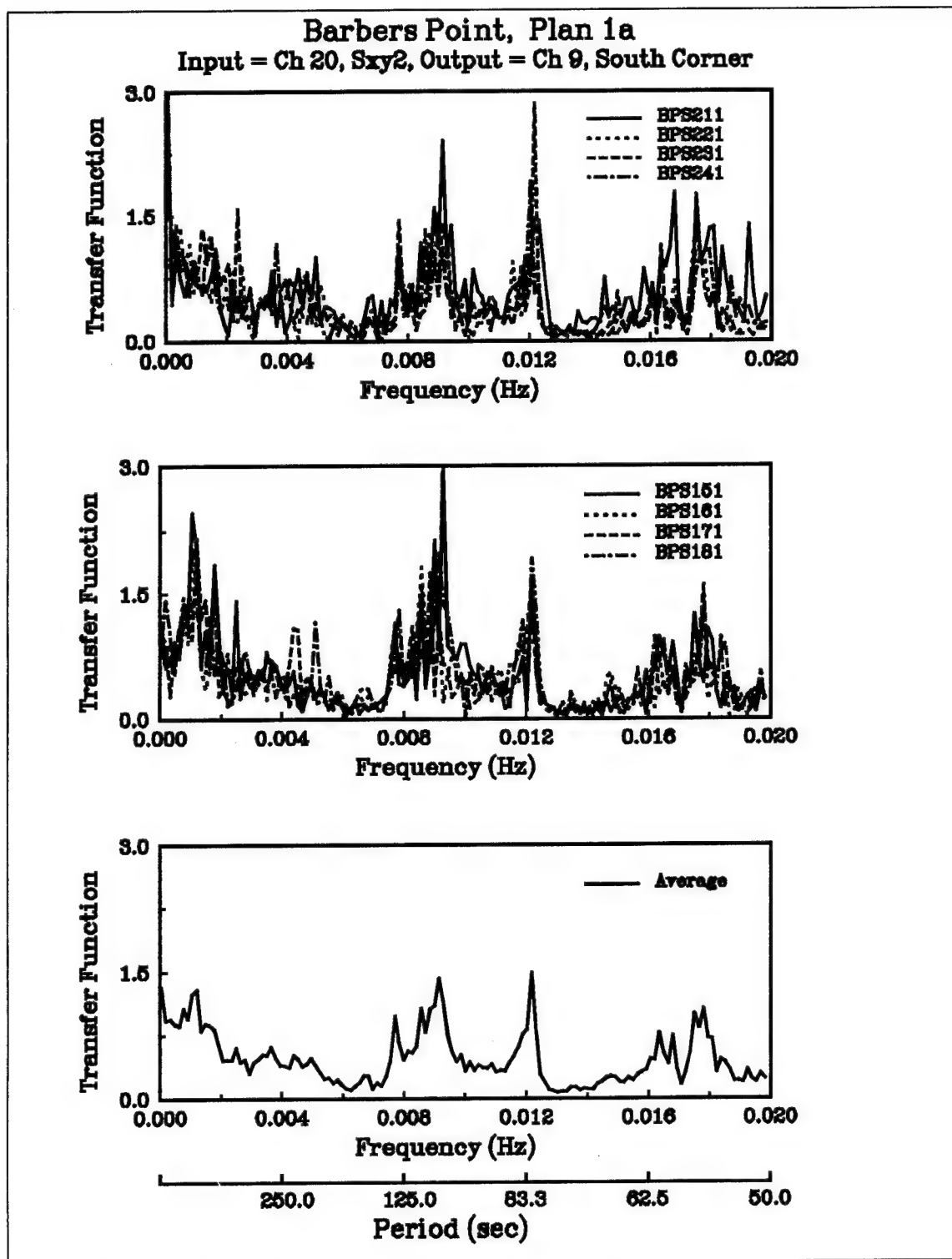


Figure 70. South corner transfer functions for test plan 1a

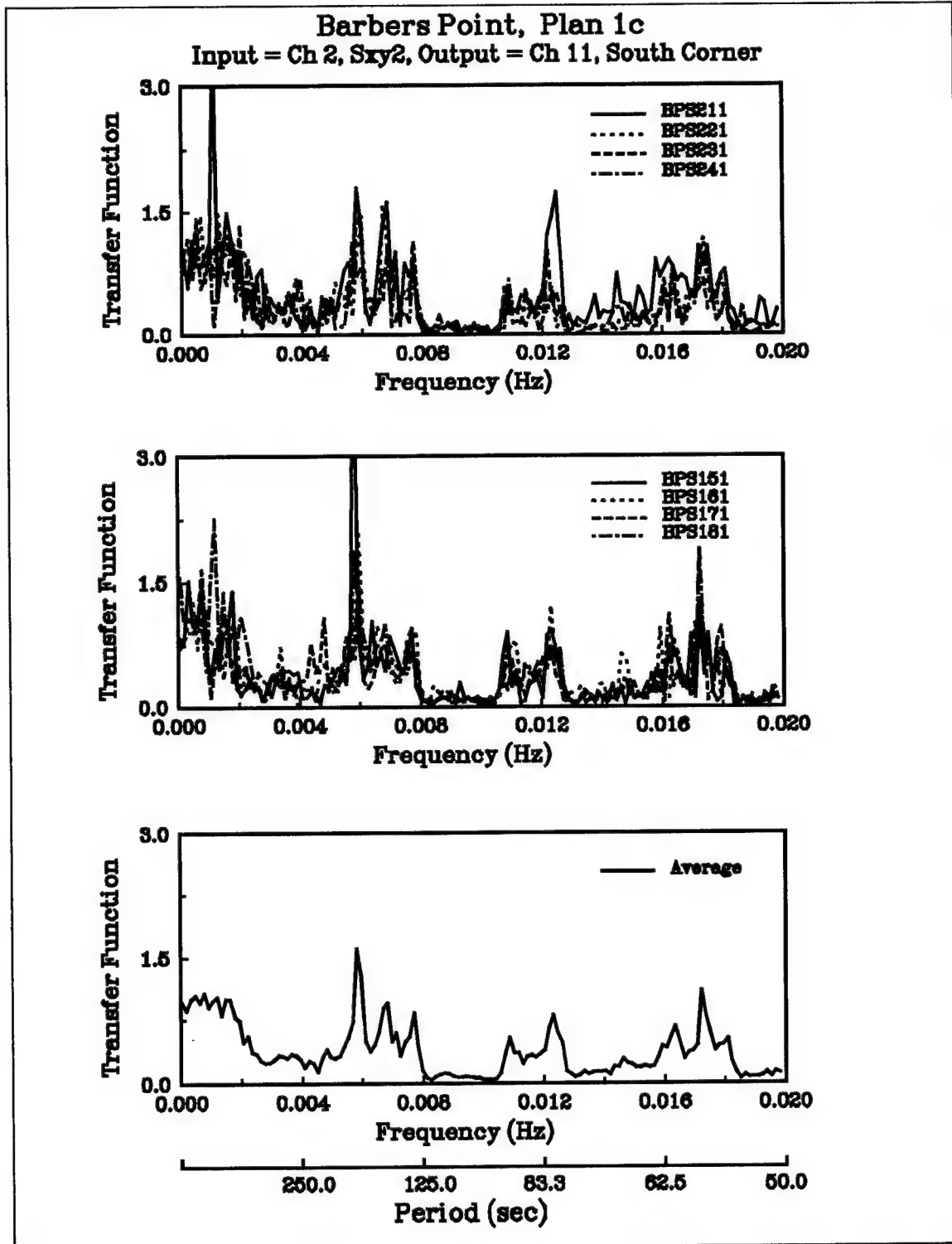


Figure 71. South corner transfer functions for test plan 1c

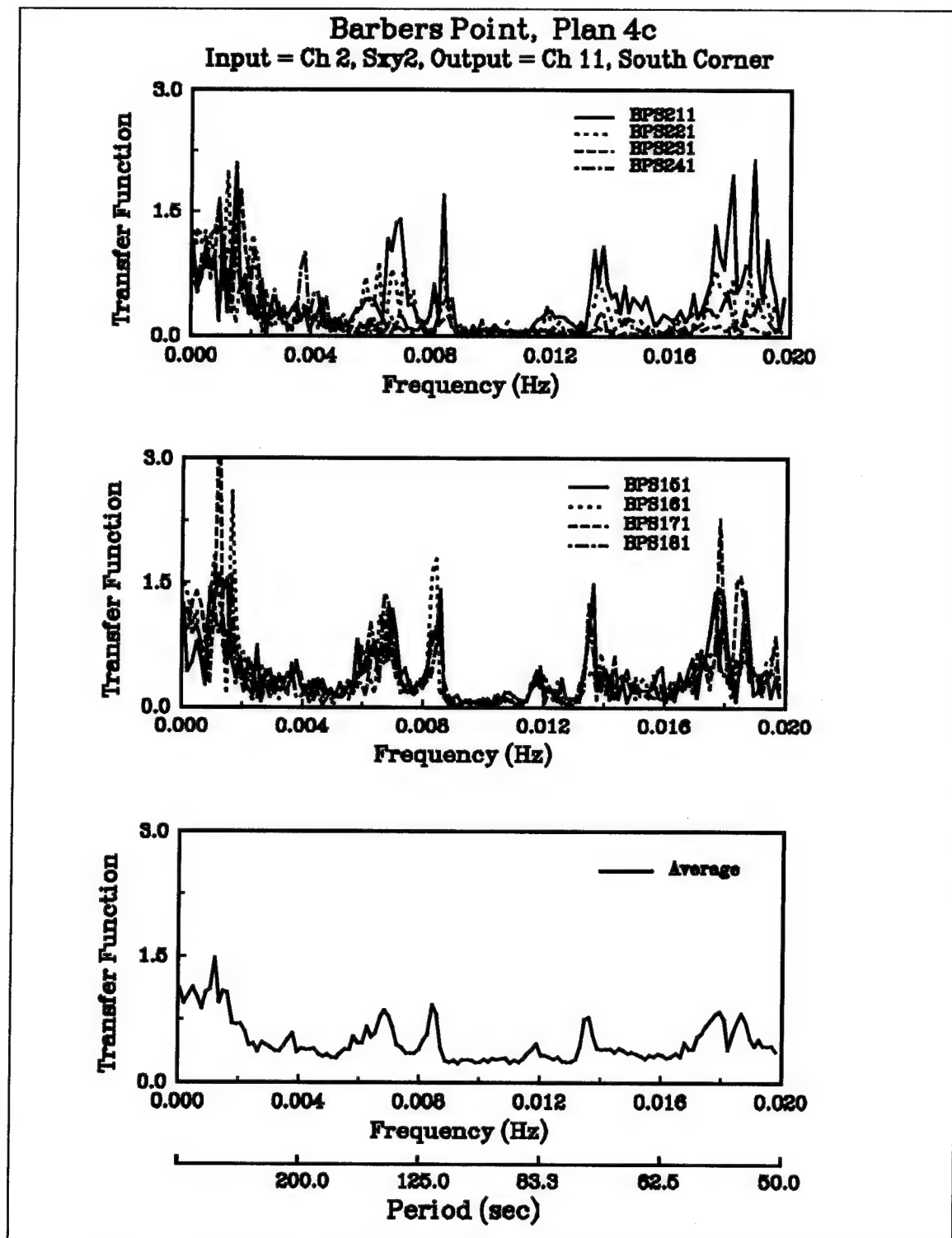


Figure 72. South corner transfer functions for test plan 4c

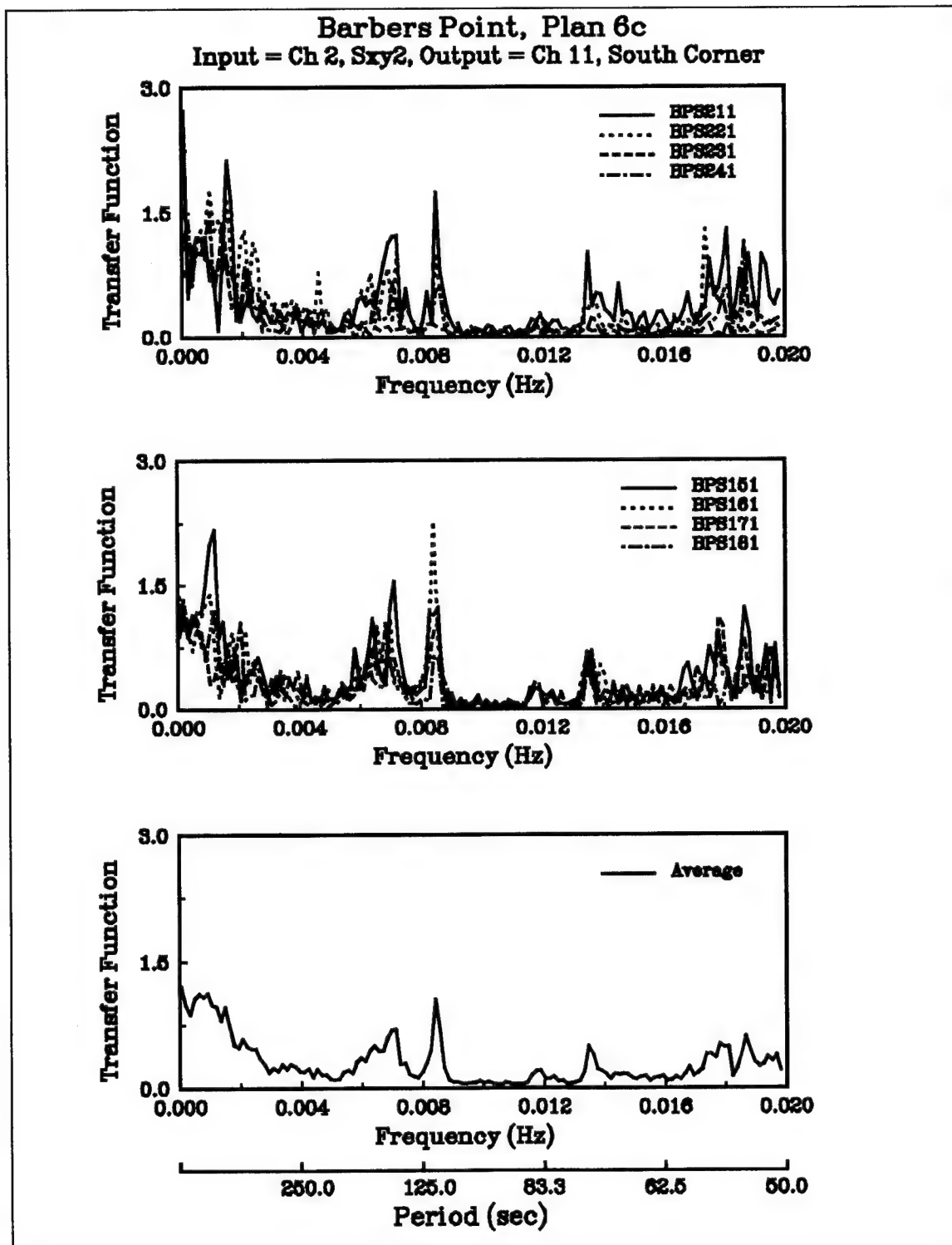


Figure 73. South corner transfer functions for test plan 6c

at 85 sec. Perhaps the fact that the wave was aligned with the entrance channel offsets some of the directional spreading for this case.

The harbor master should be able to predict what the long-wave response of the harbor will be for different wave conditions outside the harbor. This would be useful for forecasting “bad” mooring days for the C9 container ship and other similar vessels.

Again, addition of the 36 empirical wave cases tested in the physical model should complement the long-wave data from the eight wave cases and provide further insight into the long-wave response of the harbor.

6 Operational Considerations

Inbound ship transits are considerably more difficult than outbound transits. Wave effects are the most influential for navigation. Waves that approach at an angle, especially following swell, can produce serious maneuvering problems. Waves from the west with wave periods of 12.6 sec produced severe resonance rolling of the ship both offshore and inside the channel entrance. This wave condition is especially critical because there is no way to get the ship out once it is in the channel. Longshore currents from the north are more difficult than those from the south. Longshore currents are unpredictable, especially in combination with waves from the south to west. Offshore currents are stronger than inside the entrance channel, but in the channel current reversals or shears can make navigation difficult. Harbor pilots should be aware of these conditions so that they can delay ship transits if conditions appear to be dangerous.

The existing channel has insufficient width and depth for continued safe navigation for vessels as large as the C9 container ship used in this model study. Under certain wave, current, wind, and tide conditions, the C9 container ship can be safely navigated into and through the harbor. However, extreme care must be exercised if larger bulk carriers and container ships are brought into the harbor prior to the recommended modifications.

Ship speeds during channel transit should be maintained between 3 and 6 knots, decreasing to 3 knots at the harbor entrance (station 33). This speed range provides a reasonable trade-off between maneuverability and stopping distance inside the harbor. Tugs attached to the bow will provide additional resistance and control for the ship. The jetty will probably allow a higher ship speed in the inner part of the channel because the effective stopping distance at the end of the channel will be increased by 450 ft and entry maneuvers can be started earlier because of the jetty effect in minimizing crosscurrents and wind wave energy.

Since moored vessels can experience resonant oscillation if their natural periods in surge or sway correspond to a harbor resonance mode, care should be taken to avoid the vicinity of nodes and nodal lines for the harbor resonant modes. These nodal lines correspond to locations where amplitude of seiche motion is lowest and horizontal water particle velocities are largest. It is this property of the horizontal seiche-induced velocities which is most important to

harbor operations. Surge natural periods for a moored C9 container ship ranged from a low of 78 sec to a high of 143 sec. These values assume a constant mooring line tension from 10 to 30 tons and ship displacements from light operational to fully loaded.

A summary of locations where nodal lines from harbor resonant modes in this period range intersect existing or proposed harbor boundaries in the vicinity of the berthing areas is shown in Figure 74. For the existing harbor configuration (test plan 1a), a nodal line for the fundamental harbor length mode H_1 at 107 sec intersects the southeast wall. This mode could potentially pose a problem during loading/unloading operations if the ship should reach a medium load configuration. A nodal line for the second harmonic along the north-south diagonal H_{ns2} at 85 sec intersects the middle of the southeast wall. Extreme care should be exercised for the C9 containership in a light ship configuration. For test plan 1c, the second harmonic along the north-south diagonal H_{ns2} at 83 sec and the second harmonic along the length of the harbor H_{l2} at 96 sec intersect the southeast wall in two places, one in the expansion. Both of these modes would affect a C9 container ship with a light to medium ship displacement. For test plans 4c and 6c, the same two modes as for test plan 1c, H_{ns2} at 78 sec and H_{l2} at 91 sec, intersect at two places along the southeast wall. Again, one of these nodal lines intersects the harbor perimeter inside the proposed expansion. Care should be exercised if the C9 container ship reaches a light to medium ship displacement.

As the ship is offloaded, displacement of the ship will decrease, which will change the ship's response characteristics. Proper ballasting can be used to prevent surge and sway conditions from developing. If this is not possible, other remedies can be sought. The natural period of the moored ship can be adjusted by changing the mooring line configuration or tension. Increased tension will make the moored ship stiffer and will reduce its resonant period of oscillation. A decrease in the mooring line tension will make the moored ship less prone to shorter period resonant modes. If this is not practical, the number and type of mooring lines can be changed to affect the response of the moored ship.

Wind-wave and long-wave responses of the harbor to the eight different wave conditions are contained in the report for the four test plans 1a, 1c, 4c, and 6c. Harbor response data for the other test plans are contained in the appendices. These data can be used to help predict the response of the harbor to incident wind waves with different heights, periods, directions, and directional spreading. The harbor master could then know what type of conditions (i.e. wind-wave "chop" or long-period surge) to expect at different locations inside the harbor for various incident waves. In general, waves from the west produce the largest wind-wave response in the harbor. The addition of the 450-ft-long jetty should help alleviate this problem with wind waves. Long-wave response is greatest for waves with dominant swell energy and narrow directional spreading, in agreement with prototype observations. This long-wave response of the harbor should be useful for forecasting "bad" mooring days for the C9 container ship and other similar vessels.

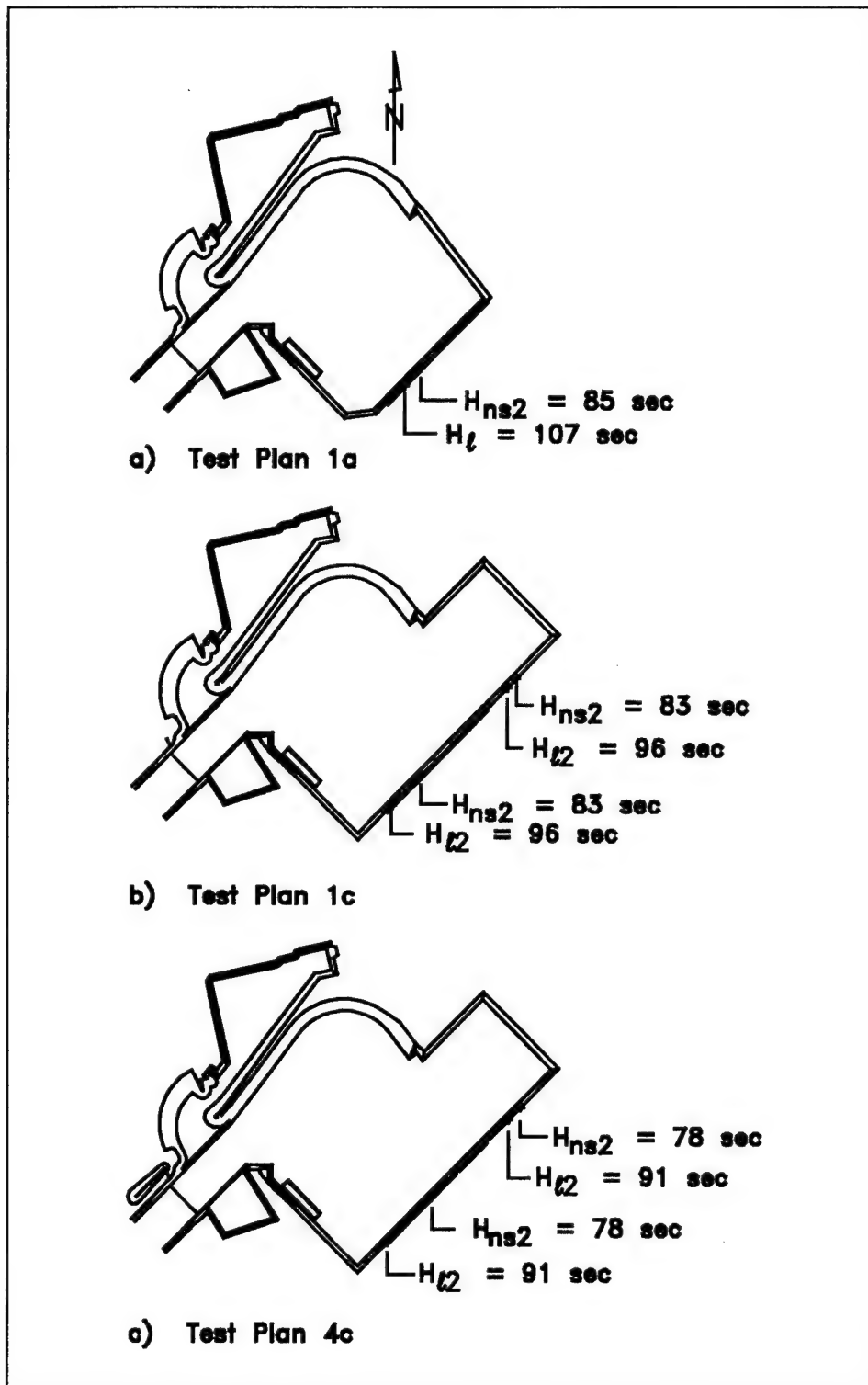


Figure 74. Locations of C9 moored ship potential surge problems

Additional insight into wind-wave and long-wave response of the harbor should be available in the future with the inclusion of 36 empirical wave cases tested in the physical model as part of an expanded research effort on harbor modeling. These wave cases covered a range of directional spectral parameters: half were unidirectional and half had directional spreading. All were unimodal with narrow and broad frequency spreading representative of sea and swell conditions.

Tilting (i.e. spar) buoys along the entrance channel and quartering ranges on both sides of the mid-channel central range would help in detecting changes in cross-channel currents, delineating the channel boundaries, and keeping the pivot point of the ship on the center-line range. Real-time knowledge of wave and current conditions along the entrance channel would improve navigation and safety conditions in actual day-to-day operations. Finally, long-term wave gauging for the harbor and additional longshore current data along the entrance channel would make it possible to calculate probabilities of critical wave and current occurrences for more extreme environmental conditions.

This study demonstrated that both numerical and physical models, in conjunction with prototype measurements, accurately predict harbor wave response. Given the strengths and limitations of each model, it is recommended that both models be used to evaluate the response of the harbor to long- and short-period wave conditions for future harbor expansions.

7 Recommendations and Conclusions

Based on tests and results reported herein, test plan 4c is the best design alternative for Barbers Point Harbor. This plan consists of (a) flaring the outer 1,000 ft of the entrance channel from a width of 450 ft to 750 ft, (b) constructing a 450-ft-long, shore-connected, rubble-mound jetty on the north side of the entrance channel, (c) deepening the harbor to 45 ft and the channel to 49 ft, and (d) adding the 1,100-ft by 1,100-ft harbor expansion. The channel flare improved navigation conditions at the entrance without significantly increasing wave energy entering the harbor. The jetty improved wind-wave conditions within the harbor, especially at the barge basin, and reduced an existing cross-current at the shoreline. Expanding the harbor improved wind-wave conditions in the interior part of the harbor, while conditions in the barge basin remained unchanged. The combination of the deeper flared channel, deeper harbor with the harbor expansion, and the jetty significantly improved wind-wave conditions throughout the harbor (including the proposed ferry terminal site) and barge basin. The effect of the jetty in reducing wind-wave conditions was less than the other changes to the channel and harbor. Surge conditions into the harbor were also significantly improved by the harbor expansion. Deepening the harbor and adding the jetty had a minimal effect on the harbor surge response. Surge conditions in the barge basin were not noticeably affected by the harbor expansion, harbor deepening, or the jetty. Ships frequently turn into the harbor too close to the wave absorbing point at station 41 between pier 1 and the "Big Mike" dry dock. The addition of the jetty will help alleviate this potential problem area. Recommended modifications to Barbers Point Harbor significantly improved wind-wave conditions at West Beach Marina over existing conditions. A slight improvement in surge conditions was observed.

Probabilities of groundings or accidents have been estimated for test plan 4c. Based on 200 ship calls per year, one accident could be expected every 22 to 56 years, depending on the combination of wind, wave, and current test conditions assumed. For maximum utilization of the harbor, a vessel density of 500 ship calls per year, the corresponding number of years between accidents would vary from 4 to 15 years. These results are comparable to worldwide experience. All estimates are based on the use of C9 container ships at two berths in the existing harbor and four berths in the expanded harbor. Also, this study did not include a mix of smaller vessels in

combination with the larger C9 container ship. It should be emphasized that these estimates are based on a probabilistic approach. An accident predicted to occur every 4 to 15 years might actually occur next year, several years in a row, or in a variety of possible combinations. Over a span of many years, they would average out as one every 4 to 15 years. These probabilities of unacceptable navigation events or accidents can also be related to downtime of the harbor. For example, one accident every 4 years for 500 ship calls per year utilization rate is equivalent to only 0.05 percent downtime of the harbor, a very low rate of downtime relative to worldwide standards.

Other recommendations include the following:

- This study demonstrated that both numerical and physical models, in conjunction with prototype measurements, accurately predict harbor wave response. Bottom friction coefficients in the numerical model HARBD were calibrated using prototype measurements. Given the strengths and limitations of each model, it is recommended that both models be used to evaluate the response of the harbor for future harbor expansions. Future modifications to the harbor can be evaluated using these models with a good degree of confidence in the results.
- Navigation tests were conducted using a model container ship. Since different hull shapes “feel (react to) the entrance channel” in different ways, navigation test results do not apply equally to all types of ships. Although a few qualitative (model was not in proper similitude) tests were conducted with a small bulk carrier model, it would be beneficial to conduct model tests with a larger bulk carrier (i.e., 900-ft length and 106-ft beam), representative of Barbers Point Harbor. This type ship has larger block coefficients (i.e., drag), less power, smaller rudders, slower response, larger metacentric heights, and faster roll periods than the container ships.
- Install tilting (i.e. spar) buoys as navigation aids along the entrance channel to identify current flows and delineate the channel boundaries. Buoys should be placed at the entrance (station 0), at the dogleg at the beginning of the flare (station 10), midway along the channel (station 21 to 24), and at the shoreline on both sides of the channel (station 33 to 36).
- Install quartering ranges on both sides of the mid-channel central range. Increase the distance between the existing central range marks. These changes will help in detecting changes in cross-channel currents and keeping the pivot point of the ship on the center-line range and yaw angles from becoming excessive (i.e. greater than 12 to 15 deg).
- Collect data on the mooring response of an actual container ship to compare to the predictions in this report.

- Investigate the feasibility of installing a computerized mooring line tensioning device, where tension winches with varying pulling force could actually prevent or bring the ship out of harmful resonance conditions. Also, use the "forced fendering" principle to maximize the design of fenders.

- Long-term wave gauging should be done for the harbor so that probabilities of critical wave occurrences can be calculated. Collect additional longshore current data along the entrance channel because previous prototype measurements may not be representative of extreme conditions which might exist. Real-time knowledge of wave and current conditions along the entrance channel will improve navigation and safety conditions in actual day-to-day operations.

- Once a long period of climatological data is available, conduct additional desktop study to develop more extensive operational guidelines for the harbor based on predictions from transfer functions for different wave and current conditions. If the incident wave conditions outside the harbor are known, or a representative yearly climate is described, the wind-wave and long-wave energy in the harbor can be predicted. Also, additional insight into the wind-wave and long-wave response of the harbor can be obtained in the future with the inclusion of 36 empirical wave cases tested in the physical model as part of an expanded research effort on harbor modeling. These wave cases covered a range of directional spectral parameters: half were unidirectional and half had directional spreading. All were unimodal with narrow and broad frequency spreading representative of sea and swell conditions.

- Calculate expected downtime per year from harbor resonance for the variety of ships using, or expected to use, Barbers Point Harbor. A more extensive wave and current database would be required. Investigate the joint probabilities of critical wave and current occurrences and their effects on ship downtime.

- Identify prevailing wave and current conditions present during past groundings to determine if they were a significant reason for the accident. Make recommendations for operational guidelines.

- Predict the dynamic response of the C9 container ship and other moored ships in surge using stochastic methods. Significant surge (like a significant wave height) can be estimated from the response amplitude operator for the ship and representative sea states. Thus, for a particular sea state, the ship's dynamic response in surge could be estimated, much like a "cause and effect" relationship.

- Additional physical model tests with quantitative measurements of underkeel clearances could be used to optimize the dredging depth required for the entrance channel and harbor. This information could be

used to relate different harbor depths to expected downtime of the harbor.

- The physical model proved to be an excellent learning aid for the two harbor pilots who participated in the navigation tests. Both noted the realism of the model and the benefit this had for navigating the prototype entrance channel.

References

- Berteaux, H. O. (1976). "Buoy engineering." John Wiley & Sons, New York, 314.
- Bottin, R. R., Jr., Sargent, F. E., and Mize, M. G. (1985). "Fisherman's Wharf Area, San Francisco Bay, California, design for wave protection: Physical and numerical model investigation," Technical Report CERC-86-7, U.S. Army Engineer Waterways Experiment Station, Vicksburg, Ms.
- Bowers, E. C. (1977). "Harbor resonance due to set-down beneath wave groups," *J. Fluid Mech.* 79, 71-92.
- _____. (1993). "Low frequency waves in intermediate depth." *Proceedings of 23rd International Conference on Coastal Engineering (ICCE)*.
- Bratteland, E. (1987). "Advances in berthing and mooring of ships and offshore structures," *NATO ASI-Series*, Trondheim, Norway. Kluwer Academic Publishers, Dordrecht, The Netherlands, 1988.
- _____. (1991). "Barbers Point: Currents and navigation tests, preliminary report," (unpublished manuscript), U.S. Army Engineer Waterways Experiment Station, Vicksburg, MS, 1-51.
- _____. (1992a). "Barbers Point navigation tests: Flared channel, 550 to 450 ft and parallel channel 550 ft, preliminary report No. 2," (unpublished manuscript), U.S. Army Engineer Waterways Experiment Station, Vicksburg, MS, 1-23.
- _____. (1992b). "Barbers Point navigation study: Engineering probability assessment, preliminary report No. 3," (unpublished manuscript), U.S. Army Engineer Waterways Experiment Station, Vicksburg, MS, 1-28.
- _____. (1992c). "Barbers Point navigation tests: Flared outer channel and breakwater north shore, preliminary report No. 4," (unpublished manuscript), U.S. Army Engineer Waterways Experiment Station, Vicksburg, MS, 1-46.

- Bratteland, E. (1992d). "Barbers Point navigation tests: Final tests at June, '92 conference, preliminary report No. 5," (unpublished manuscript), U.S. Army Engineer Waterways Experiment Station, Vicksburg, MS, 1-31.
- _____. (1992). "Probability assessment of physical model navigation tests," (unpublished journal manuscript), 1-28.
- Briggs, M. J. (1993). "Making waves at CERC," *Journal of Coastal Research* 9(2) Spring, 448-61.
- _____. (1994). "Physical and numerical model studies of Barbers Point Harbor, Oahu, Hawaii." *Proceedings of the 57th Meeting of the Coastal Engineering Research Board*. 27-29 October 1992, Honolulu, HI, 1-6.
- Briggs, M. J., and Boc, S. J. (1991). "Physical model testing of Barbers Point Harbor and Marina Complex." *World Marina '91*, Long Beach, CA, 391-401.
- Briggs, M. J., and Bratteland, E. (1992). "Barbers Point Harbor: A unique solution for port upgrade." *Ports '92*, Seattle, WA, 777-90.
- Briggs, M. J., Borgman, L. E., and Outlaw, D. G. (1987). "Generation and analysis of directional spectral waves in a laboratory basin." *Offshore Technology Conference*. Paper OTC 5416, Houston, TX, 495-502.
- Briggs, M. J., Lillycrop, L. S., and McGehee, D. D. (1992). "Comparison of model and field results for Barbers Point Harbor." *Coastal Engineering Practice '92*, Long Beach, CA, 387-99.
- Bruun, P. (1990). *Port engineering*. 4th ed., Vol. 1 and 2, Gulf Publishing Company, Houston, TX.
- Chen, H. S. (1984). "Hybrid element modeling of harbor resonance." *Proceedings of the 4th international conference on applied numerical modeling*. 312-316.
- _____. (1986). "Effects of bottom friction and boundary absorption on water wave scattering," *Applied Ocean Research* 8(2), 99-104.
- Chen, H. S., and Houston, J. R. (1987). "Calculation of water oscillation in coastal harbors: HARBS and HARBD user's manual," Instruction Report CERC-87-2, U.S. Army Engineer Waterways Experiment Station, Vicksburg, MS.
- Chen, H. S., and Mei, C. C. (1974). "Oscillations and wave forces in an offshore harbor," Report No. 190, Department of Civil Engineering, Massachusetts Institute of Technology, Cambridge, MA.

- Cialone, M. A., Mark, D. J., Chou, L. W., Leenknecht, D. A., Davis, J. E., Lillycrop, L. S., and Jensen, R. E. (1991). "Coastal Modeling System (CMS) User's Manual," Instruction Report CERC-91-1, U.S. Army Engineer Waterways Experiment Station, Vicksburg, MS.
- Clausner, J. E., and Abel, C. E. (1987). "Contained aquatic disposal: Site location and cap material investigations for outer Indiana Harbor, Indiana, and Southern Lake Michigan," Appendix J, Vol II, *Disposal alternatives for PCB-contaminated sediments from Indiana Harbor*, Miscellaneous Paper EL-87-9, U.S. Army Engineer Waterways Experiment Station, Vicksburg, MS.
- Crawford, P. L., and Chen, H. S. (1988). "Comparison of numerical and physical models of wave response in a harbor," Miscellaneous Paper CERC-88-11, U.S. Army Engineer Waterways Experiment Station, Vicksburg, MS.
- Davis, J. D., and MacKnight S., et al. (1990). "Environmental considerations for port and harbor developments," World Bank Technical Paper No. 126, Washington, DC.
- Durham, D. L. (1978). "Numerical analysis of harbor oscillations for Barbers Point deep-draft harbor," Technical Report HL-78-20, U.S. Army Engineer Waterways Experiment Station, Vicksburg, MS.
- Elgar, S., Herbers, T. C., Okihiro, M., Oltman-Shay, J., and Guza, R. T. (1992). "Observations of infragravity waves," *Journal of Geophysical Research* 97(C10), 15573-77.
- Farrar, P. D., and Chen, H. S. (1987). "Wave response of the proposed harbor at Agat, Guam: Numerical model investigation," Technical Report CERC-97-4, U.S. Army Engineer Waterways Experiment Station, Vicksburg, MS.
- Fittschen, T., and Scheffer, H. J. (1987). "Simulation of group bounded long waves with a self-correcting system." *IAHR Seminar on Wave Analysis and Generation in Laboratory Basins*. Lausanne, Switzerland, 341-50.
- Harkins, G. S. (1991). "Sensitivity analysis for multi-element wavemakers," M.S. thesis, University of Delaware, Newark.
- Harkins, G. S., and Briggs, M. J. (1993). "Physical modelling of Barbers Point Harbor." *Coastal Zone '93*, New Orleans, LA, 1-15.
- Herbers, T. C., Elgar, S., Guza, R. T., and O'Reilly, W. C. (1992). "Infragravity-frequency (0.005-0.05 Hz) motions on the shelf." *Proceedings of 23rd International Conference on Coastal Engineering (ICCE)*.

- Herbich, J. B., ed. (1990, 1991, 1992). *Handbook of coastal and ocean engineering*. Vols. 1, 2 and 3, Gulf Publishing Company, Houston, TX.
- Houston, J. R. (1976). "Long Beach Harbor numerical analysis of harbor oscillation; Report 1, existing conditions and proposed improvements," Miscellaneous Paper H-76-20, U.S. Army Engineer Waterways Experiment Station, Vicksburg, MS.
- _____. (1981). "Combined refraction and diffraction of short waves using the finite element method," *Applied Ocean Research* 3(4), 163-170.
- Kaihatu, J. M., Lillycrop, L. S., and Thompson, E. F. (1989). "Effects of entrance channel dredging at Morro Bay, California," Miscellaneous Paper CERC-89-3, U.S. Army Engineer Waterways Experiment Station, Vicksburg, MS.
- Kwik, K. H. (1992). "A system analysis for optimal management of canal ship traffic," *PIANC Bulletin* 76.
- Lee, T. T. (1985). "Proposed West Beach Marina hydraulic model investigation," TR No. 59, Univ. of Hawaii, Look Lab-85-1, Honolulu, HI.
- LeMehaute, B., and Hanes, D. (1990). *Ocean engineering science, the sea*. Vol. 9, Wiley Interscience, John Wiley & Sons, Inc., NY, 1-1301.
- Lillycrop, L. S., and Briggs, M. J. (1992). "Capabilities in harbor design and monitoring: A case study," CETN-I-54, U.S. Army Engineer Waterways Experiment Station, Vicksburg, MS.
- Lillycrop, L. S., Bratos, S. M., and Thompson, E. F. (1990). "Wave response of proposed improvements to the shallow-draft harbor at Kawaihae, Hawaii," Miscellaneous Paper CERC-90-8, U.S. Army Engineer Waterways Experiment Station, Vicksburg, MS.
- Lillycrop, L. S., Bratos, S. M., Thompson, E. F., and Rivers, P. (1993a). "Wave response of proposed improvements to the small boat harbor at Maalaea, Maui, HI," Miscellaneous Paper CERC-93-4, U.S. Army Engineer Waterways Experiment Station, Vicksburg, MS.
- Lillycrop, L. S., Briggs, M. J., Harkins, G. S., Boc, S. J., and Okihiro, M. S. (1993b). "Barbers Point Harbor, Oahu, Hawaii monitoring study," Technical Report CERC-93-18, U.S. Army Engineer Waterways Experiment Station, Vicksburg, MS.
- Lillycrop, L. S., Thompson, E. F., and Briggs, M. J. (1991). "Model comparisons of harbor wave response." *Coastal Zone '91*, Long Beach, CA, 894-903.

- Marine Safety International. (1988). "American President Lines Barbers Point Harbor simulation study," MSI/CAORF TR CAORF 24-8806-01, National Maritime Research Center, Kings Point, NY.
- Mei, C. C., and Agnon, Y. (1989). "Long-period oscillations in a harbor induced by incident short waves," *J. Fluid Mech.* 208, 595-608.
- Miller, I. R., Freund, J. E., and Johnson, R. (1990). *Probability and statistics for engineers*. 4th ed., Prentice Hall, NJ.
- Noda, Edward K., and Associates, Inc. (1988). "Evaluation of surge forces for the Barbers Point deep-draft harbor," prepared for Nakamura and Tyau, Inc. and DOT, Harbors Division, State of Hawaii.
- Norwegian Society for Chartered Engineers. (1988). *Guidelines for port engineering*. Vol. 1, "Port planning," Vol. 2, "Port structures and equipment," Oslo, Norway.
- Okihiro, M. (1991). "Barbers Point Harbor transfer function," Scripps Institution of Oceanography, (unpublished manuscript), 1-5.
- _____. (1993). "Seiche in a small harbor," Ph.D. diss. Scripps Institution of Oceanography, University of California, San Diego.
- Okihiro, M., and Seymour, R. J. (1992). "Barbers Point Harbor resonance study," Scripps Institution of Oceanography, (unpublished manuscript), 1-26.
- Okihiro, M., Guza, R. T., and Seymour, R. J. (1992). "Bound infragravity waves," *Journal of Geophysical Research* 97(C7), 11,453-469.
- Oltman-Shay, J. M. (1987). "Linear Arrays: Wind Wave Directional Measurement Systems," Seminar at U.S. Army Engineer Waterways Experiment Station, Vicksburg, MS, 1-28.
- Outlaw, D. G., and Briggs, M. J. (1986). "Directional irregular wave generator design for shallow wave basins." *21st American Towing Tank Conference*, August 7, Washington, DC, 1-6.
- Palmer, R. Q. (1970). "Study of proposed Barbers Point Harbor, Hawaii: Hydraulic model investigation," TR No. 8, U.S. Army Engineer District, Honolulu, HI.
- Sand, S. E., Terslov, O., and Cheong, T. A. (1991). "Simulation study of Singapore's Brani container terminal," *The Dock & Harbour Authority* 72 (November).

- Sargent, F. E. (1989). "Los Angeles - Long Beach Harbor Complex 2020 Plan harbor resonance analysis: Numerical model investigation," Technical Report CERC-89-16, U.S. Army Engineer Waterways Experiment Station, Vicksburg, MS.
- Sea Engineering, Inc. (1988). "Barbers Point Entrance Channel current study," Technical Report No. 8, October, Waimanalo, HI.
- Sea Engineering, Inc. (1991). "Barbers Point Harbor Entrance Channel, Summary of Ocean Currents and Conceptual Design of a Real Time Measurement Program," August, Waimanalo, HI.
- Seitz, F. C., Jr. (1988). "American President Lines Barbers Point Harbor simulation study," Marine Safety International, MSI/CAORF TR CAORF 24-8806-01, National Maritime Research Center, Kings Point, NY.
- Seymour, R. J., Castel, D., and Thomas, J. O. "Coastal data information program," Annual Reports, University of California, San Diego, Scripps Institution of Oceanography.
- Smith, E. R., Sargent, F. E., Lillycrop, L. S., Briggs, M. J., and Boc, S. J. (1990). "Model studies of Barbers Point Harbor and Marina," *Applied Marina Research*, San Diego, CA, 1-18.
- Stevens, J. C., et al. (1942). "Hydraulic models," *Manuals of Engineering Practice No. 25*, American Society of Civil Engineers, New York.
- Thoresen, C. A. (1988). *Port design. Guidelines and recommendations*. Tapir Publishers, Trondheim, Norway.
- U.S. Army Engineer Division, Pacific Ocean. (1990). "Barbers Point Harbor modification study," preliminary draft, U.S. Army Engineer District, Honolulu, July.
- Weishar, L. L., and Aubrey, D. G. (1986). "Inlet hydraulics at Green Harbor, Marshfield, Massachusetts," Miscellaneous Paper CERC-88-10, U.S. Army Engineer Waterways Experiment Station, Vicksburg, MS.
- Wu, J. -K., and Liu, P. L. -F. (1990). "Harbor excitations by incident wave groups," *J. Fluid Mech.* 217, 595-613.

Appendix A

Physical Model

List of Figures

Figure A1.	Model gauge locations for plan 1a-1	A2
Figure A2.	Model gauge locations for plan 1a-2	A3
Figure A3.	Model gauge locations for plan 1a-3	A4
Figure A4.	Model gauge locations for plan 1c	A5
Figure A5.	Model gauge locations for plan 2c	A6
Figure A6.	Model gauge locations for plan 3a	A7
Figure A7.	Model gauge locations for plan 3c	A8
Figure A8.	Model gauge locations for plan 4c	A9
Figure A9.	Model gauge locations for plan 5c	A10
Figure A10.	Model gauge locations for plan 6c	A11

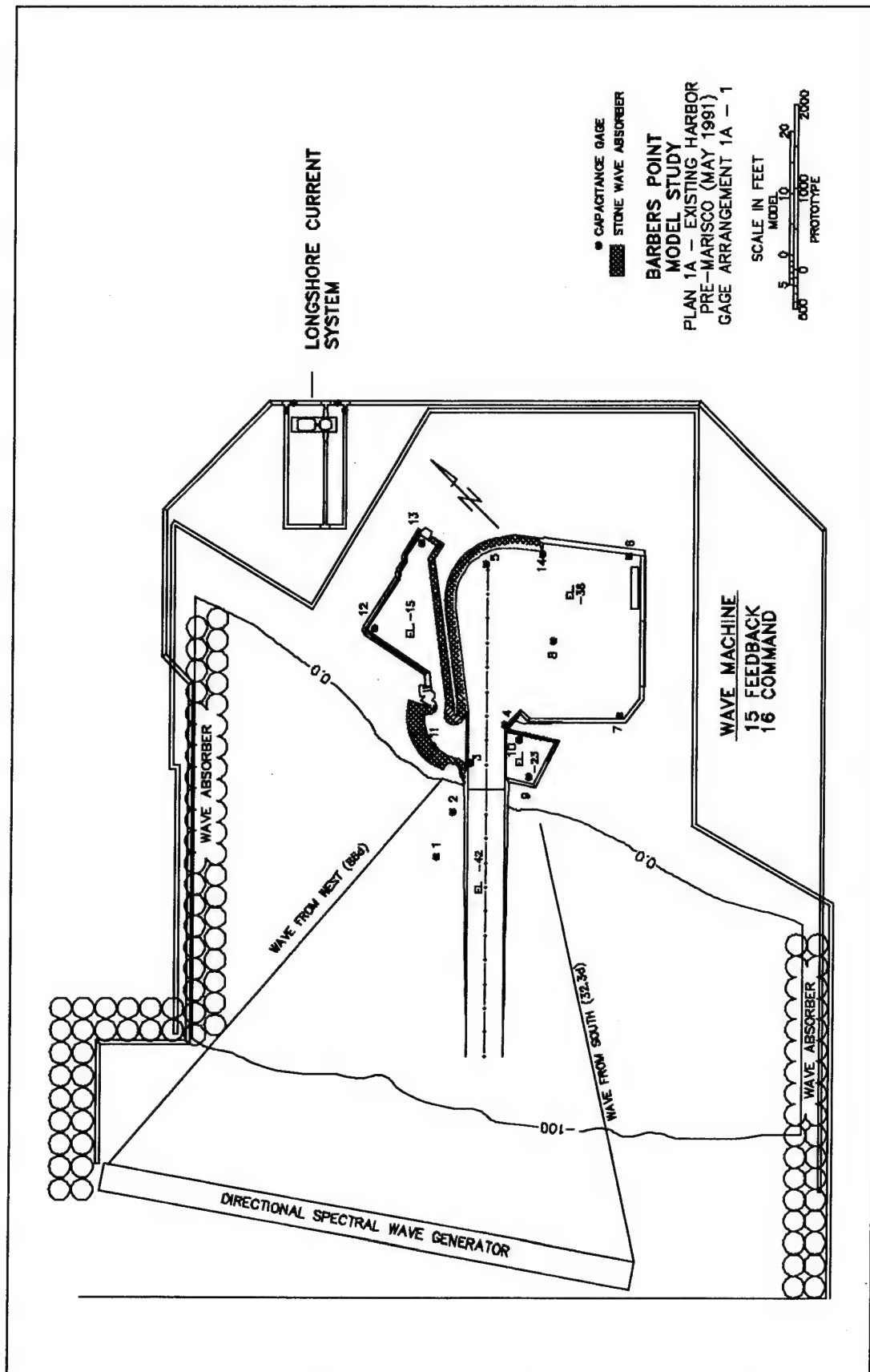


Figure A1. Model gauge locations for plan 1a-1

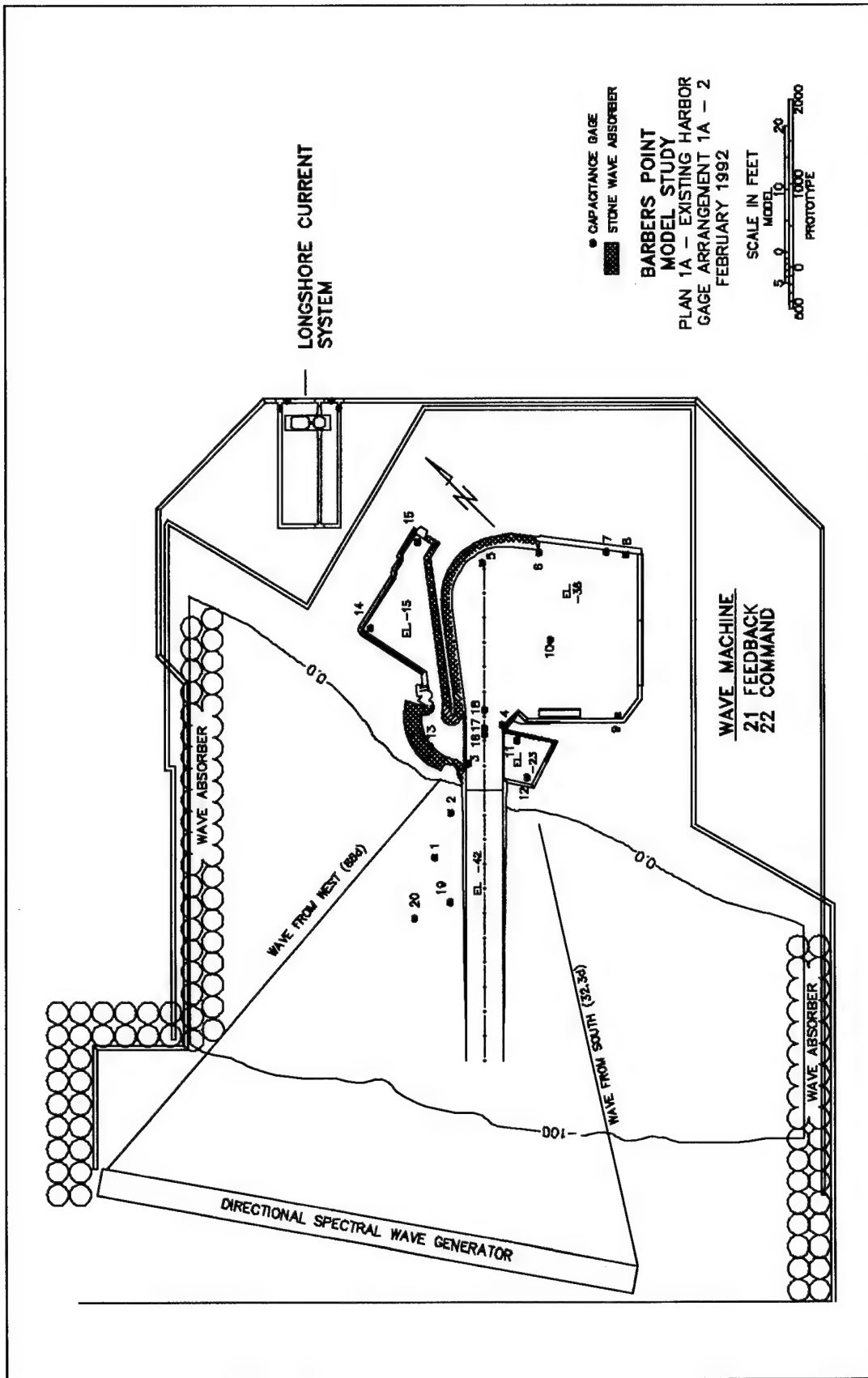


Figure A2. Model gauge locations for plan 1a-2

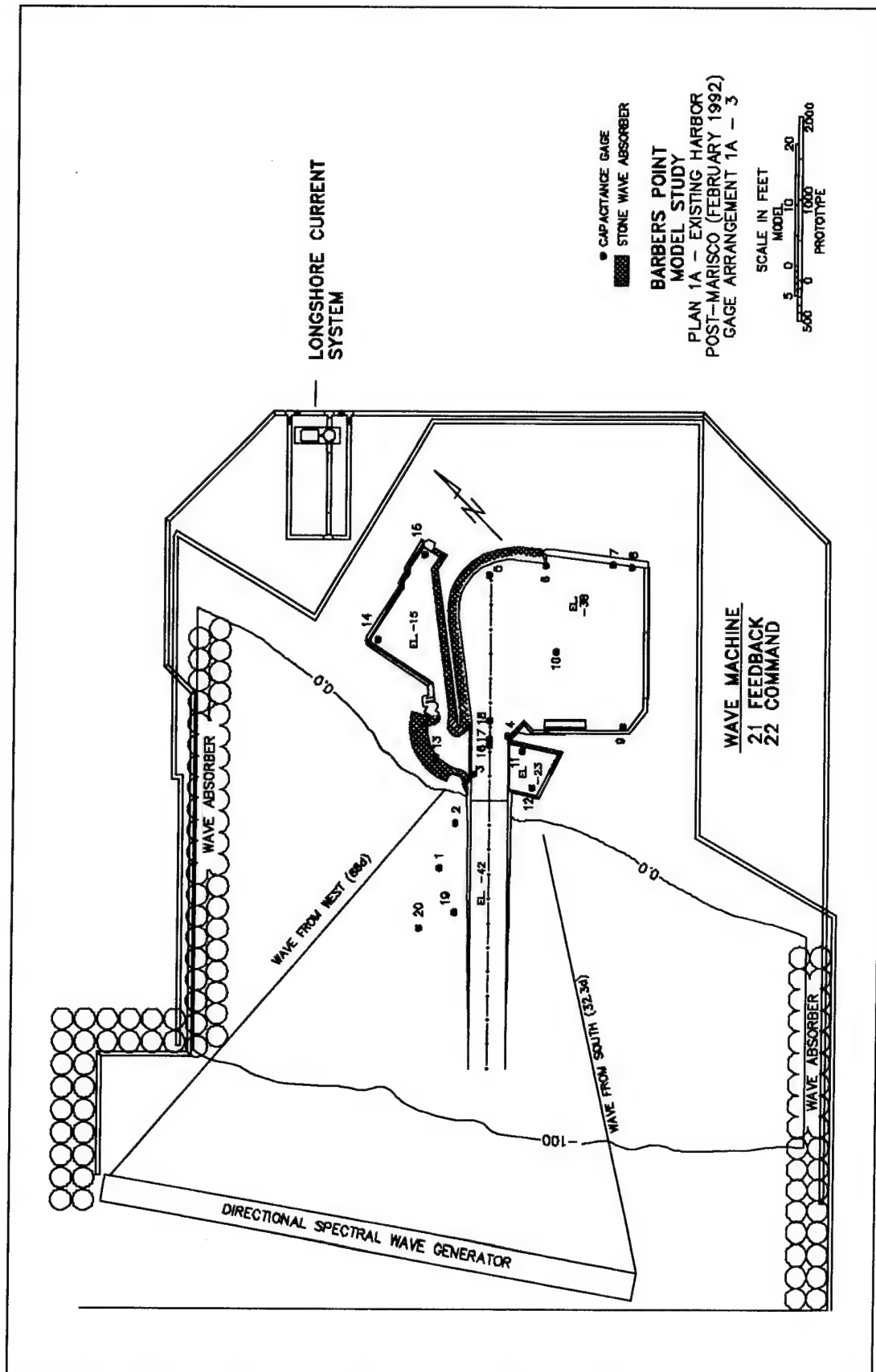


Figure A3. Model gauge locations for plan 1a-3

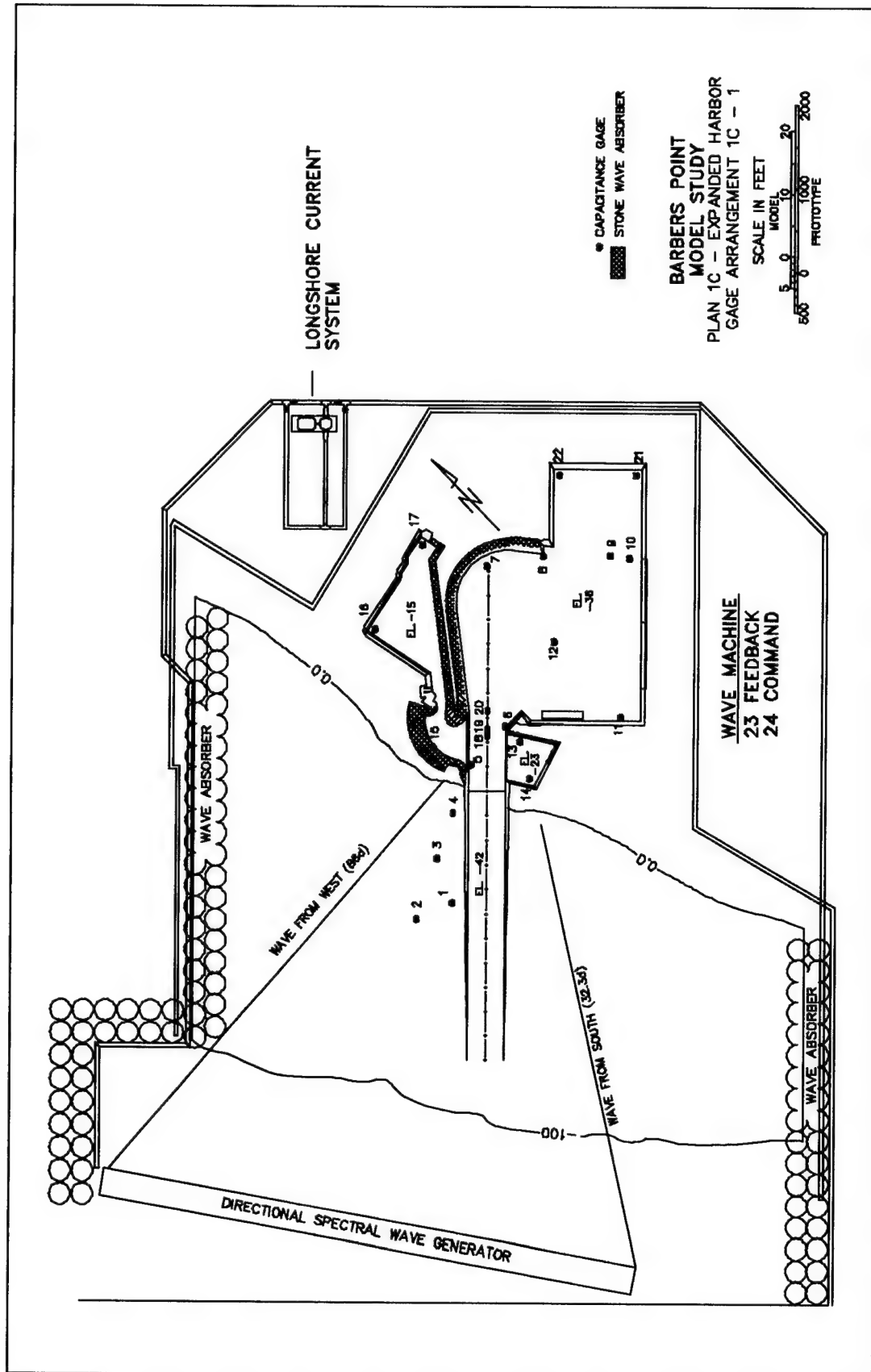


Figure A4. Model gauge locations for plan 1c

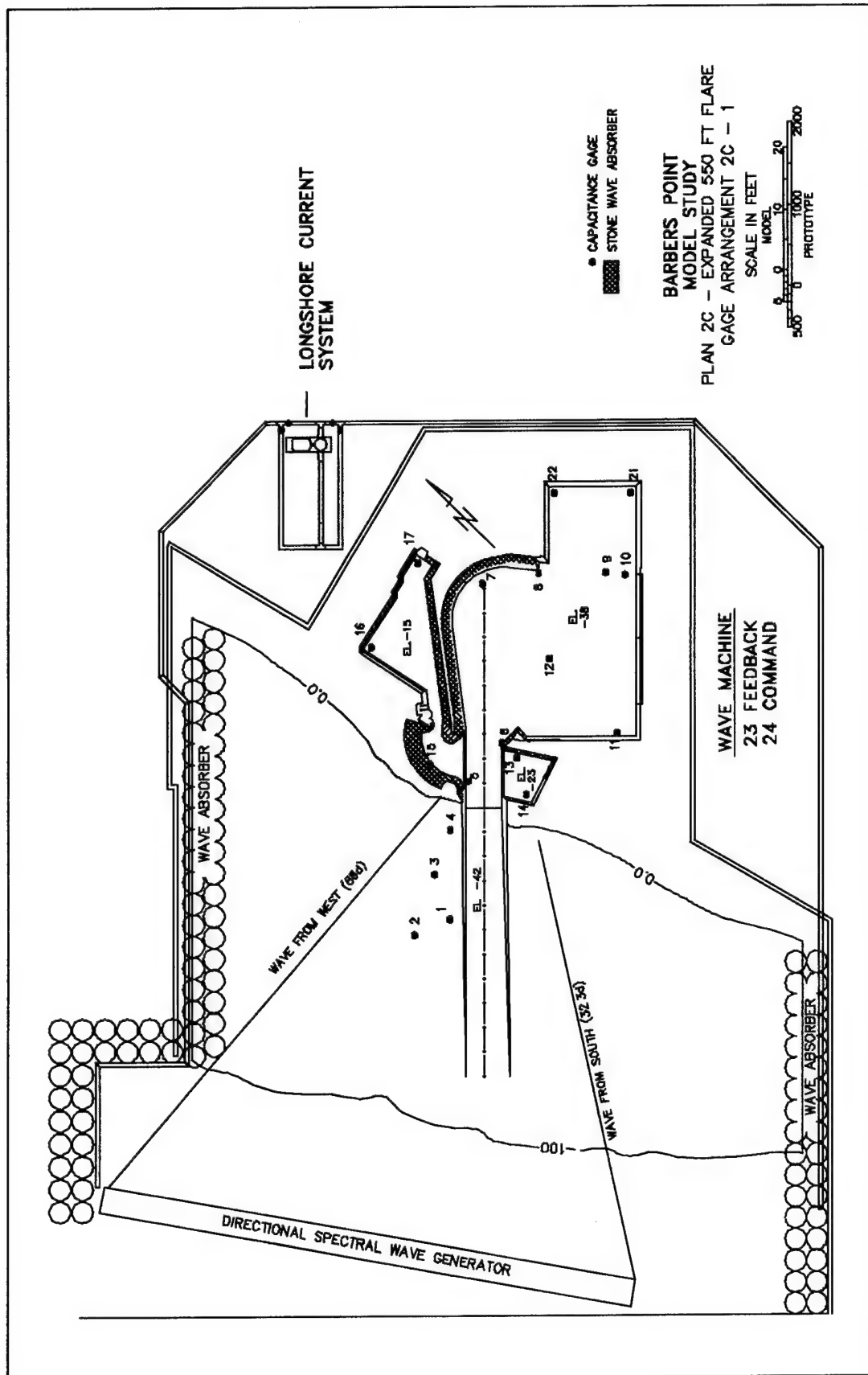


Figure A5. Model gauge locations for plan 2c

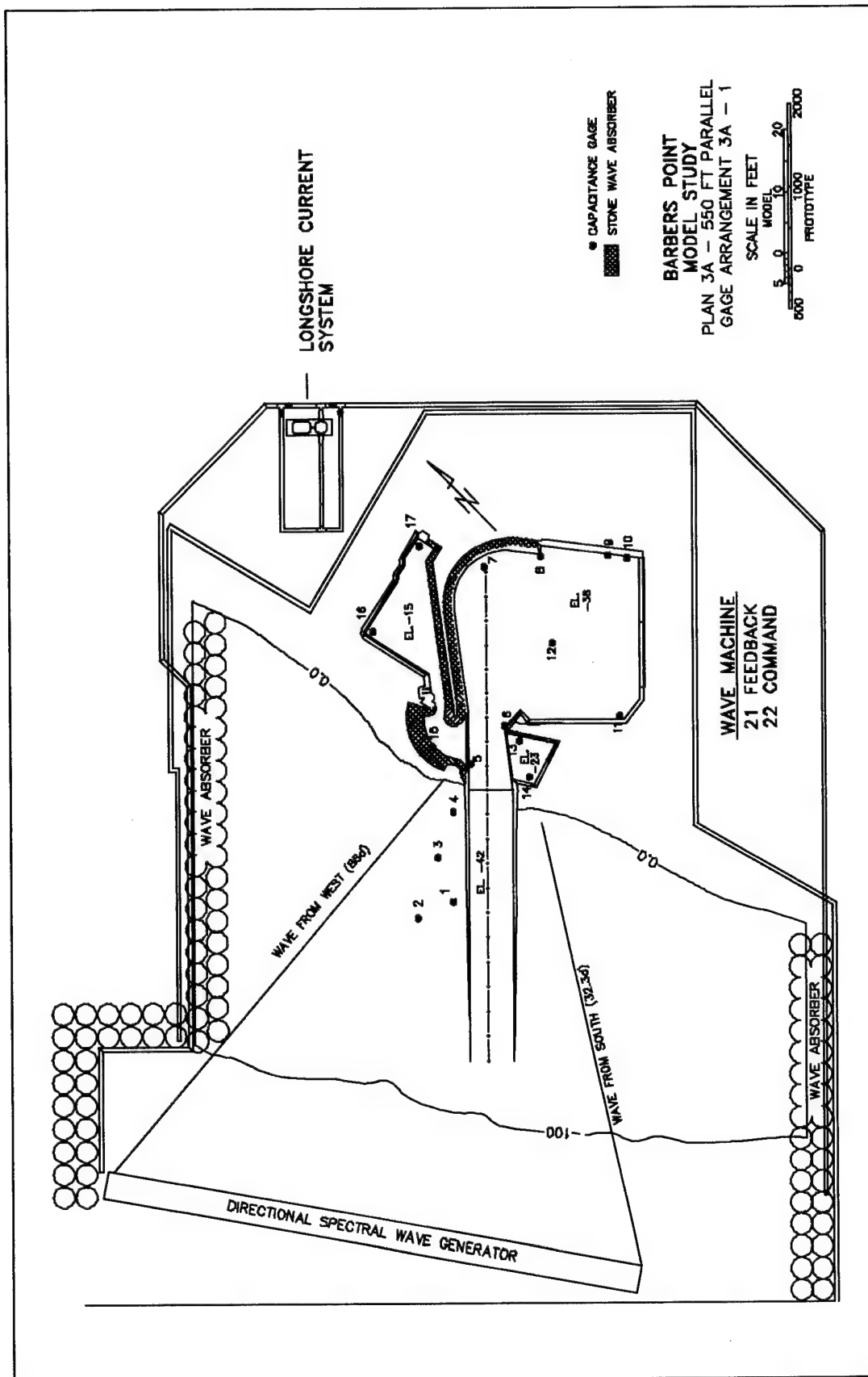


Figure A6. Model gauge locations for plan 3a

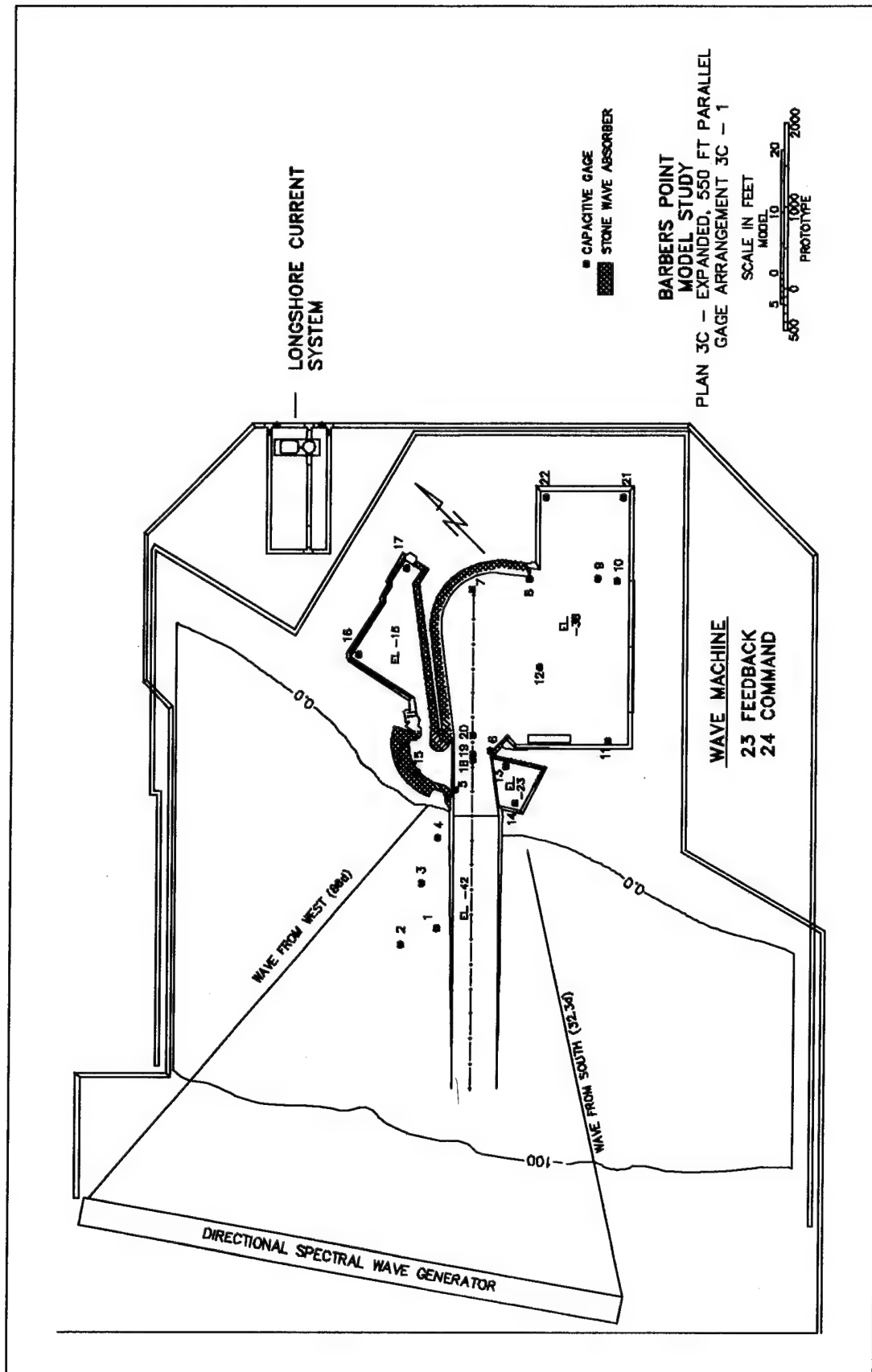


Figure A7. Model gauge locations for plan 3c

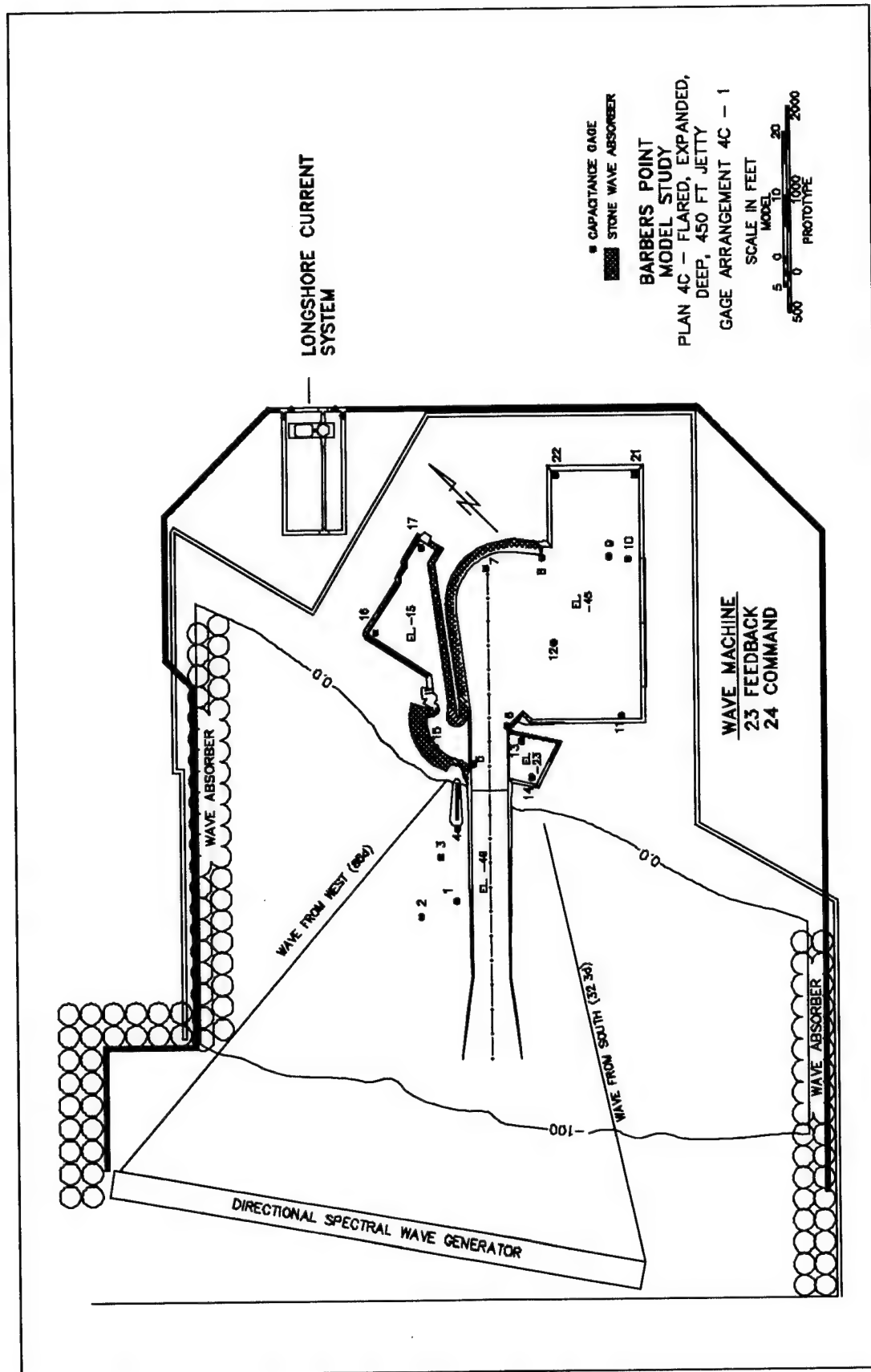


Figure A8. Model gauge locations for plan 4c

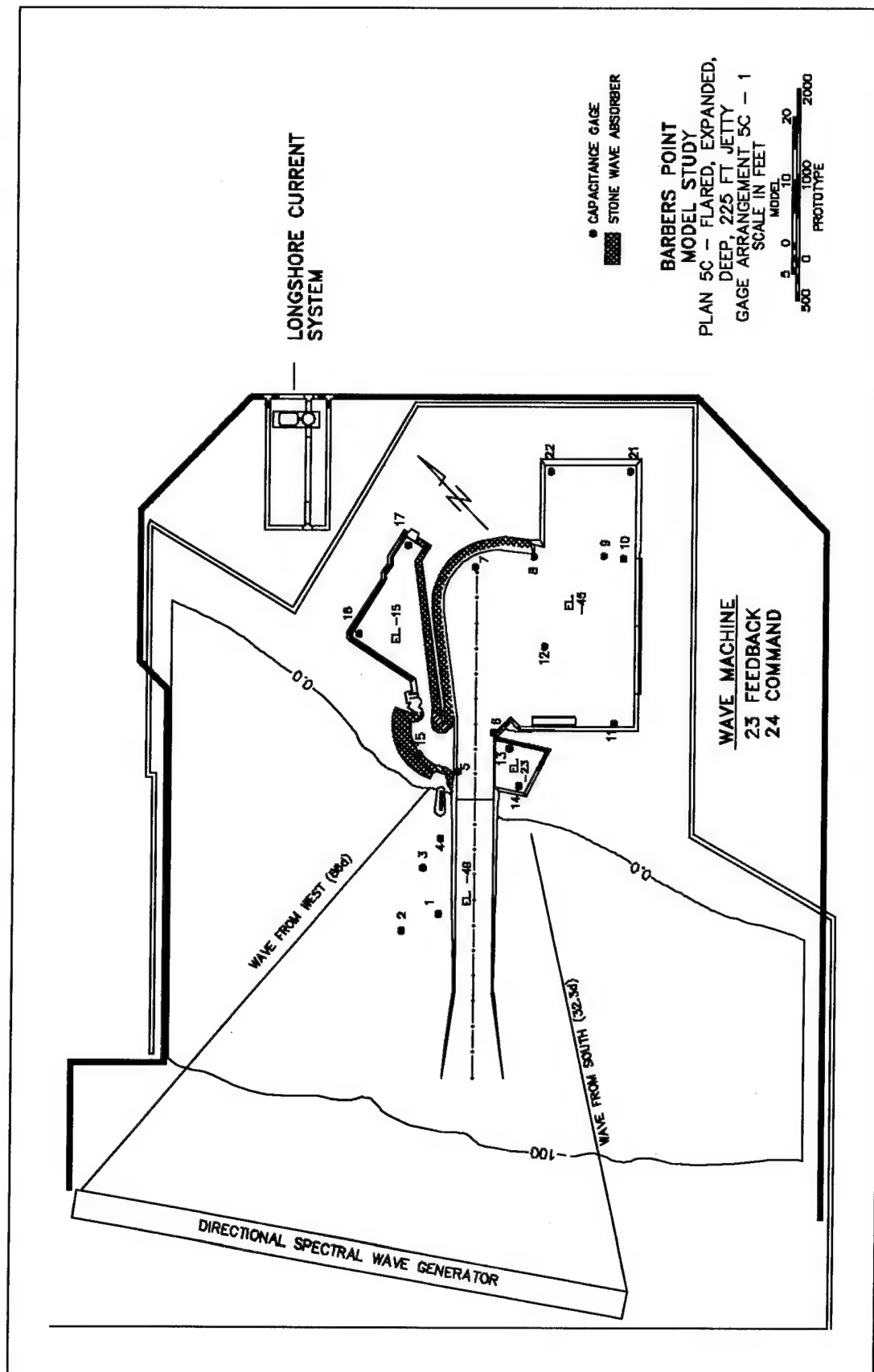


Figure A9: Model gauge locations for plan 5c

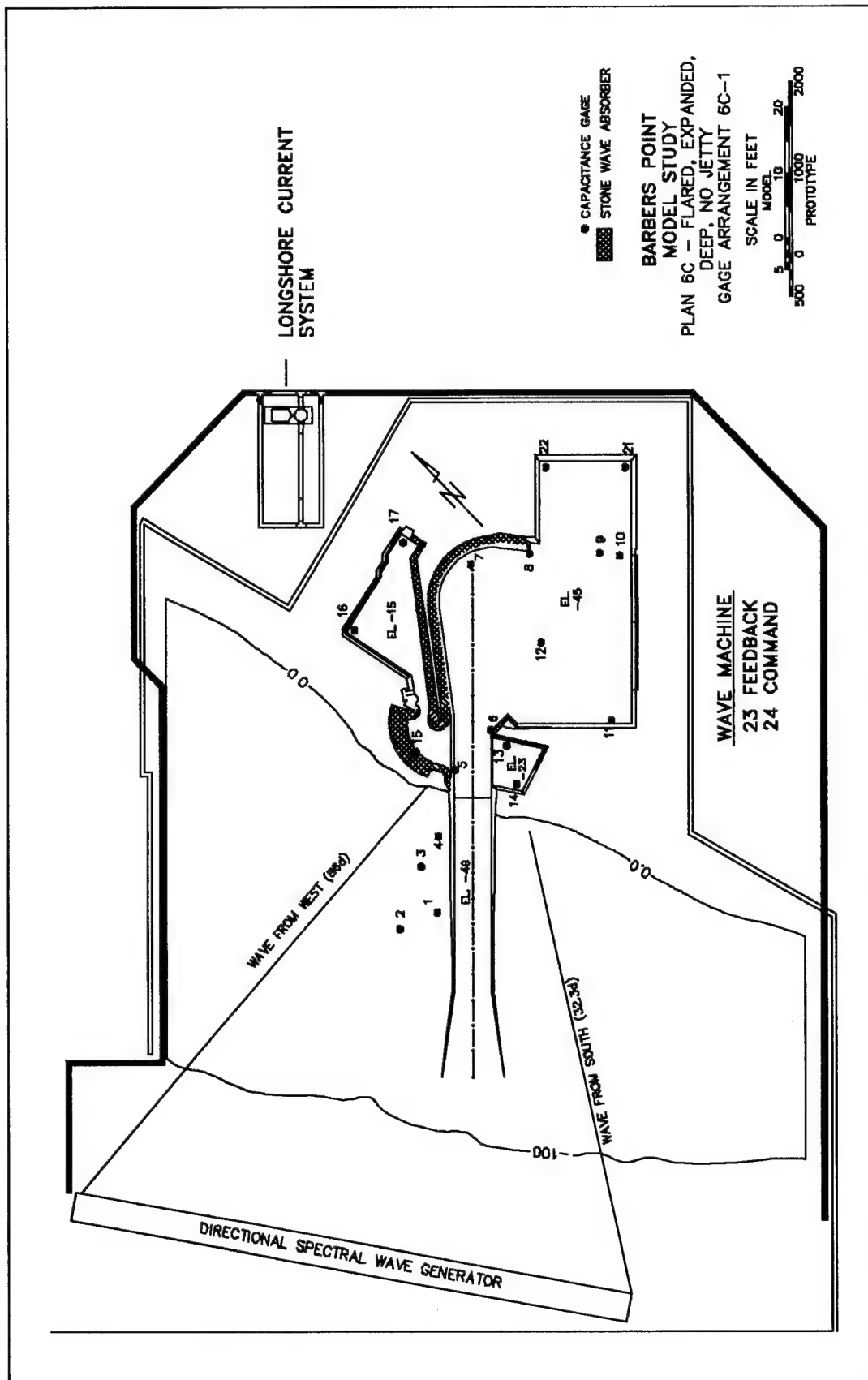


Figure A10. Model gauge locations for plan 6c

Appendix B

Wave Calibration

List of Figures

Figure B1.	S_{xy} time series for wave case 1	B6
Figure B2.	S_{xy} frequency spectra for wave case 1	B8
Figure B3.	Measured versus prototype directional wave spectra for wave case 1	B11
Figure B4.	Measured versus prototype directional wave spectra for wave case 2	B12
Figure B5.	Measured versus prototype directional wave spectra for wave case 3	B13
Figure B6.	Measured versus prototype directional wave spectra for wave case 4	B14
Figure B7.	Measured versus prototype directional wave spectra for wave case 5	B15
Figure B8.	Measured versus prototype directional wave spectra for wave case 6	B16
Figure B9.	Measured versus prototype directional wave spectra for wave case 7	B17
Figure B10.	Measured versus prototype directional wave spectra for wave case 8	B18

List of Tables

Table B1.	Distribution of Wave Period for All Wave Heights	B3
Table B2.	S_{xy} Pressure Conversion Parameters	B5
Table B3.	Peak Frequency and Period Comparison	B10

Notes for Figures B3 to B10

HS	=	Significant wave height, cm
D	=	Water depth, cm
BW	=	Bandwidth for frequency spectrum, Hz
FP	=	Peak frequency, Hz
THP	=	Overall mean wave direction, deg
SIG	=	Directional spreading standard deviation, deg
S(F)	=	Frequency spectrum, normalized
D(FP,THETA)	=	Directional spreading function estimate, normalized
MLM	=	Maximum Likelihood Method (MLM) analysis used
RAW	=	Directional spectral estimates were not smoothed
NGA=8-14	=	Nearshore gauge array (NGA) Gauges 8 to 14 used in the analysis

Table B1
Distribution of Wave Period for all Wave Heights

Gauge	Date	Peak Period, sec									Total
		22+	20	17	15	13	11	9	7	5	
Bu	6-8, 11-12 86	0	6	12	26	86	40	47	77	13	307
	1-12 87	0	13	62	196	303	201	183	240	44	1,242
	1-10 88	0	6	31	122	168	175	151	228	24	905
	1-12 89	0	10	48	166	269	212	177	312	68	1,262
Sum		0	35	153	510	826	628	558	857	149	3,716
%		0%	1%	4%	14%	22%	17%	15%	23%	4%	
S _{xy1}	6-11 86	0	8	30	98	128	83	23	0	108	478
	1-12 87	1	29	117	239	269	202	43	21	163	1,084
Sum		1	37	147	337	397	285	66	21	271	1,562
%		0%	2%	9%	22%	25%	18%	4%	1%	17%	
S _{xy2}	6-12 88	0	4	31	67	137	261	180	49	32	761
	1-12 89	0	8	41	112	263	460	221	70	76	1,251
Sum		0	12	72	179	400	721	401	119	108	2,012
%		0%	1%	4%	9%	20%	36%	20%	6%	5%	
Of	1-12 89	0	14	26	49	207	110	104	8	33	551
Sum		0	14	26	49	207	110	104	8	33	551
%		0%	1%	1%	2%	10%	5%	5%	0%	2%	
On	1-12 89	0	7	8	53	81	93	29	4	23	298
Sum		0	7	8	53	81	93	29	4	23	298
%		0%	2%	3%	18%	27%	31%	10%	1%	8%	
Note: 1. Numbers under Date correspond to months data were available, i.e. 1 = Jan, 2 = Feb, etc. 2. B _u = Buoy, S _{xy1} = First location of S _{xy} gauge, S _{xy2} = Second location of S _{xy} gauge, Of = Offshore gauge, On = Onshore gauge.											

Prototype Data Retrieval and Analysis

Pre-processing

Archived prototype data from the Scripps Institution of Oceanography (SIO) were received on a 9T, 1,600-bpi magnetic tape. A command file (TAPEIT.COM) was written to download the data from this tape onto the CERC VAX 3600 microcomputer for further analysis.

Raw wave data were blocked in card image form (i.e. characters) with one wave record of 1,024 samples per block and one or two header cards for identification. Each block consisted of two 80-column card image header records and sixty-four 80-column card images of wave data in ASCII, A2 format. Blanks were inserted in cases where less than 1,024 samples were collected. If more than 1,024 samples were collected, they were continued in the sequential block and a sequence indicator was used on the header record to flag this condition. Data were calibrated and edited according to the CDIP specifications.

A FORTRAN program (RDTAPEBAR.FOR) was written to read all coded header records from the raw data file and output specific information in a file (BARHDR2.DAT) which could be printed. This was done to better identify which blocks of data needed to be extracted from the data file. For example, 02 in the header record was written out as a pressure gauge (strain gauge).

This program was then modified to be interactive, allowing the user to select blocks of data by specifying date, time (PST), gauge type and location, and number of points per channel. The block of data, along with the header information, was written to an output file named by the user.

Another program (SIOFORMAT.FOR) was written to modify the SIO data format to conform with CERC's format for TSAF and NUSPEC programs. Data were read in and then written out in the proper format so that they could be further analyzed.

Pressure conversion

The first step in the analysis was to convert the pressure time series to equivalent surface elevation time series for input in the directional spectral analysis routine. This conversion was done in the frequency domain by adjusting the real and imaginary Fourier coefficients using the pressure response factor K_p defined as

$$K_p(z) = \frac{\cosh \kappa(h+z)}{\cosh \kappa h} \quad (B1)$$

where

κ = wave number

h = water depth, ft

z = distance below surface to pressure gauge

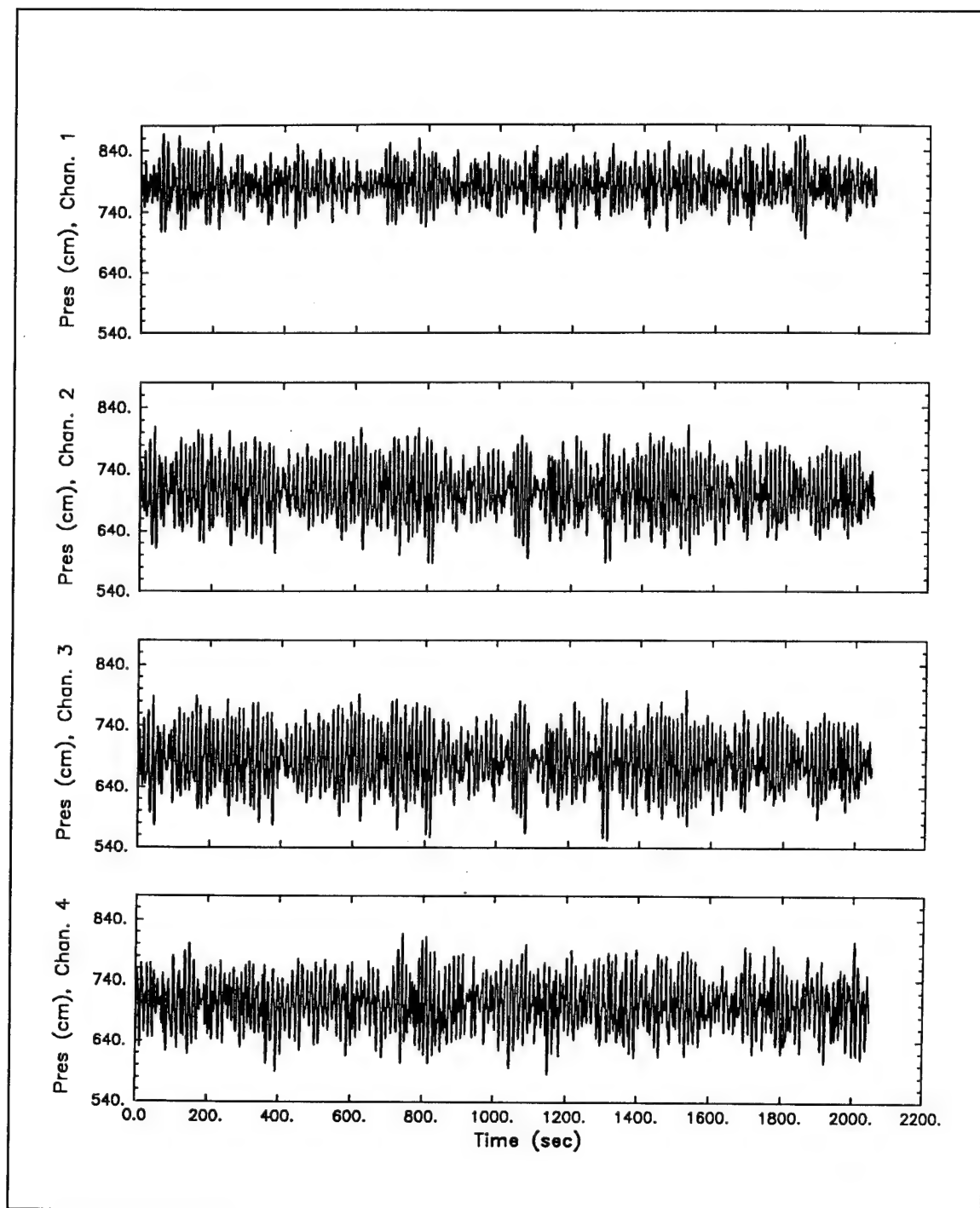
If K_p was less than 0.1, a low signal-to-noise condition was detected and the Fourier coefficients were set to zero. A high-frequency check was also made to end processing for each wave gauge. If the ratio of z to deepwater wavelength at each frequency exceeded 0.5, then no conversion was made to the Fourier coefficients. The converted Fourier coefficients were then transformed back to the time domain as a surface elevation time series.

Table B2 lists the number of data points N , frequency increment Δf , water depth h , and depth above the bottom used in the pressure conversion for the eight wave cases. Time series of the original pressure time series and corresponding surface elevation time series for case 1 are shown in Figure B1 for each of the four S_{xy} gauges. Units of pressure are in centimeters as supplied by SIO. Therefore, pressure time series and spectral analysis plots of the raw pressure data are in metric units.

Table B2					
S _{xy} Pressure Conversion Parameters					
No.	N	Tr sec	Δf Hz, x10-4	h ft	Z+h ft
1	2,048	2,048	4.88	27.60	Varies
2				27.89	
3					
4					
5	1,024	1,024	9.77	29.90	4
6				28.63	
7				29.72	
8				27.97	

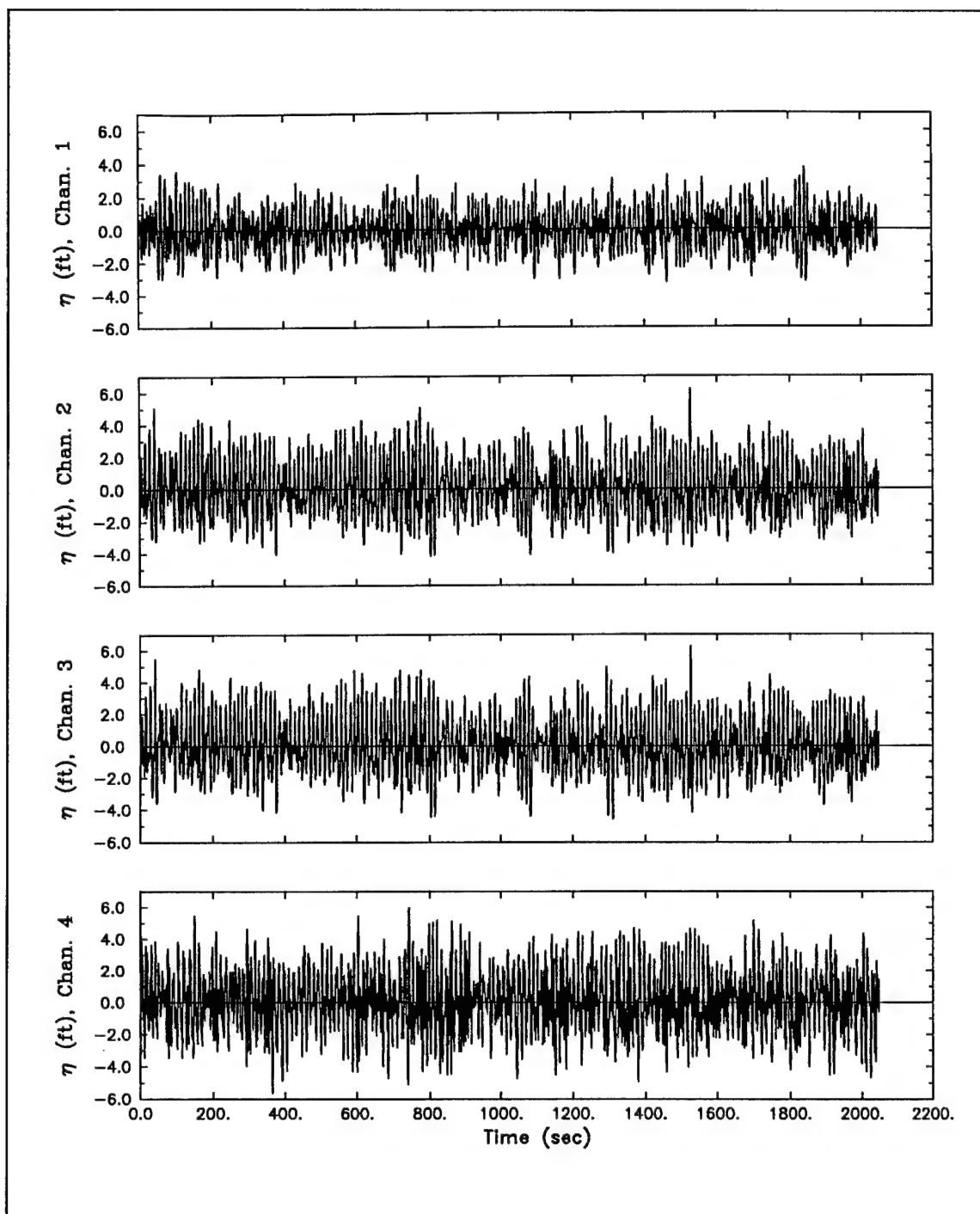
Notes:
1. Sampling rate = 1 Hz.
2. Varies = Depth above bottom varies for each gauge.

Single-channel frequency spectra were also calculated to compare the original pressure data to the corresponding surface elevation. Data records were zero-meaned, tapered by a 10-percent cosine bell window, and band averaged within lower and upper cutoff frequencies of 0.001 and 0.50 Hz, respectively. The same resolution bandwidth of 0.01 Hz was used for all cases. This resulted in 10 bands being averaged for the cases with $N = 1,024$ points and 20 bands for the cases with $N = 2,048$ points. Figure B2 shows the frequency spectra for each of the four gauges in wave case 1 for the pressure data and the equivalent surface elevation.



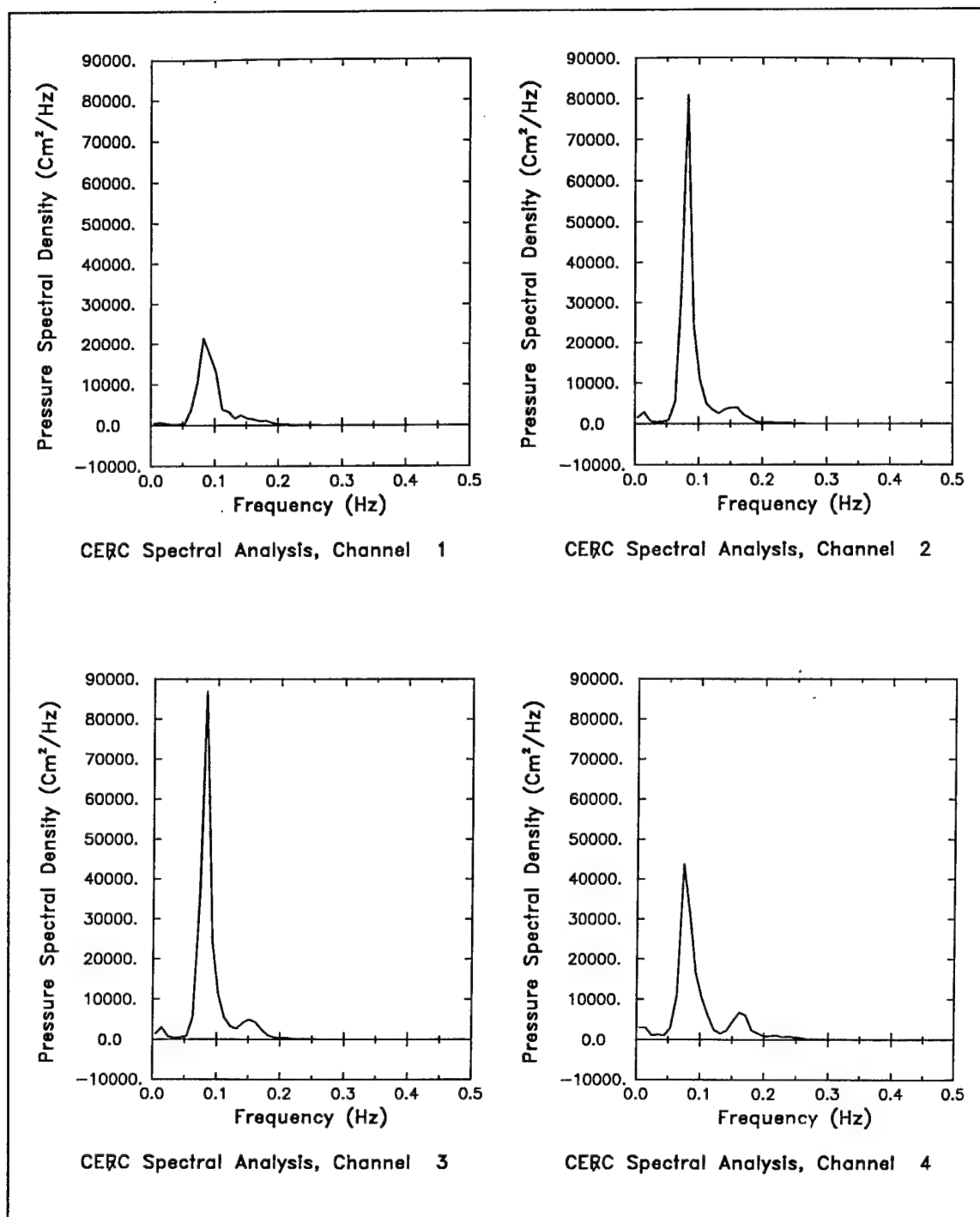
a. Pressure time series

Figure B1. S_{xy} time series for wave case 1 (Continued)



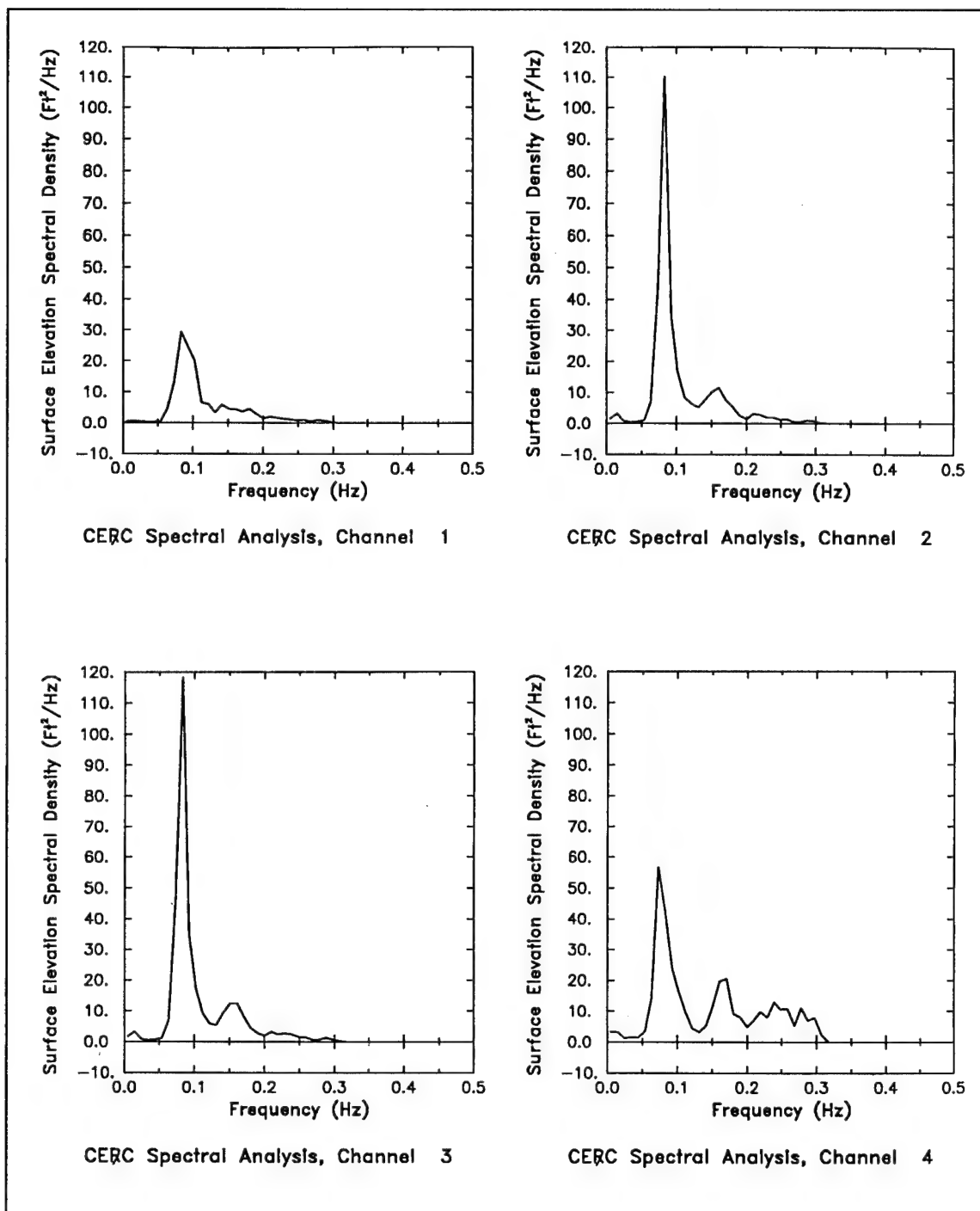
b. Surface elevation time series

Figure B1. (Concluded)



a. Pressure spectra

Figure B2. S_{xy} frequency spectra for wave case 1 (Continued)

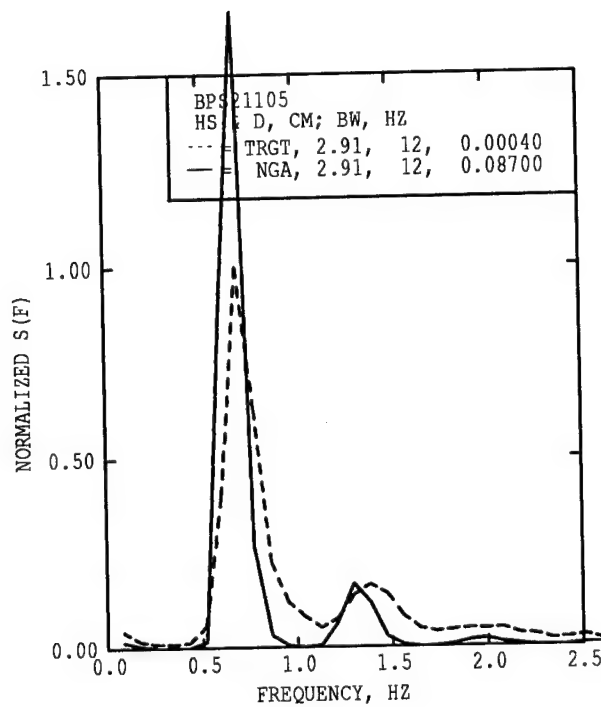


b. S_{xy} surface elevation spectra

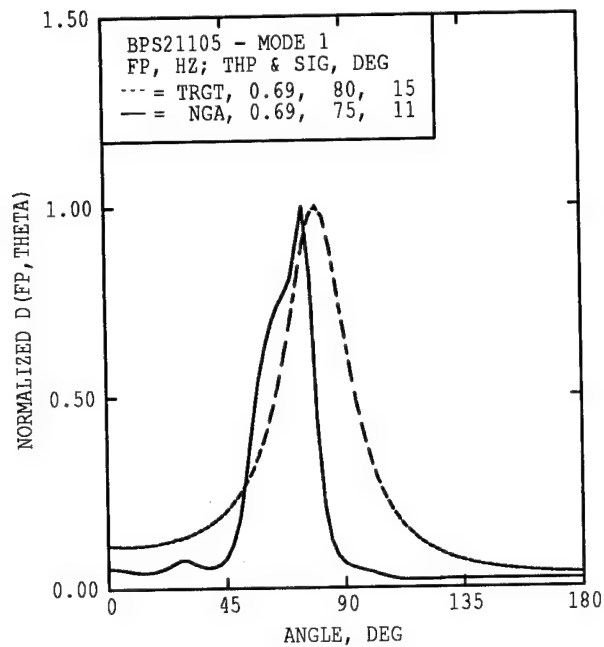
Figure B2. (Concluded)

Table B3**Peak Frequency and Period Comparison**

Prototype Scale		Model Scale	
Freq Hz	Period sec	Freq Hz	Period sec
0.01	100.00	0.09	11.55
0.02	50.00	0.17	5.77
0.03	33.33	0.26	3.85
0.04	25.00	0.35	2.89
0.05	20.00	0.43	2.31
0.06	16.67	0.52	1.92
0.07	14.29	0.61	1.65
0.08	12.50	0.69	1.44
0.09	11.11	0.78	1.28
0.10	10.00	0.87	1.15
0.11	9.09	0.95	1.05
0.12	8.33	1.04	0.96
0.13	7.69	1.13	0.89
0.14	7.14	1.21	0.82
0.15	6.67	1.30	0.77
0.16	6.25	1.39	0.72
0.17	5.88	1.47	0.68
0.18	5.56	1.56	0.64
0.19	5.26	1.65	0.61
0.20	5.00	1.73	0.58
0.21	4.76	1.82	0.55
0.22	4.55	1.91	0.52
0.23	4.35	1.99	0.50
0.24	4.17	2.08	0.48
0.25	4.00	2.17	0.46
0.26	3.85	2.25	0.44
0.27	3.70	2.34	0.43
0.28	3.57	2.42	0.41
0.29	3.45	2.51	0.40
0.30	3.33	2.60	0.38
Note: 1. Model scale: 1:75			

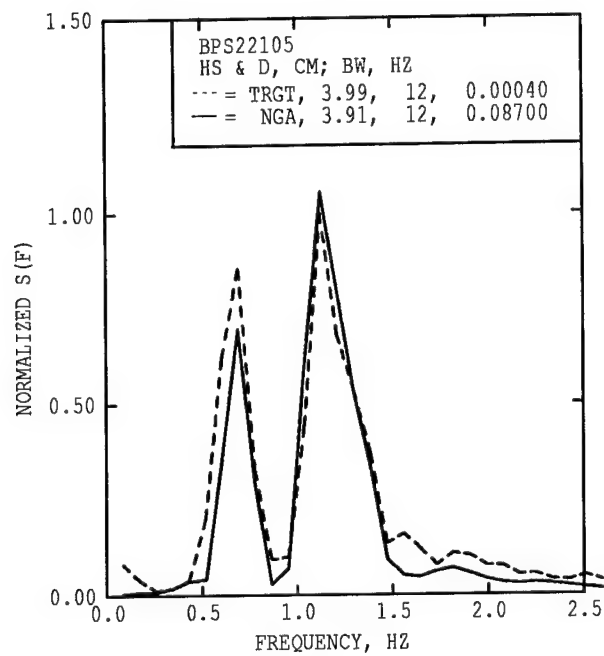


A) TARGET VS. NGA FREQUENCY SPECTRA
MLM, NGA=8-14, RAW

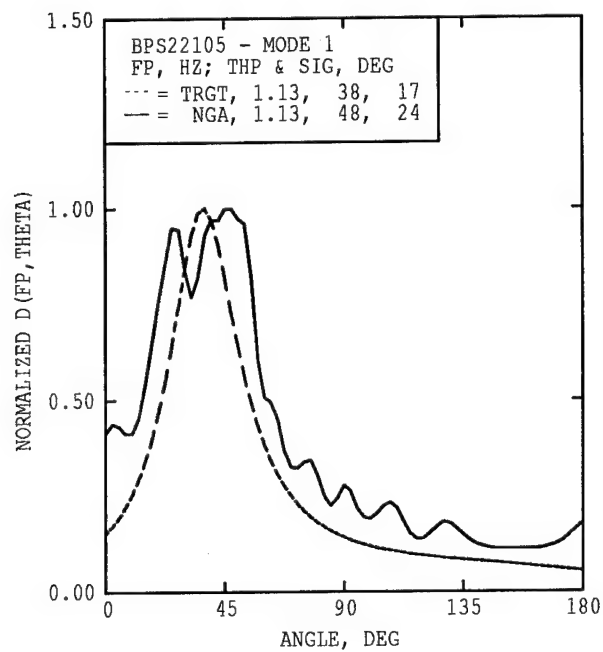


B) TARGET VS. NGA SPREADING @ PEAK FREQ
MLM, NGA=8-14, RAW

Figure B3. Measured versus prototype directional wave spectra for wave case 1

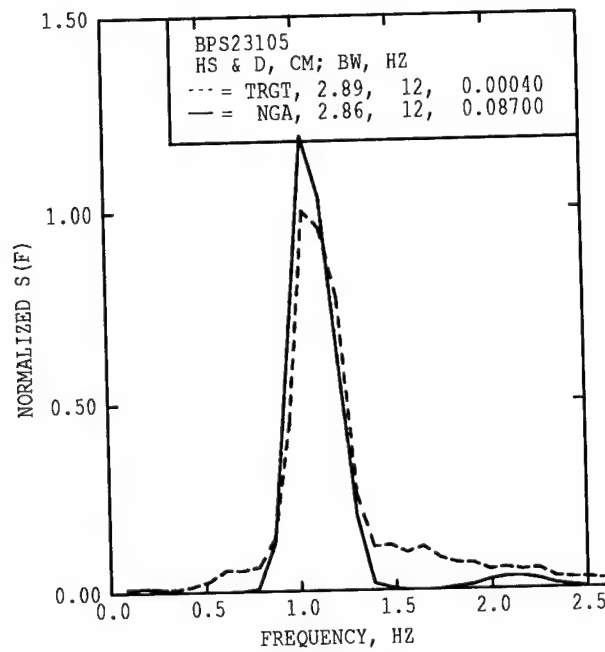


A) TARGET VS. NGA FREQUENCY SPECTRA
MLM, NGA=8-14, RAW

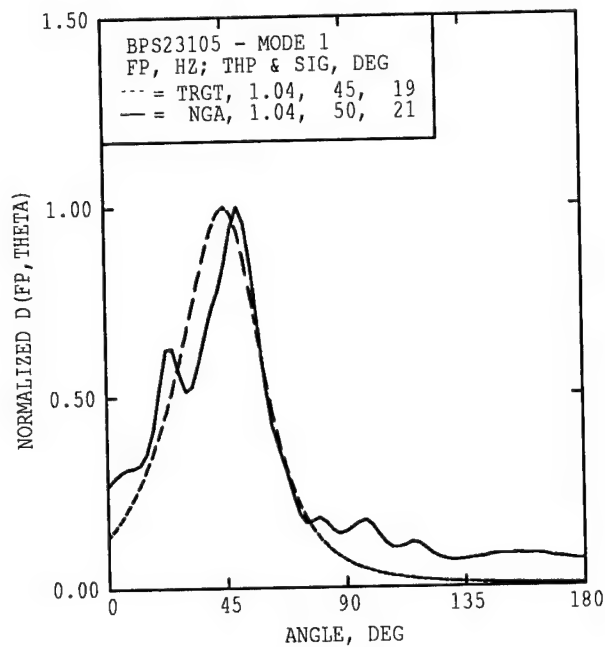


B) TARGET VS. NGA SPREADING @ PEAK FREQ
MLM, NGA=8-14, RAW

Figure B4. Measured versus prototype directional wave spectra for wave case 2

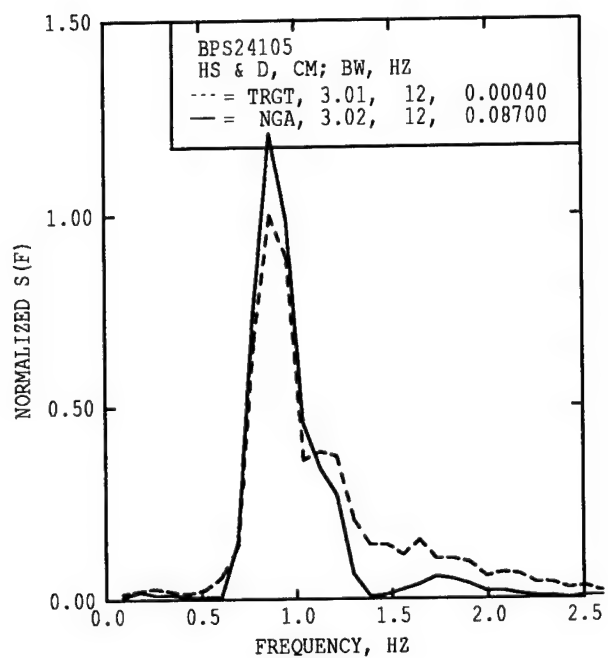


A) TARGET VS. NGA FREQUENCY SPECTRA
MLM, NGA=8-14, RAW

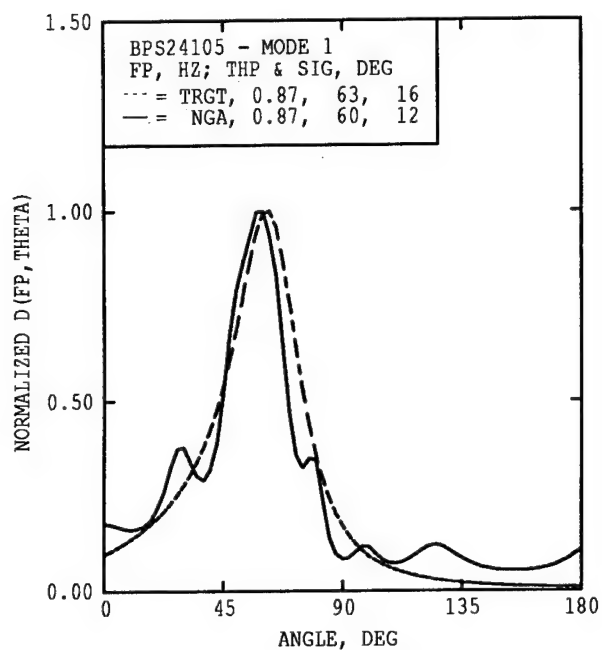


B) TARGET VS. NGA SPREADING @ PEAK FREQ
MLM, NGA=8-14, RAW

Figure B5. Measured versus prototype directional wave spectra for wave case 3

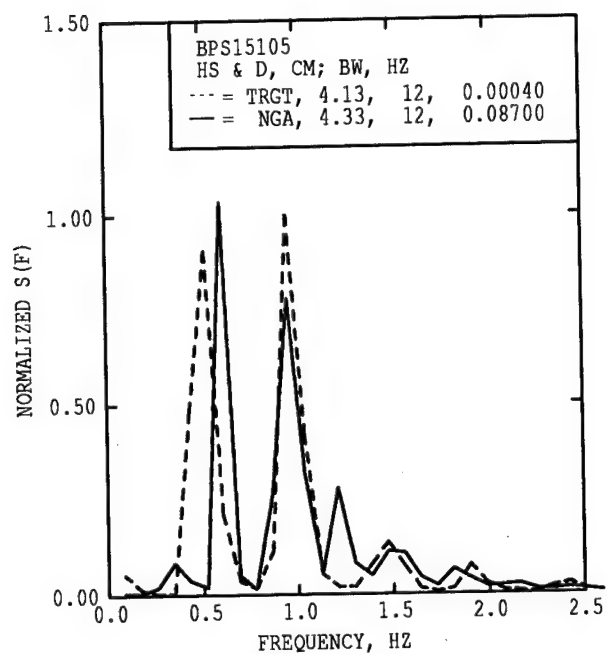


A) TARGET VS. NGA FREQUENCY SPECTRA
MLM, NGA=8-14, RAW

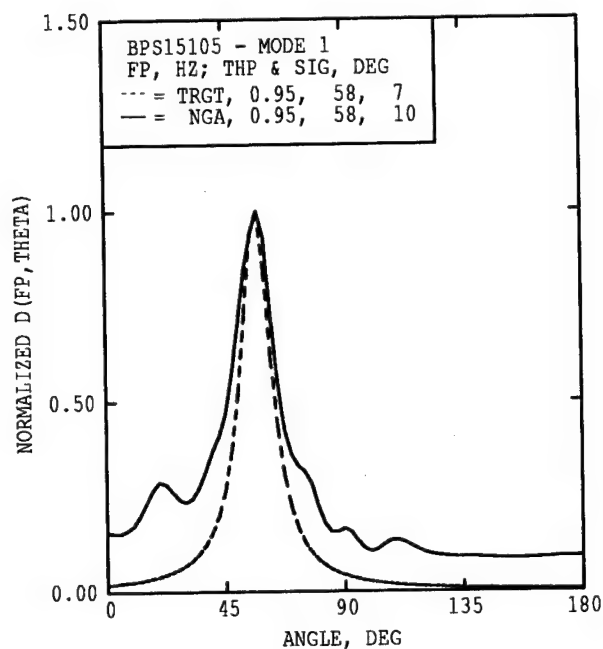


B) TARGET VS. NGA SPREADING @ PEAK FREQ
MLM, NGA=8-14, RAW

Figure B6. Measured versus prototype directional wave spectra for wave case 4

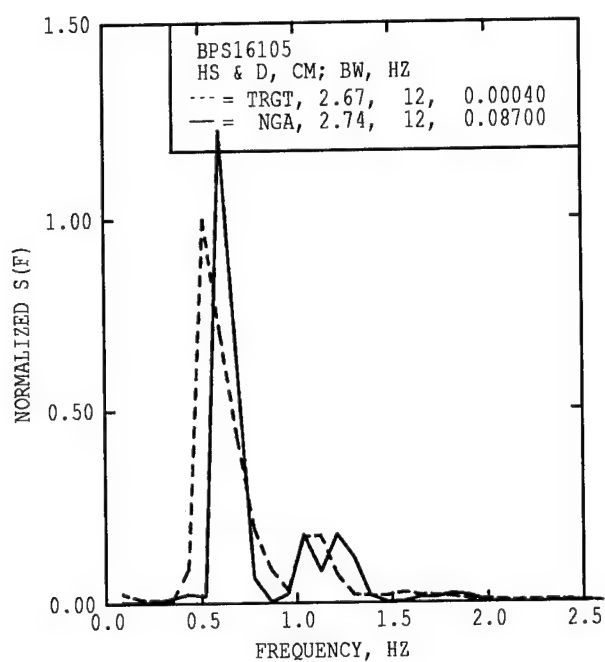


A) TARGET VS. NGA FREQUENCY SPECTRA
MLM, NGA=8-14, RAW

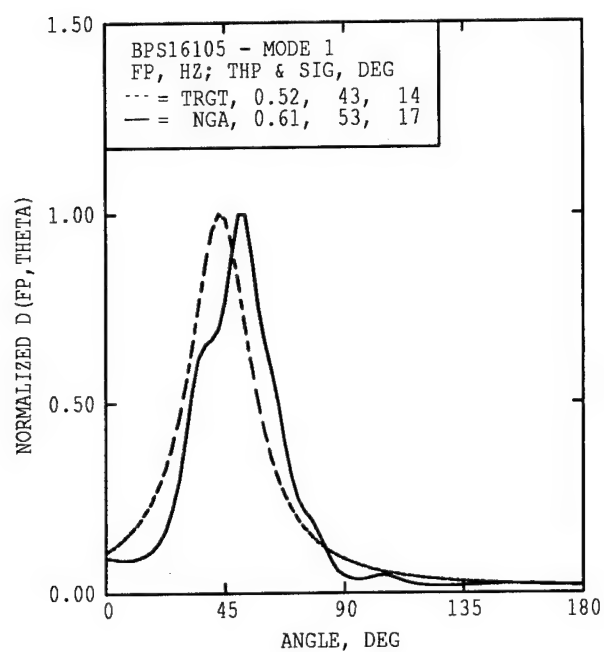


B) TARGET VS. NGA SPREADING @ PEAK FREQ
MLM, NGA=8-14, RAW

Figure B7. Measured versus prototype directional wave spectra for wave case 5

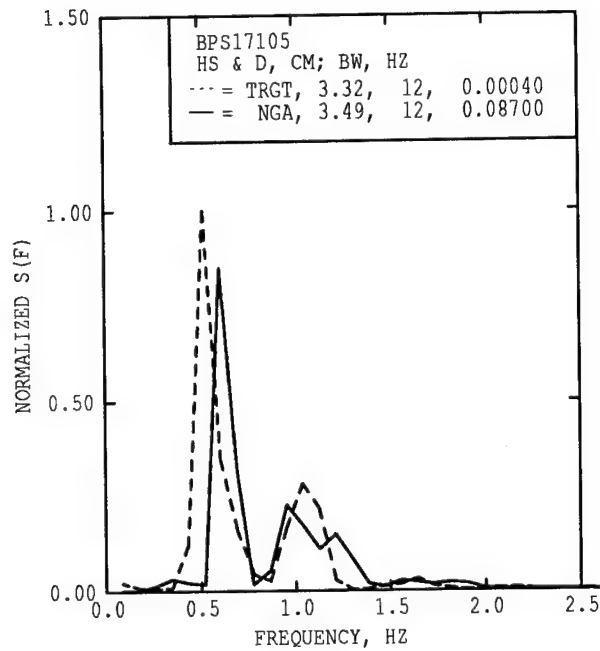


A) TARGET VS. NGA FREQUENCY SPECTRA
MLM, NGA=8-14, RAW

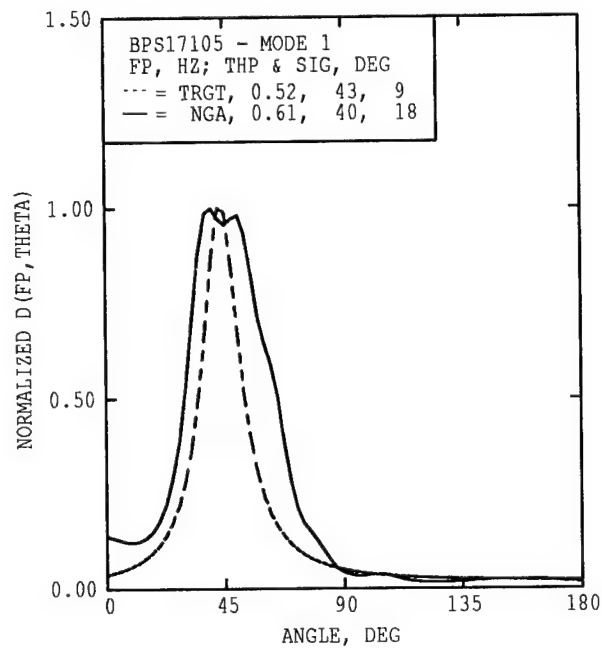


B) TARGET VS. NGA SPREADING @ PEAK FREQ
MLM, NGA=8-14, RAW

Figure B8. Measured versus prototype directional wave spectra for wave case 6

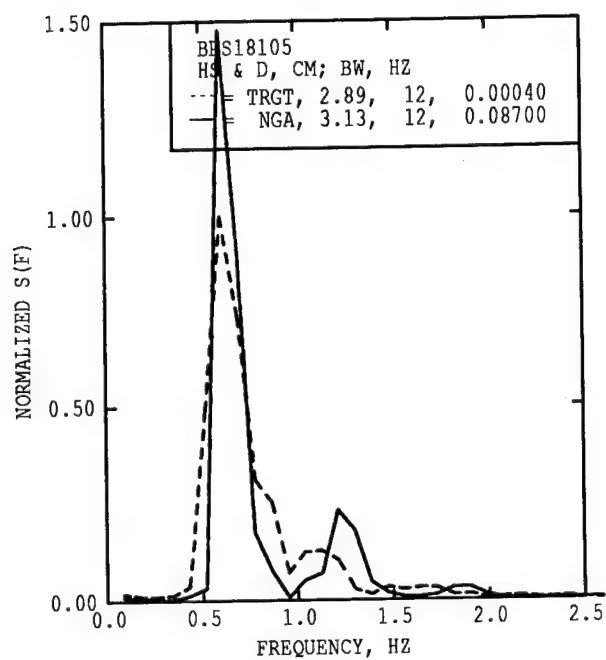


A) TARGET VS. NGA FREQUENCY SPECTRA
MLM, NGA=8-14, RAW

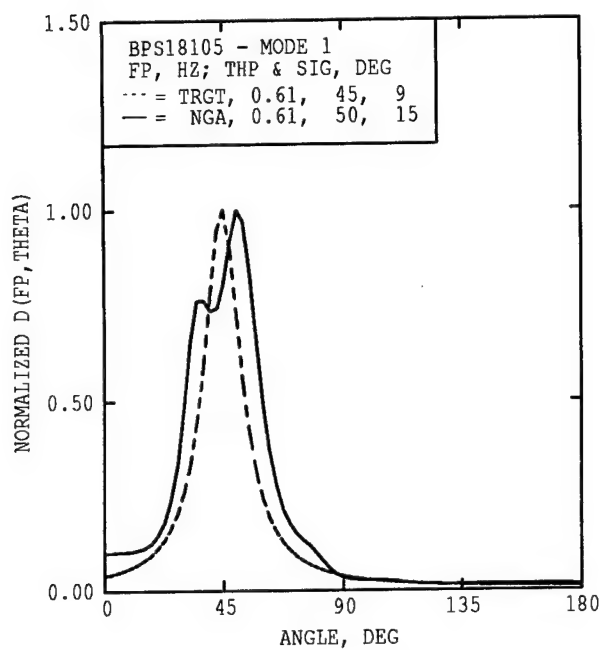


B) TARGET VS. NGA SPREADING @ PEAK FREQ
MLM, NGA=8-14, RAW

Figure B9. Measured versus prototype directional wave spectra for wave case 7



A) TARGET VS. NGA FREQUENCY SPECTRA
MLM, NGA=8-14, RAW



B) TARGET VS. NGA SPREADING @ PEAK FREQ
MLM, NGA=8-14, RAW

Figure B10. Measured versus prototype directional wave spectra for wave case 8

Appendix C

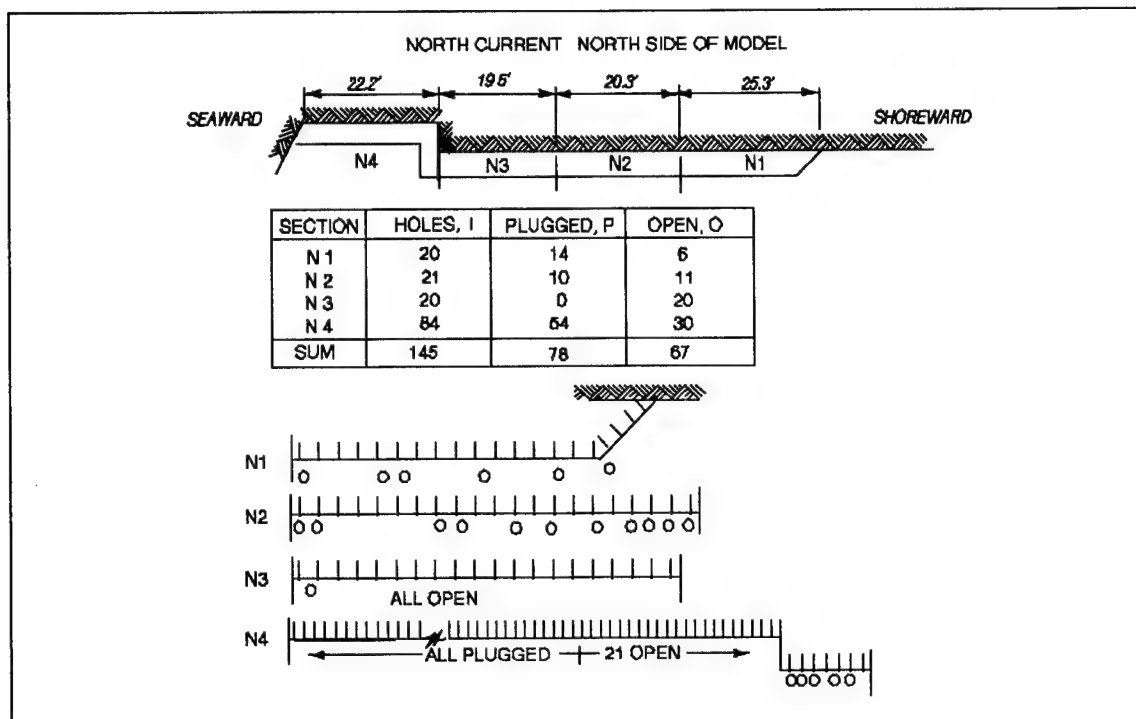
Longshore Current Calibration

List of Figures

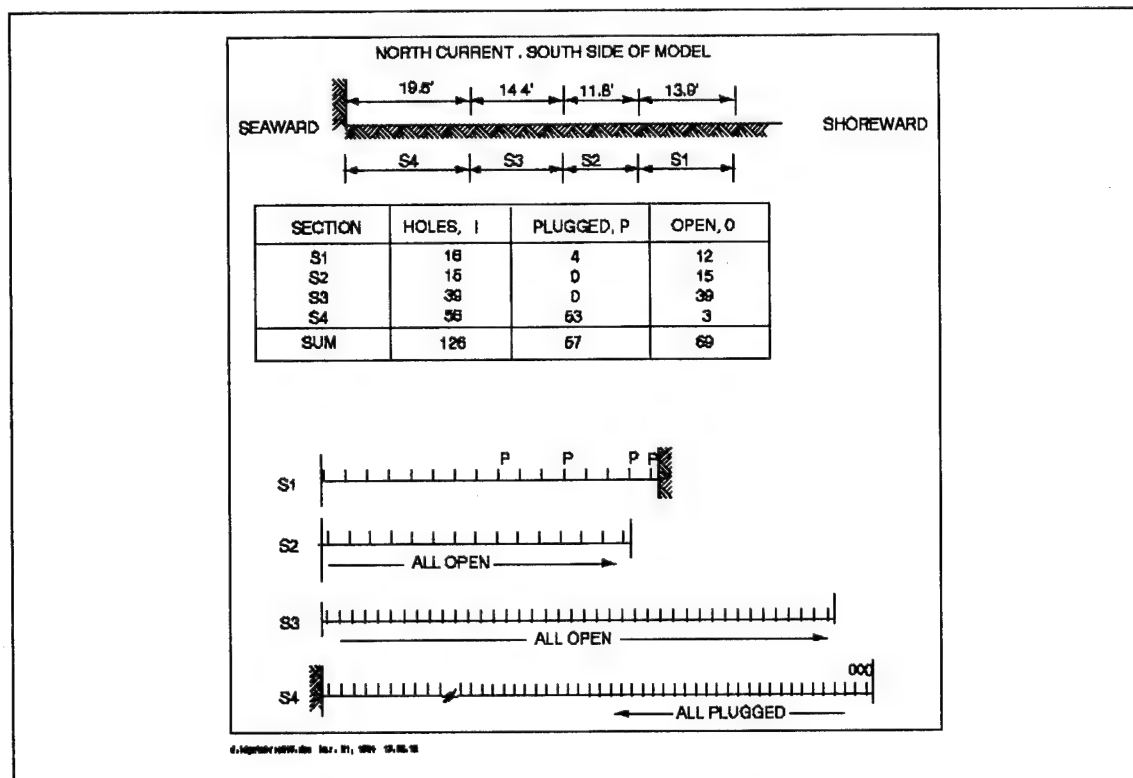
- Figure C1. Manifold hole patterns for north longshore current C3
- Figure C2. Manifold hole patterns for south longshore currents C4

Manifold Hole Patterns

Figures C1 and C2 show the manifold hole patterns for the calibration of the north and south longshore currents, respectively. North and south manifolds for each are shown in the top and bottom of each figure. A schematic of each manifold is shown for orientation. The manifolds on each side were broken into four sections for ease of documenting the hole patterns. The north side manifold sections are labeled "N1," "N2," etc. Similarly, the south side manifold sections are labeled "S1," "S2," etc. The length of each section is given in feet. A tabular listing summarizes the number of holes and the total holes plugged (symbol "P") or open (symbol "O"). Finally, schematics of each section identify which holes were open or plugged and their respective locations. If individual holes are not specifically identified as being open or plugged, they are the opposite condition of the ones identified.

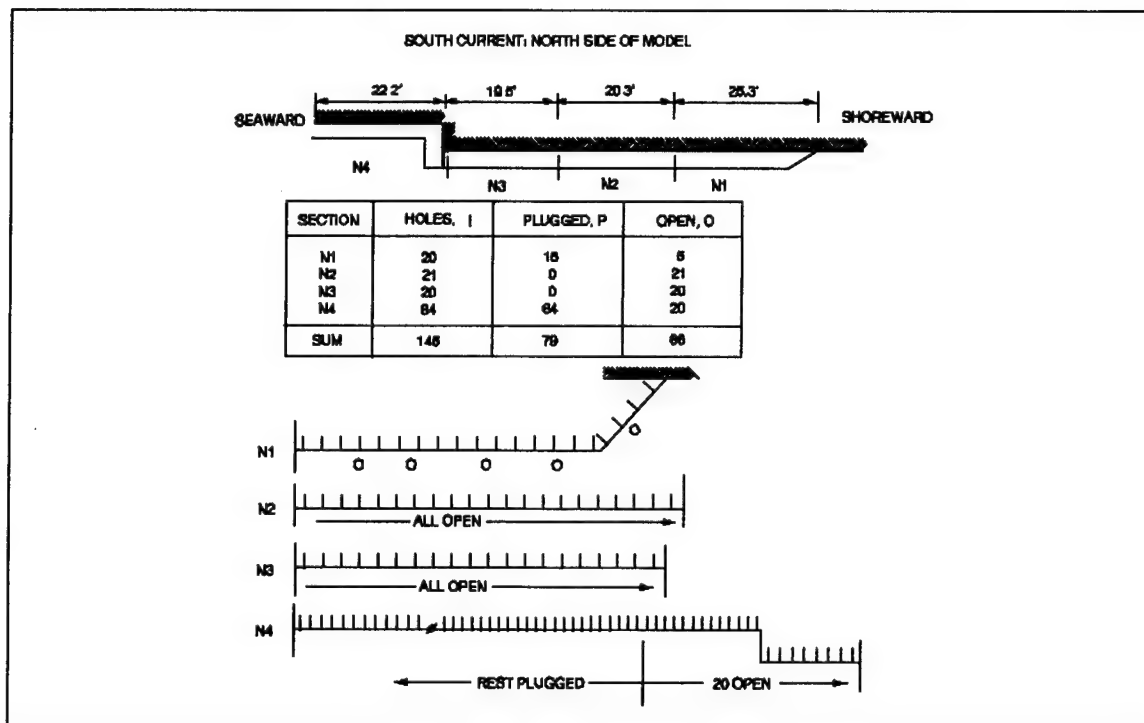


a. North manifold

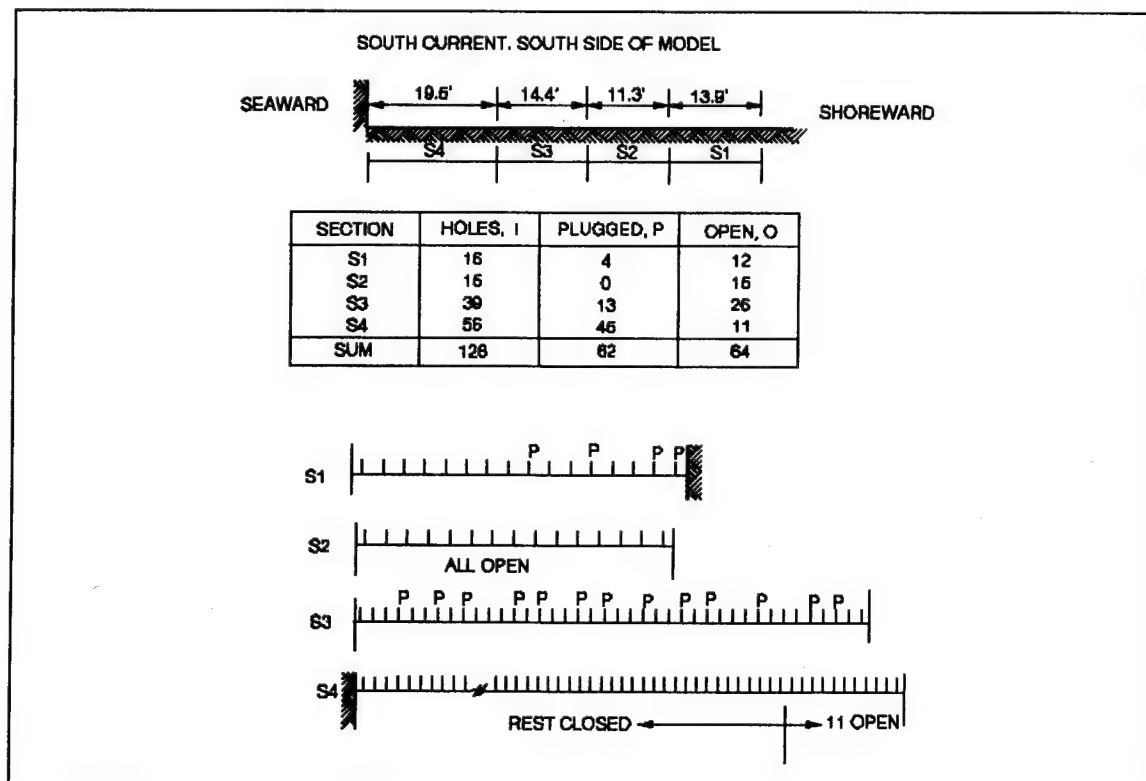


b. South manifold

Figure C1. Manifold hole patterns for north longshore currents



a. North manifold



b. South manifold

Figure C2. Manifold hole patterns for south longshore currents

Appendix D

Numerical Model

List of Figures

Figure D1. Finite element grid for plan 2c	D2
Figure D2. Finite element grid for plan 3a	D3
Figure D3. Finite element grid for plan 3c	D4
Figure D4. Finite element grid for plan 5c	D5

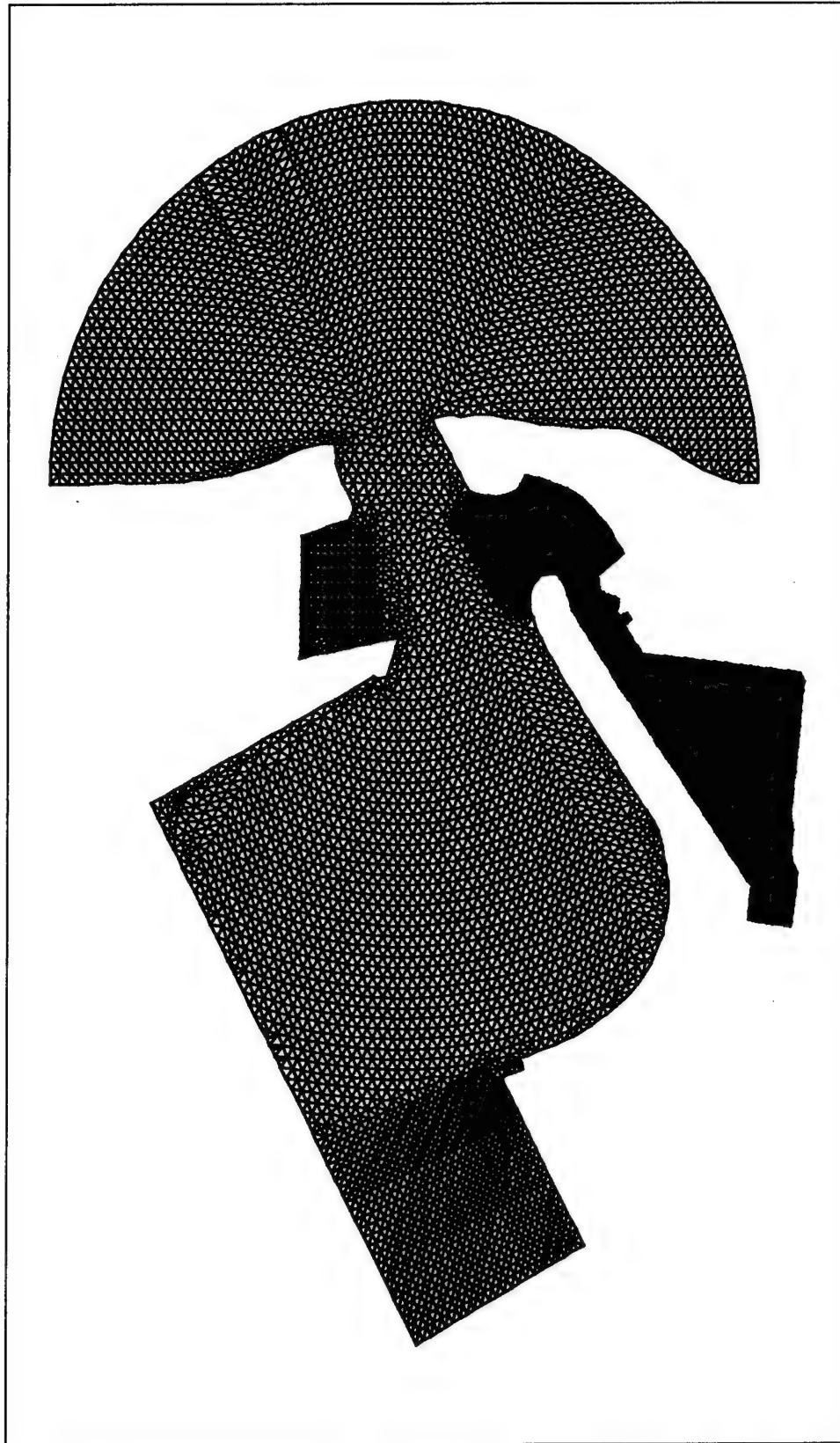


Figure D1. Finite element grid for plan 2c

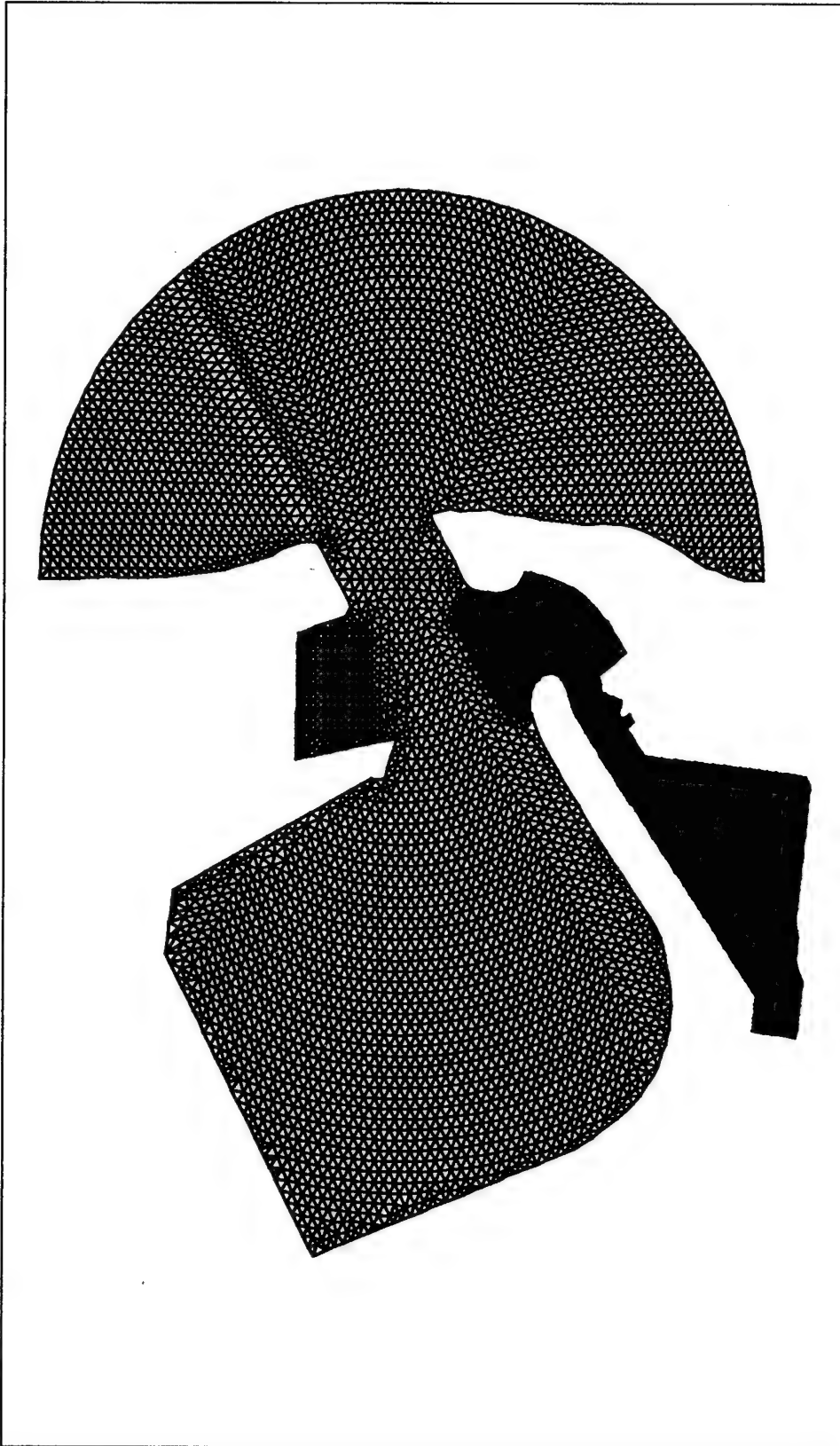


Figure D2. Finite element grid for plan 3a

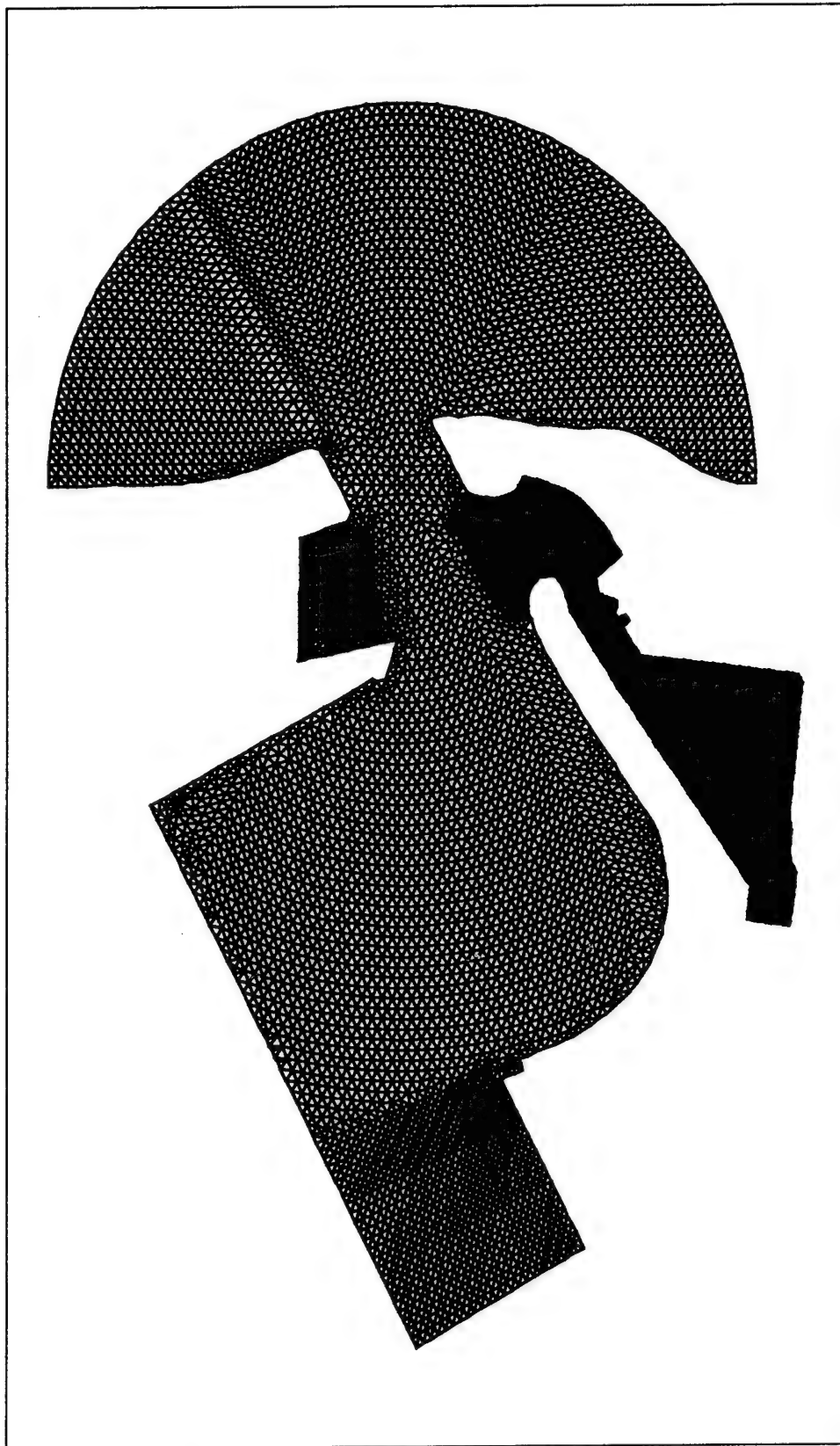


Figure D3. Finite element grid for plan 3c

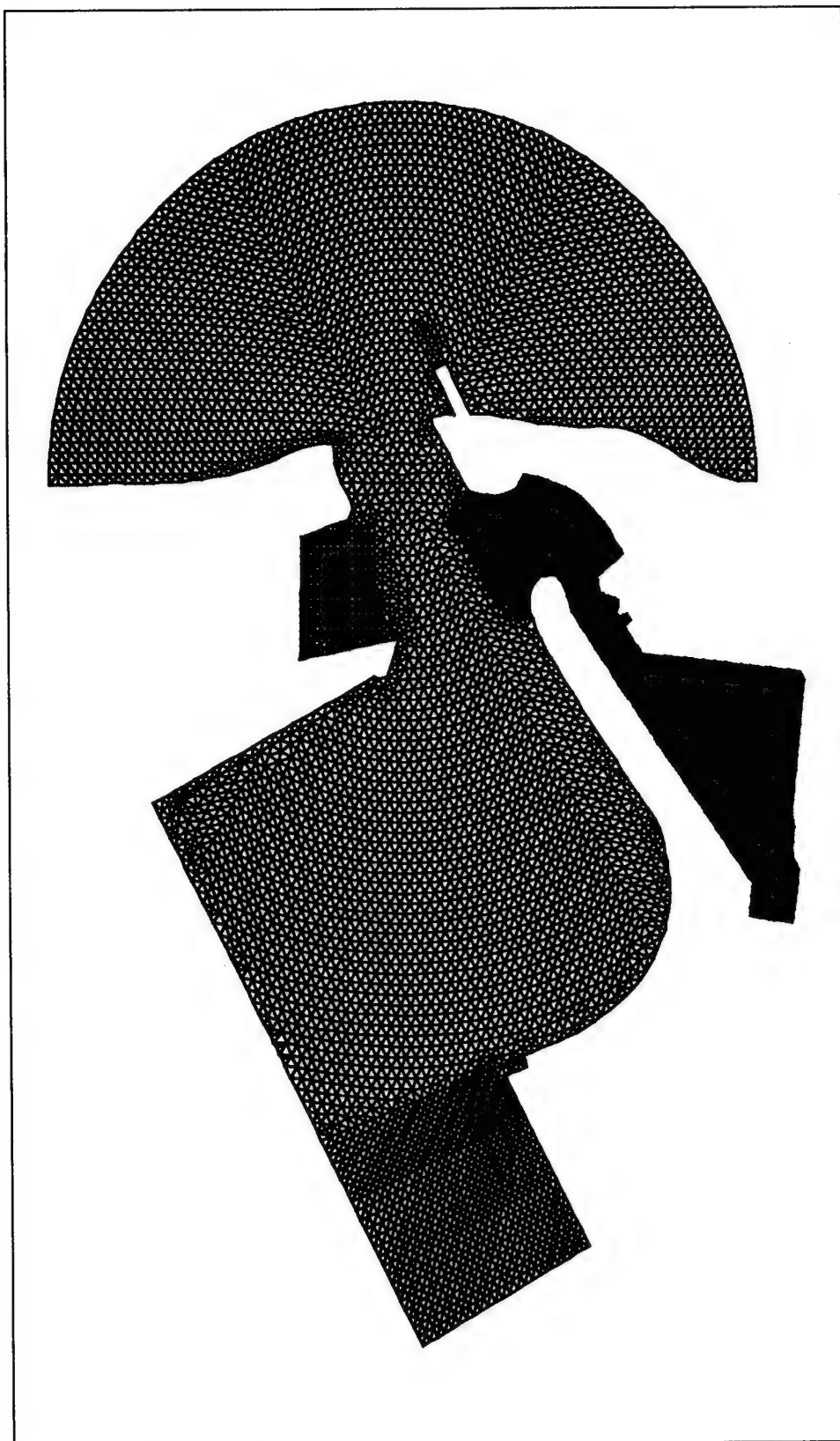


Figure D4. Finite element grid for plan 5c

Appendix E

Design Ship

List of Figures

Figure E1. Design ship turning radius	E2
Figure E2. Contact circuit for bottom of design ship	E3

List of Tables

Table E1. Engine Orders and Related RPM and Ship Speed	E4
Table E2. Prototype Ship Turning Circle Parameters	E4
Table E3. Crash Stop Maneuvers	E4
Table E4. Bow Thruster Performance Characteristics	E5
Table E5. Model Ship Speed Trials	E5
Table E6. Turning Circle Parameters for Half Speed Ahead	E5
Table E7. Bow Thruster Performance at Zero Ship Speed	E6

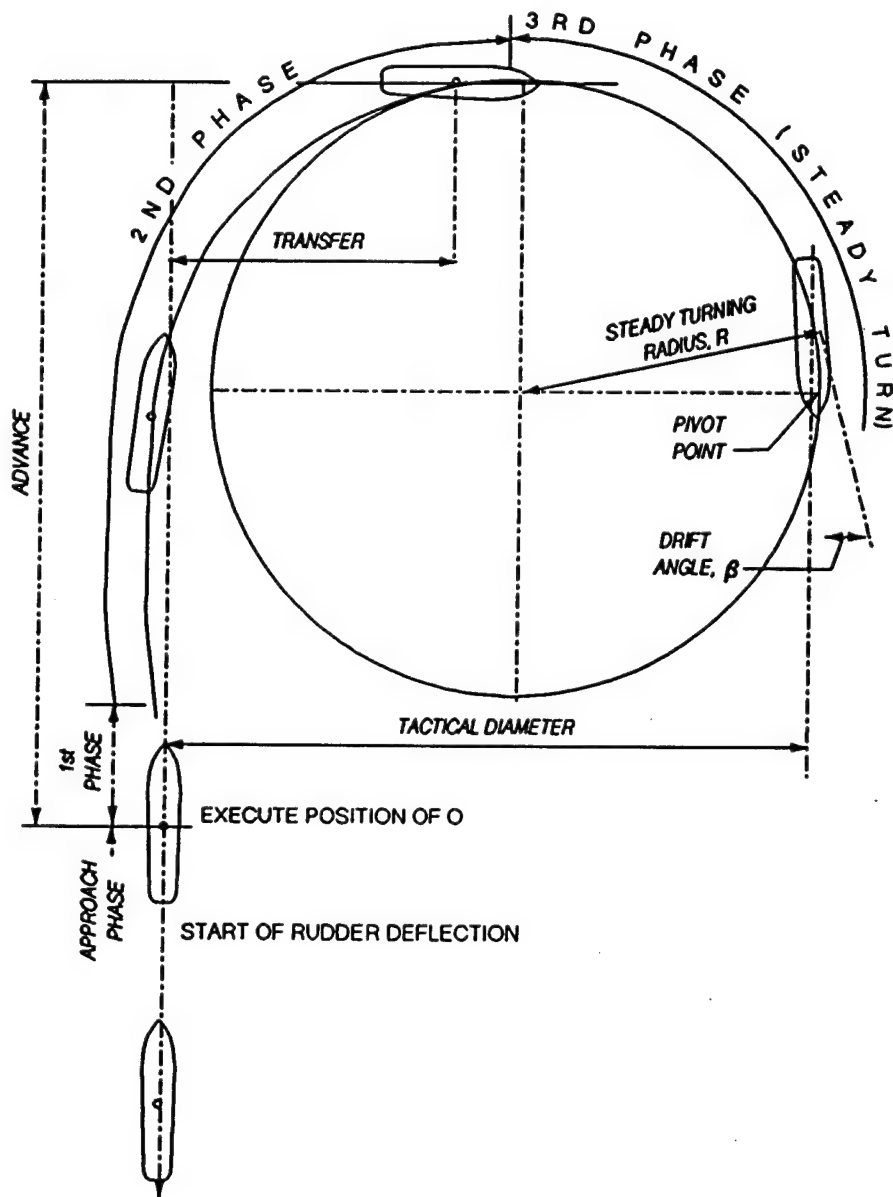
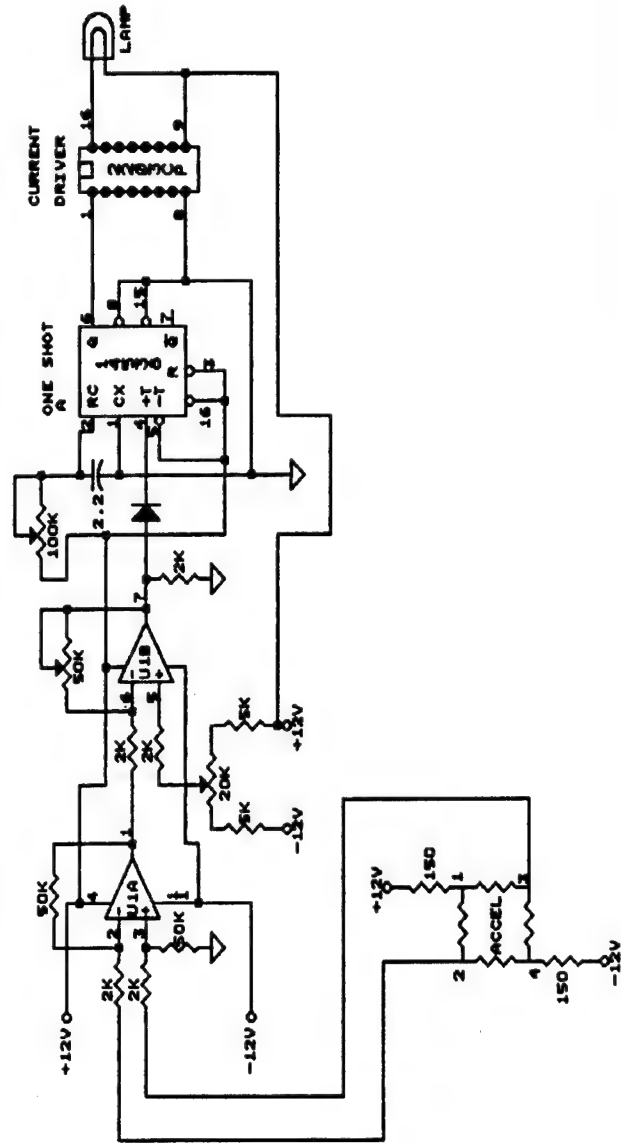


Figure E1. Design ship turning radius

BOAT BOTTOM CONTACT CIRCUIT FOR BARBER'S POINT BY: WALLACE GUY (CEWES-JO-A)



CEWES-JO-A	(BOTTOM CONTACT CIRCUIT)
SIZE DOCUMENT NUMBER	ORCAD FILE: BARBERS.PT
REV	
DATE	05/08/87, 1991/05/01
BY	PT

E3 Figure E2. Contact circuit for bottom of design ship

Table E1 Engine Orders and Related RPM and Ship Speed		
Engine Order	RPM	Speed, kts
Nav Full	126	25.00
Full Ahead	85	17.10
Half Ahead	55	10.60
Slow Ahead	45	8.40
Dead Slow Ahead	35	6.40
Dead Slow Astern	35	
Slow Astern	40	
Half Astern	45	
Full Astern	50	

Table E2 Prototype Ship Turning Circle Parameters				
Engine Order	RPM	Advance miles	Tactical Diameter miles	Time for Maneuver min
Nav Full	126	0.50	0.62	0.95
Full Ahead	85	0.48	0.55	1.50
Half Ahead	55	0.39	0.54	1.85

Table E3 Crash Stop Maneuvers		
Engine Order	Time min	Distance miles
Nav Full	10.8	2.1
Full Ahead	9.2	1.4
Half Ahead	6.1	0.7

Table E4
Bow Thruster Performance Characteristics

Ship Speed knots	Degree Per Minute	
	To Port	To Starboard
0	10.88	11.00
4.5	4.73	5.00
5.7	4.61	5.14
7.0	5.45	4.39
8.6	5.00	4.00

Table E5
Model Ship Speed Trials

Engine Order	RPM			Speed		
	Prototype	Model		Prototype knots	Model, fps	
		Target	Measured		Target	Measured
Nav Full	126					
Full Ahead	85	735	610	17.1	3.2	3.3
Half Ahead	55	475	330	10.6	2.0	2.1
Slow Ahead	45	390	240	8.4	1.6	1.6
Dead Slow Ahead	35	305	150	6.4	1.2	1.2
Dead Slow Astern	35	305	150			
Slow Astern	40	345	190			
Half Astern	45	390	240			
Full Astern	50	435	280			

Table E6
Turning Circle Parameters for Half Speed Ahead

Parameter	Prototype miles	Model, ft	
		Target	Measured
Advance	0.39	31.8	32.2
Tactical diameter	0.54	43.3	44.6

Table E7 Bow Thruster Performance at Zero Ship Speed			
Parameter	Prototype	Model	
		Target	Measured
Degrees Per Minute	10.95	95	90 - 100
Time for 90 Deg Turn in sec	492	57	53 - 62

Appendix F

Navigation Study

List of Figures

Figure F1. Navigation tests log sheet	F3
Figure F2. Prototype speed versus time	F22

List of Tables

Table F1. Navigation Test Summary for All Inbound Runs, Test Plan 1a	F6
Table F2. Navigation Test Summary for All Inbound Runs, Test Plan 2c	F7
Table F3. Navigation Test Summary for All Inbound Runs, Test Plan 3c	F8
Table F4. Navigation Test Summary for All Inbound Runs, Test Plan 4c	F9
Table F5. Navigation Test Summary for All Inbound Runs, Test Plan 5c	F10
Table F6. Navigation Test Summary for All Inbound Runs, Test Plan 6c	F11
Table F7. Navigation Test Summary for All Outbound Runs, Test Plan 1a	F12
Table F8. Navigation Test Summary for All Inbound Runs, Test Plan 4c with Region B Waves and Current	F13
Table F9. Pilot Navigation Test Summary for All Inbound Runs, Test Plan 4c	F14
Table F10. Inbound Navigation Test Results for Test Plan 1a	F15
Table F11. Inbound Navigation Test Results for Test Plan 2c	F16
Table F12. Inbound Navigation Test Results for Test Plan 3c	F17

Table F13. Inbound Navigation Test Results for Test Plan 4c	F18
Table F14. Inbound Navigation Test Results for Test Plan 5c	F19
Table F15. Inbound Navigation Test Results for Test Plan 6c	F20
Table F16. Outbound Navigation Test Results for Test Plan 1a	F21
Table F17. Videotape Log of Selected Navigation Test Runs	F23

BARBERS POINT NAVIGATION TESTS

TEST _____	DATE _____
Vessel Heading	<input type="checkbox"/> INBOUND <input type="checkbox"/> OUTBOUND
1. Wave Condition (Visual Assessment)	<input type="checkbox"/> LOW <input type="checkbox"/> MODERATE <input type="checkbox"/> HIGH
<input type="checkbox"/> NON BREAKING	<input type="checkbox"/> BREAKING AT LOCATION _____
2. Vessel Behaviour (Outside Channel)	<input type="checkbox"/> ACCEPTABLE <input type="checkbox"/> MODERATE <input type="checkbox"/> UNACCEPTABLE
3. Navigation	
A. Entering Channel	<input type="checkbox"/> EASY <input type="checkbox"/> MODERATE <input type="checkbox"/> DIFFICULT <input type="checkbox"/> FAILURE
B. In Channel	<input type="checkbox"/> EASY <input type="checkbox"/> MODERATE <input type="checkbox"/> DIFFICULT <input type="checkbox"/> FAILURE
C. Exiting Channel	<input type="checkbox"/> EASY <input type="checkbox"/> MODERATE <input type="checkbox"/> DIFFICULT <input type="checkbox"/> FAILURE
COMMENTS _____	

4. Ship Trackline Through Channel	
	<input type="checkbox"/> OPTIMUM (SMOOTH) <input type="checkbox"/> VARIABLE (OSCILLATING) <input type="checkbox"/> CRITICAL (HAZARDOUS) <input type="checkbox"/> GROUNDING <input type="checkbox"/> SIDES
<input type="checkbox"/> BOTTOM LOCATION _____	LOCATION _____
	Channel side <input type="checkbox"/> North <input type="checkbox"/> South Hit by ship <input type="checkbox"/> Bow <input type="checkbox"/> Stern
ESTIMATED MAXIMUM YAW ANGLE _____ DEGREES.	
COMMENTS _____	

Figure F1. Navigation tests log sheet (Sheet 1 of 3)

5. Applied Engine and Rudder

- A. Engine:
- Number of changes applied ☐ FEW (<4)
☐ MEDIUM (4-8)
☐ LARGE (>8)
- Changes in engine power applied ☐ LITTLE
☐ MEDIUM
☐ LARGE
- B. Rudder:
- Number of changes applied ☐ FEW (<4)
☐ MEDIUM (4-8)
☐ LARGE (>8)
- Rudder angles applied ☐ SMALL
☐ MEDIUM
☐ LARGE

COMMENTS _____

6. Average Vessel Speed

- A. Model: Distance: _____ m
Time: _____ sec
Speed: _____ cm/sec
- B. Prototype: Speed: _____ knots

7. Stopping in Basin (Inbound)

- A. General: ☐ SAFE
☐ MARGINAL
☐ UNSAFE
- B. A stern power applied ☐ SMALL
☐ MEDIUM
☐ HIGH
- C. Use of bow thruster ☐ NO
☐ YES

COMMENTS _____

8. Maneuvering (Safety) Rating Overall.

- ☐ EASY (SAFE)
☐ MODERATE (MARGINAL)
☐ DIFFICULT (UNSAFE)
☐ FAILURE

COMMENTS _____

Figure F1. (Sheet 2 of 3)

BARBERS POINT NAVIGATION TESTS

SUPPLEMENT TO TEST SHEETS.

1. Location of breaking is given according to the markings in the model, starting with 0 at the entrance of the channel, and increasing values up to the harbor basin. Numbers corresponding to 100 ft in the prototype.
2. Vessel behavior is a simple subjective assessment of vessel movement outside the channel.
3. The navigation is here split up in three sections, entering the channel, going through the channel, and exiting the channel. Marks here will of necessity be related to markings given in 4,7 and 8.
4. Evaluation of the conditions for the ship going through the channel. If grounding, the location should be given as in 1.
5. In the number counts, each change of engine power or rudder angle is counted, meaning that an increase in engine power counts for one, and coming back to a "normal" engine power counts for two.
6. Average vessel speed is evaluated by the following procedures:
 - Time elapsed for bow to travel from the entrance of the channel to the shoreline, or vice versa.
 - This give a distance of 3300 ft, or 1005 m in the prototype - corresponding to 13.4 m in the model.
 - To be timed on the video recording from location 0 to 33.
7. Stopping in basin is only applicable for inbound runs, and this is overlapping with 3.C, exiting the channel.
8. This gives an overall assessment of the run.

In addition to the boxes, comments could be included to expand on observations, or to clarify observations made which is not covered by the form.

Figure F1. (Sheet 3 of 3)

Table F1
Navigation Test Summary for All Inbound Runs, Test Plan 1a

Conditions		Ratings	Number	Percentage
N A V I G A T I O N	Ent. Channel	Easy	13	37
		Moderate	10	29
		Difficult	11	31
		Failure	1	3
	In Channel	Easy	5	15
		Moderate	16	47
		Difficult	13	38
		Failure	0	0
	Exit. Channel	Easy	15	45
		Moderate	18	55
		Difficult	0	0
		Failure	0	0
Ship Trackline		Optimum	5	16
		Variable	9	29
		Critical	16	52
		Grounding	1	3
E N G I N E	Changes	Few (<4)	25	74
		Medium (4-8)	8	23
		Large (>8)	1	3
	Power	Little (<4)	4	11
		Medium (4-8)	16	46
		Large (>8)	15	43
R U D D E R	Changes	Few (<4)	5	14
		Medium (4-8)	26	74
		Large (>8)	4	12
	Angles	Small (<4)	1	3
		Medium (4-8)	5	14
		Large (>8)	29	83
OVERALL MANEUVERING RATING		Safe	5	14
		Marginal	13	37
		Unsafe	16	46
		Failure	1	3
Note: 1. Average ship speed = 4.9 knots (prototype). 2. Average ship range = 3.5 - 6.3 knots.				

Table F2
Navigation Test Summary for All Inbound Runs, Test Plan 2c

Conditions		Ratings	Number	Percentage
N A V I G A T I O N	Ent. Channel	Easy	36	80
		Moderate	7	16
		Difficult	2	4
		Failure	0	0
	In Channel	Easy	17	38
		Moderate	25	56
		Difficult	2	4
		Failure	1	2
	Exit. Channel	Easy	33	73
		Moderate	12	27
		Difficult	0	0
		Failure	0	0
Ship Trackline		Optimum	16	36
		Variable	28	62
		Critical	0	0
		Grounding	1	2
E N G I N E	Changes	Few (<4)	42	93
		Medium (4-8)	3	7
		Large (>8)	0	0
	Power	Little	20	44
		Medium	23	51
		Large	2	4
R U D D E R	Changes	Few (<4)	27	60
		Medium (4-8)	18	40
		Large (>8)	0	0
	Angles	Small	2	4
		Medium	7	16
		Large	36	80
OVERALL MANEUVERING RATING		Safe	18	40
		Marginal	26	58
		Unsafe	0	0
		Failure	1	2
Note: 1. Average ship speed = 5.9 knots (prototype). 2. Average ship range = 4.6 - 7.3 knots.				

Table F3
Navigation Test Summary for All Inbound Runs, Test Plan 3c

Conditions		Ratings	Number	Percentage
N A V I G A T I O N	Ent. Channel	Easy	31	67
		Moderate	12	26
		Difficult	3	7
		Failure	0	0
	In Channel	Easy	28	61
		Moderate	18	39
		Difficult	0	0
		Failure	0	0
	Exit. Channel	Easy	29	63
		Moderate	15	33
		Difficult	2	4
		Failure	0	0
Ship Trackline		Optimum	18	39
		Variable	26	57
		Critical	2	4
		Grounding	0	0
E N G I N E	Changes	Few (<4)	41	89
		Medium (4-8)	5	11
		Large (>8)	0	0
	Power	Little	20	43
		Medium	22	48
		Large	4	9
R U D D E R	Changes	Few (<4)	28	61
		Medium (4-8)	18	39
		Large (>8)	0	0
	Angles	Small	1	2
		Medium	16	35
		Large	29	63
OVERALL MANEUVERING RATING		Safe	21	46
		Marginal	22	48
		Unsafe	3	7
		Failure	0	0
Note: 1. Average ship speed = 5.7 knots (prototype). 2. Average ship range = 4.5 - 7.0 knots.				

Table F4
Navigation Test Summary for All Inbound Runs, Test Plan 4c

Conditions		Ratings	Number	Percentage
N A V I G A T I O N	Ent. Channel	Easy	38	84
		Moderate	7	16
		Difficult	0	0
		Failure	0	0
	In Channel	Easy	25	56
		Moderate	19	42
		Difficult	1	2
		Failure	0	0
	Exit. Channel	Easy	37	82
		Moderate	8	18
		Difficult	0	0
		Failure	0	0
Ship Trackline		Optimum	14	31
		Variable	30	67
		Critical	1	2
		Grounding	0	0
E N G I N E	Changes	Few (<4)	40	89
		Medium (4-8)	5	11
		Large (>8)	0	0
	Power	Little	27	60
		Medium	16	36
		Large	2	4
R U D D E R	Changes	Few (<4)	22	49
		Medium (4-8)	23	51
		Large (>8)	0	0
	Angles	Small	2	4
		Medium	15	33
		Large	28	63
OVERALL MANEUVERING RATING		Safe	32	71
		Marginal	12	27
		Unsafe	1	2
		Failure	0	0
Note: 1. Average ship speed = 4.9 knots (prototype). 2. Average ship range = 3.9 - 5.6 knots.				

Table F5
Navigation Test Summary for All Inbound Runs, Test Plan 5c

Conditions		Ratings	Number	Percentage
N A V I G A T I O N	Ent. Channel	Easy	38	83
		Moderate	7	15
		Difficult	1	2
		Failure	0	0
	In Channel	Easy	22	48
		Moderate	18	39
		Difficult	6	13
		Failure	0	0
	Exit. Channel	Easy	36	78
		Moderate	8	18
		Difficult	2	4
		Failure	0	0
Ship Trackline		Optimum	17	37
		Variable	23	50
		Critical	6	13
		Grounding	0	0
E N G I N E	Changes	Few (<4)	37	80
		Medium (4-8)	9	20
		Large (>8)	0	0
	Power	Little	22	48
		Medium	20	43
		Large	4	9
R U D D E R	Changes	Few (<4)	24	52
		Medium (4-8)	22	48
		Large (>8)	0	0
	Angles	Small	0	0
		Medium	15	33
		Large	31	67
OVERALL MANEUVERING RATING		Safe	24	52
		Marginal	15	33
		Unsafe	7	15
		Failure	0	0
Note: 1. Average ship speed = 5.2 knots (prototype). 2. Average ship range = 4.1 - 6.8 knots.				

Table F6
Navigation Test Summary for All Inbound Runs, Test Plan 6c

Conditions		Ratings	Number	Percentage
N A V I G A T I O N	Ent. Channel	Easy	43	93
		Moderate	3	7
		Difficult	0	0
		Failure	0	0
	In Channel	Easy	30	65
		Moderate	15	33
		Difficult	1	2
		Failure	0	0
	Exit. Channel	Easy	38	83
		Moderate	8	17
		Difficult	0	0
		Failure	0	0
Ship Trackline		Optimum	26	57
		Variable	19	41
		Critical	1	2
		Grounding	0	0
E N G I N E	Changes	Few (<4)	45	98
		Medium (4-8)	1	2
		Large (>8)	0	0
	Power	Little	30	65
		Medium	14	31
		Large	2	4
R U D D E R	Changes	Few (<4)	34	74
		Medium (4-8)	12	26
		Large (>8)	0	0
	Angles	Small	1	2
		Medium	21	46
		Large	24	52
OVERALL MANEUVERING RATING		Safe	32	70
		Marginal	13	28
		Unsafe	1	2
		Failure	0	0
Note: 1. Average ship speed = 5.3 knots (prototype). 2. Average ship range = 4.2 - 6.3 knots.				

Table F7
Navigation Test Summary for All Outbound Runs, Test Plan 1a

Conditions		Ratings	Number	Percentage
N A V I G A T I O N	Ent. Channel	Easy	28	90
		Moderate	3	10
		Difficult	0	0
		Failure	0	0
	In Channel	Easy	22	71
		Moderate	8	26
		Difficult	1	3
		Failure	0	0
	Exit. Channel	Easy	20	65
		Moderate	10	32
		Difficult	1	3
		Failure	0	0
Ship Trackline		Optimum	20	65
		Variable	10	32
		Critical	1	3
		Grounding	0	0
E N G I N E	Changes	Few (<4)	29	94
		Medium (4-8)	2	6
		Large (>8)	0	0
	Power	Little (<4)	22	71
		Medium (4-8)	9	29
		Large (>8)	0	0
R U D D E R	Changes	Few (<4)	18	58
		Medium (4-8)	13	42
		Large (>8)	0	0
	Angles	Small (<4)	3	9
		Medium (4-8)	20	65
		Large (>8)	8	26
OVERALL MANEUVERING RATING		Safe	24	78
		Marginal	6	19
		Unsafe	1	3
		Failure	0	0

Note:

1. Average ship speed = 5.3 knots (prototype).
2. Average ship range = 3.5 - 6.6 knots.

Table F8
Navigation Test Summary for All Inbound Runs, Test Plan 4c
with Region B Waves and Current

Conditions		Ratings	Number	Percentage
N A V I G A T I O N	Ent. Channel	Easy	41	91
		Moderate	4	9
		Difficult	0	0
		Failure	0	0
	In Channel	Easy	33	73
		Moderate	12	27
		Difficult	0	0
		Failure	0	0
	Exit. Channel	Easy	45	100
		Moderate	0	0
		Difficult	0	0
		Failure	0	0
Ship Trackline		Optimum	28	62
		Variable	17	38
		Critical	0	0
		Grounding	0	0
E N G I N E	Changes	Few (<4)	39	87
		Medium (4-8)	6	13
		Large (>8)	0	0
	Power	Little	37	82
		Medium	8	18
		Large	0	0
R U D D E R	Changes	Few (<4)	15	33
		Medium (4-8)	30	67
		Large (>8)	0	0
	Angles	Small	5	11
		Medium	23	51
		Large	17	38
OVERALL MANEUVERING RATING		Safe	38	84
		Marginal	7	16
		Unsafe	0	0
		Failure	0	0
Note: 1. Average ship speed = 4.7 knots (prototype). 2. Average ship range = 3.8 - 5.5 knots.				

Table F9
Pilot Navigation Test Summary for All Inbound Runs, Test
Plan 4c

Conditions		Ratings	Number	Percentage
N A V I G A T I O N	Ent. Channel	Easy	14	31
		Moderate	21	47
		Difficult	8	18
		Failure	2	4
	In Channel	Easy	12	27
		Moderate	16	36
		Difficult	13	29
		Failure	4	9
	Exit. Channel	Easy	31	97
		Moderate	1	3
		Difficult	0	0
		Failure	0	0
Ship Trackline		Optimum	9	20
		Variable	23	51
		Critical	11	25
		Grounding	2	4
E N G I N E	Changes	Few (<4)	28	62
		Medium (4-8)	11	24
		Large (>8)	6	13
	Power	Little	20	44
		Medium	11	24
		Large	14	31
R U D D E R	Changes	Few (<4)	1	2
		Medium (4-8)	8	18
		Large (>8)	36	80
	Angles	Small	1	2
		Medium	17	38
		Large	27	60
OVERALL MANEUVERING RATING		Safe	16	36
		Marginal	15	33
		Unsafe	11	24
		Failure	3	7

Note:

1. Average ship speed = 5.7 knots (prototype).
2. Average ship range = 3.8 - 8.1 knots.

Table F10 Inbound Navigation Test Results for Test Plan 1a							
Environmental Condition	Staff/ Pilot	Onsite/ Video	Acceptable		Unacceptable		Total
			No.	%	No.	%	
Staff Tests							
Waves	Staff	Onsite	3	30	7	70	10
		Video	6	60	4	40	10
Waves & CN2	Staff	Onsite	5	50	5	50	10
		Video	5	63	3	38	8
Waves & CS2	Staff	Onsite	5	63	3	38	8
		Video	4	50	4	50	8
Waves, CN2 & Wind	Staff	Onsite	4	100	0	0	4
		Video	3	75	1	25	4
Waves & CN3	Staff	Onsite	1	33	2	67	3
		Video	1	50	1	50	2
Waves & CS3	Staff	Video	0	0	1	100	1
Total:		Onsite	18	51	17	49	35
		Video	19	58	14	42	33
Pilot Tests							
Waves	Pilot	Video	4	44	5	56	9
Waves & CN2	Pilot	Video	4	44	5	56	9
Waves & CS2	Pilot	Video	3	33	6	67	9
Waves & CN3	Pilot	Video	3	27	8	73	11
Waves & CS3	Pilot	Video	1	25	3	75	4
Total:		Video	15	36	27	64	42
Note: 1. CN2 = current north 2. 2. CS2 = current south 2.							

Table F11
Inbound Navigation Test Results for Test Plan 2c

Environmental Condition	Staff/ Pilot	Onsite/ Video	Acceptable		Unacceptable		Total
			No.	%	No.	%	
Waves	Staff	Onsite	9	100	0	0	9
		Video	9	100	0	0	9
Waves & CN2	Staff	Onsite	9	100	0	0	9
		Video	9	100	0	0	9
Waves & CS2	Staff	Onsite	9	100	0	0	9
		Video	7	78	2	22	9
Waves, CN2 & Wind	Staff	Onsite	9	100	0	0	9
		Video	6	67	3	33	9
Waves & CN3	Staff	Onsite	8	89	1	11	9
		Video	7	78	2	22	9
Total:		Onsite	44	98	1	2	45
		Video	38	84	7	16	45
Note: 1. CN2 = current north 2. 2. CS2 = current south 2.							

Table F12
Inbound Navigation Test Results for Test Plan 3c

Environmental Condition	Staff/ Pilot	Onsite/ Video	Acceptable		Unacceptable		Total
			No.	%	No.	%	
Waves	Staff	Onsite	9	100	0	0	9
		Video	8	89	1	11	9
Waves & CN2	Staff	Onsite	8	89	1	11	9
		Video	6	67	3	33	9
Waves & CS2	Staff	Onsite	9	90	1	10	10
		Video	8	80	2	20	10
Waves, CN2 & Wind	Staff	Onsite	8	89	1	11	9
		Video	7	78	2	22	9
Waves & CN3	Staff	Onsite	9	100	0	0	9
		Video	7	78	2	22	9
Total:		Onsite	43	93	3	7	46
		Video	36	78	10	22	46
Note: 1. CN2 = current north 2. 2. CS2 = current south 2.							

Table F13
Inbound Navigation Test Results for Test Plan 4c

Environmental Condition	Staff/ Pilot	Onsite/ Video	Acceptable		Unacceptable		Total
			No.	%	No.	%	
Staff Tests							
Waves	Staff	Onsite	9	100	0	0	9
		Video	8	89	1	11	9
Waves & CN2	Staff	Onsite	8	89	1	11	9
		Video	9	100	0	0	9
Waves & CS2	Staff	Onsite	9	100	0	0	9
		Video	7	78	2	22	9
Waves, CN2 & Wind	Staff	Onsite	9	100	0	0	9
		Video	9	100	0	0	9
Waves & CN3	Staff	Onsite	9	100	0	0	9
		Video	9	100	0	0	9
Total:		Onsite	44	98	1	2	45
		Video	42	93	3	7	45
Pilot Tests							
Waves	Pilot	Onsite	11	73	4	27	15
		Video	11	73	4	27	15
Waves & CS2	Pilot	Onsite	10	67	5	33	15
		Video	14	93	1	7	15
Waves & CN3	Pilot	Onsite	10	67	5	33	15
		Video	12	80	3	20	15
Total:		Onsite	31	69	14	31	45
		Video	37	82	8	18	45
Region B Tests							
Wave W9 & CN4	Staff	Onsite	45	100	0	0	45
		Video	43	96	2	4	45
	Pilot	Video	5	100	0	0	5
Region B - Ore Carrier Tests							
Wave W9 & CN4	Pilot	Video	2	100	0	0	2
Note: 1. CN2 = current north 2 2. CS2 = current south 2							

Table F14
Inbound Navigation Test Results for Test Plan 5c

Environmental Condition	Staff/ Pilot	Onsite/ Video	Acceptable		Unacceptable		Total
			No.	%	No.	%	
Waves	Staff	Onsite	9	100	0	0	9
		Video	8	89	1	11	9
Waves & CN2	Staff	Onsite	7	78	2	22	9
		Video	8	89	1	11	9
Waves & CS2	Staff	Onsite	8	89	1	11	9
		Video	7	78	2	22	9
Waves, CN2 & Wind	Staff	Onsite	9	100	0	0	9
		Video	9	100	0	0	9
Waves & CN3	Staff	Onsite	6	60	4	40	10
		Video	7	70	3	30	10
Total:		Onsite	39	85	7	15	46
		Video	39	85	7	15	46

Note:

1. CN2 = current north 2.
2. CS2 = current south 2.

Table F15
Inbound Navigation Test Results for Test Plan 6c

Environmental Condition	Staff/ Pilot	Onsite/ Video	Acceptable		Unacceptable		Total
			No.	%	No.	%	
Staff Tests							
Waves	Staff	Onsite	9	90	1	10	10
		Video	8	80	2	20	10
Waves & CN2	Staff	Onsite	9	100	0	0	9
		Video	9	100	0	0	9
Waves & CS2	Staff	Onsite	9	100	0	0	9
		Video	8	89	1	11	9
Waves, CN2 & Wind	Staff	Onsite	9	100	0	0	9
		Video	8	89	1	11	9
Waves & CN3	Staff	Onsite	9	100	0	0	9
		Video	8	89	1	11	9
Total:		Onsite	45	98	1	2	46
		Video	41	89	5	11	46
Pilot Tests							
Waves & CS2	Pilot	Video	8	73	3	27	11
Region B Tests							
Waves & CS4	Pilot	Video	3	100	0	0	3
Note: 1. CN2 = current north 2. 2. CS2 = current south 2.							

Table F16
Outbound Navigation Test Results for Test Plan 1a

Environmental Condition	Staff/ Pilot	Onsite/ Video	Acceptable		Unacceptable		Total
			No.	%	No.	%	
Staff Tests							
Waves	Staff	Onsite	9	90	1	10	10
		Video	9	90	1	10	10
Waves & CN2	Staff	Onsite	10	100	0	0	10
		Video	10	100	0	0	10
Waves & CS2	Staff	Onsite	8	100	0	0	8
		Video	7	100	0	0	7
Waves, CN2 & Wind	Staff	Video	4	100	0	0	4
Waves & CN3	Staff	Onsite	3	100	0	0	3
		Video	2	100	0	0	2
Waves & CS3	Staff	Video	1	100	0	0	1
Total:		Onsite	30	97	1	3	31
		Video	33	97	1	3	34
Pilot Tests							
Waves	Pilot	Video	7	78	2	22	9
Waves & CN2	Pilot	Video	8	89	1	11	9
Waves & CS2	Pilot	Video	3	33	6	67	9
Waves & CN3	Pilot	Video	10	100	0	0	10
Waves & CS3	Pilot	Video	0	0	4	100	4
Total:		Video	28	68	13	32	41
Note: 1. CN2 = current north 2. 2. CS2 = current south 2.							

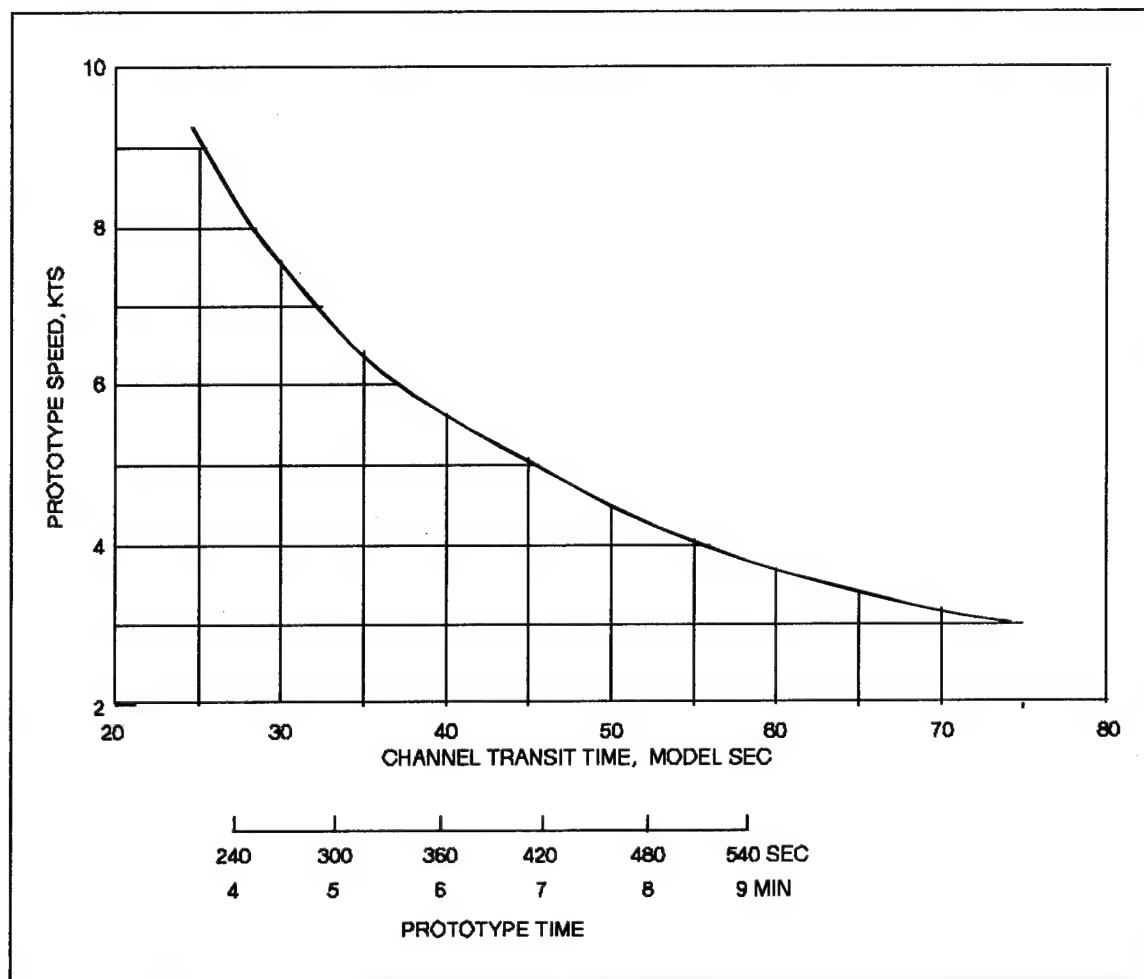


Figure F2. Prototype speed versus prototype and model channel transit time

Table F17
Videotape Log of Selected Navigation Test Runs

Test Plan	Tape Timer	Test ID	Prototype Waves			Prot. Current knots	Average Ship Speed knots	Overall Maneuv. Rating	Comments
			H, ft	T, sec	D, deg				
1a	0.15	E7W CN	6.9	8.3	45	0.5		Safe	Outbound. Optimum, easy run. Yaw angle in channel entrance to counteract current
	1.35						5.1	Safe	Inbound. Smooth trackline. Large yaw-angle in channel entrance
	2.55	E5W CN Run 10	7.5	12.6	80		6.1	Marg	Outbound, pilot run. Problems in outer part of channel due to slow speed there
	4.45	E5W CN	6.9	16.7	42.5		4.8	Marg	Inbound, pilot run. Subjective assessment was safe
	6.00	E2W CS						Unsafe	Unsafe at station 0-3
	7.30	E4W CN WIND		14.2	45		5.1	Marg	Listed as marginal at station 3-9, actually closer to safe
4c	8.50	171 CN Run 3	8.2	16.7	42.5	0.5	5.1	Safe	Good, easy run. Ship parallel to flare
	10.25	211 CN MAX Run 3	7.5	12.6	80	0.8	5.4	Marg	Marginal/critical in outer part of channel Station 0-3. Very large waves. Variable ship trackline
	11.50	151CN MAX Run 4	10.5	9.1	57.5		5.9	Marg/Safe	Pilot run. Bursts of 1/2 ahead in entrance and in channel. Subjective assessment was marginal
	13.05	211 CS Run 5	7.5	12.6	80	0.5	6.4	Marg	Pilot run. Large waves. Strong setting towards north around station 21
	14.15	211 CS Run 2					5.9	Failure	Pilot run. Very difficult channel entrance with slow speed. Although failure according to video evaluations, the vessel never actually hit the channel sides
(Continued)									

Table F17 (Concluded)

Test Plan	Tape Timer	Test ID	Prototype Waves			Prot. Current knots	Average Ship Speed knots	Overall Maneuv. Rating	Comments
			H, ft	T, sec	D, deg				
4c	15.30	Generic	4.6	12.6	80	0.4	5.6	Safe	Pilot run. Safe run, but burst of 1/2 ahead to adjust course
	16.45						4.0	Safe	Very slow, easy run by CERC - staff
6c	18.05	171 CN Run 3	8.2	16.7	42.5	0.5	4.8	Safe	Close to marginal. Too slow speed at channel entrance. Off center-line
	19.45	151 CS Run 1	10.5	9.1	57.5		5.1	Marg	Close to unsafe
	21.10	211 CS Run 5	7.5	12.6	80		5.5	Marg/Unsafe	Pilot run. Difficult with large waves
5c	22.20	211 CN MAX Run 2	7.5	12.6	80	0.8	5.4	Marg	Yaw angle larger than flare angle
	23.50	211 CN MAX Run 4					6.8	Failure	Very difficult run. Too slow speed in channel entrance. Ship taken by high waves. No actual touching of channel sides
2c	25.00	F5W CN Run 2	7.5	12.6	80	0.5	6.1	Marg	Large waves
	26.30	F5W CN MAX Run 3				0.8	5.9	Failure	Extreme waves. Hitting bottom, and strong north setting around station 27-30
3c	27.50	P5W CN WIND Run 3	7.5	12.6	80	0.5	5.9	Marg	Difficult, close to critical run at channel entrance and at station 41. North setting at shoreline
4c	29.15	Generic	4.6	12.6	80	0.4	5.1	Safe	Demo run with ore carrier. Safe, easy run
4c	30.10	211 CN	7.5	12.6	80	0.5			Dye test
5c	31.10								Dye test
6c	32.35								Dye test

Appendix G

Wind-Wave Response

List of Figures

Figure G1. Measured wind-wave heights for test plan 2c	G2
Figure G2. Measured wind-wave heights for test plan 3a	G2
Figure G3. Measured wind-wave heights for test plan 3c	G3
Figure G4. Measured wind-wave heights for test plan 5c	G3

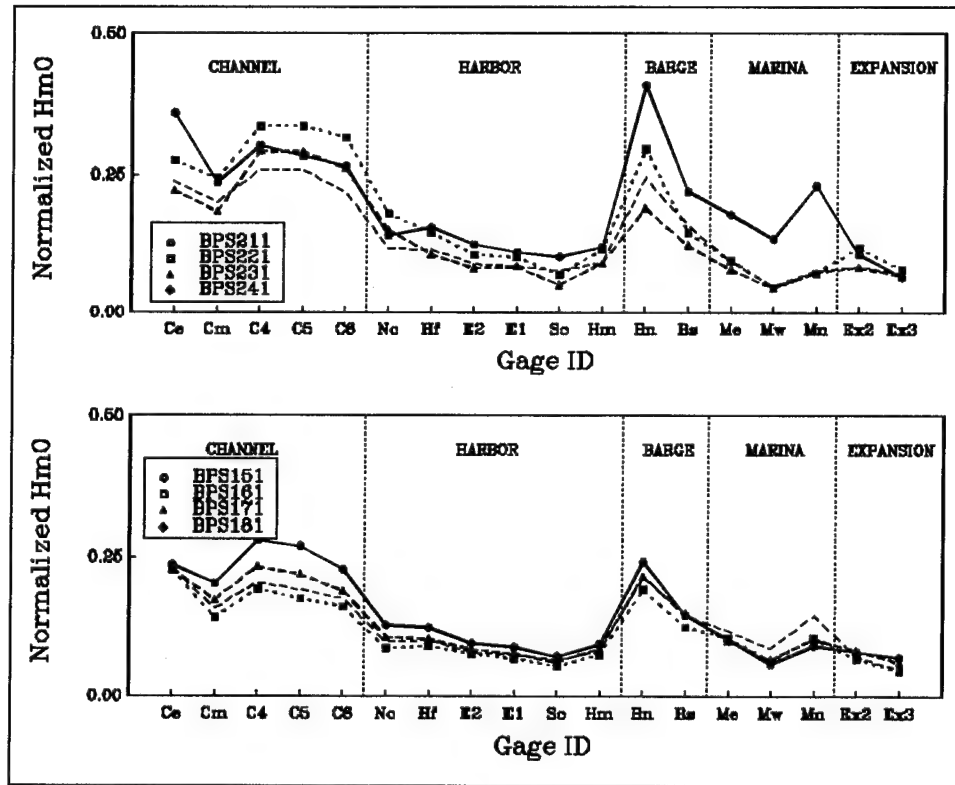


Figure G1. Measured wind-wave heights for test plan 2c

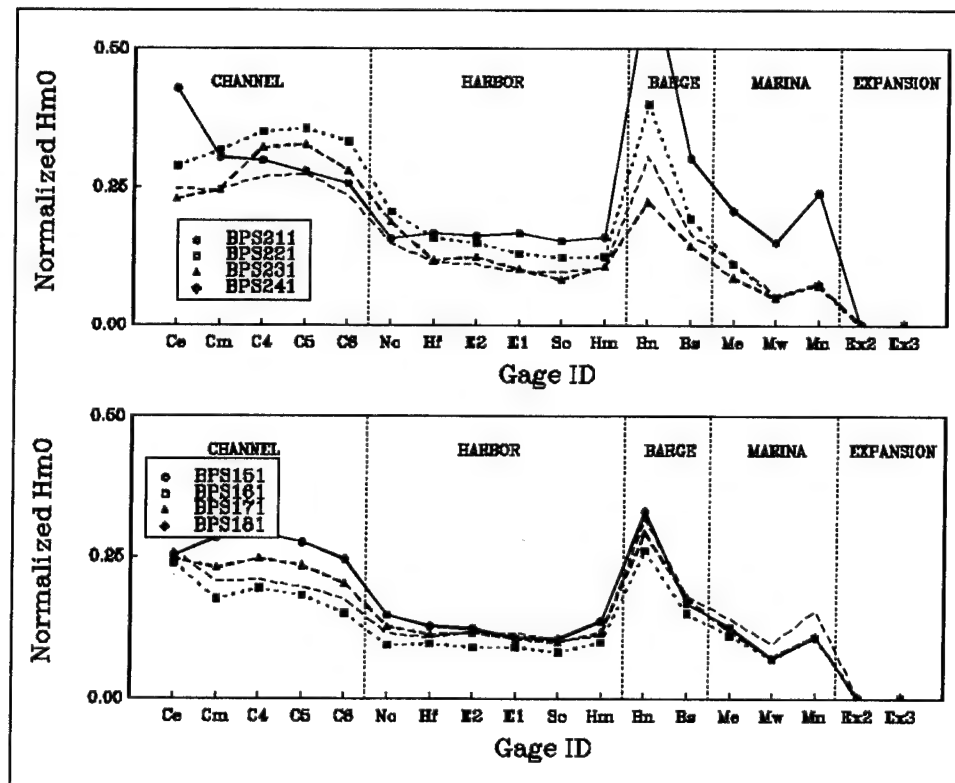


Figure G2. Measure wind-wave heights for test plan 3a

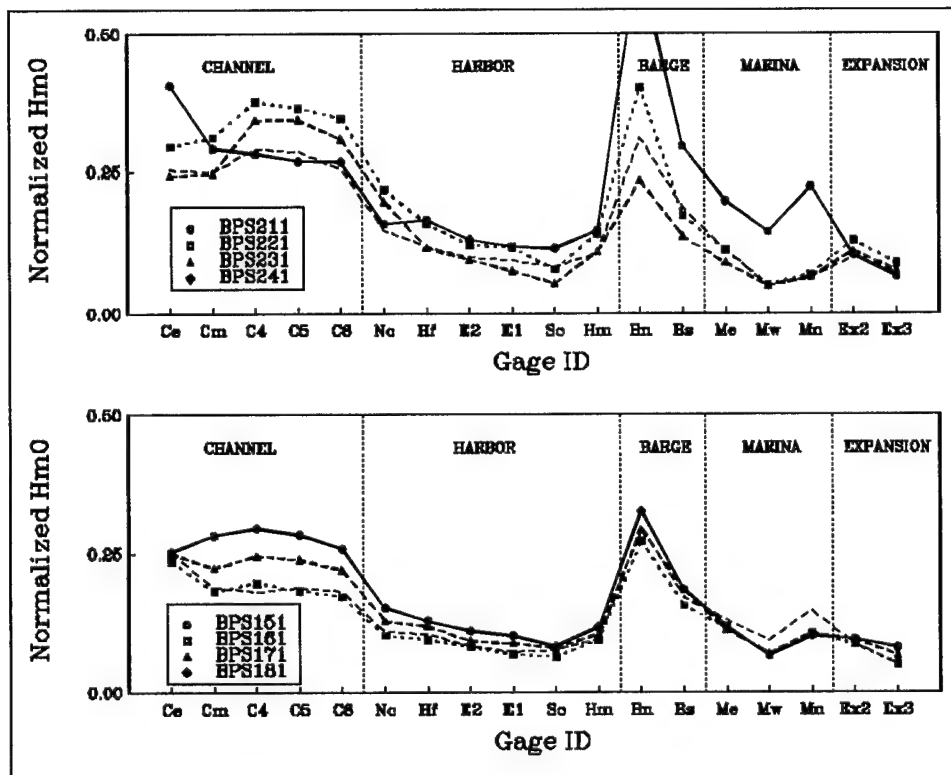


Figure G3. Measured wind-wave heights for test plan 3c

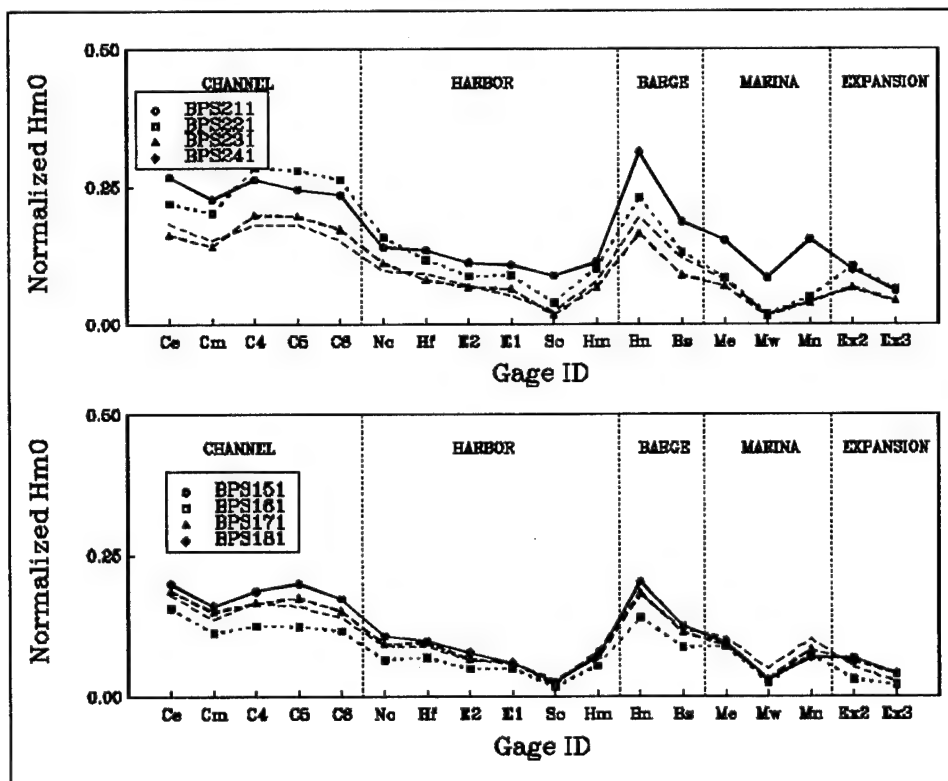


Figure G4. Measured wind-wave heights for test plan 5c

Appendix H

Long-Wave Response

List of Figures

Figure H1.	Transfer functions for test plan 2c	H3
Figure H2.	Transfer functions for test plan 3a	H4
Figure H3.	Transfer functions for test plan 3c	H5
Figure H4.	Transfer function for test plan 5c	H6
Figure H5.	Amplitude contour plots for test plan 2c	H7
Figure H6.	Amplitude contour plots for test plan 3a	H8
Figure H7.	Amplitude contour plots for test plan 3c	H9
Figure H8.	Amplitude contour plots for test plan 5c	H10
Figure H9.	Amplitude contour plots for test plan 6c	H11
Figure H10.	Phase plots for test plan 2c	H12
Figure H11.	Phase plots for test plan 3a	H13
Figure H12.	Phase plots for test plan 3c	H14
Figure H13.	Phase plots for test plan 5c	H15
Figure H14.	Phase plots for test plan 6c	H16
Figure H15.	Channel middle transfer functions for test plan 1a	H17
Figure H16.	North corner transfer functions for test plan 1a	H18
Figure H17.	East corner transfer functions for test plan 1a	H19
Figure H18.	Channel middle transfer functions for test plan 1c	H20
Figure H19.	North corner transfer functions for test plan 1c	H21
Figure H20.	East corner transfer functions for test plan 1c	H22
Figure H21.	Channel middle transfer functions for test plan 2c	H23
Figure H22.	North corner transfer functions for test plan 2c	H24

Figure H23.	East corner transfer functions for test plan 2c	H25
Figure H24.	South corner transfer functions for test plan 2c	H26
Figure H25.	Channel middle transfer functions for test plan 3a	H27
Figure H26.	North corner transfer functions for test plan 3a	H28
Figure H27.	East corner transfer functions for test plan 3a	H29
Figure H28.	South corner transfer functions for test plan 3a	H30
Figure H29.	Channel middle transfer functions for test plan 3c	H31
Figure H30.	North corner transfer functions for test plan 3c	H32
Figure H31.	East corner transfer functions for test plan 3c	H33
Figure H32.	South corner transfer functions for test plan 3c	H34
Figure H33.	Channel middle transfer functions for test plan 4c	H35
Figure H34.	North corner transfer functions for test plan 4c	H36
Figure H35.	East corner transfer functions for test plan 4c	H37
Figure H36.	Channel middle transfer functions for test plan 5c	H38
Figure H37.	North corner transfer functions for test plan 5c	H39
Figure H38.	East corner transfer functions for test plan 5c	H40
Figure H39.	South corner transfer functions for test plan 5c	H41
Figure H40.	Channel middle transfer functions for test plan 6c	H42
Figure H41.	North corner transfer functions for test plan 6c	H43
Figure H42.	East corner transfer functions for test plan 6c	H44

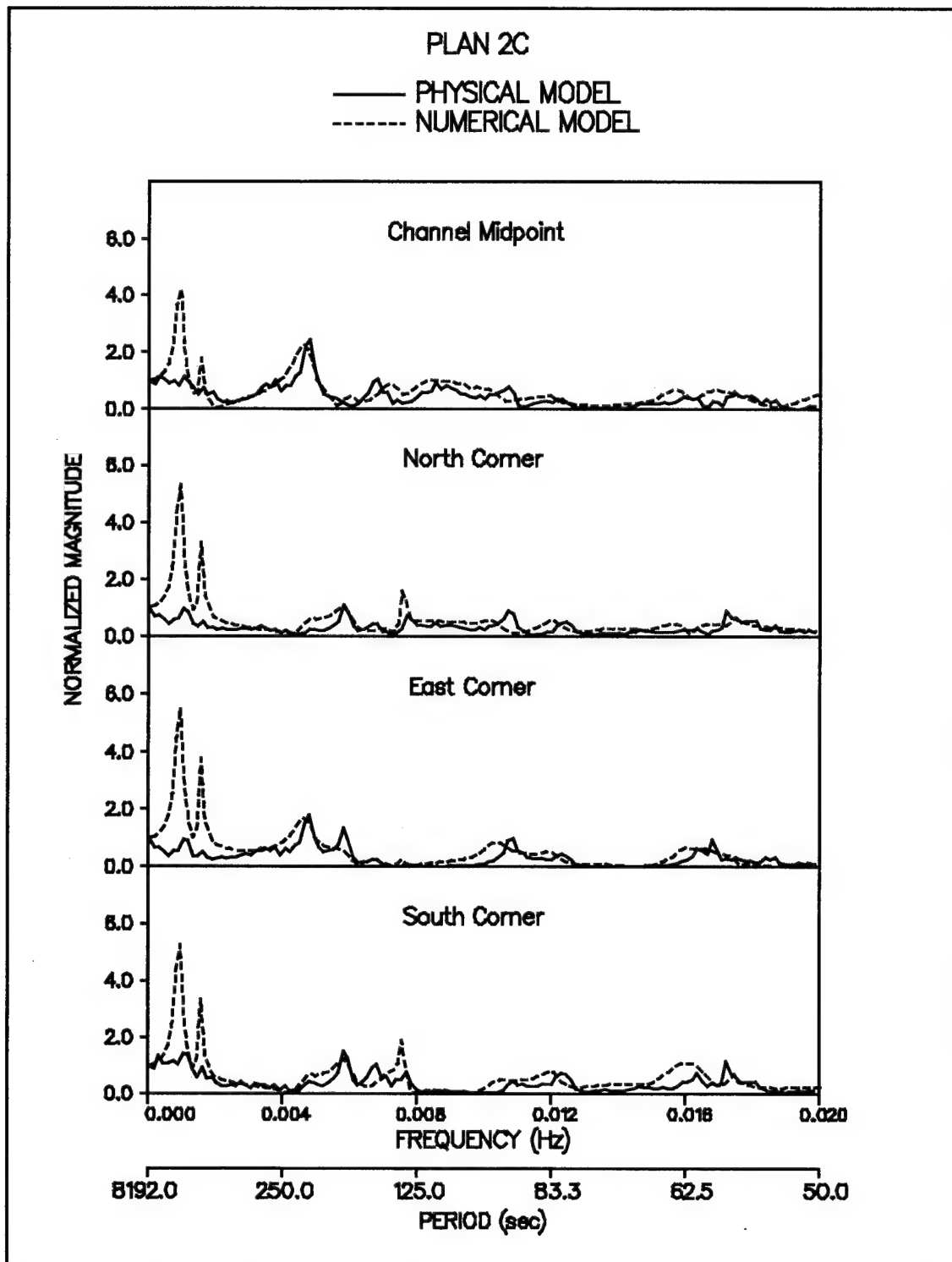


Figure H1. Transfer functions for test plan 2c

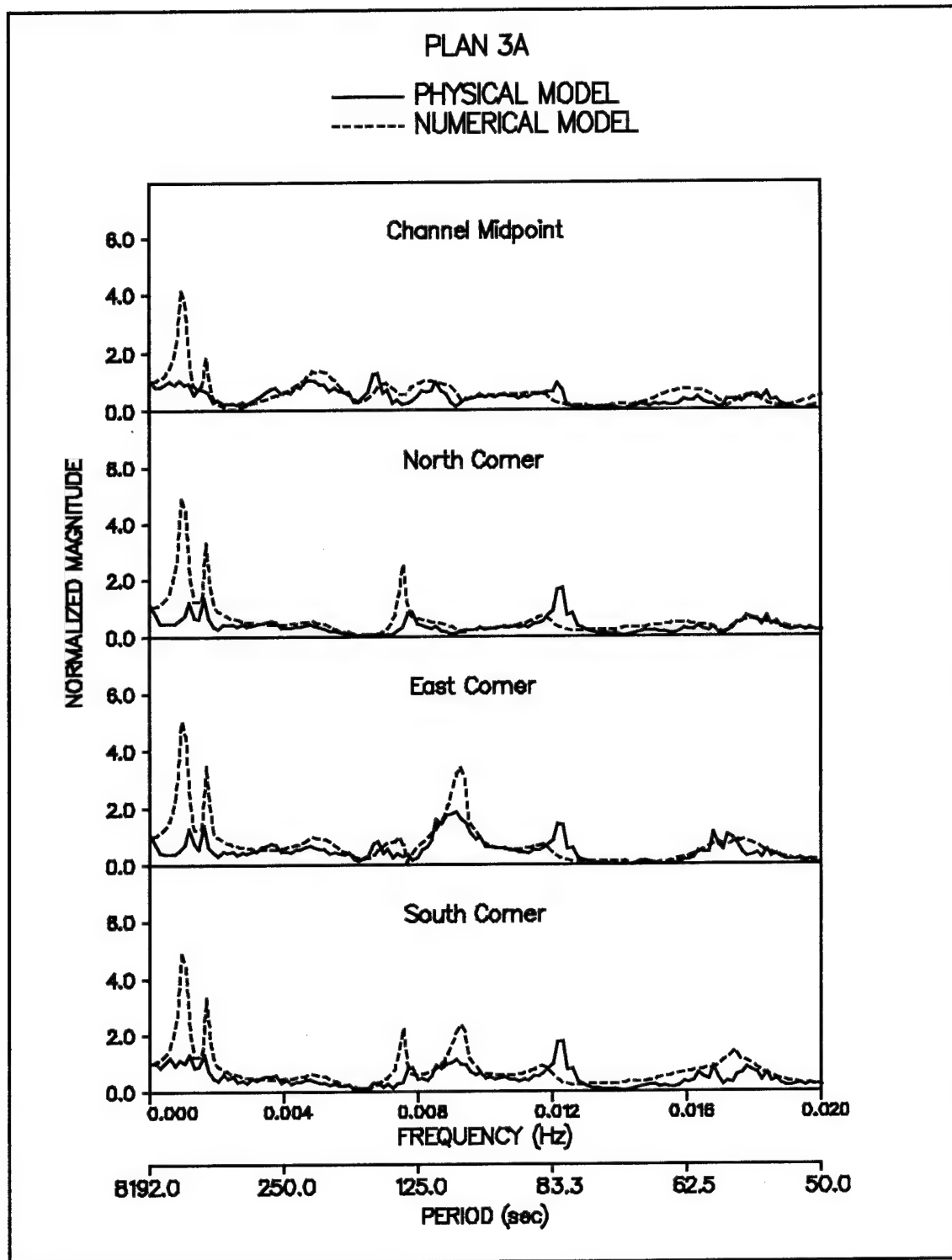


Figure H2. Transfer functions for test plan 3a

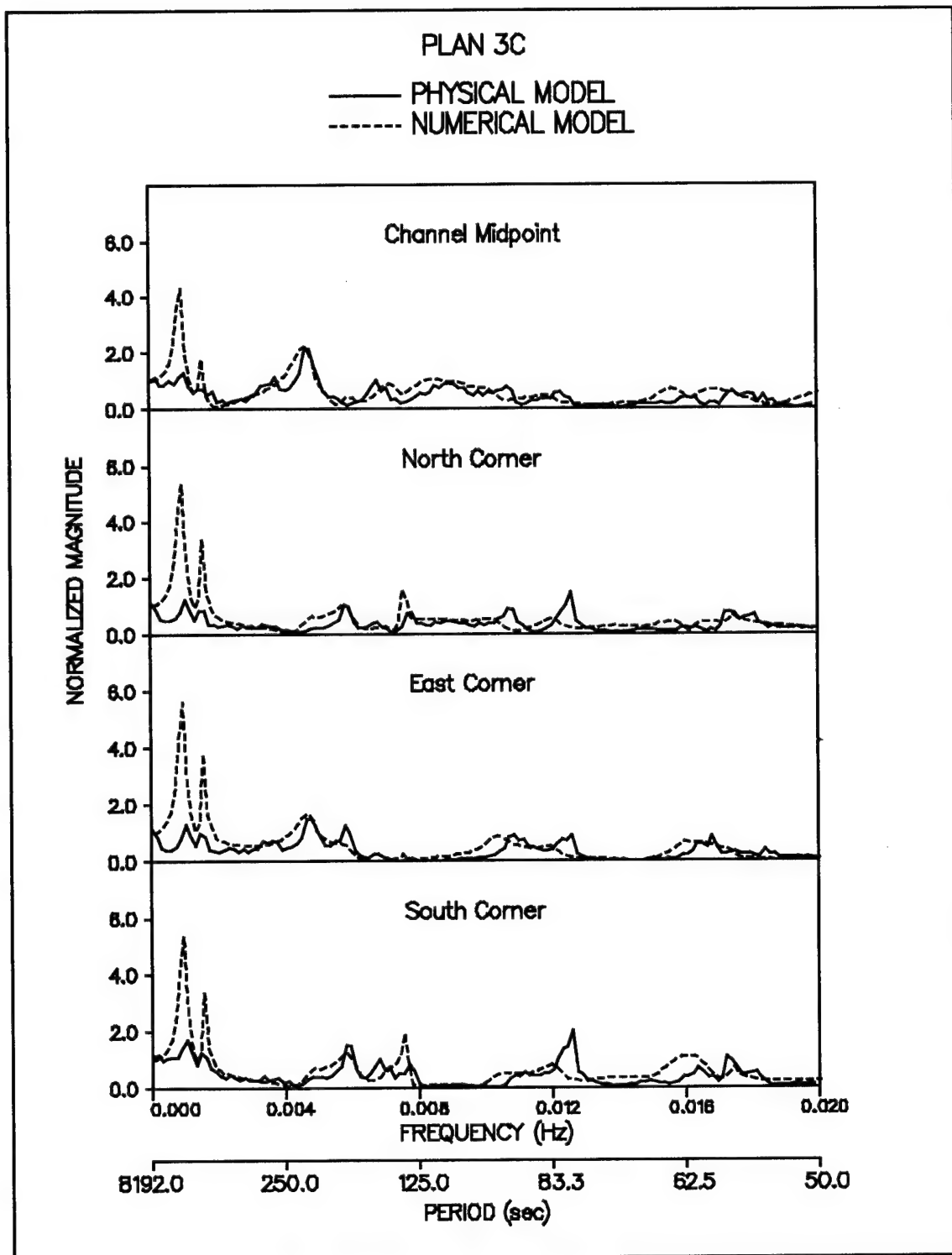


Figure H3. Transfer functions for test plan 3c

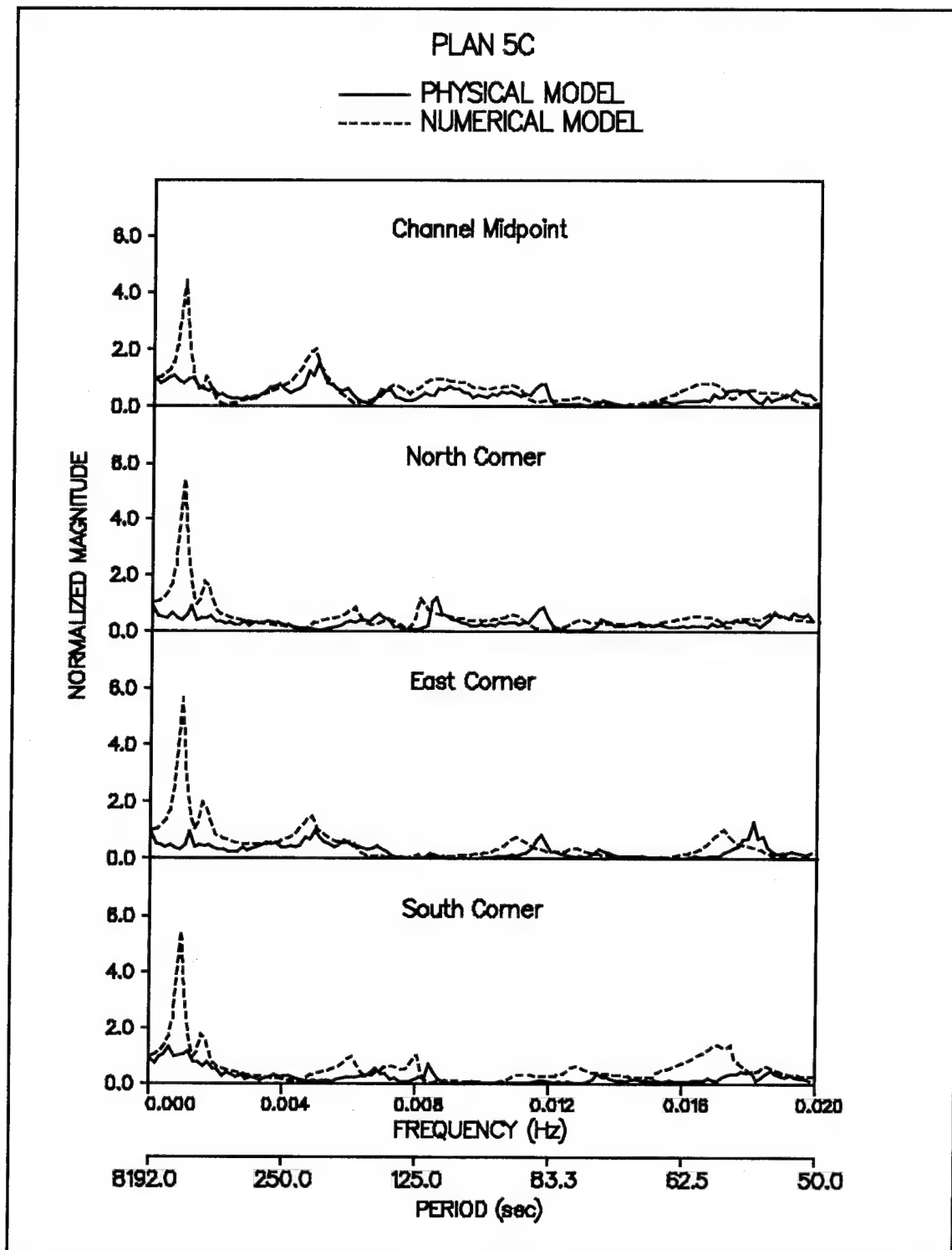


Figure H4. Transfer functions for test plan 5c

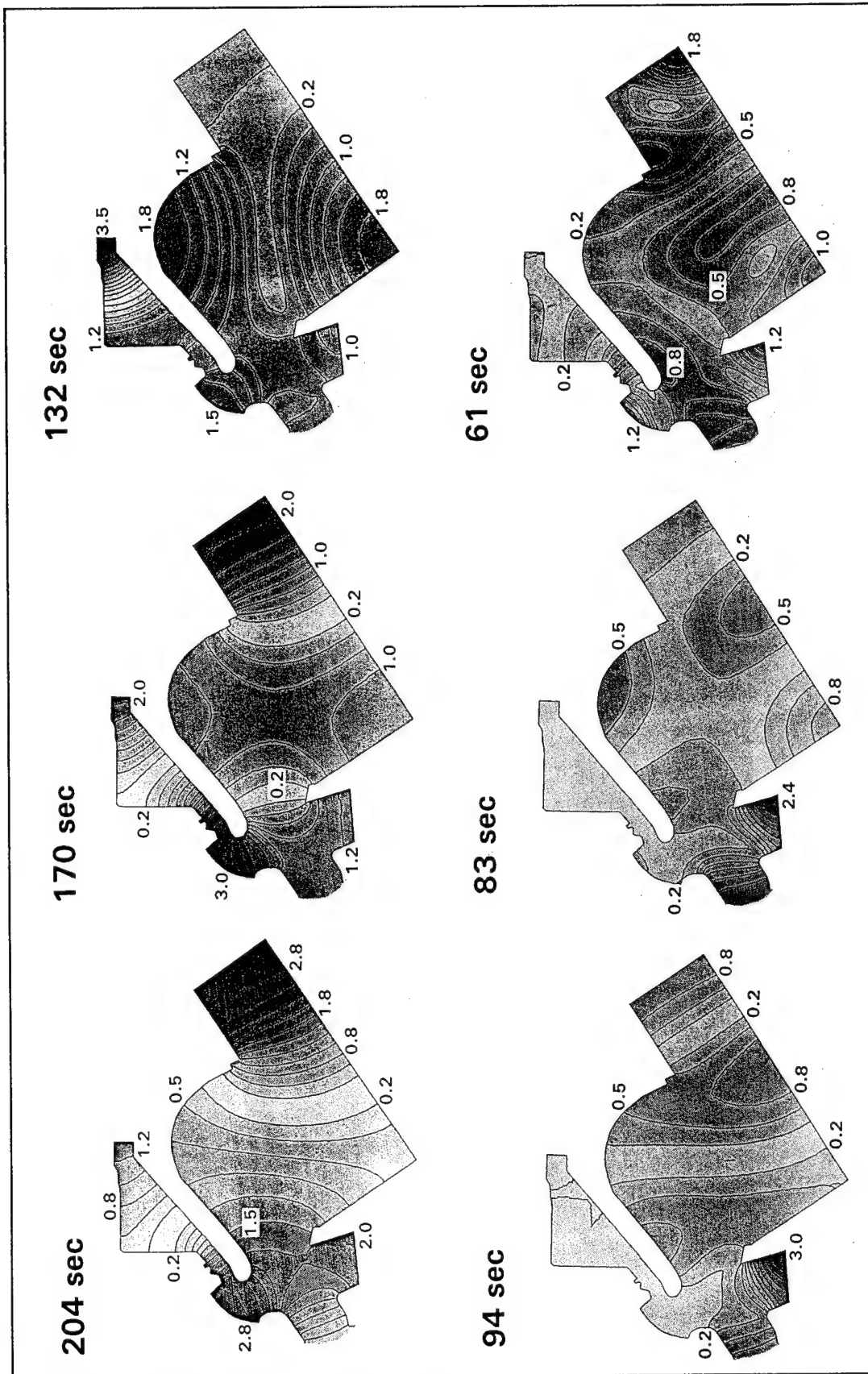


Figure H5. Amplitude contour plots for test plan 2c

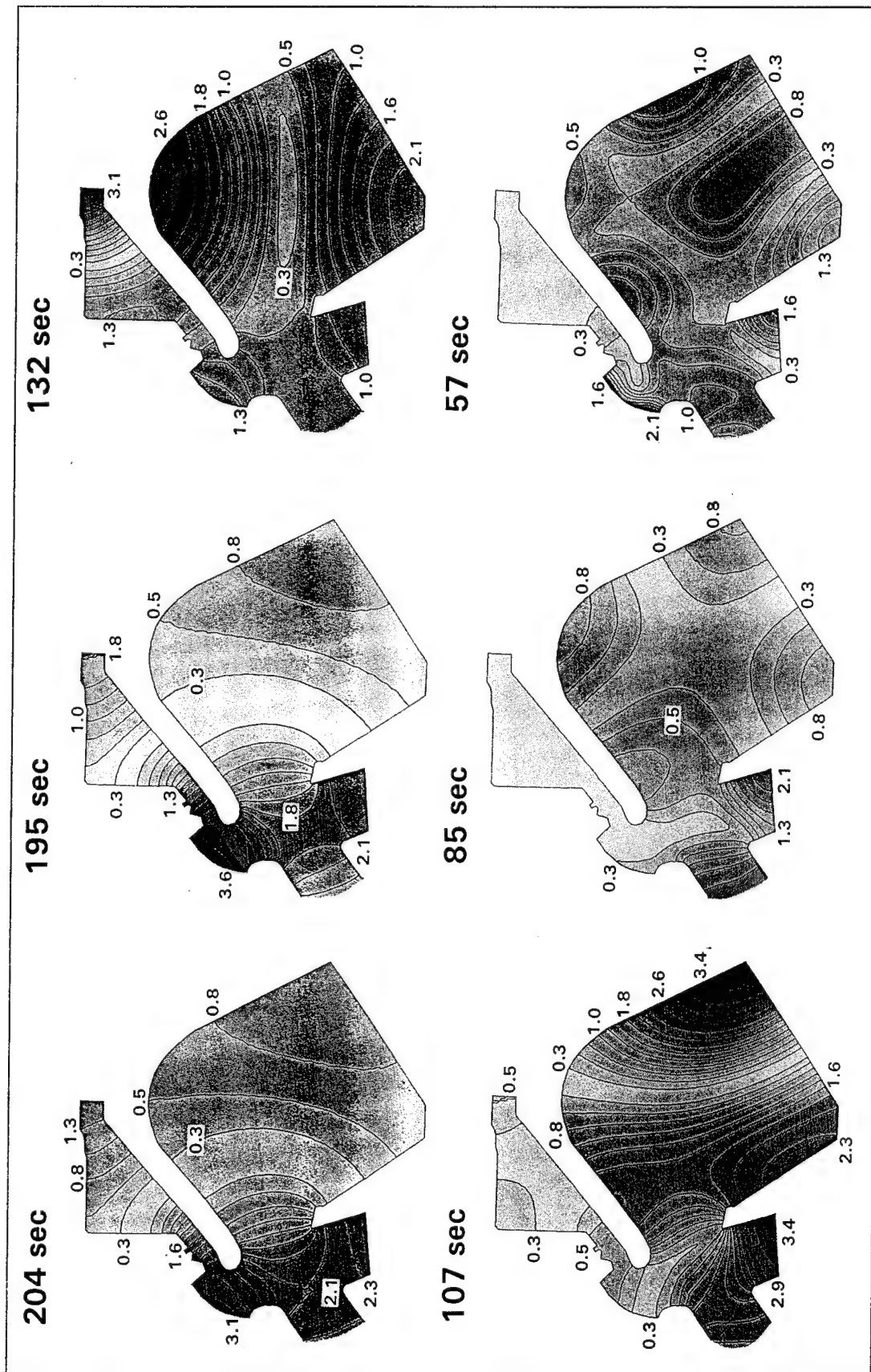


Figure H6. Amplitude contour plots for test plan 3a

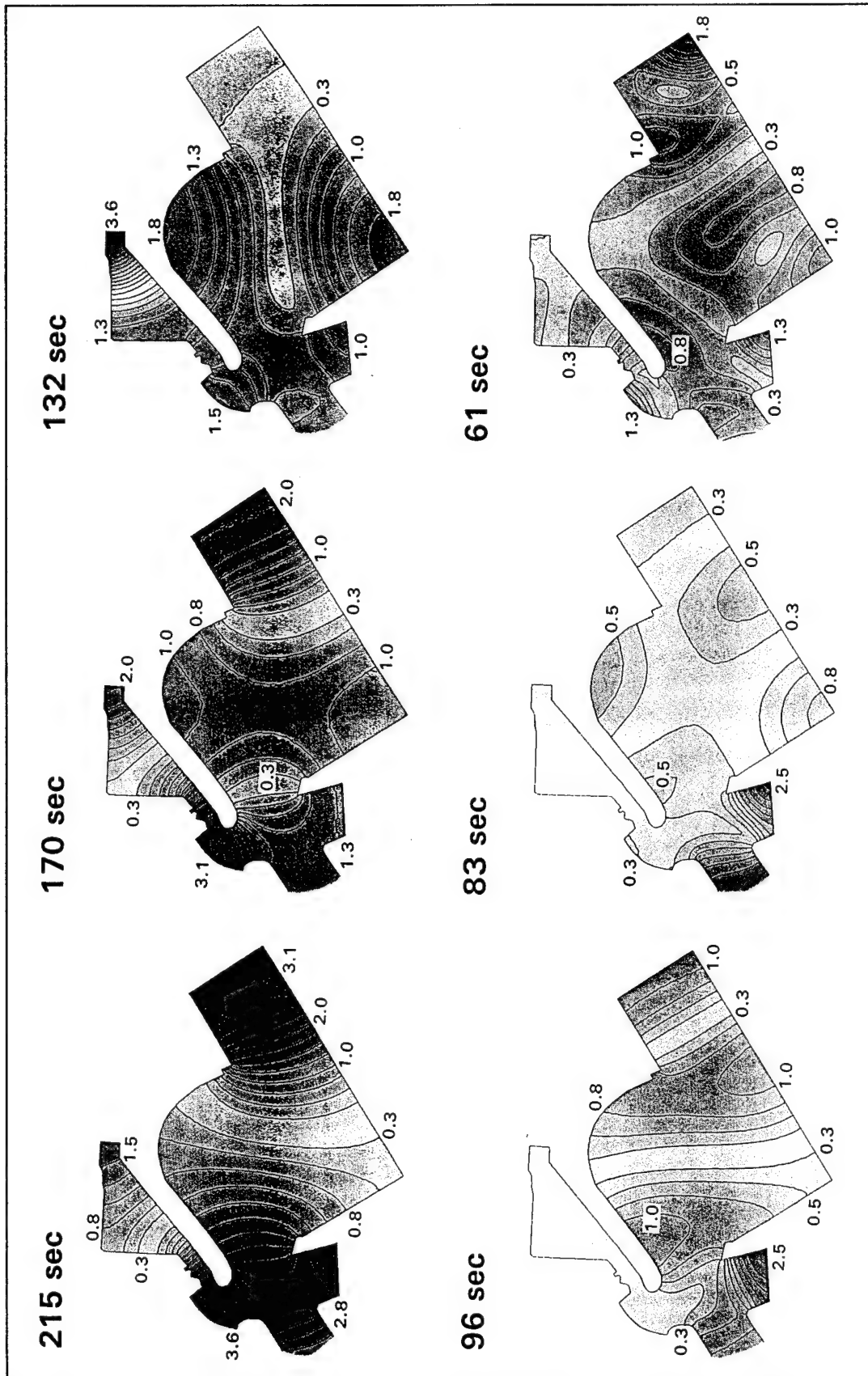


Figure H7. Amplitude contour plots for test plan 3c

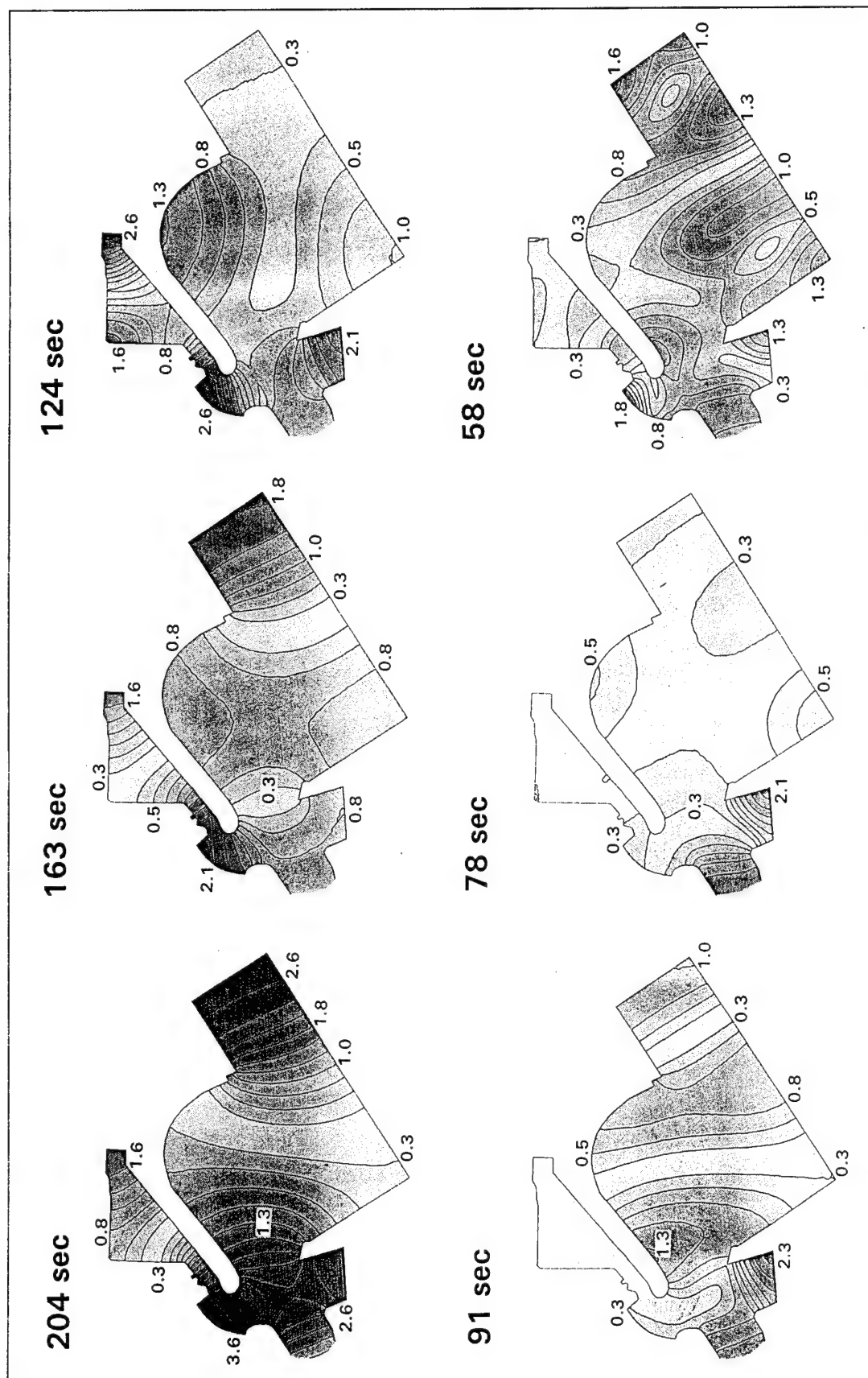


Figure H8. Amplitude contour plots for test plan 5c

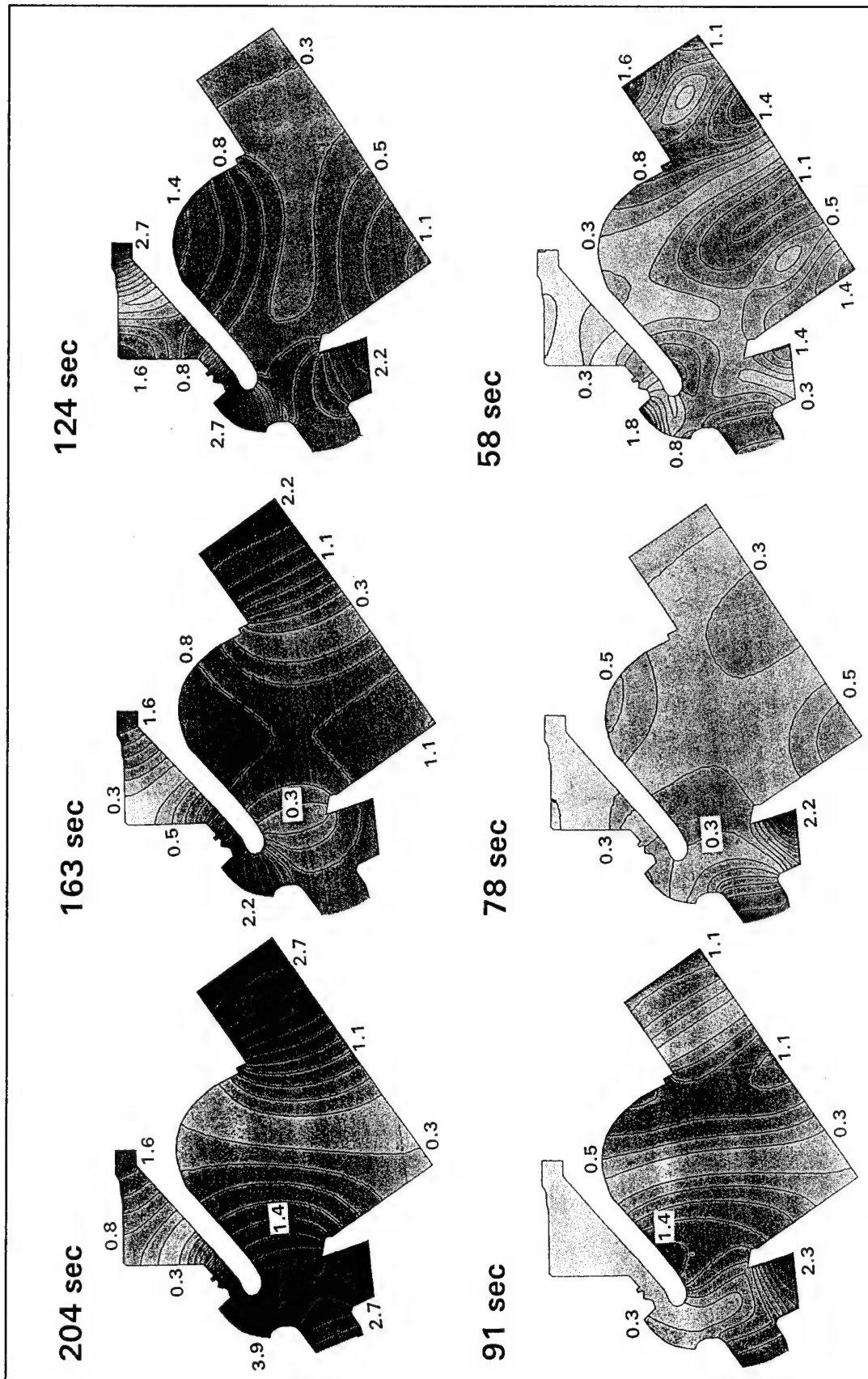


Figure H9. Amplitude contour plots for test plan 6c

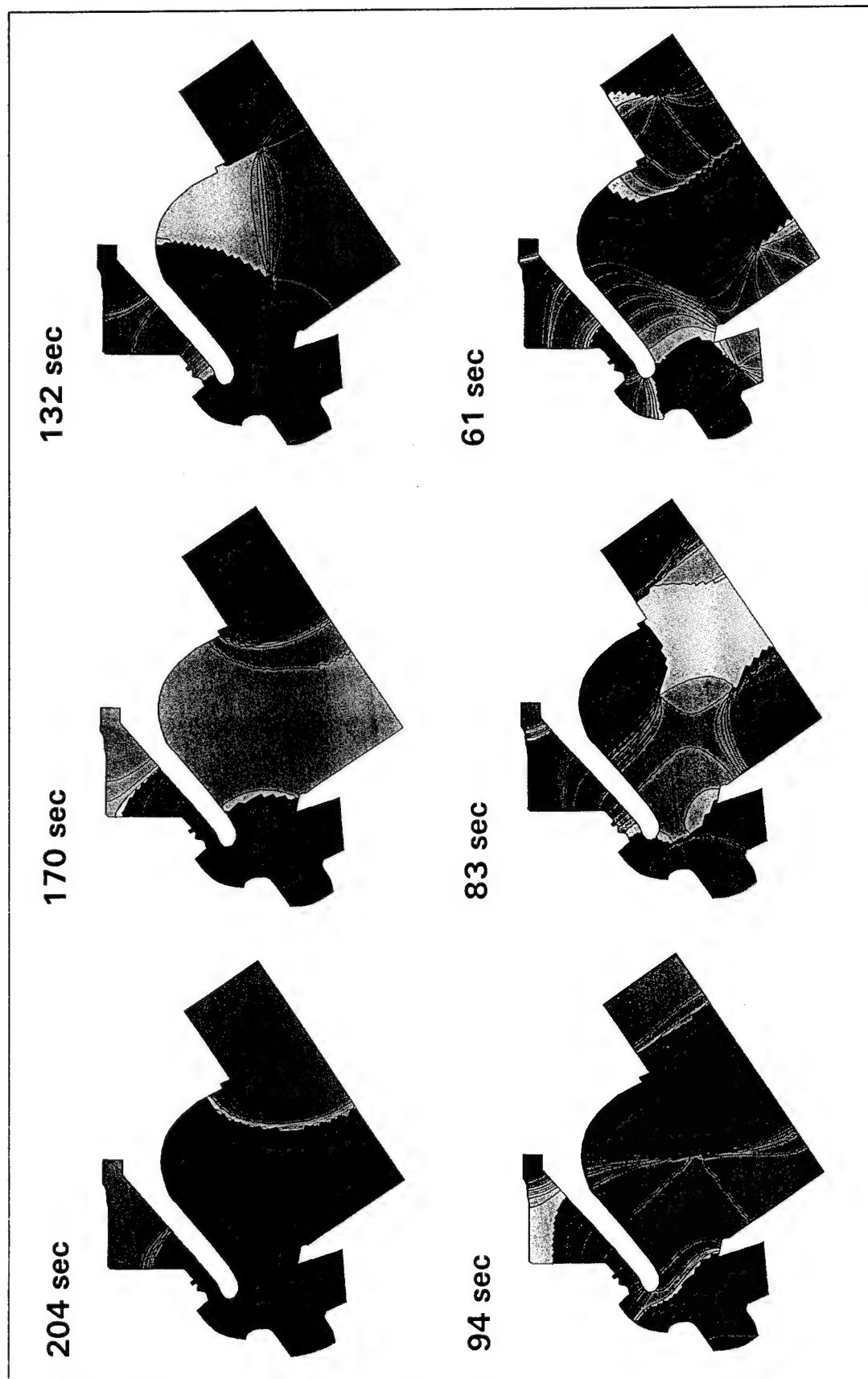


Figure H10. Phase plots for test plan 2c

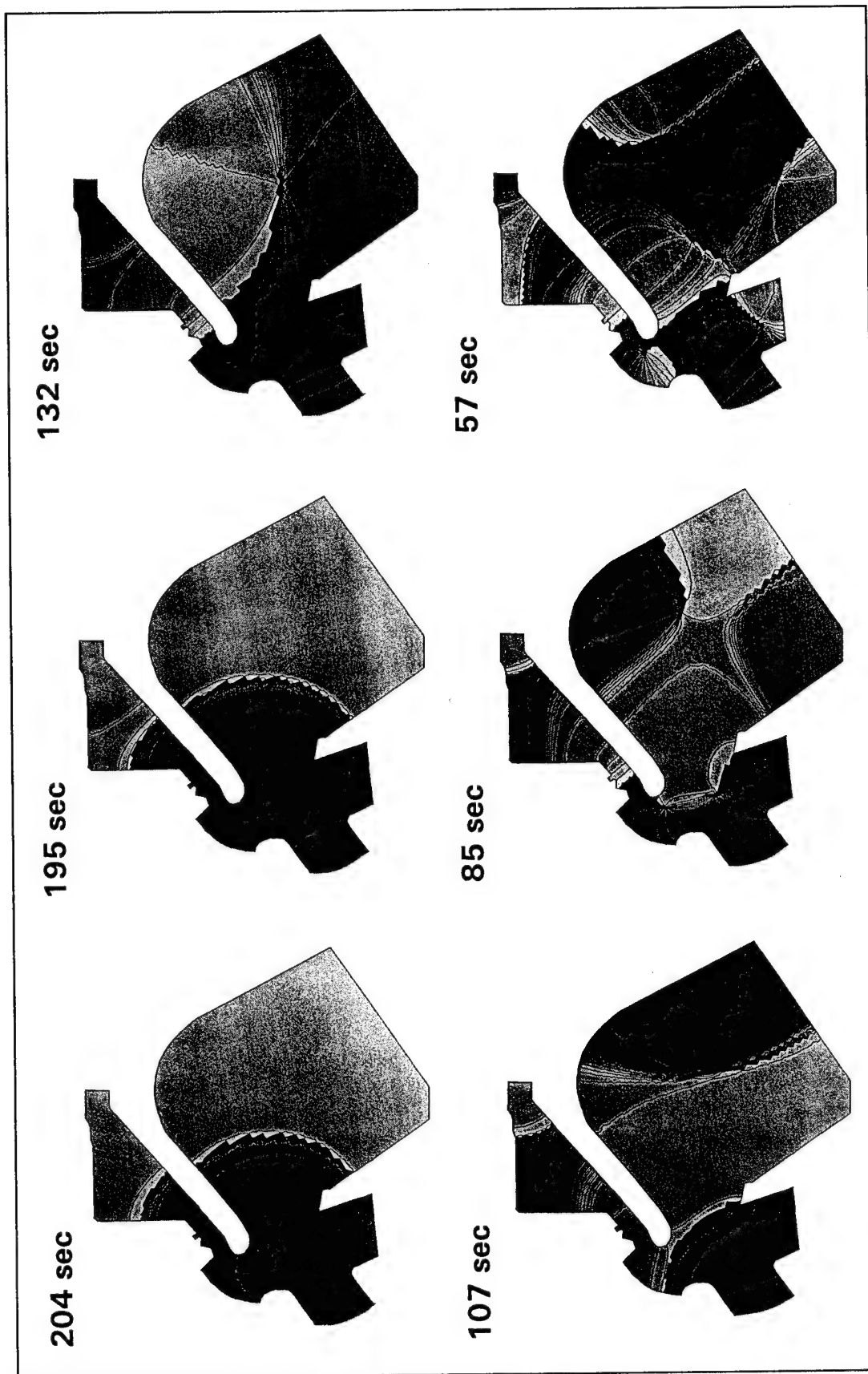


Figure H11. Phase plots for test plan 3a

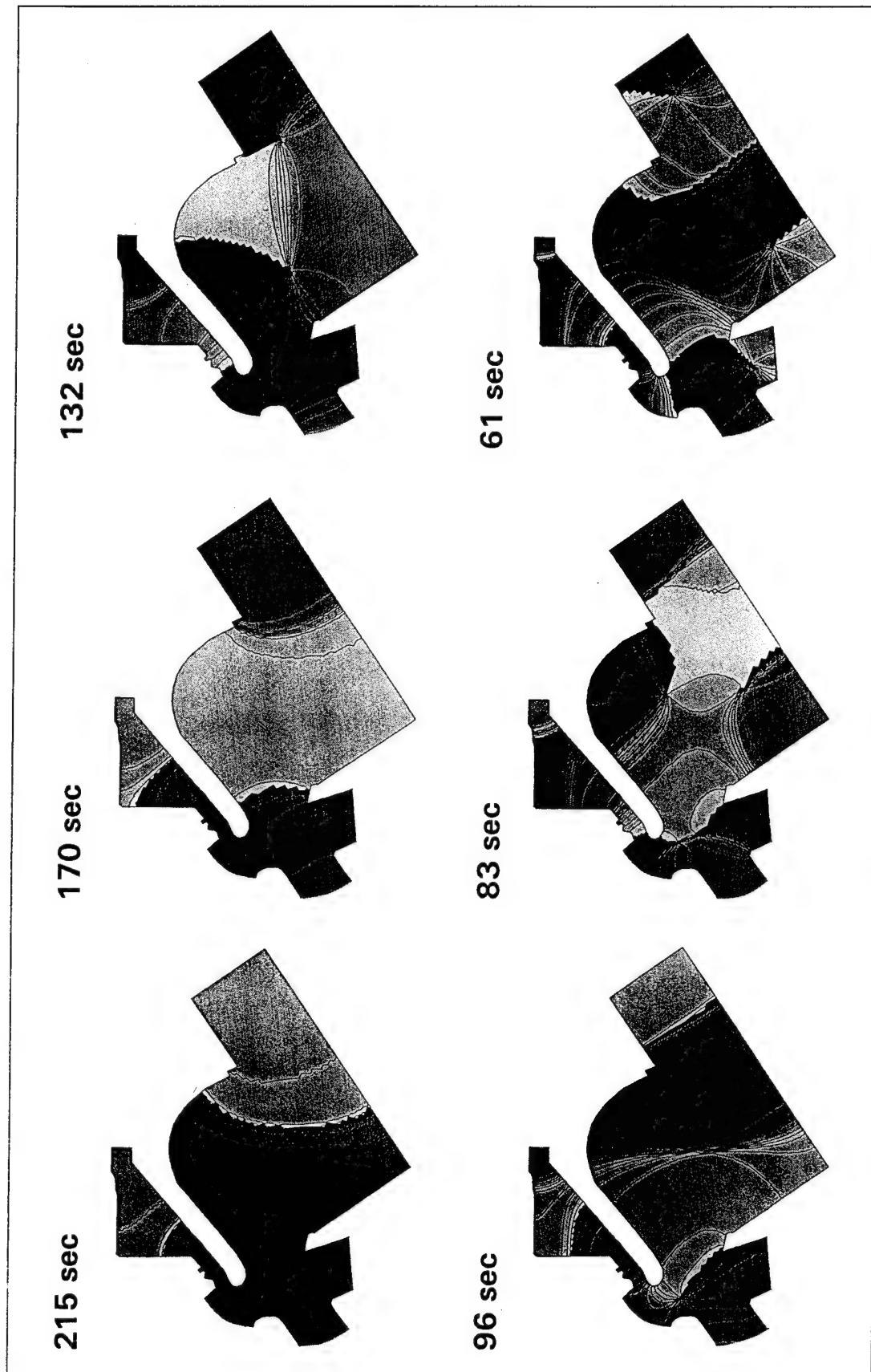


Figure H12. Phase plots for test plan 3c

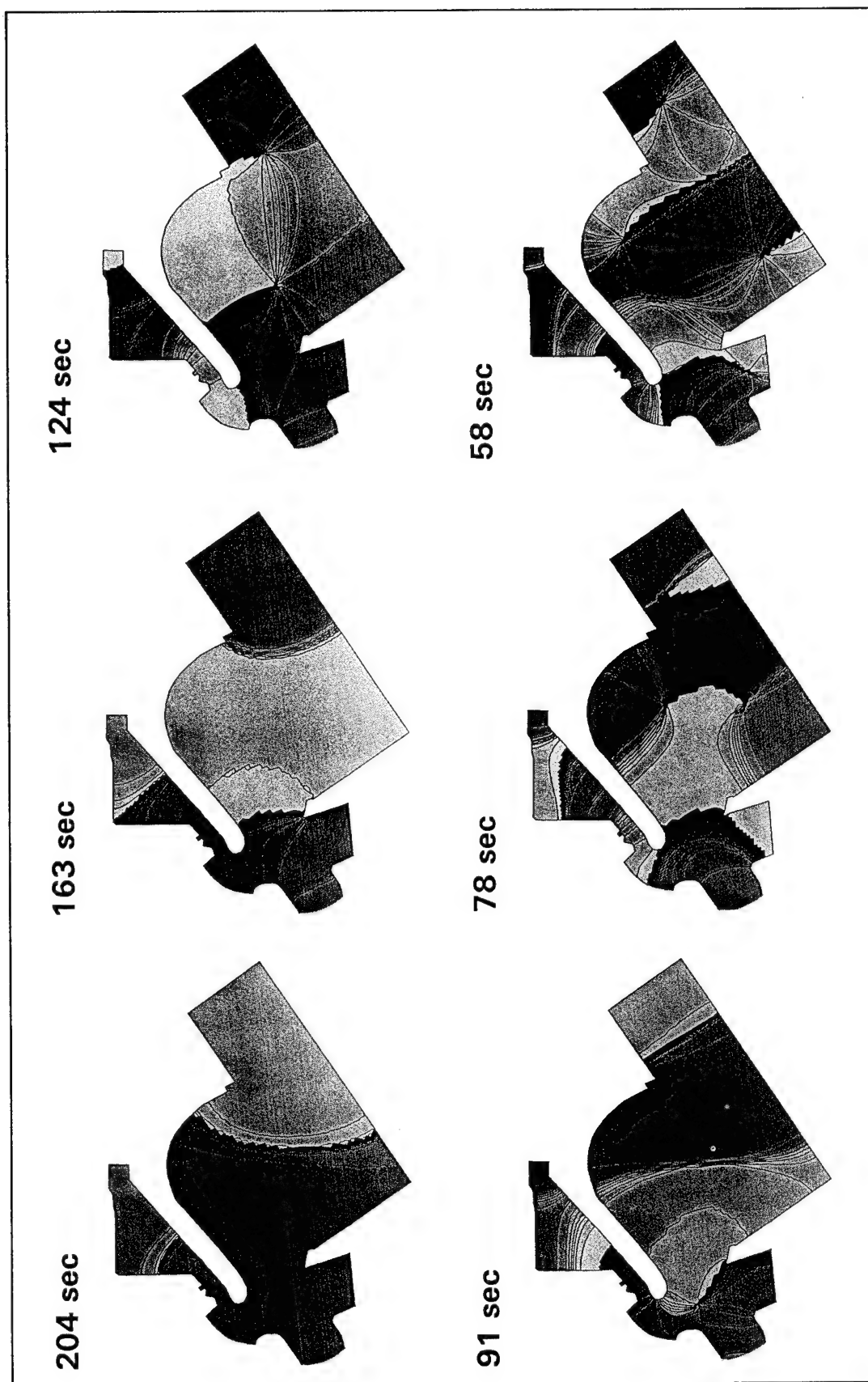


Figure H13. Phase plots for test plan 5c

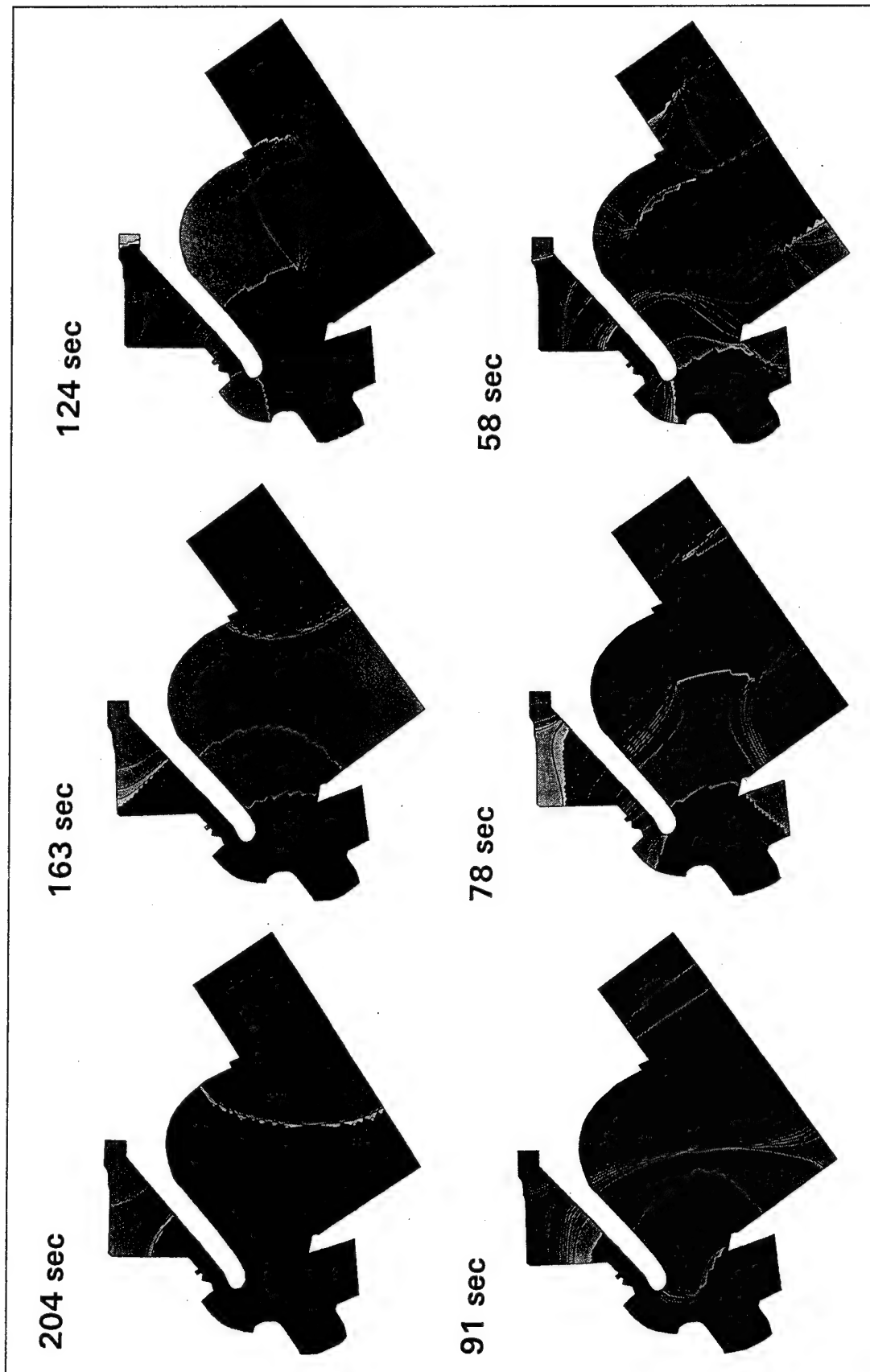


Figure H14. Phase plots for test plan 6c

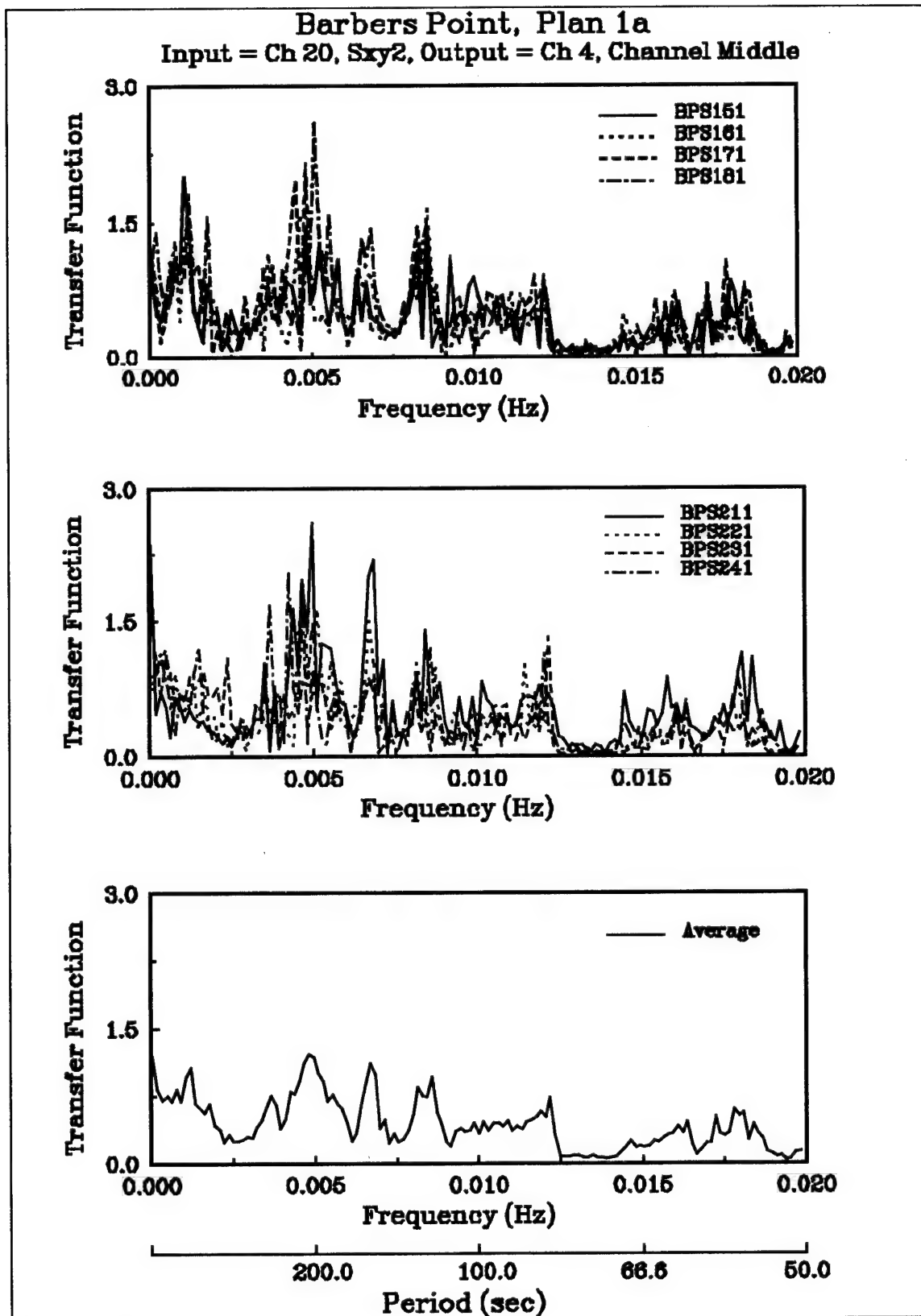


Figure H15. Channel middle transfer functions for test plan 1a

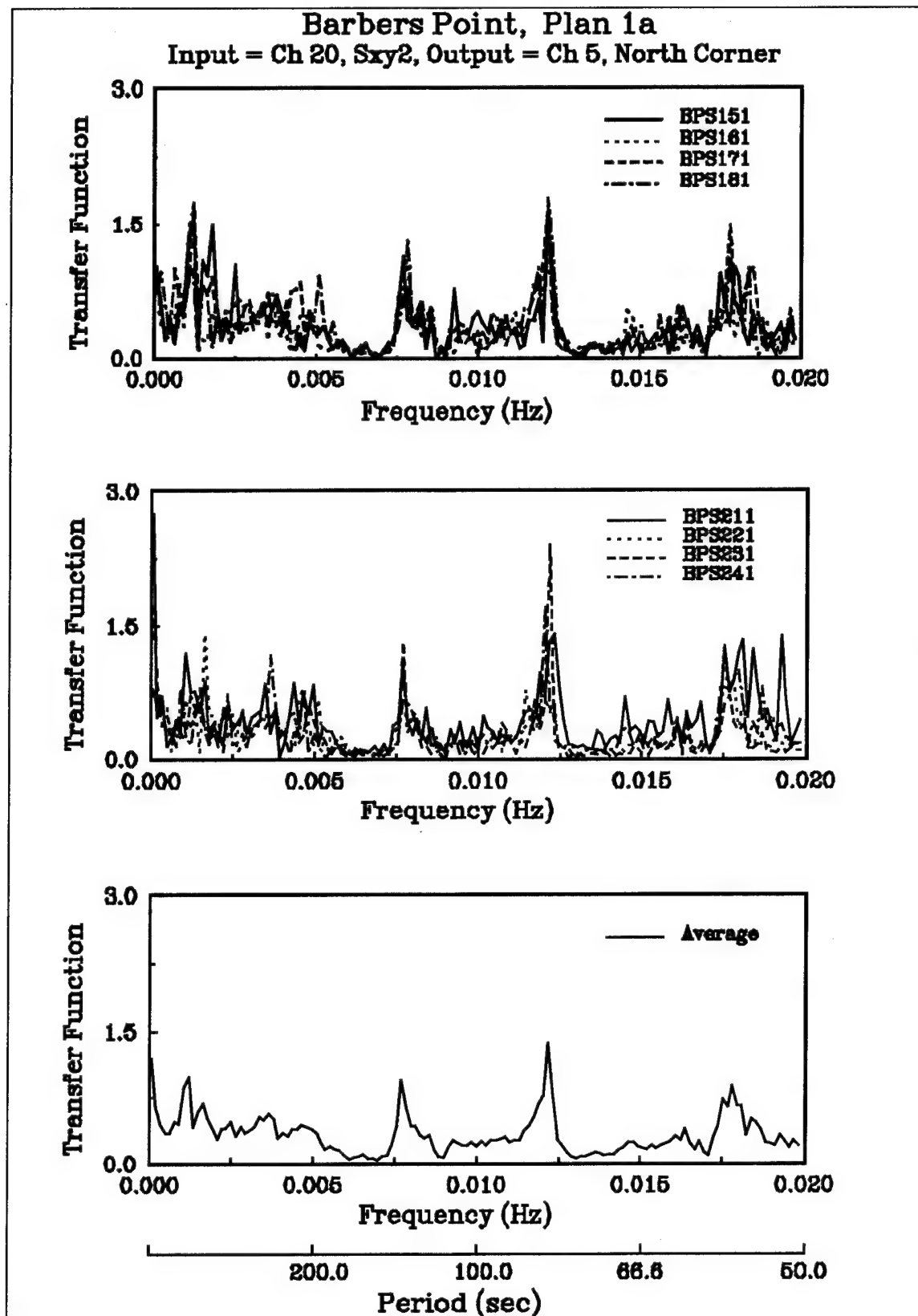


Figure H16. North corner transfer functions for test plan 1a

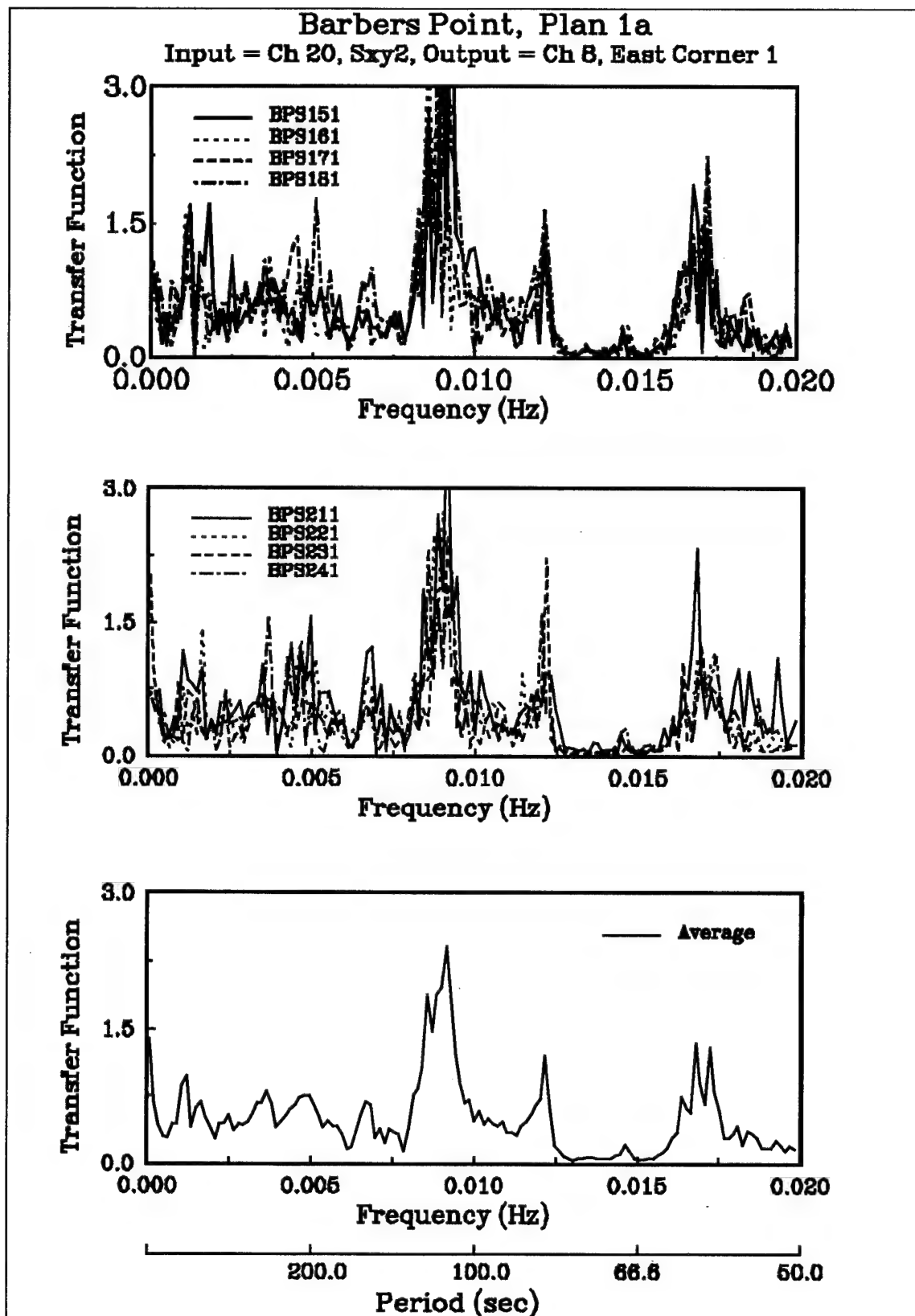


Figure H17. East corner transfer functions for test plan 1a

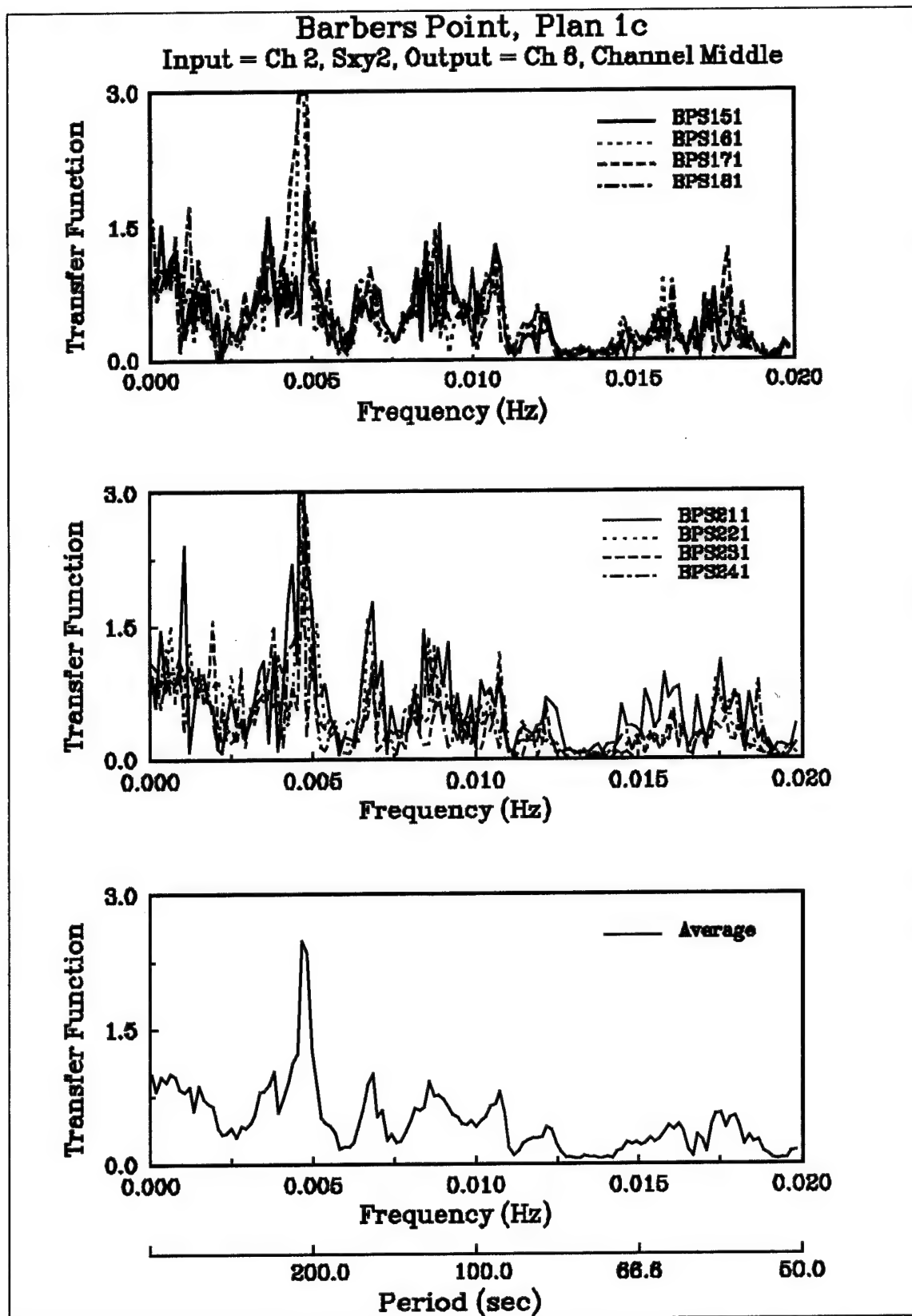


Figure H18. Channel middle transfer function for test plan 1c

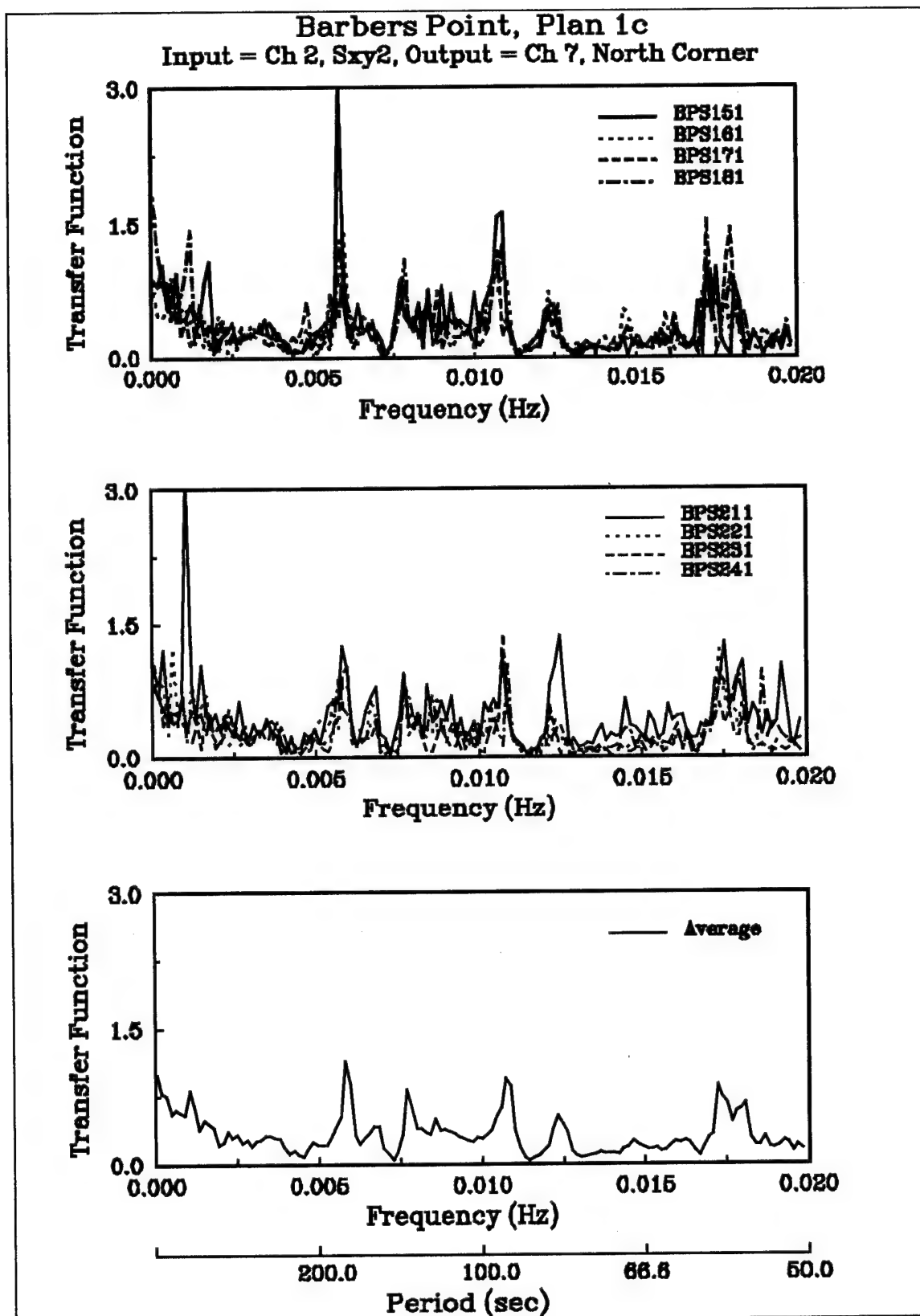


Figure H19. North corner transfer functions for test plan 1c

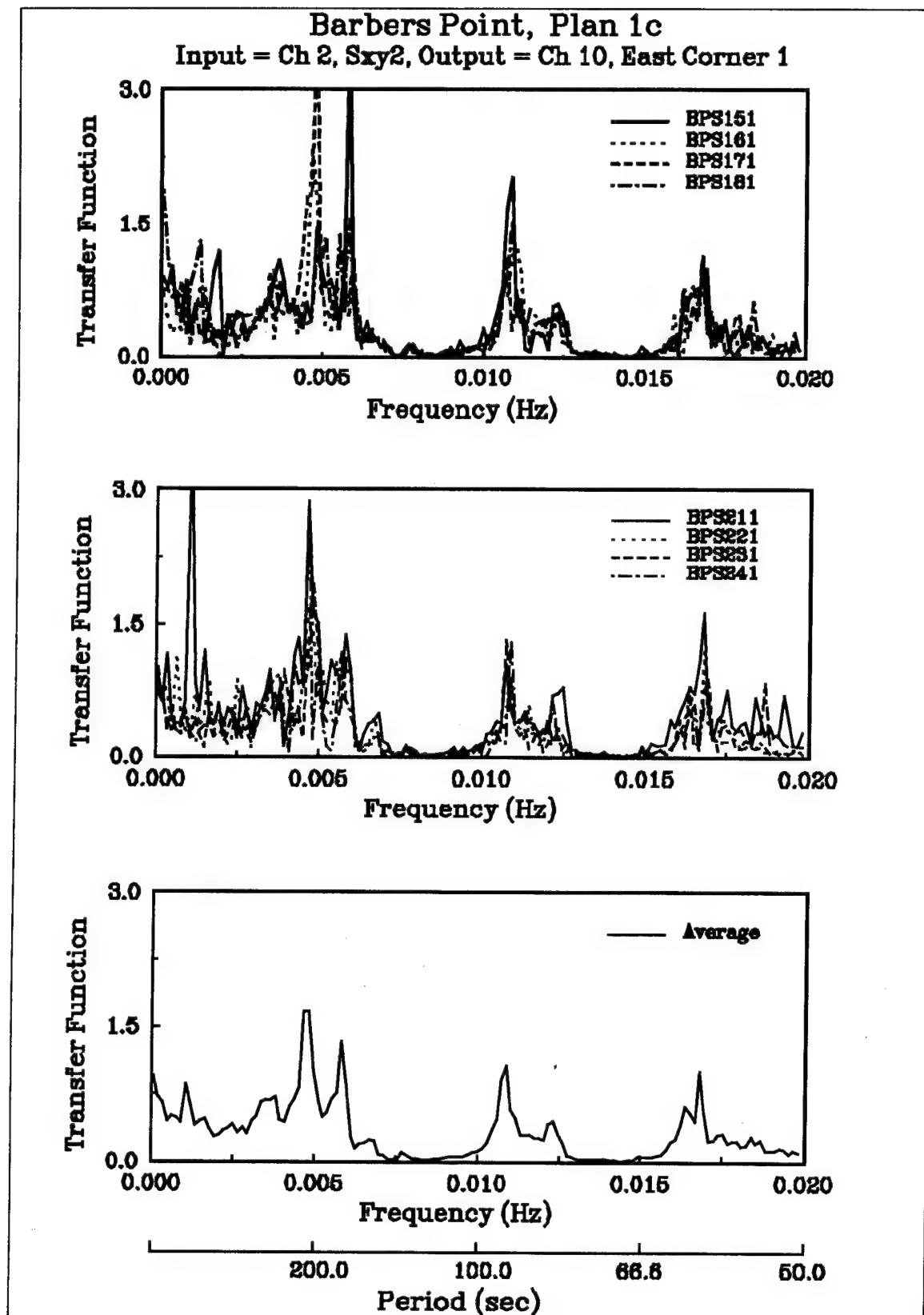


Figure H20. East corner transfer functions for test plan 1c

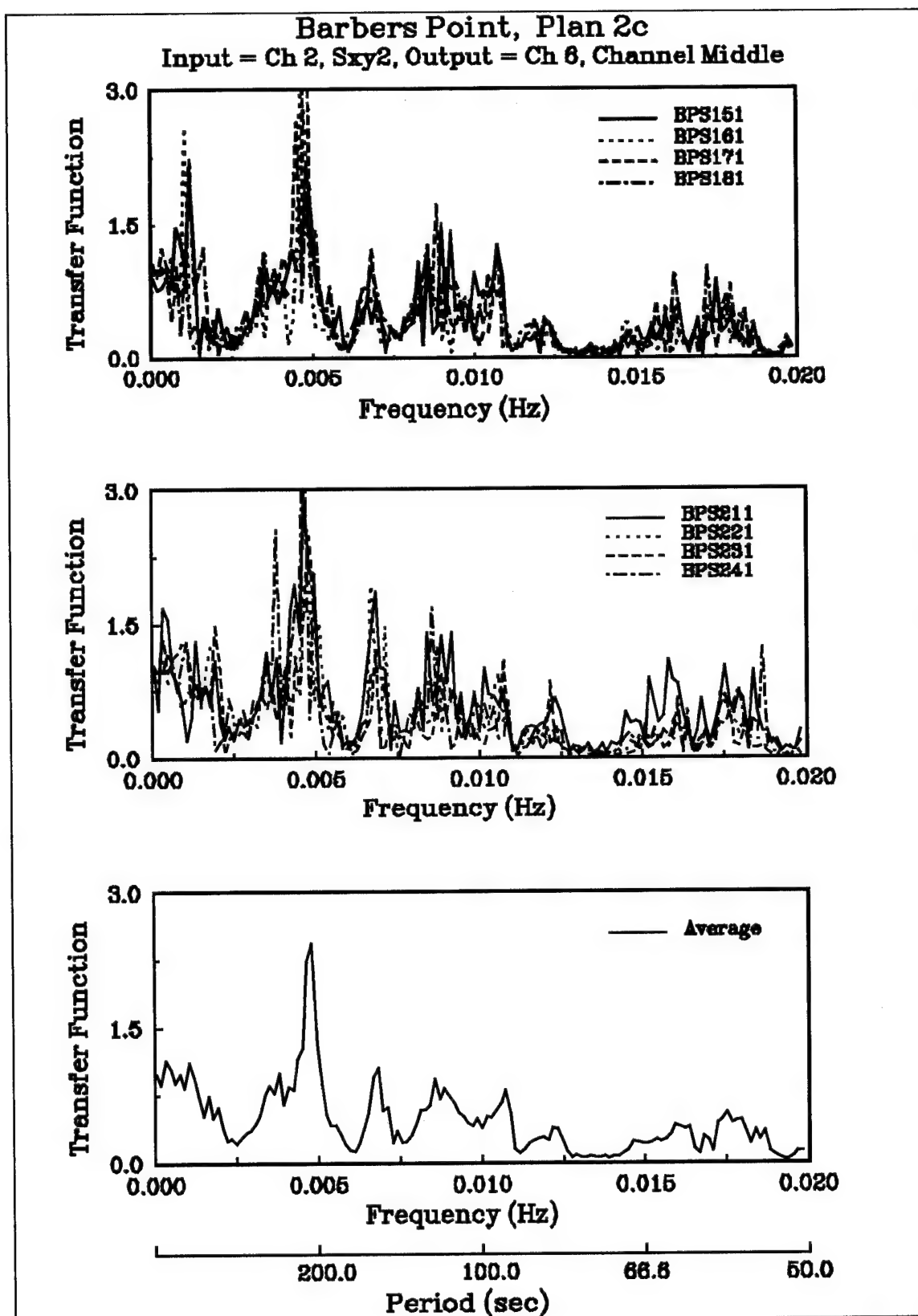


Figure H21. Channel middle transfer functions for test plan 2c

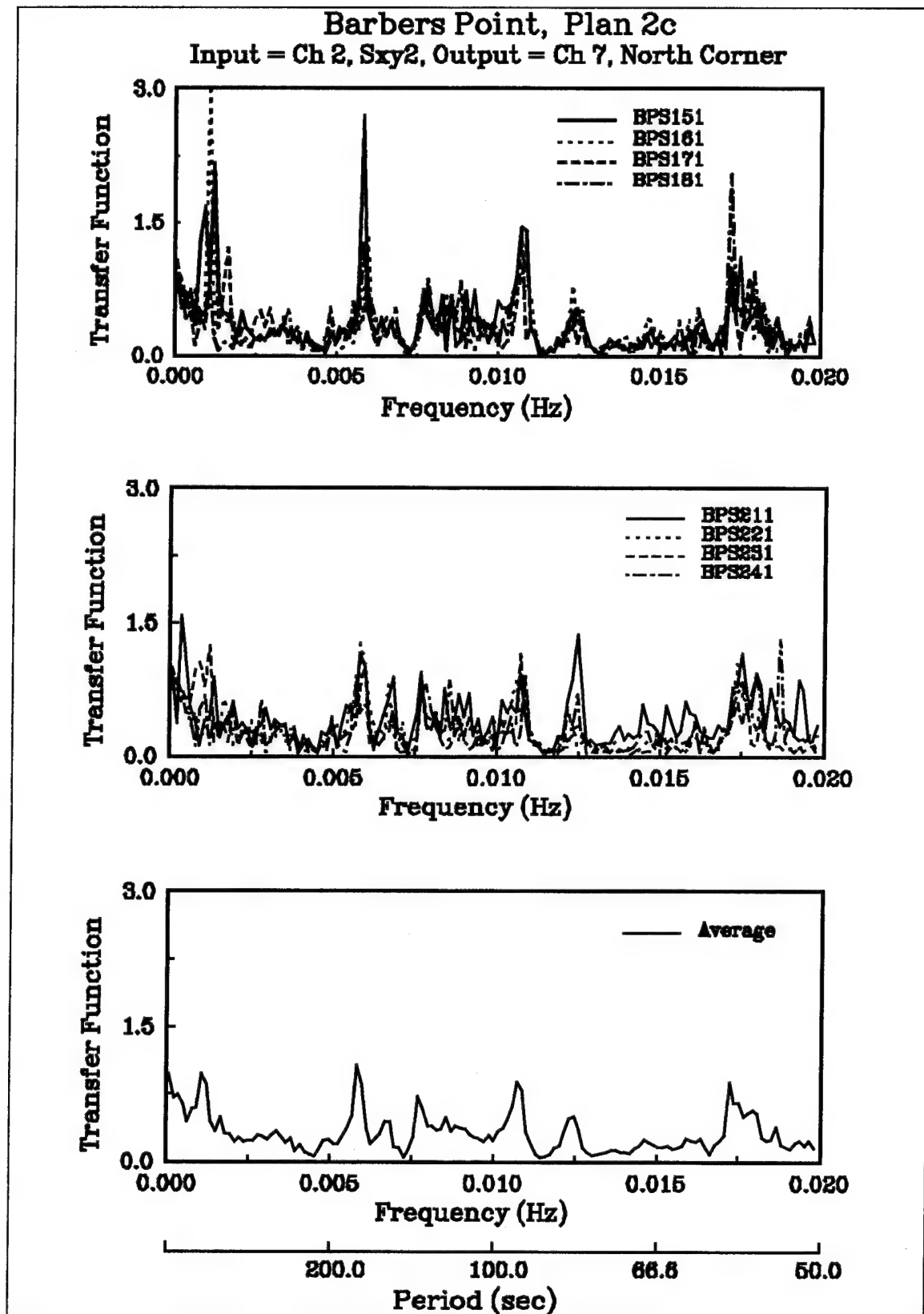


Figure H22. North corner transfer functions for test plan 2c

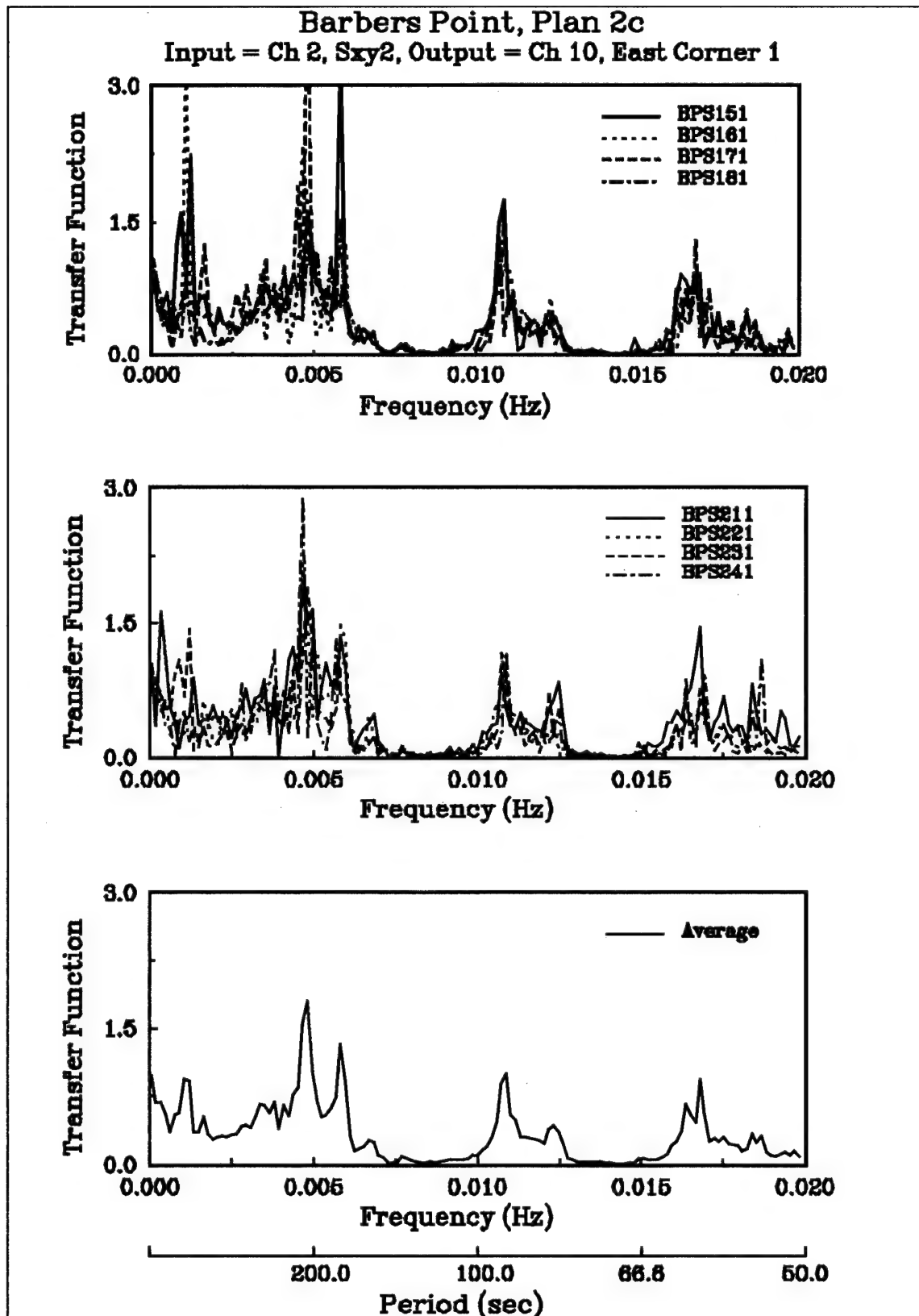


Figure H23. East corner transfer functions for test plan 2c

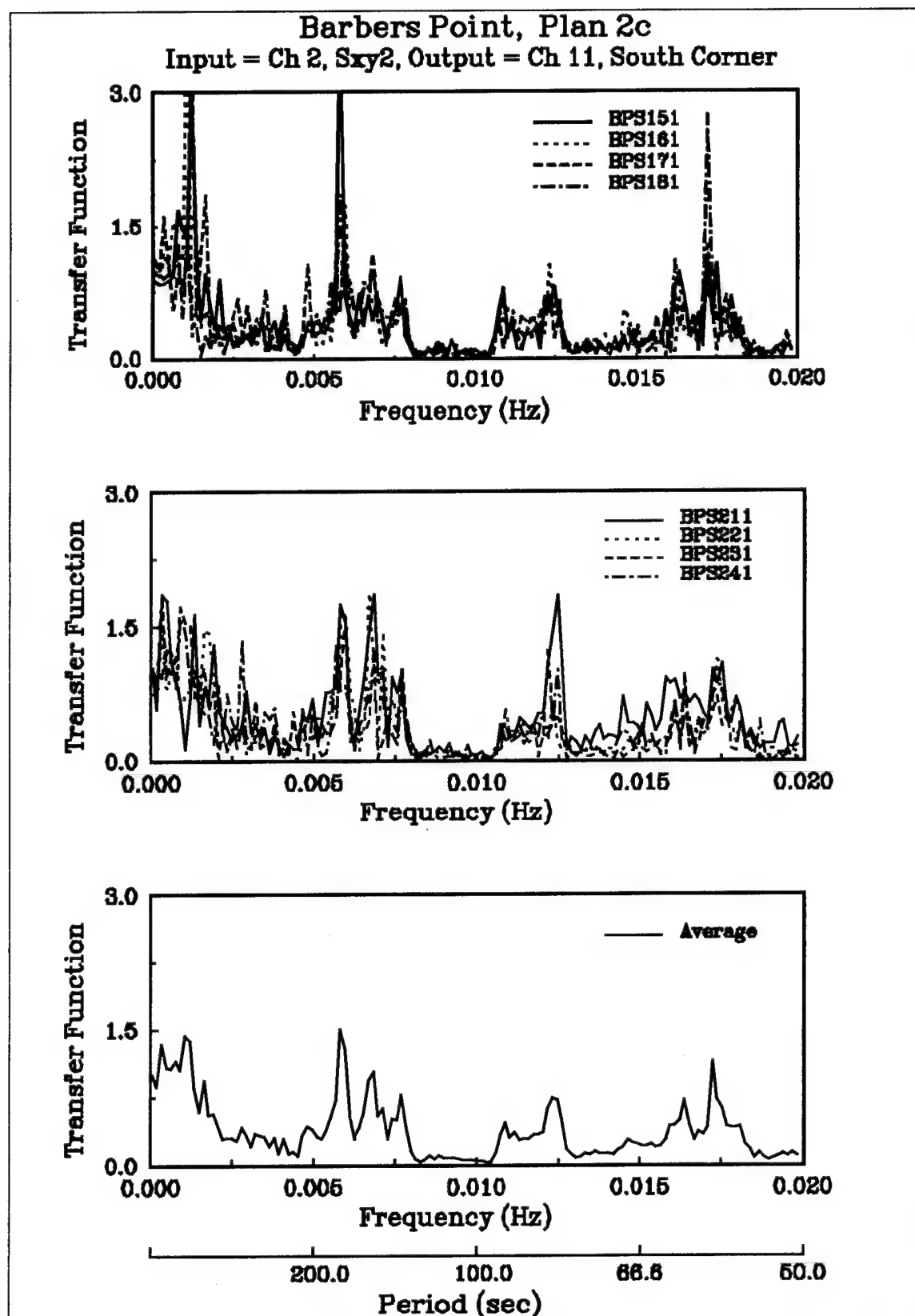


Figure H24. South corner transfer functions for test plan 2c

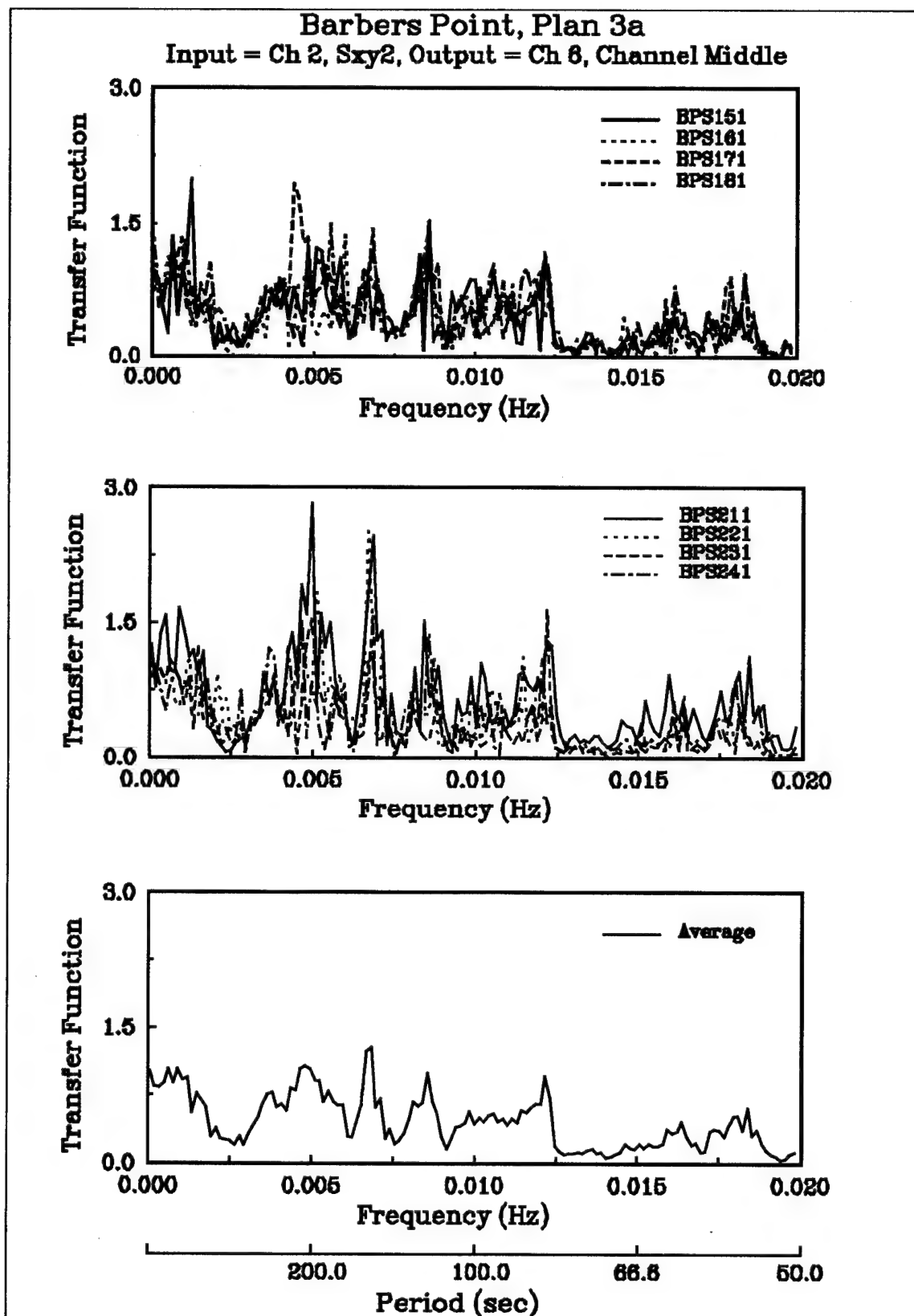


Figure H25. Channel middle transfer functions for test plan 3a

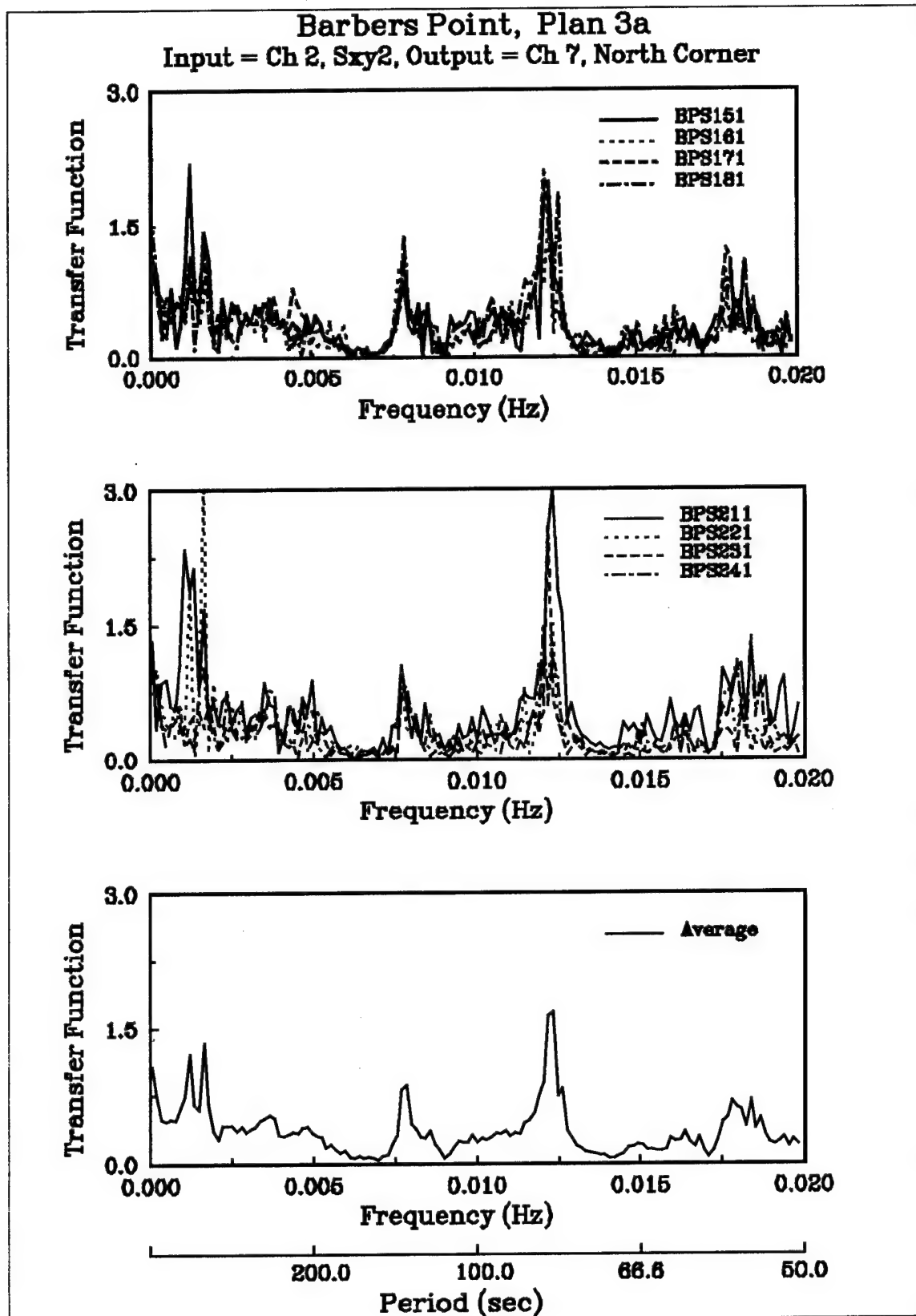


Figure H26. North corner transfer functions for test plan 3a

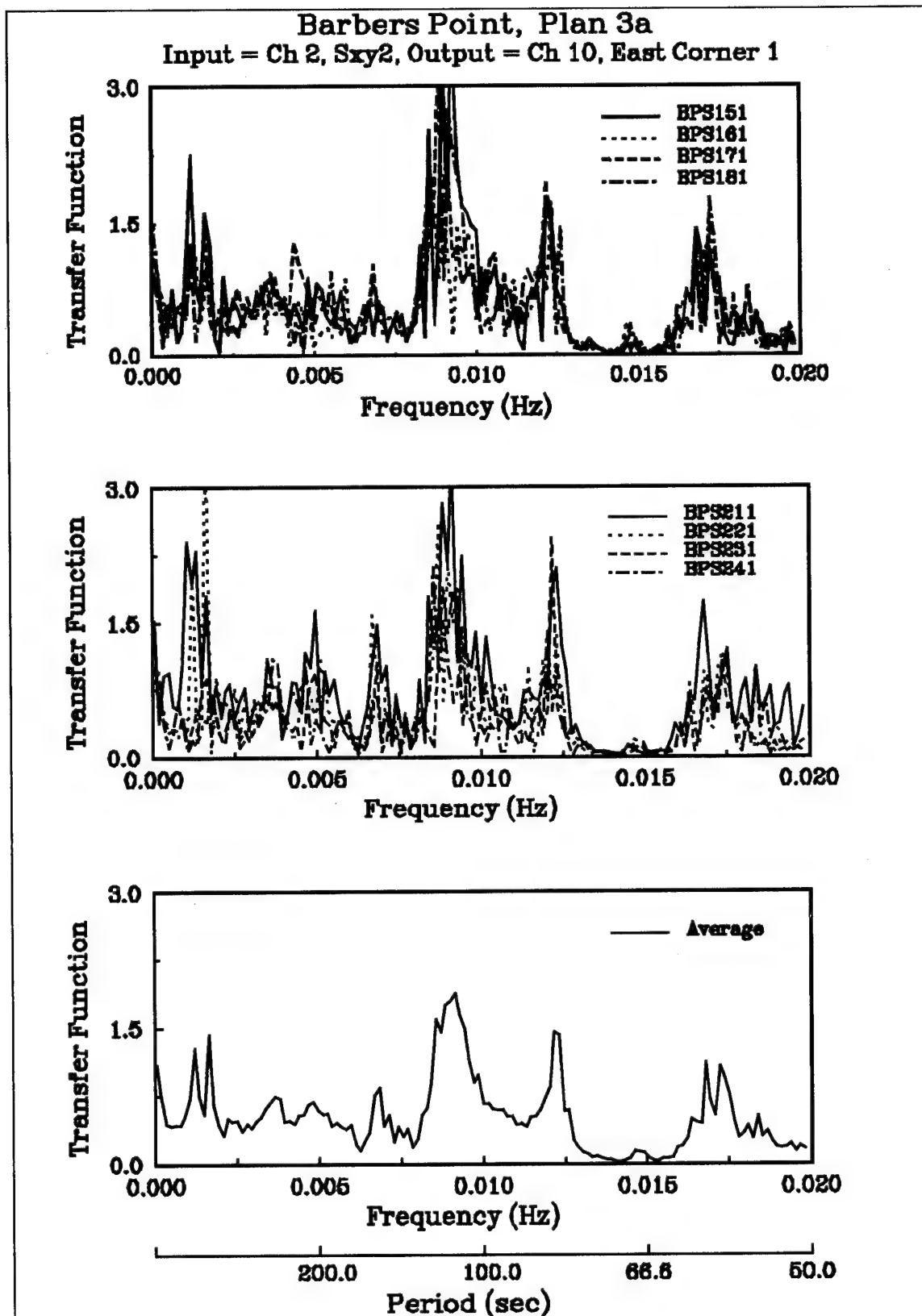


Figure H27. East corner transfer functions for test plan 3a

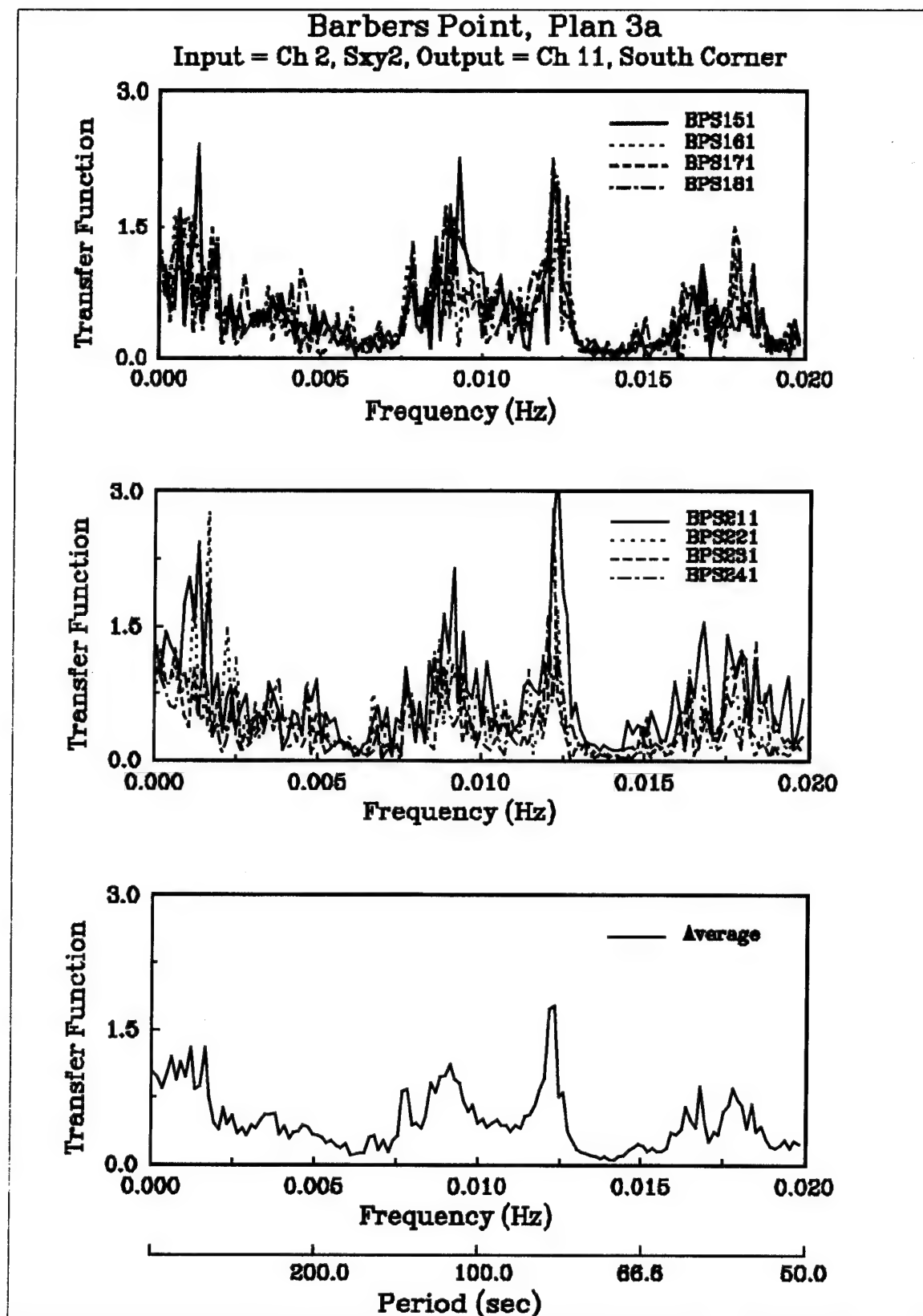


Figure H28. South corner transfer functions for test plan 3a

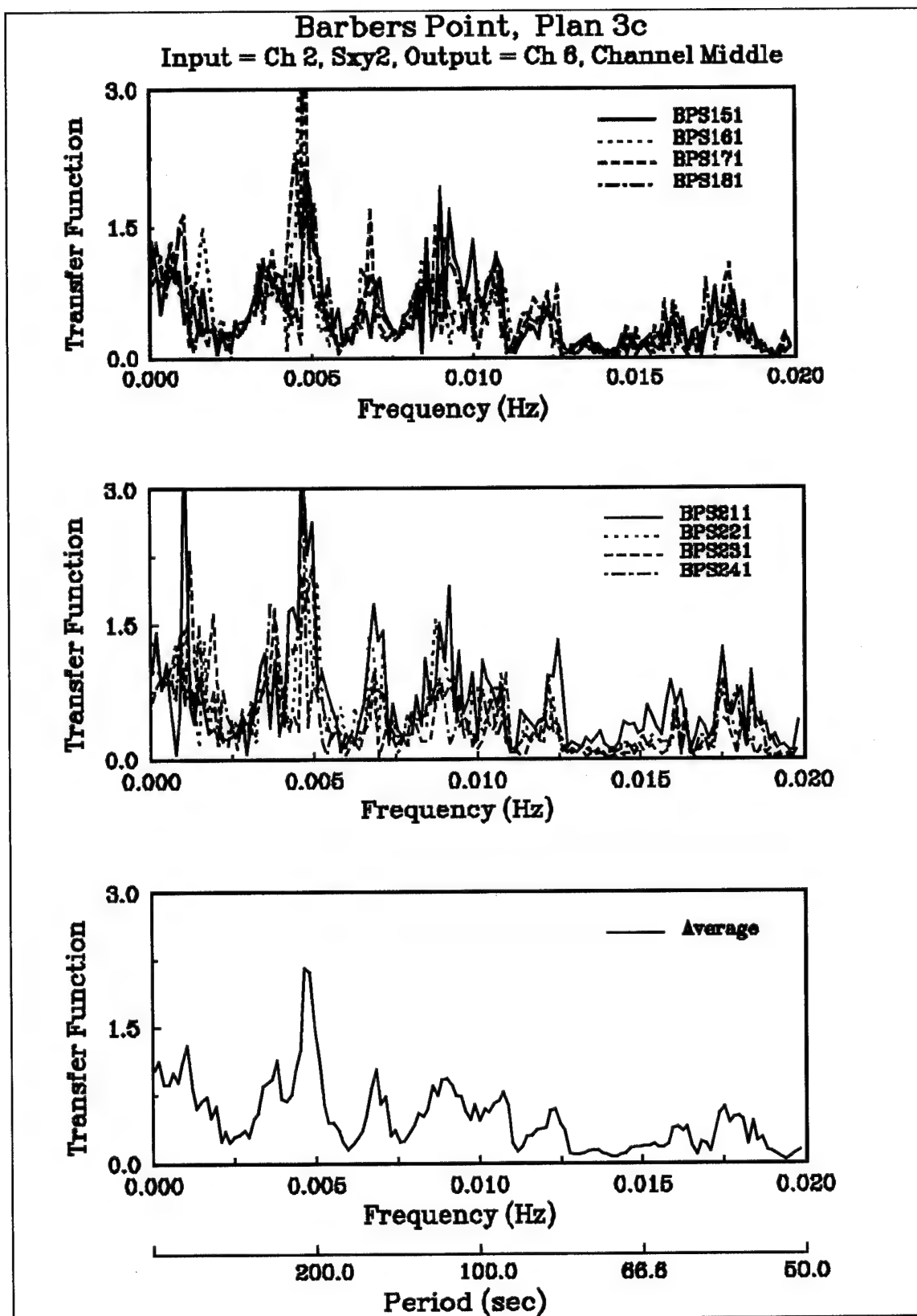


Figure H29. Channel middle transfer functions for test plan 3c

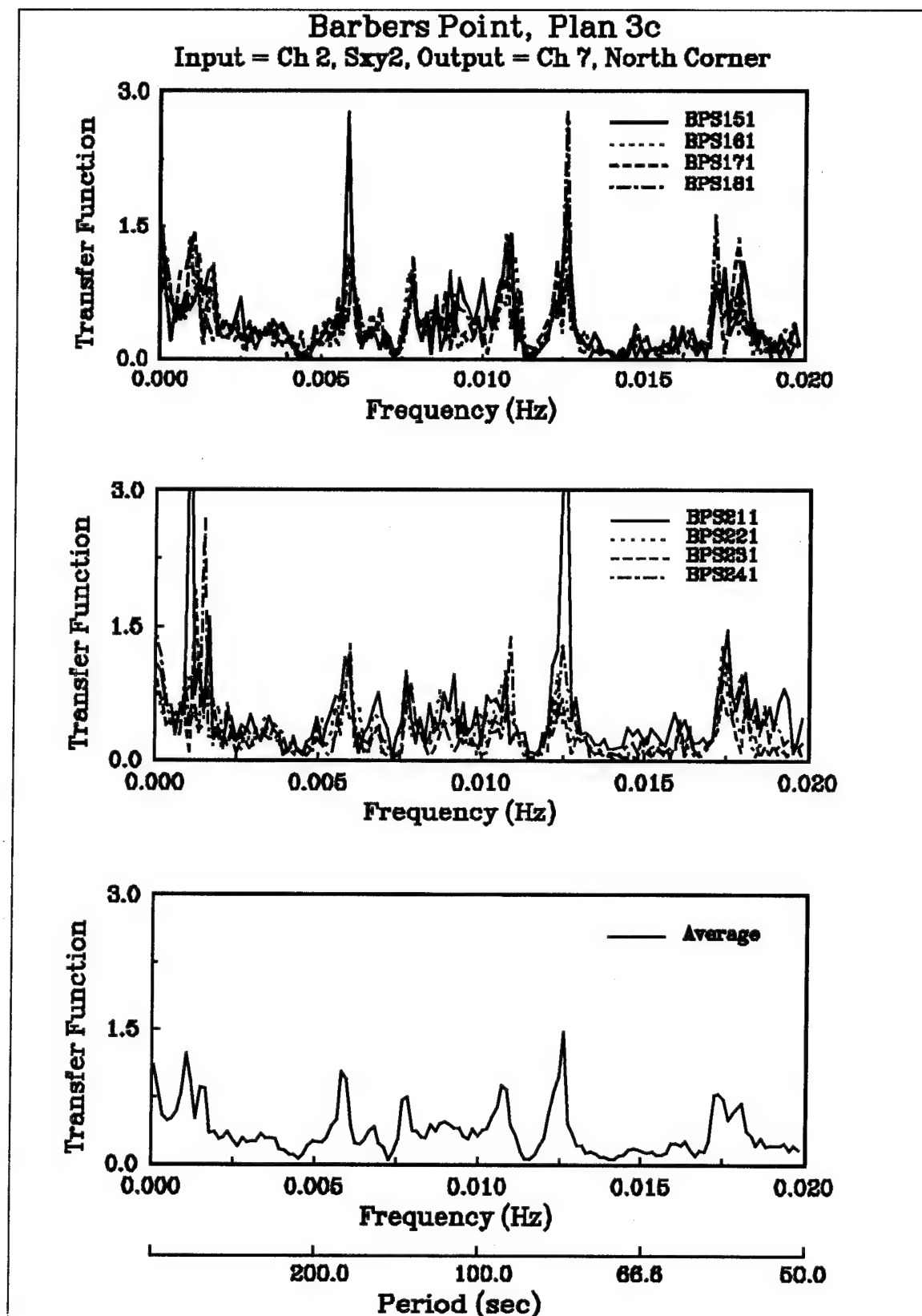


Figure H30. North corner transfer functions for test plan 3c

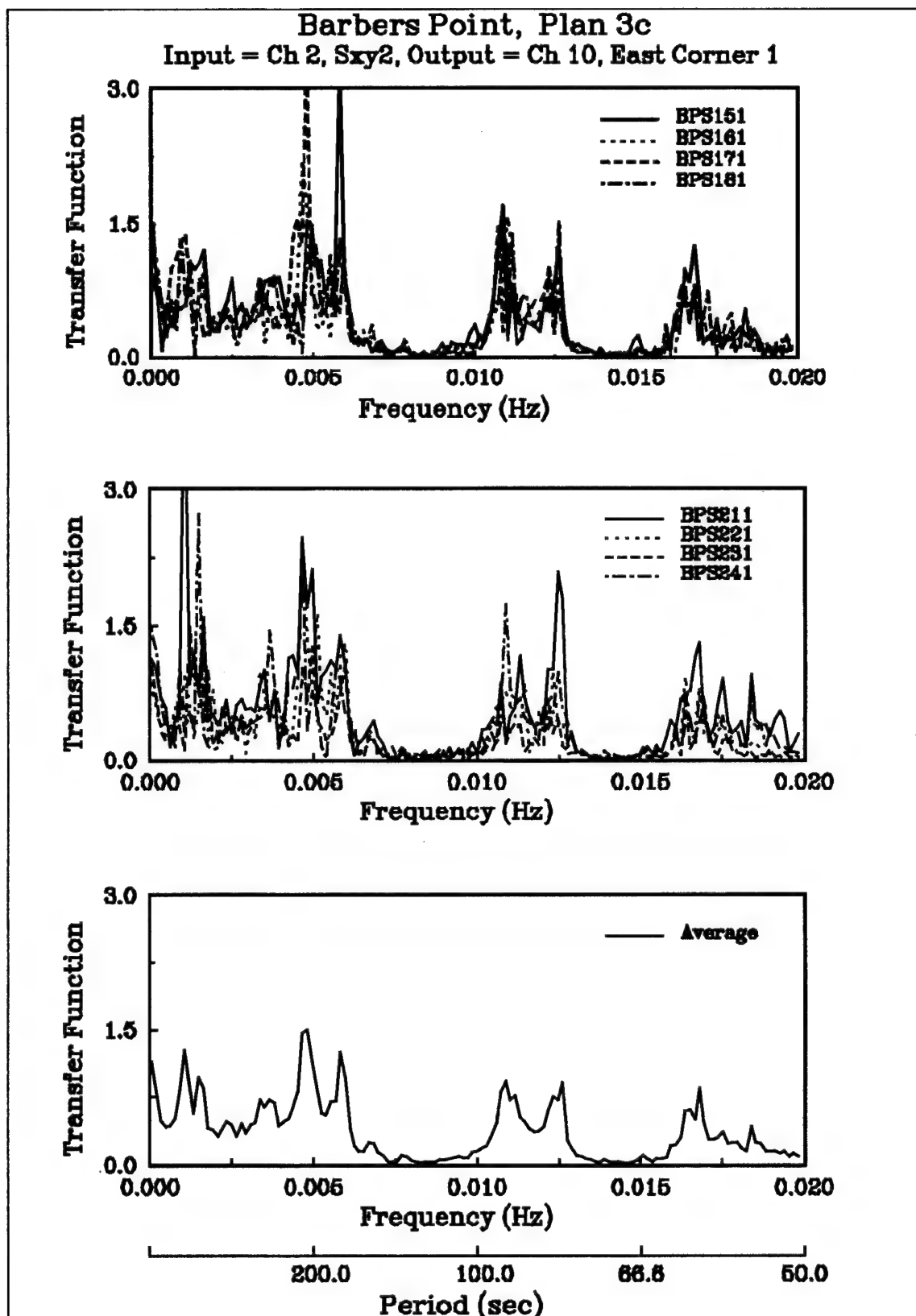


Figure H31. East corner transfer functions for test plan 3c

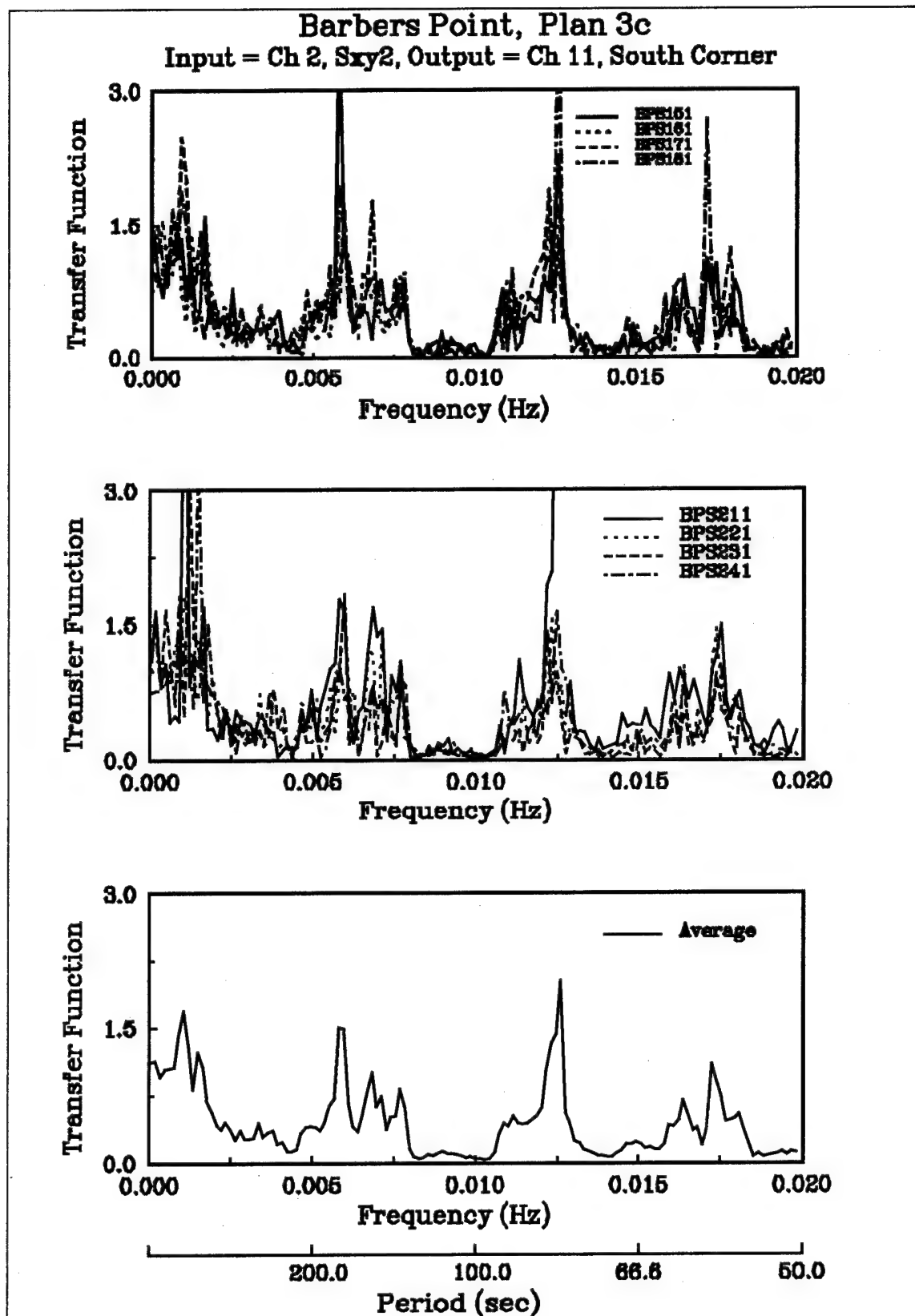


Figure H32. South corner transfer functions for test plan 3c

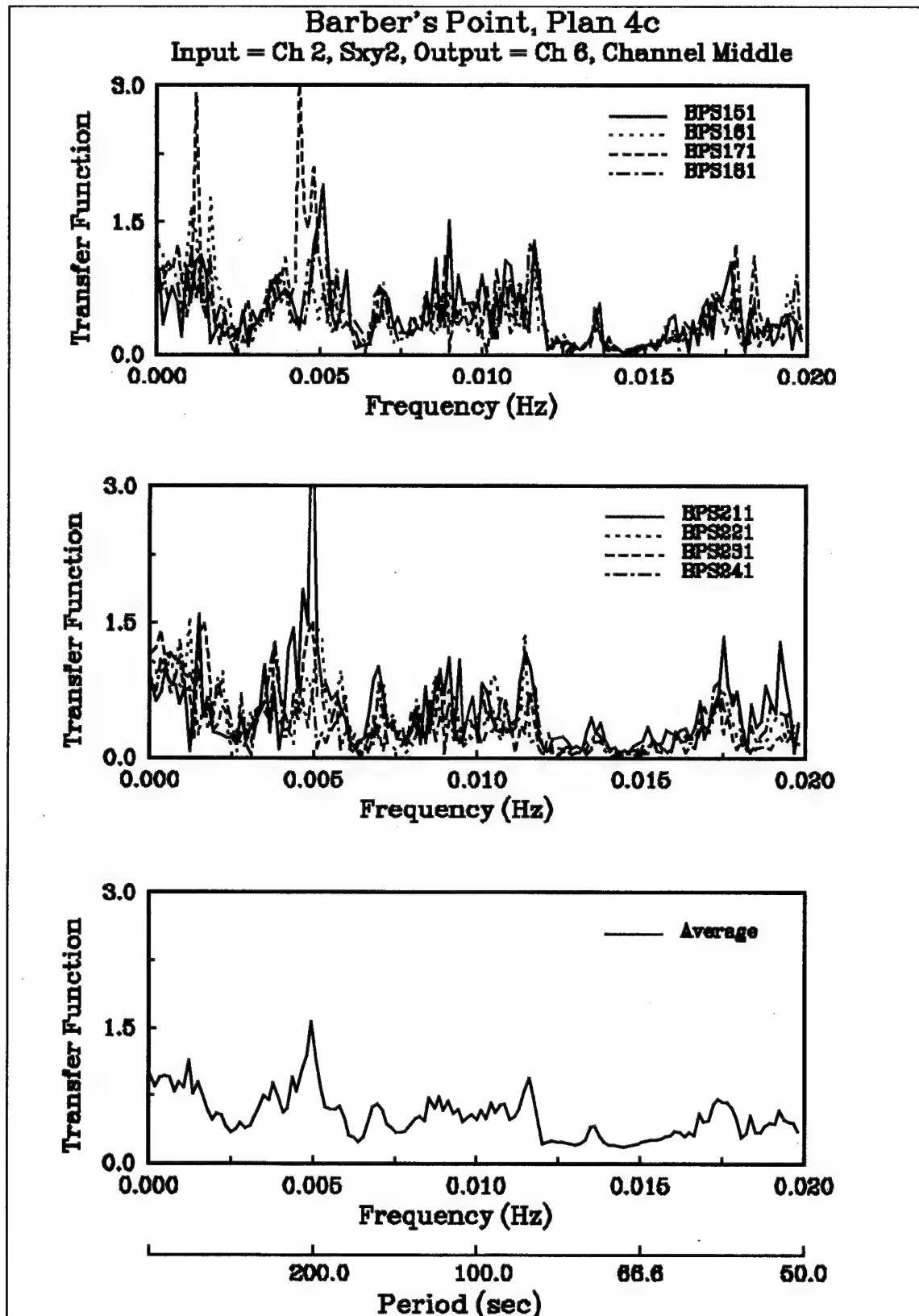


Figure H33. Channel middle transfer functions for test plan 4c

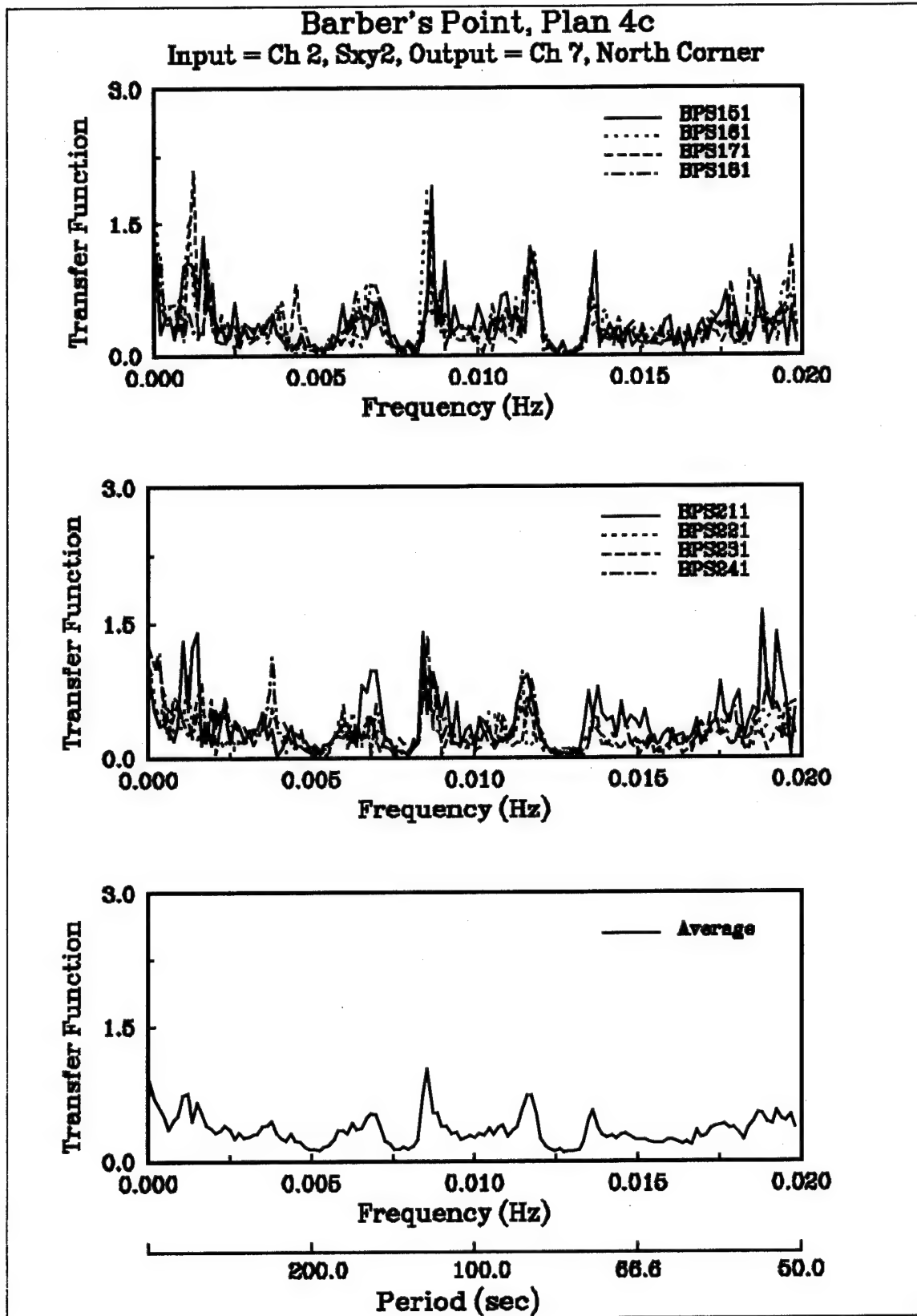


Figure H34. North corner transfer functions for test plan 4c

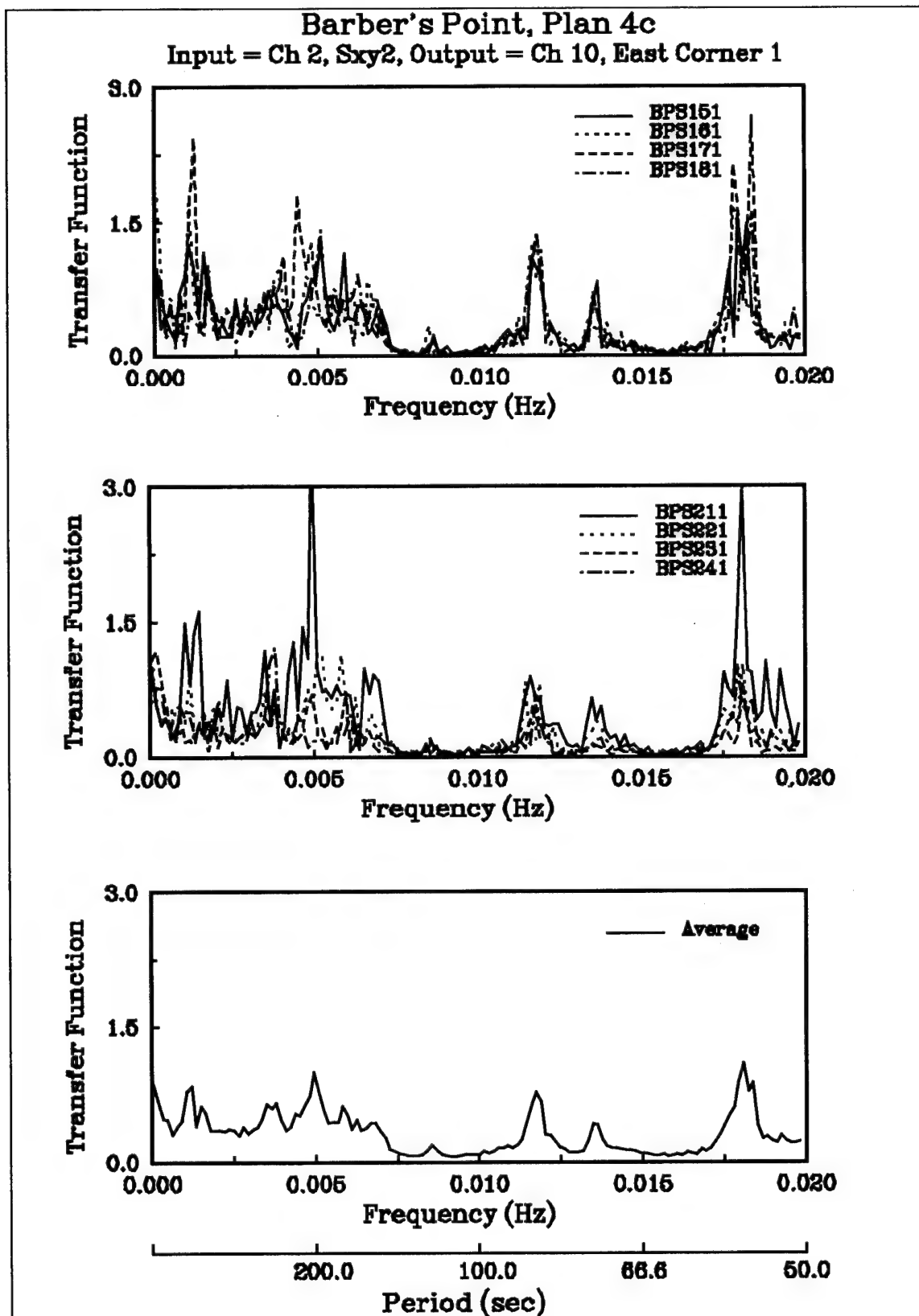


Figure H35. East corner transfer functions for test plan 4c

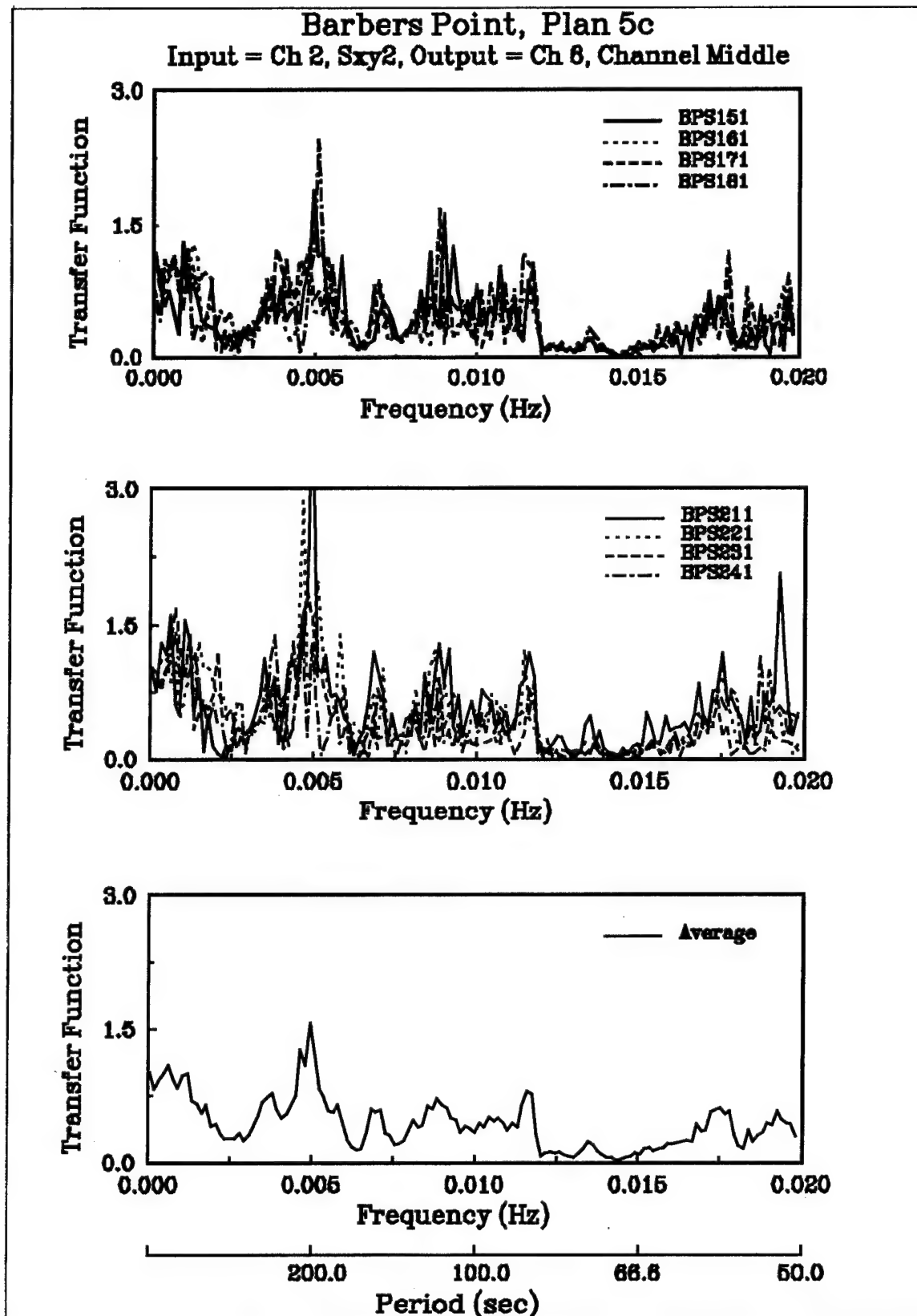


Figure H36. Channel middle transfer functions for test plan 5c

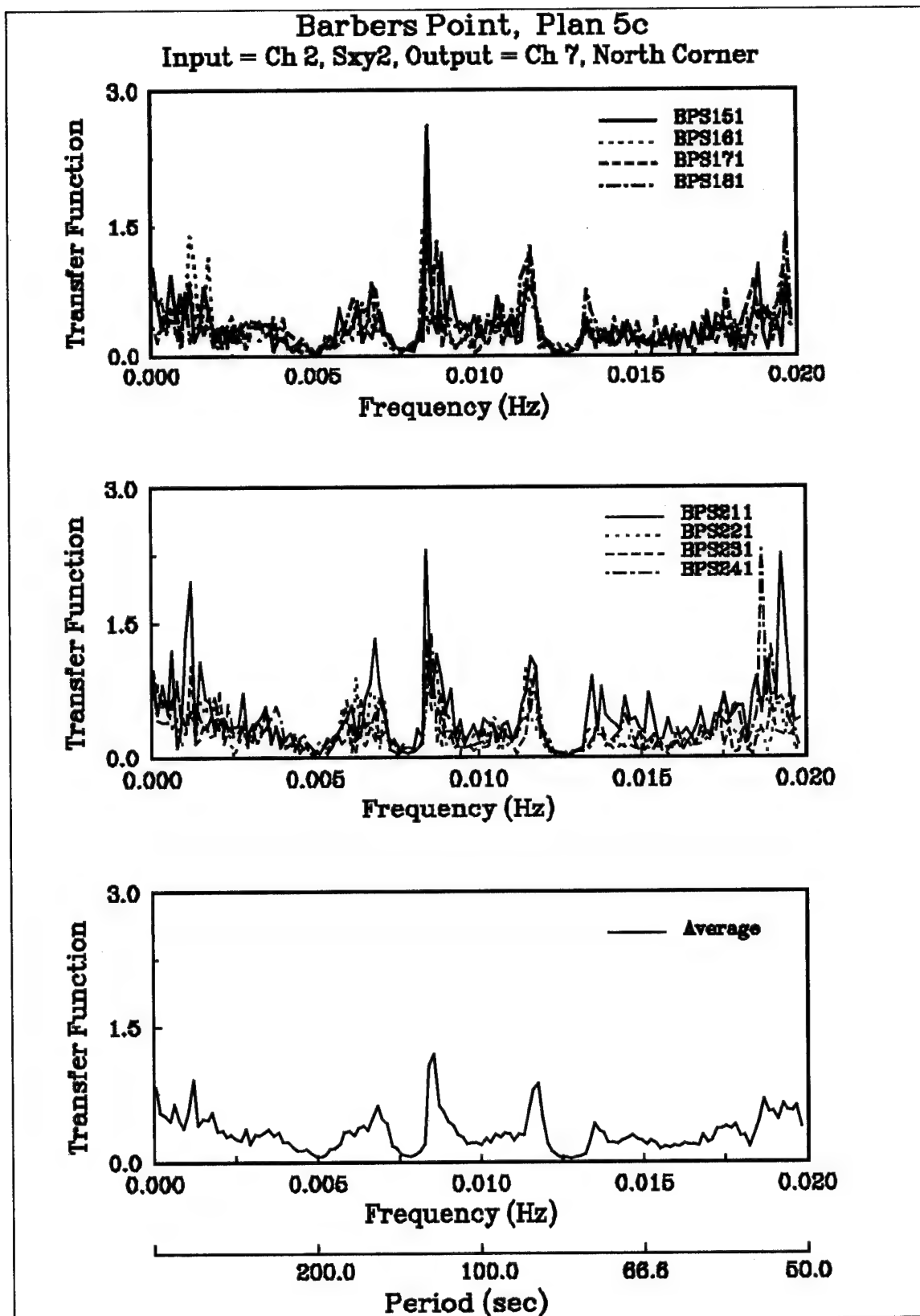


Figure H37. North corner transfer functions for test plan 5c

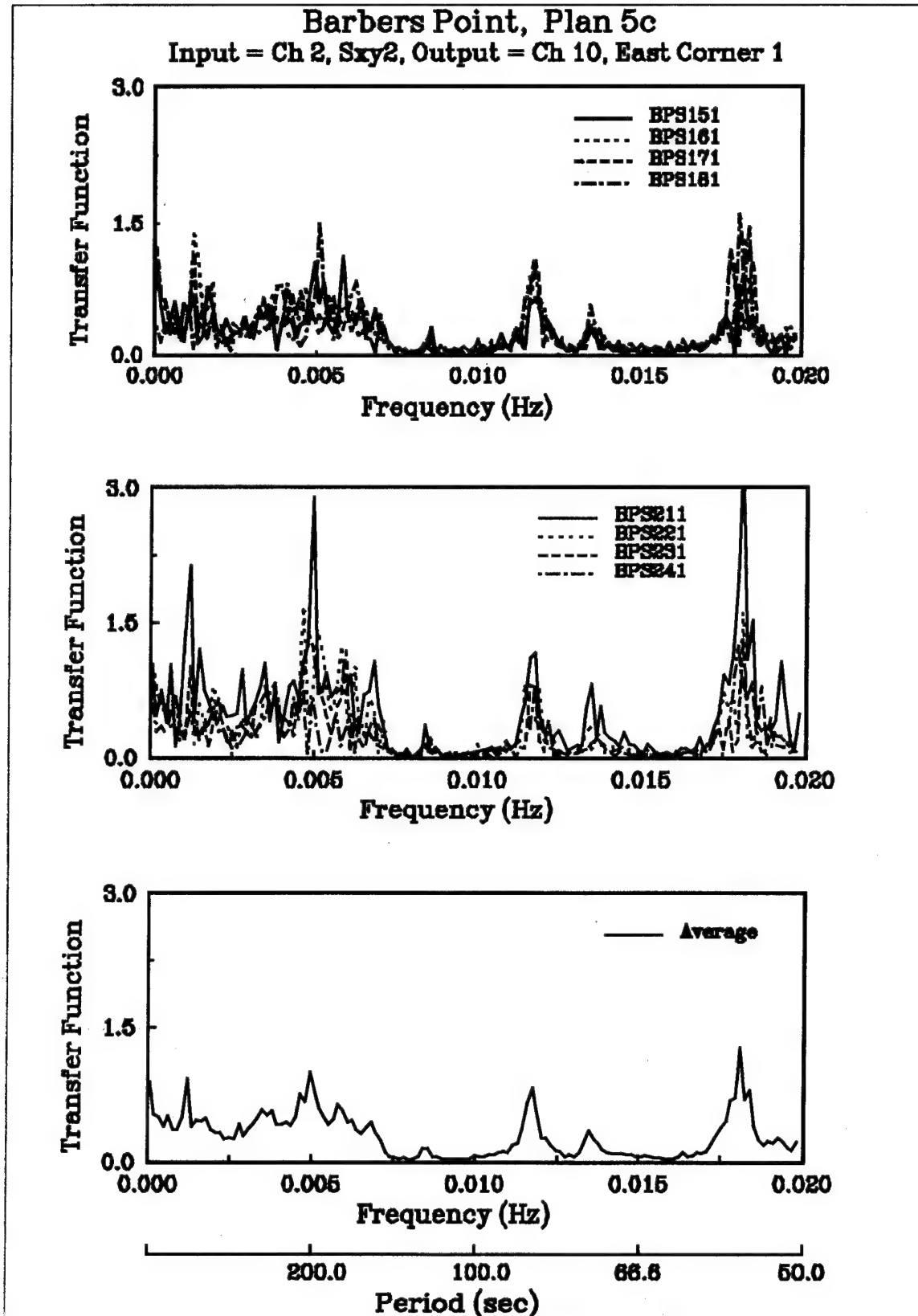


Figure H38. East corner transfer functions for test plan 5c

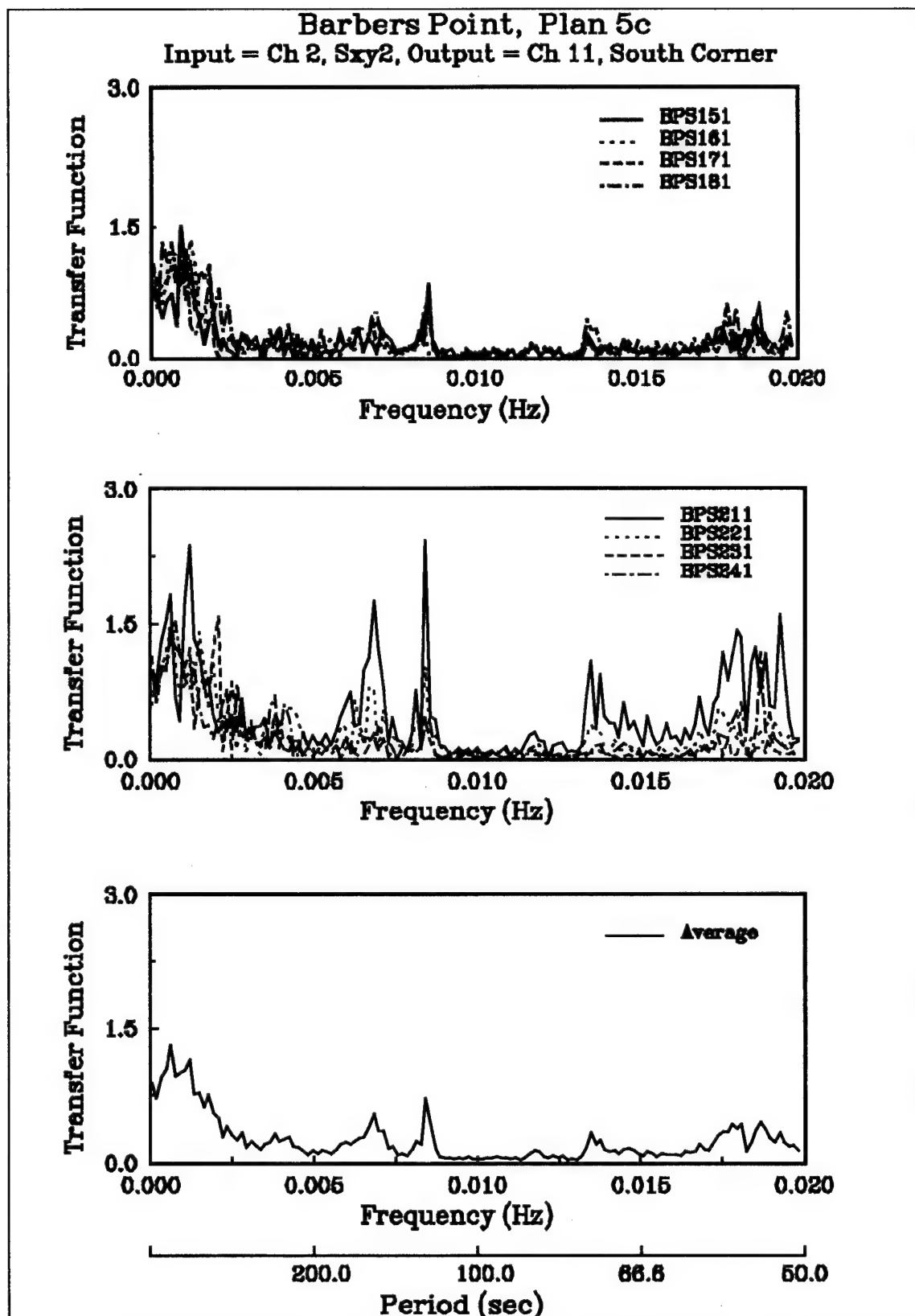


Figure H39. South corner transfer functions for test plan 5c

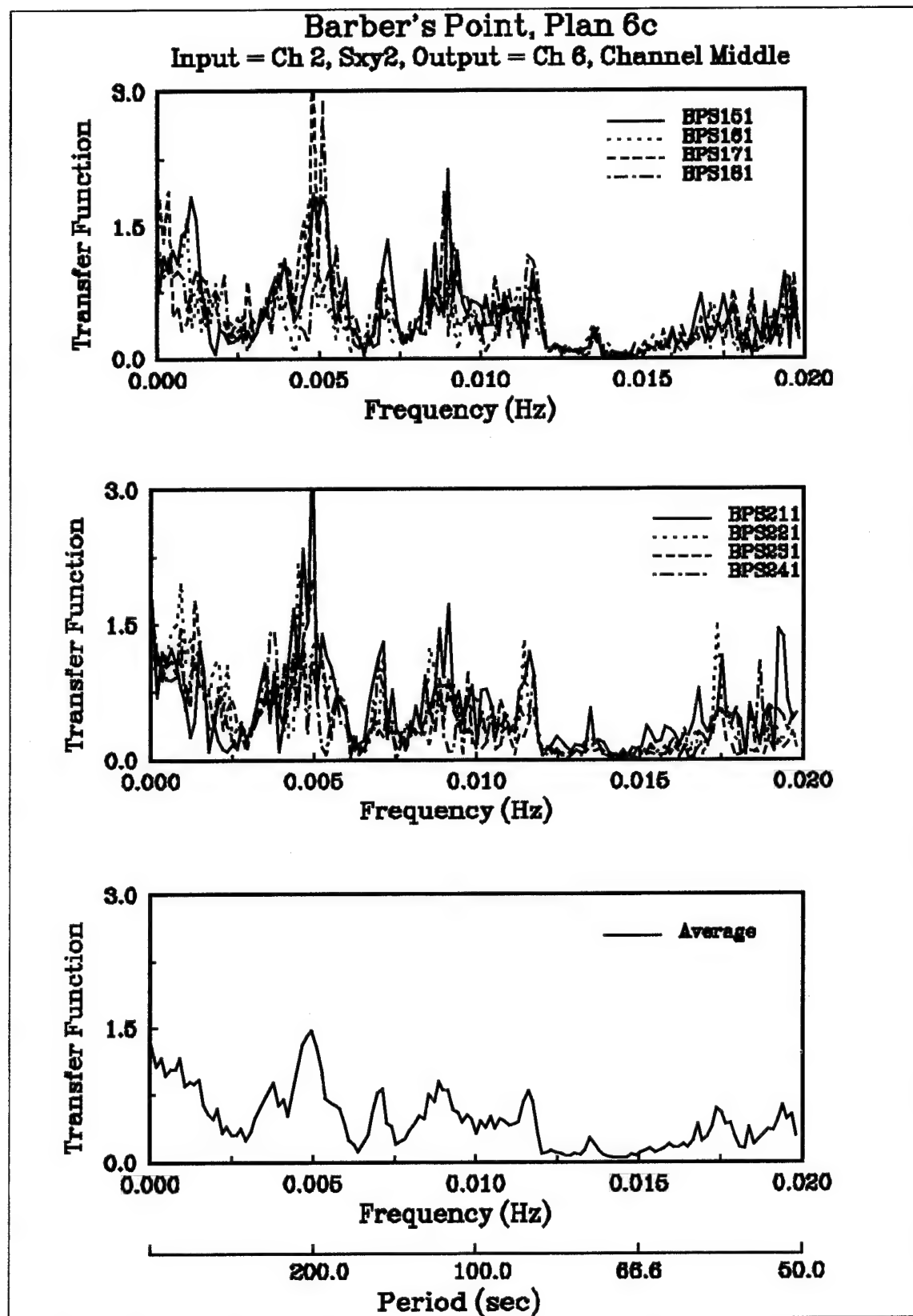


Figure H40. Channel middle transfer functions for test plan 6c

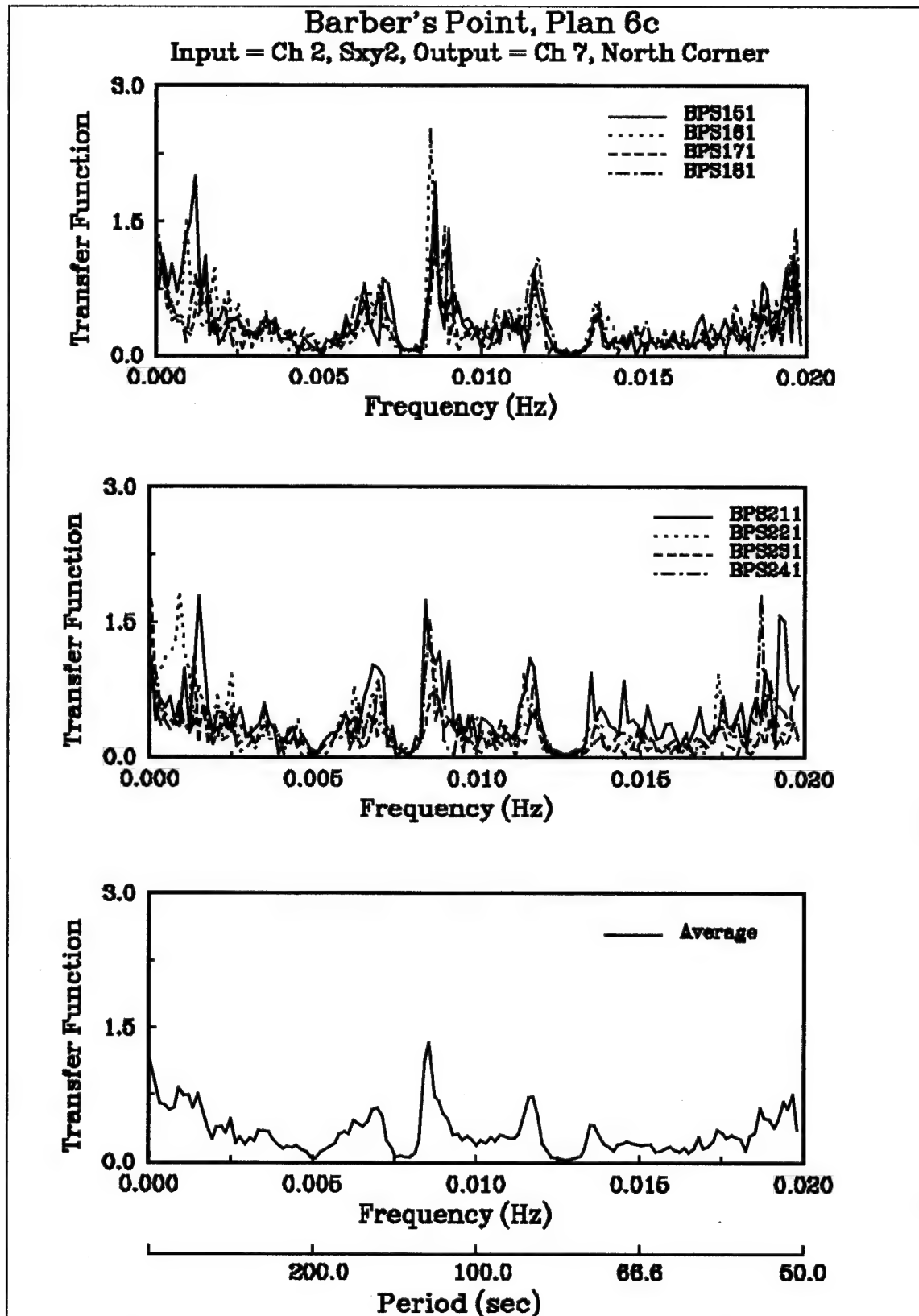


Figure H41. North corner transfer functions for test plan 6c

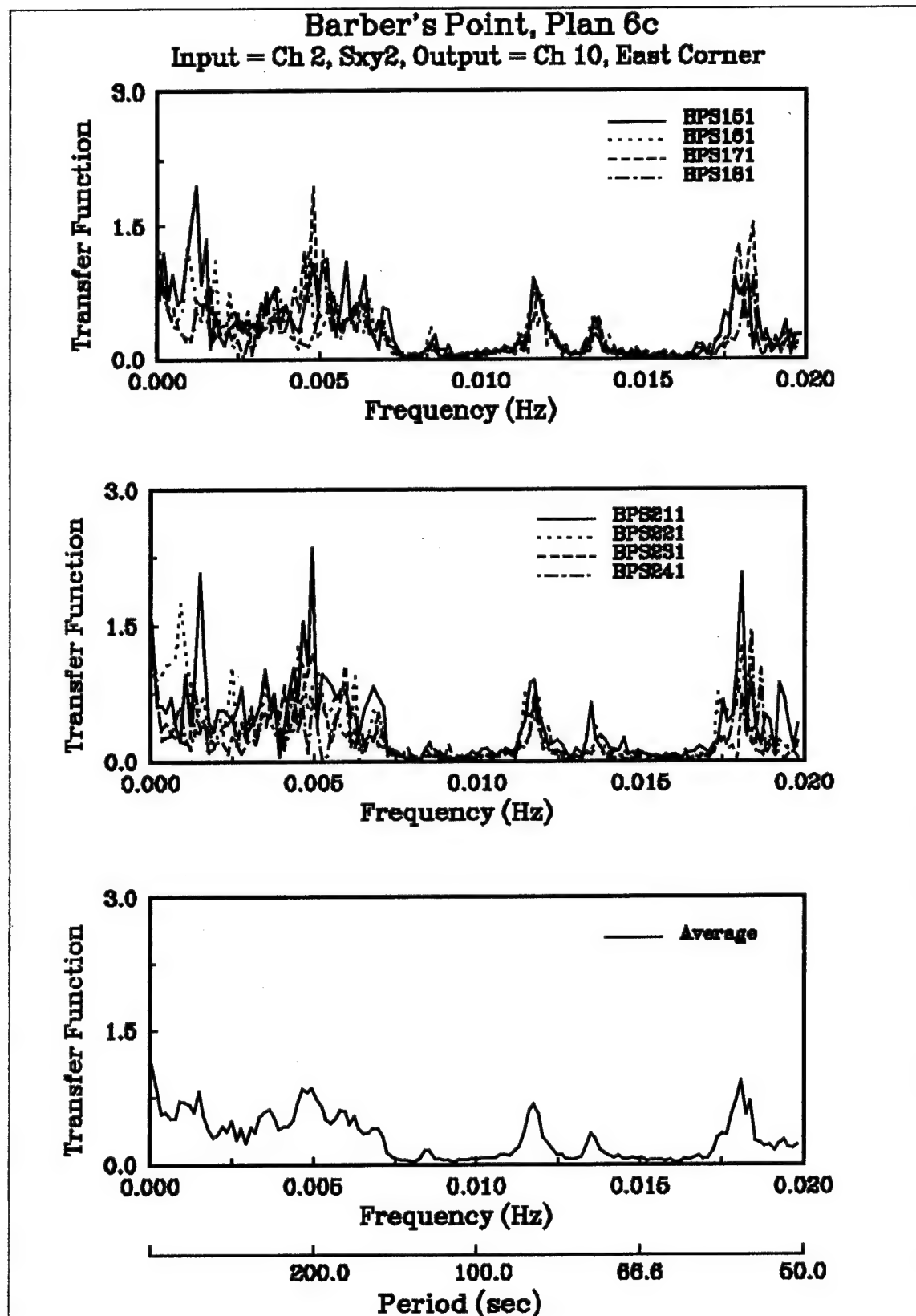


Figure H42. East corner transfer functions for test plan 6c

Appendix I

Notation

$a_1(f)$	Real first Fourier coefficient
A	First shallow-water prototype current meter location
A'	Second shallow-water prototype current meter location
A_c	Cross-sectional area of the cable, in ²
A(f)	Amplitude as a function of the frequency
a_M	Fourier coefficients of the even terms
a_o	Incident wave amplitude
$b_1(f)$	Imaginary first Fourier coefficient
B	Ship beam, ft
B	Prototype current meter location in 30' of water
B_e	Bandwidth for Gaussian smoothing, Hz
b_M	Fourier coefficients of the odd terms
Bn	Barge north gauge
Bs	Barge south gauge
B_{w2}	Barge basin second harmonic in width dimension
c	Damping coefficient
c	Wave phase velocity = (ω/κ)
C	\sqrt{gh} = wave celerity for shallow water, ft/sec
C4	Entrance channel Goda array gauge
C5	Entrance channel Goda array gauge
C6	Entrance channel Goda array gauge
Ce	Channel entrance gauge
C_{ij}	Co-spectra, the real part of the cross-spectrum
Cm	Channel middle
c_g	Wave group velocity, ft/sec
d	Water depth, ft
D(f,θ)	Spreading coefficients
E1	First location of the east corner gauge
E2	Second location of the east corner gauge
E_c	Equivalent modulus of elasticity, Young's modulus, psi
Ex1	Expansion northeast corner gauge
Ex2	Expansion east corner gauge
Ex3	Expansion north corner gauge
F_0	Exciting force
f	Frequency, Hz
f_l	Lower frequency cutoff limit for spectral calculations, Hz
f_u	Upper frequency cutoff limit for spectral calculations, Hz
$\hat{G}_{xx}(f)$	Auto-spectral density, ft ² /Hz
$\hat{G}_{xy}(f)$	Cross-spectral density between input x and output y, ft ² /Hz
g	Acceleration due to gravity, ft/sec ²
h	Water depth, ft
H	Wave height, ft
H_σ	Significant wave height, ft
H_1	Fundamental southeast mode along length of harbor
H_2	Southeast second harmonic along length of harbor
H_3	Southeast third harmonic along length of harbor
H_{ew}	Fundamental mode along east-west diagonal

H_{ew2}	East-west second harmonic
$\hat{H}(f)$	Transfer function value
H_f	Harbor ferry gauge
H_m	Harbor middle gauge
H_{ns}	Fundamental north-south mode
H_{ns2}	North-south second harmonic
H_h	Harbor Helmholtz mode
H_{m0}	Four times the square root of the zeroth moment of the wave height spectra, ft
$H_s(\omega)$	Response amplitude operator in surge
i	$\sqrt{-1}$
I	Movement of inertia of the water plane
I_a	Added mass moment of inertia of water entrained by ship's rotation
I_v	Virtual moment of inertia, $I + I_a$
k	Stiffness, effective spring constant of mooring lines
κ_p	Pressure response factor
K_r	Boundary reflection coefficient
k_y	Component of the wave number in the y-direction, ft^{-1}
l	Length of ship, ft
l	Length of the mooring line, ft
L	Number of harmonics in a truncated Fourier series expansion used to calculate an initial directional spreading function
L	Wavelength, ft
L_r	Scale ratio between model and prototype
L_y	Component of the wavelength in the y-direction, ft
m_a	Added mass due to inertial effects of water entrained with the ship
M_t	Marina fundamental mode
M_{t2}	Marina second harmonic
M_h	Marina Helmholtz mode
m_0	Zeroth moment
m_{0s}	The zeroth moment of the surge response
M_e	Marina entrance gauge
M_n	Marina north gauge
m_v	Virtual mass of system
M_w	Marina west gauge
n	Unit-normal vector directed outward from the fluid domain
N	Number of gauges
N_c	North corner gauge
NGA	Nearshore gauge array
Of	Offshore gauge
OGA	Offshore gauge array
On	Onshore gauge
$P(c_i)$	Probability of occurrence of currents in region i
$P(e_B)$	Probability of occurrence for environment B
$P(e_i)$	Probability for environmental conditions in region i to occur
$P(g_i)$	Percentage of unacceptable navigation conditions in region i assessed in physical model tests

$P(g_i)$	Probability of occurrence of groundings in region i
$P(s)$	Probability for ship to be present in the entrance channel for inbound or outbound run
$P(T_A)$	Probability for unacceptable navigation in region A
$P(T_B)$	Probability for unacceptable navigation in region B
$P(T_C)$	Probability for unacceptable navigation in region C
$P(T_i)$	Probability for unacceptable navigation in region i
$P(w_i)$	Probability of occurrence of waves in region i
$P(w_i)$	Probability of occurrence of wind in region i
Q_{ij}	Quad-spectra, the imaginary part of the cross-spectrum
r_θ	Correlation coefficients for the wave direction
r_σ	Correlation coefficients for the directional spread
RAO	Transfer function used to correct control signal to better match the target spectra
r_H	Correlation coefficients for the wave height
r_T	Correlation coefficients for the wave period
s	Distance between bottom and keel of ship, ft
$s_{1/3}$	Significant surge, ft
$S(f)$	One-sided spectral density, ft^2/Hz
$S(f)$	Frequency spectrum, ft^2/Hz
$S(f, \theta)$	Directional wave spectrum, ft^2/Hz
Sc	South corner gauge
$S_{ii}(f)$	Auto spectral density, ft^2/Hz
$S_{ij}(f)$	Cross-spectral density estimate
S_m	Gaussian smoothed line spectra
S_{m-j}	Raw auto spectral or cross-spectral estimate at frequency (m-j) ΔF
$S_p(f)$	Target spectral shape as a function of frequency
$S_s(\omega)$	Response spectrum of the ship in surge
$S_w(\omega)$	Sea spectrum as a function of frequency
S_{xy}	Directional wave gauge
S_{xy1}	First location of the directional wave gauge
S_{xy2}	Second location of the directional wave gauge
T	Axial tension in the mooring line, lb
T_{basin}	Natural period of the basin
T_{flat}	Natural periods of model resonance for the flat portion of the models, sec
T_{Roll}	Roll period of the prototype ship, sec
T_s	Undamped natural period of the ship in surge, sec
T_{slope}	Natural periods of model resonance for the sloped portion of the models, sec
w_j	Weighting function
W	Weight of displaced water
x	Direction perpendicular to wavemaker, ft
x	Displacement in surge, ft
x	Dummy variable of integration
x'	Velocity in surge, ft/sec
x''	Acceleration in surge, ft/sec^2
x_{flat}	Distance between DSWG and toe of slope, ft
x_{slope}	Distance between the toe of the slope and the shoreline, ft

y	Direction parallel to wavemaker, ft
z	Direction perpendicular to still-water level, ft (distance below surface to pressure gauge)
θ	Maximum wave direction to the linear array
$\bar{\theta}$	Peak wave direction
$\theta_m(f)$	Mean wave direction at each frequency
\bar{g}_m	Metacentric height, ft
α	Dimensional coefficient related to the boundary reflection
β	Dimensionless bottom friction coefficient that can vary spatially
γ	Phase shift between stress and flow velocity
∇	Horizontal gradient operator, ft^{-1}
Δf	Frequency increment
$\Delta\theta$	Mean wave direction as a function of the frequency
ΔT	Wave period increment used in the numerical model, sec
ξ	Damping factor, ratio of damping C to critical damping
$\eta_{x,y,t}$	Wave elevation time series at DSWG paddle location (x,y)
$C_c\Theta$	The angle between the wave direction and the y -direction
$\theta(f)$	Mean wave direction as a function of the frequency
θ_{cm}	The direction of current flow measured by the current meter
θ_g	The direction of current flow in the global northeast coordinate system
κ	Wave number, $(2\pi/L)$, where L = wavelength, ft^{-1}
λ	Complex bottom friction factor
σ_θ	Root mean square error for wave direction
σ_H	Root mean square error for wave height
σ_m	Standard deviation of the spreading function
σ_n	Standard deviation of the time series of surface wave elevations
σ_T	Root mean square error for wave period
Φ	Independent random phase, uniformly distributed on $(0,2\pi)$
ϕ	Velocity potential
ω	Radian frequency, rad/sec
ω	Angular frequency
ω_n	Natural frequency

REPORT DOCUMENTATION PAGEForm Approved
OMB No. 0704-0188

Public reporting burden for this collection of information is estimated to average 1 hour per response, including the time for reviewing instructions, searching existing data sources, gathering and maintaining the data needed, and completing and reviewing the collection of information. Send comments regarding this burden estimate or any other aspect of this collection of information, including suggestions for reducing this burden, to Washington Headquarters Services, Directorate for Information Operations and Reports, 1215 Jefferson Davis Highway, Suite 1204, Arlington, VA 22202-4302, and to the Office of Management and Budget, Paperwork Reduction Project (0704-0188), Washington, DC 20503.

1. AGENCY USE ONLY (Leave blank)**2. REPORT DATE**
September 1994**3. REPORT TYPE AND DATES COVERED**
Final report**4. TITLE AND SUBTITLE**Physical and Numerical Model Studies of Barbers Point Harbor,
Oahu, Hawaii**5. FUNDING NUMBERS****6. AUTHOR(S)**Michael J. Briggs, Linda S. Lillycrop, Gordon S. Harkins,
Edward F. Thompson, Debra R. Green**7. PERFORMING ORGANIZATION NAME(S) AND ADDRESS(ES)**U.S. Army Engineer Waterways Experiment Station
3909 Halls Ferry Road, Vicksburg, MS 39180-6199**8. PERFORMING ORGANIZATION
REPORT NUMBER**Technical Report
CERC-94-14**9. SPONSORING / MONITORING AGENCY NAME(S) AND ADDRESS(ES)**U.S. Army Corps of Engineers, Washington, DC 20314-1000
U.S. Army Engineer Division, Pacific Ocean, Ft. Shafter, HI
96858-5440**10. SPONSORING / MONITORING
AGENCY REPORT NUMBER****11. SUPPLEMENTARY NOTES**

Available from National Technical Information Service, 5285 Port Royal Road, Springfield, VA 22161.

12a. DISTRIBUTION / AVAILABILITY STATEMENT

Approved for public release; distribution is unlimited.

12b. DISTRIBUTION CODE**13. ABSTRACT (Maximum 200 words)**

The state of Hawaii identified the need for Barbers Point Harbor to accommodate larger ships and increase the number of available berths. Modifications to the harbor were proposed, including widening the entrance channel, and deepening (from 38 to 45 ft) and expanding the harbor basin (an 1,100-ft by 1,100-ft area on the northeast side of the harbor). Physical and numerical (computer) model studies were conducted from September 1990 to June 1992 at the U.S. Army Engineer Waterways Experiment Station to evaluate the technical feasibility and optimize the design of the proposed modifications. In addition to physical and computer model studies, navigation studies were also conducted using a scale model C9 container ship in the physical model.

Recommended modifications to Barbers Point Harbor include flaring of the outer 1,000 ft of the entrance channel from 450 ft wide to 750 ft wide, deepening the channel to 49 ft, constructing a 450-ft jetty along the north side of the entrance channel, deepening the harbor to 45 ft, and dredging a 1,100-ft by 1,100-ft expansion area in the harbor basin.

14. SUBJECT TERMS**15. NUMBER OF PAGES**
282**16. PRICE CODE****17. SECURITY CLASSIFICATION
OF REPORT**

UNCLASSIFIED

**18. SECURITY CLASSIFICATION
OF THIS PAGE**

UNCLASSIFIED

**19. SECURITY CLASSIFICATION
OF ABSTRACT****20. LIMITATION OF ABSTRACT**

Destroy this report when no longer needed. Do not return it to the originator.